AM-68-1
May 1, 1968

Final Report
Lunar Module (LM)
Soil Mechanics Study

Volume II

GPO PRICE $ _____

CFSTI PRICE(S) $ _____

Hard copy (HC) ___*3.00*___

Microfiche (MF) ___*.65*___

ff 653 July 65

APPENDIX A

SOIL SPECIFICATIONS

The data presented in this appendix will give descriptions of the 12 basic soils used in the LM soil mechanics study. The descriptions will include pertinent chemical analysis, physical properties and handling methods used to maintain repeatable test bed preparation for each soil.

a. Clarke, F. W., The Data of Geochemistry, Bulletin 770, 5th Ed., U.S. Geol. Surv., Government Printing Office, Washington, D. C., 1924.

b. Tyrrell, G. W., The Principles of Petrology, Methuen and Co., Ltd., London, E. P. Dutton and Co., Inc., New York, 1926.

c. American Society for Testing and Materials, Procedures for Testing Soils, ASTM, Philadelphia 3, Pa., 4th Ed., 1964.

LM SOIL MECHANICS STUDY

SPECIFICATION FOR SOIL NO. 1

1. <u>Bendix Designation</u>: RS, Loose

2. <u>Description</u>: Red narrowly-graded crushed andesitic volcanic scoria (volcanic cinders).

3. <u>Source</u>: Cinder Products Company
   3450 Lakeshore Avenue, Oakland, California 94610

4. <u>Source Name</u>: Volcalite

5. <u>Chemical Analysis</u>:

		Volcalite*	Hypersthene Andesite (a, pp. 456-466)
Silica	(SiO_2)	54.22	56.88
Aluminum Oxide	(Al_2O_3)	25.04	18.25
Ferric Oxide	(Fe_2O_3)	4.28	2.35
Calcium Oxide	(CaO)	8.11	7.53
Magnesium Oxide	(MgO)	5.58	4.07
Sodium Oxide	(NaO)	1.61	3.29
Potassium Oxide	(K_2O)	0.41	1.42
		99.25	

* Chemical analysis provided by producer.

A-2

6. Petrological Description

Highly porous volcanic (extrusive) rock of "basic" composition, commonly termed volcanic scoria. A comparison of the chemical analysis provided by the producer with other published analyses (a, pp. 456-466; b, pp. 126-131) indicates that the rock type is an andesite. Figure A-1 is a photomicrograph of the RS soil.

7. Mineralogical Description

No mineralogic analysis of the test soil has been done, but a normative analysis of the hypersthene andesite reported by Clarke (a, p. 458) gives the following:

Quartz	9.1%
Orthoclase	8.3%
Albite	27.8%
Anorthite	30.9%
Diopside	5.3%
Hypersthene	13.2%
Magnetite	3.5%
Ilmenite	0.8%

The reddish color of the RS soil would indicate that this material contains iron hydroxides (e.g. limonite) rather than the magnetite and ilmenite referred to in the norm and probably constitutes a larger percentage of the RS material than the iron minerals used in the example.

Decomposition due to weathering tends to decrease the percentage of silica, calcium oxide and sodium oxide and increase the percentage of ferric oxides and aluminum oxide (leaching, chloritization and kaolinization). The iron oxides (e.g., magnetite, ilmenite) tend to form iron hydroxides (e.g., ilmenite); the femic minerals (e.g., hypersthene) to form chlorite (chloritization); and the feldspars (e.g., orthoclase, albite) to form clays (kaolinization). The chemical analyses exhibit these trends indicating that some decomposition due to weathering has occurred.

Scale Graduated In
1/32 Inch Increments

Figure A-1. Photomicrograph R.S. Soil

8. Moisture Content

All tests were run on air-dried material. Oven-drying of the air-dried soil at 230° F yielded moisture contents commonly in the range of 0.2 to 0.6% (percent of dry weight of soil).

9. Grain Size Distribution

Figure A-2 shows the range and average grain size distribution of this soil. The table on this figure lists some of the grain size parameters investigated in this study. All data shown is for unused, undegraded material.

10. Density and Relative Density

The average relative density of Soil No. 1 is zero. Figure A-3 shows the relationship between soil unit weight (density) and relative density for the RS soil as determined by the method of test suggested by D. M. Burmister (c, pp. 175-177). The solid line represents the average of several tests on unused, undegraded soil, and the dashed lines indicate the 95% confidence limits for the data.

11. Direct Shear Test Results

Figure A-4 shows the relationship between angle of internal friction and relative density obtained from the direct shear tests. This figure indicates that the angle of internal friction for Soil No. 1 is about 41°. The complete data obtained from the direct shear tests is given in Appendix C.

12. Sonic Velocity Test

The values of initial tangent modulus yielded for Soil No. 1 by this test is about 5500 psi at a confining pressure of 4 psi (no correction made for Poisson's Ratio). A detailed description of the test apparatus and procedures is given in Appendix B.

13. Soil Test Bed Placement Procedure

Soil No. 1 was placed using the hopper method.
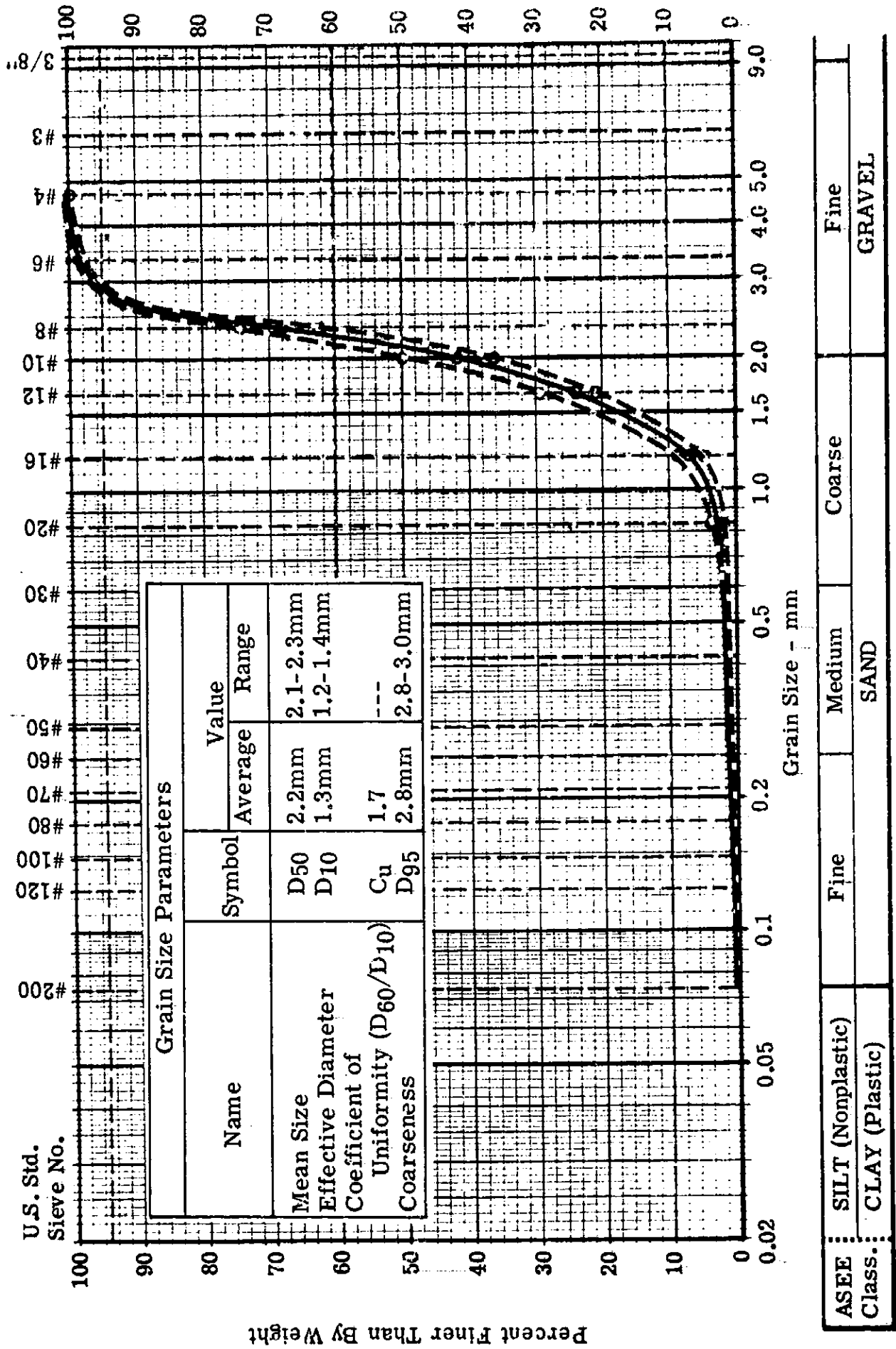
GRAIN SIZE ANALYSIS CURVES - LM SMS

Grain Size Parameters			
		Value	
Name	Symbol	Average	Range
Mean Size	D_{50}	2.2mm	2.1-2.3mm
Effective Diameter	D_{10}	1.3mm	1.2-1.4mm
Coefficient of Uniformity (D_{60}/D_{10})	C_u	1.7	---
Coarseness	D_{95}	2.8mm	2.8-3.0mm

Grain Size – mm

Percent Finer Than By Weight

U.S. Std. Sieve No.

ASEE Class.	SILT (Nonplastic) CLAY (Plastic)	Fine	Medium	Coarse	Fine
			SAND		GRAVEL

Figure A-2. Average and Range of Three Samples of Unused RS Soil
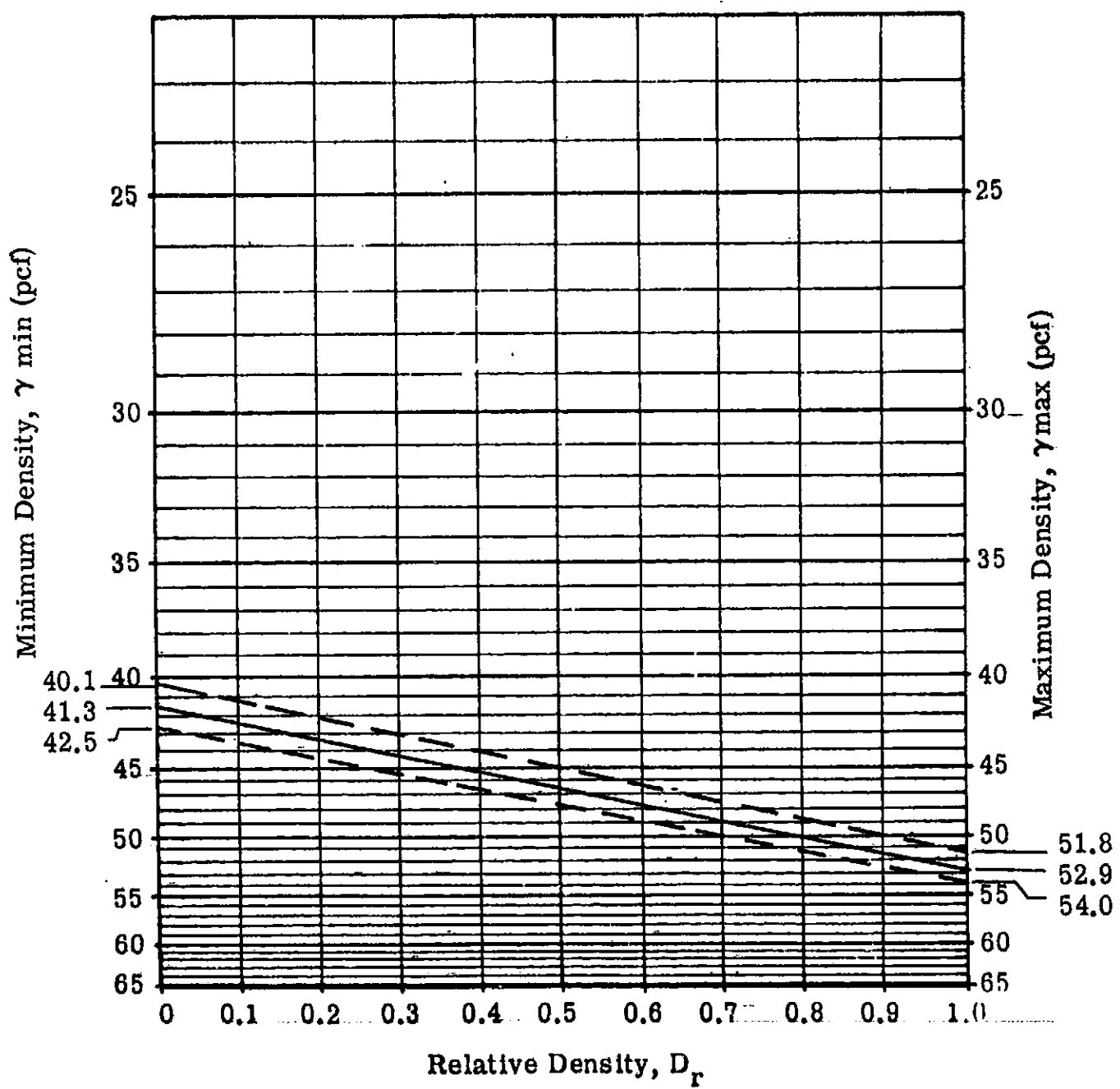
Figure A-3. Density Versus Relative Density for RS Soil
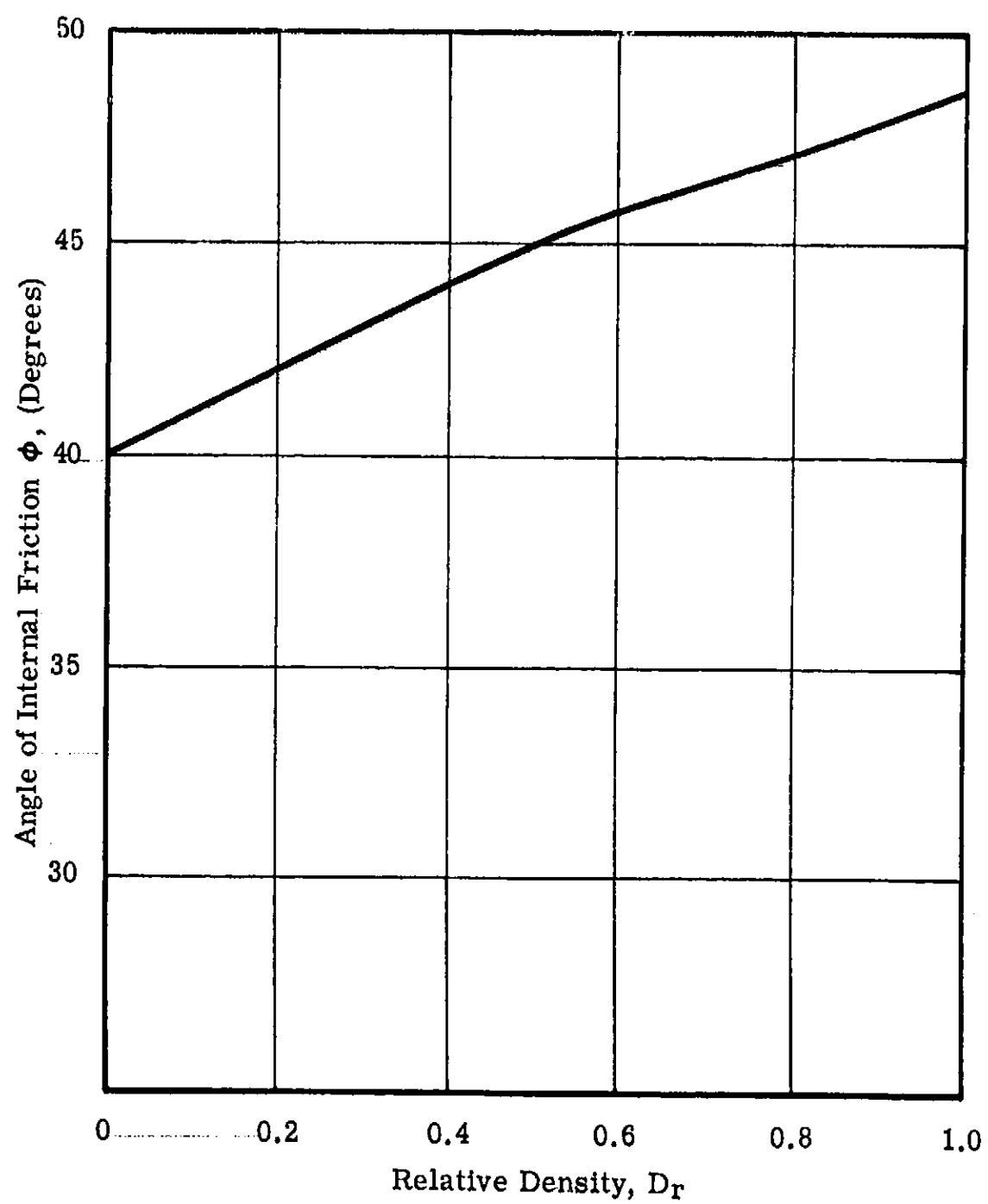
Figure A-4. Angle of Internal Friction (as determined by the direct shear test) Versus Relative Density for RS Soil

14. **Special Comments**

The RS soil is susceptible to particle breakdown or degradation due to handling and testing. Such degradation leads to changes in some soil properties, unit weight in particular. If the handling method is such that this process cannot be prevented, or the soil cannot be replaced when these effects become prominent, periodic sampling of the soil test bed should be made in order that the effects be known quantitatively.

LM SOIL MECHANICS STUDY

SPECIFICATION FOR SOIL NO. 2

1. Pendix Designation: PS Loose

2. Description: White narrowly-graded crushed pumice (volcanic cinders).

3. Source: James H. Rhodes and Company,
1026 W. Jackson Boulevard, Chicago, Illinois 60607

4. Source Name: Navajo Pumice

5. Chemical Analysis:*

Silicon Dioxide	(S_iO_2)	74.2%
Ferric Oxide	(Fe_2O_3)	1.6%
Aluminum Oxide	(Al_2O_3)	12.5%
Calcium Oxide	(CaO)	0.4%
Magnesium Oxide ——	(MgO)	0.2%
Phosphorus	(P)	Trace

Alkalies not tested for:—

Sodium Oxide	(NaO)	11.0%
Potassium Oxide	(K_2O)	11.0%
Moisture		11.0%

*Provided by the supplier.

6. Petrological Description

Very highly porous volcanic (extrusive) rock of "acid" or rhyolitic composition. The chemical analysis is typical of a pumice. The supplier reports that this material is mined in the area of Santa Fe, New Mexico. Pumice is formed when very silicic volcanic ejecta is deposited in water. The rapid cooling is responsible for the highly porous nature of this rock. Figure A-5 is a photomicrograph of the PS soil.

7. Mineralogical Description

No mineralogic analysis of the pumice has been done, but the chemical analysis would indicate that it was composed primarily of orthoclase and quartz.

8. Moisture Content

All tests were run on air-dried material. Oven-drying of the air-dried soil at 230°F yielded moisture contents commonly in the range of 0.2 to 0.6% (percent of dry weight of soil).

9. Grain Size Distribution

Figure A-6 shows the range and average grain size distribution of this soil. The table on this figure lists some of the grain size parameters investigated in this study. All data shown is for unused, undegraded material.

10. Density and Relative Density

The average relative density of Soil No. 2 is zero. Figure A-7 shows the relationship between soil unit weight (density) and relative density for PS soil as determined by the method of test suggested by D. M. Burmister (c, pp. 175-177). The solid line represents the average of several tests on unused, undegraded soil, and the dashed lines indicate the 95% confidence limits for the data.

11. Direct Shear Test Results

Figure A-8 shows the relationship between angle of internal friction and relative density obtained from the direct shear tests.

Scale Graduated In
1/32 Inch Increments

Figure A-5. Photomicrograph PS Soil
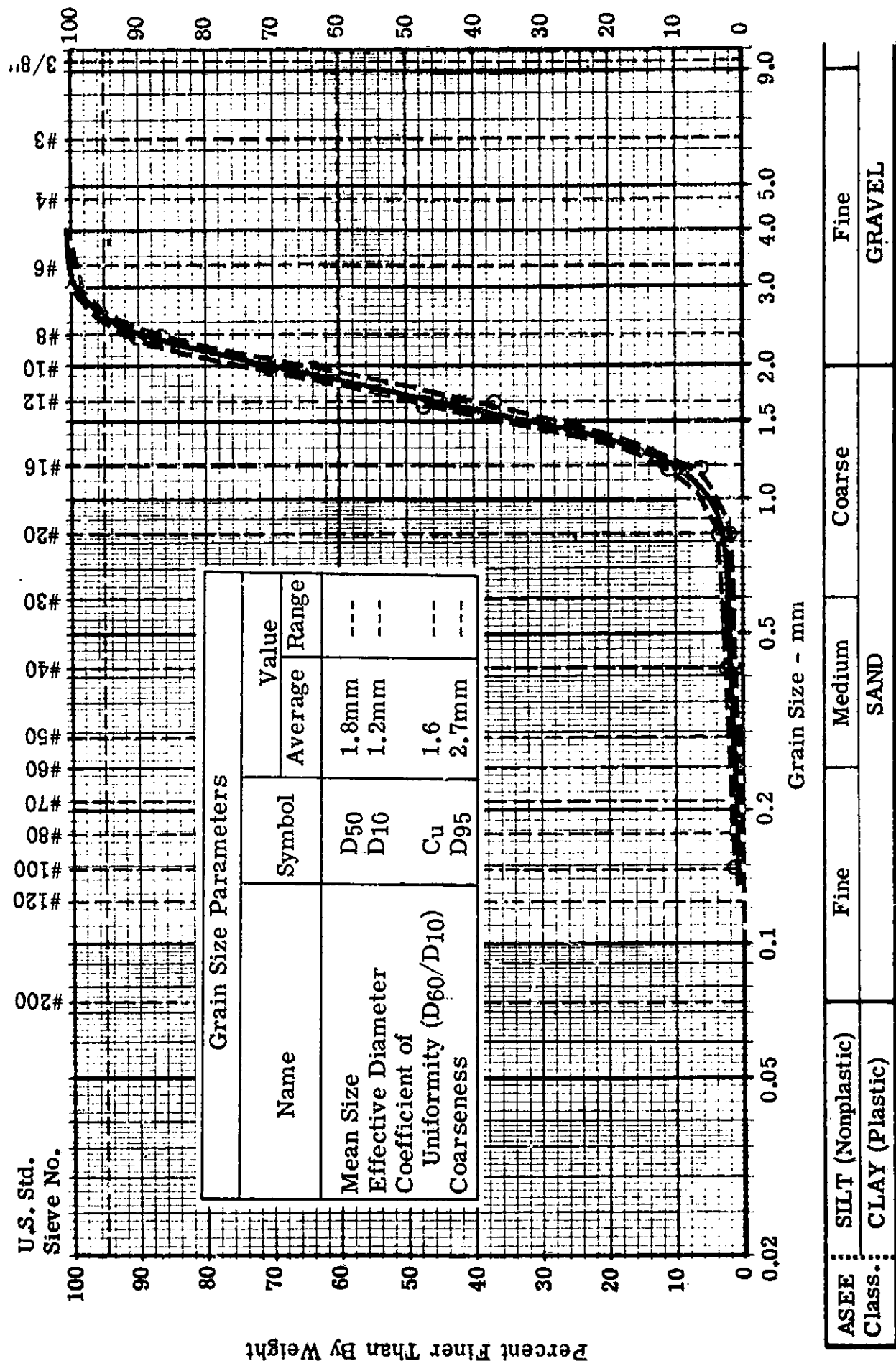
GRAIN SIZE ANALYSIS CURVES - LM SMS

Grain Size Parameters		Value	
Name	Symbol	Average	Range
Mean Size	D_{50}	1.8mm	- - -
Effective Diameter	D_{10}	1.2mm	- - -
Coefficient of Uniformity (D_{60}/D_{10})	C_u	1.6	- - -
Coarseness	D_{95}	2.7mm	- - -

U.S. Std. Sieve No.

Percent Finer Than By Weight

Grain Size - mm

ASEE	Fine	Medium	Coarse	Fine
Class.	SILT (Nonplastic)	SAND		GRAVEL
	CLAY (Plastic)			

Figure A-6. Average and Range for Three Samples of Unused PS Soil

A-13
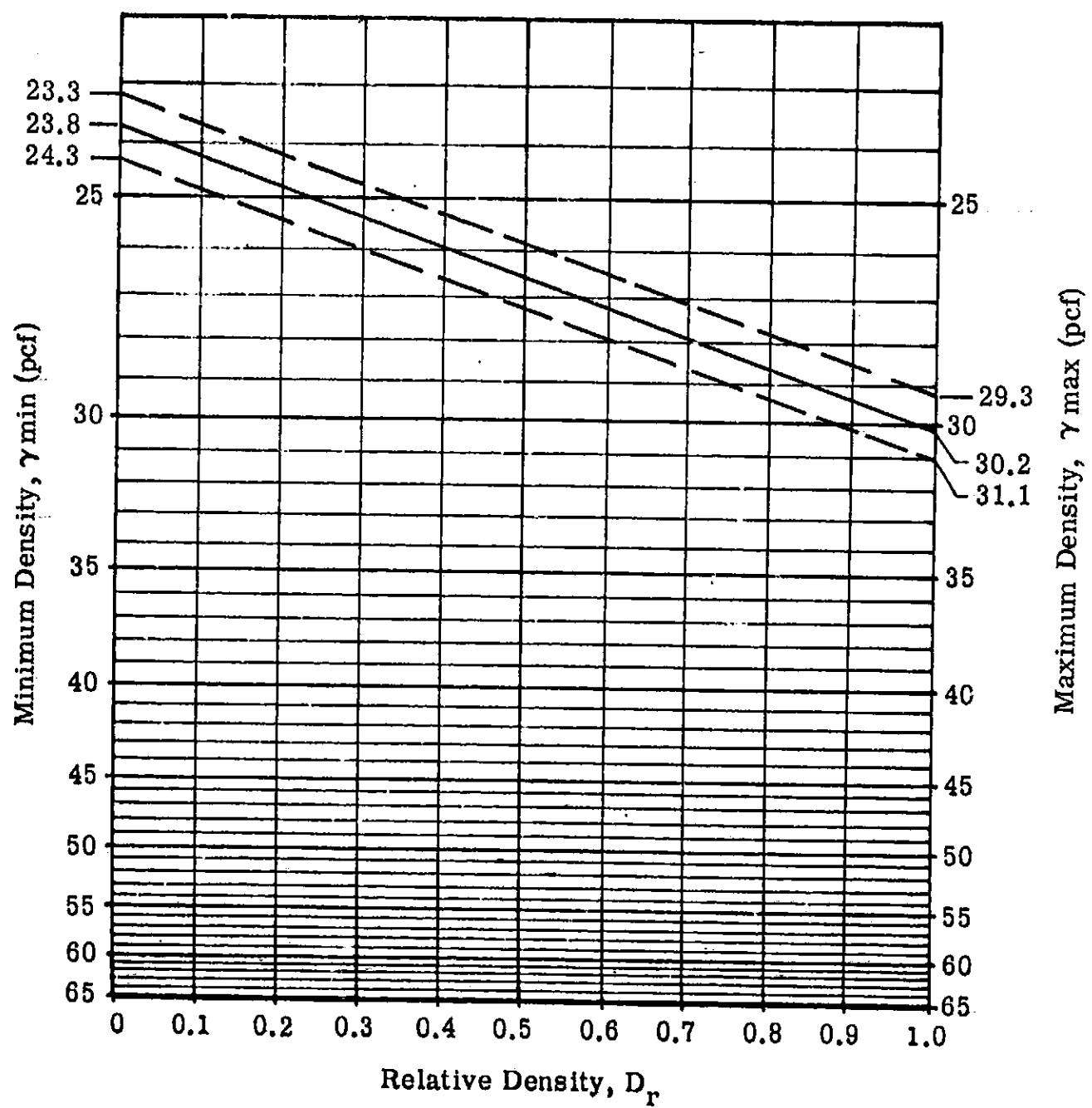
Figure A-7. Density Versus Relative Density for PS Soil
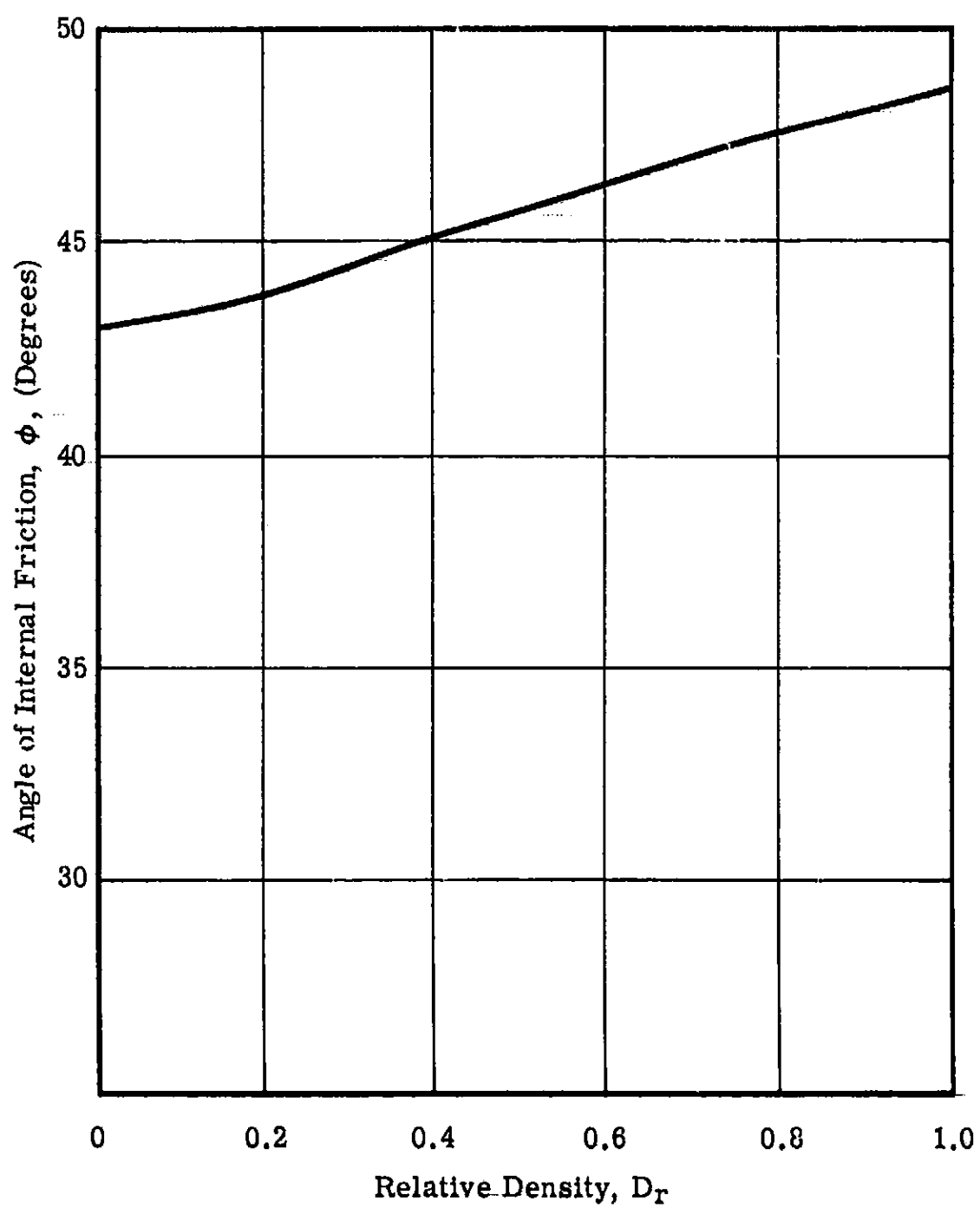
Figure A-8. Angle of Internal Friction (as determined by the direct
shear test) Versus Relative Density for PS Soil

This figure indicates that the angle of internal friction for Soil No. 2 is about 43°. The complete data obtained from the direct shear tests is given in Appendix C.

12. Sonic Velocity Test

The values of initial tangent modulus yielded for Soil No. 2 by this test is about 4500 psi at a confining pressure of 4 psi (no correction made for Poisson's Ratio). A detailed description of the test apparatus and procedures is given in Appendix B.

13. Soil Test Bed Placement Procedures

Soil No. 2 was placed using the hopper method.

14. Special Comments

The PS soil is susceptible to particle breakdown or degradation due to handling and testing. Such degradation leads to changes in some soil properties, unit weight in particular. If the handling method is such that this process cannot be prevented, or the soil cannot be replaced when these effects become prominent, periodic sampling of the soil test bed should be made in order that the effects be known quantitatively.

LM SOIL MECHANICS STUDY

SPECIFICATION FOR SOIL NO. 3

1. **Bendix Designation:** RS, Intermediate

2. **Description:** Red narrowly-graded crushed andesitic volcanic scoria (volcanic cinders).

3. **Source:** Cinder Products Company
   3450 Lakeshore Avenue, Oakland, California 94610

4. **Source Name:** Volcalite.

5. **Chemical Analysis:**

		Volcalite*	Hypersthene Andesite (a, pp. 456-466)
Silica	(SiO_2)	54.22	56.88
Aluminum Oxide	(Al_2O_3)	25.04	18.25
Ferric Oxide	(Fe_2O_3)	4.28	2.35
Calcium Oxide	(CaO)	8.11	7.53
Magnesium Oxide	(MgO)	5.58	4.07
Sodium Oxide	(NaO)	1.61	3.29
Potassium Oxide	(K_2O)	0.41	1.42
		99.25	

*Chemical analysis provided by producer.

6. Petrological Description

Highly porous volcanic (extrusive) rock of "basic" composition, commonly termed volcanic scoria. A comparison of the chemical analysis provided by the producer with other published analyses (a, pp. 456-466; b, pp. 126-131) indicates that the rock type is an andesite. Figure A-9 is a photomicrograph of the RS soil.

7. Mineralogical Description

No mineralogic analysis of the test soil has been done, but a normative analysis of the hypersthene andesite reported by Clarke (a, p. 458) gives the following:

Quartz	9.1%
Orthoclase	8.3%
Albite	27.8%
Anorthite	30.9%
Diopside	5.3%
Hypersthene	13.2%
Magnetite	3.5%
Ilmenite	0.8%

The reddish color of the RS soil would indicate that this material contains iron hydroxides (e.g., limonite) rather than the magnetite and ilmenite referred to in the norm and probably constitutes a larger percentage of the RS material than the iron minerals used in the example.

Decomposition due to weathering tends to decrease the percentage of silica, calcium oxide and sodium oxide and increase the percentage of ferric oxides and aluminum oxide (leaching, chloritization and kaolinization). The iron oxides (e.g., magnetite, ilmenite) tend to from iron hydroxides (e.g., limonite); the femic minerals (e.g., hypersthene) to form chlorite (chloritization); and the feldspars (e.g., orthoclase, albite) to form clays (kaolinization). The chemical analyses exhibit these trends indicating that some decomposition due to weathering has occurred.

A-18

Scale Graduated In
1/32 Inch Increments

Figure A-9. Photomicrograph RS Soil

A-19

8. Moisture Content

All tests were run on air-dried material. Oven-drying of the air-dried soil at 230°F yielded moisture contents commonly in the range of 0.2 to 0.6% (percent of dry weight of soil).

9. Grain Size Distribution

Figure A-10 shows the range and average grain size distribution of this soil. The table on this figure lists some of the grain size parameters investigated in this study. All data shown is for unused undegraded material.

10. Density and Relative Density

The average relative density of Soil No. 3 is about 0.45. Figure A-11 shows the relationship between soil unit weight (density) and relative density for the RS soil as determined by the method of test suggested by D. M. Burmister (c, pp. 175-177). The solid line represents the average of several tests on unused, undegraded soil, and the dashed lines indicate the 95% confidence limits for the data.

11. Direct Shear Test Results

Figure A-12 shows the relationship between angle of internal friction and relative density obtained from the direct shear tests.

This figure indicates that the angle of internal friction for Soil No. 3 is about 43.9°. The complete data obtained from the direct shear tests is given in Appendix C.

12. Sonic Velocity Test

The values of initial tangent modulus yielded for Soil No. 3 by this test is about 8600 psi at a confining pressure of 4 psi (no correction made for Poisson's Ratio).

A detailed description of the test apparatus and procedures is given in Appendix B.
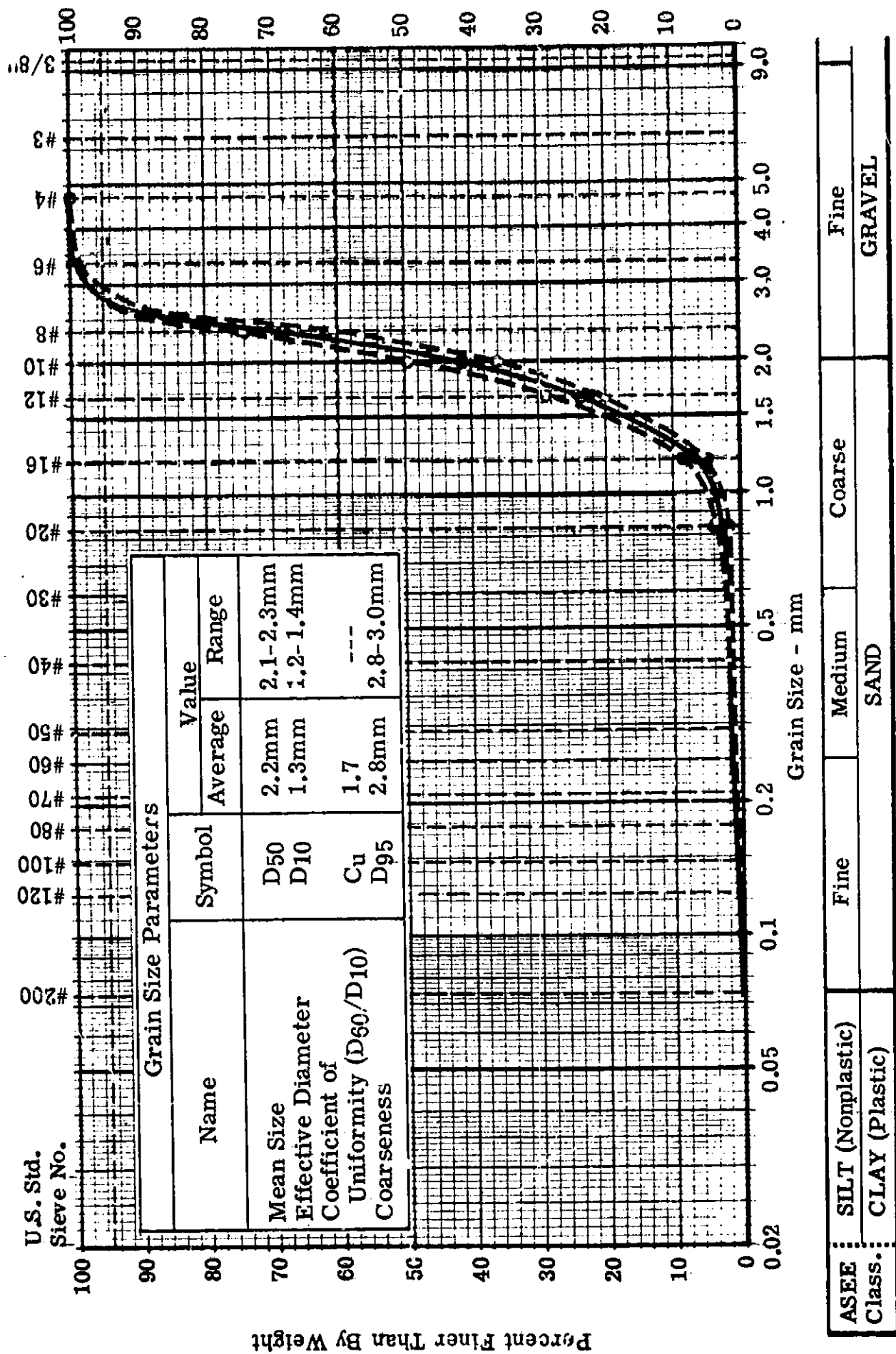
GRAIN SIZE ANALYSIS CURVES - LM SMS

Grain Size Parameters			
Name	Symbol	Value	
		Average	Range
Mean Size	D_{50}	2.2mm	2.1-2.3mm
Effective Diameter	D_{10}	1.3mm	1.2-1.4mm
Coefficient of Uniformity (D_{60}/D_{10})	C_u	1.7	---
Coarseness	D_{95}	2.8mm	2.8-3.0mm

U.S. Std. Sieve No.

Percent Finer Than By Weight

Grain Size – mm

ASEE Class.	Fine					Fine
	SILT (Nonplastic)		Medium	Coarse		GRAVEL
	CLAY (Plastic)	Fine	SAND			

Figure A-10. Average and Range of Three Samples of Unused RS Soil
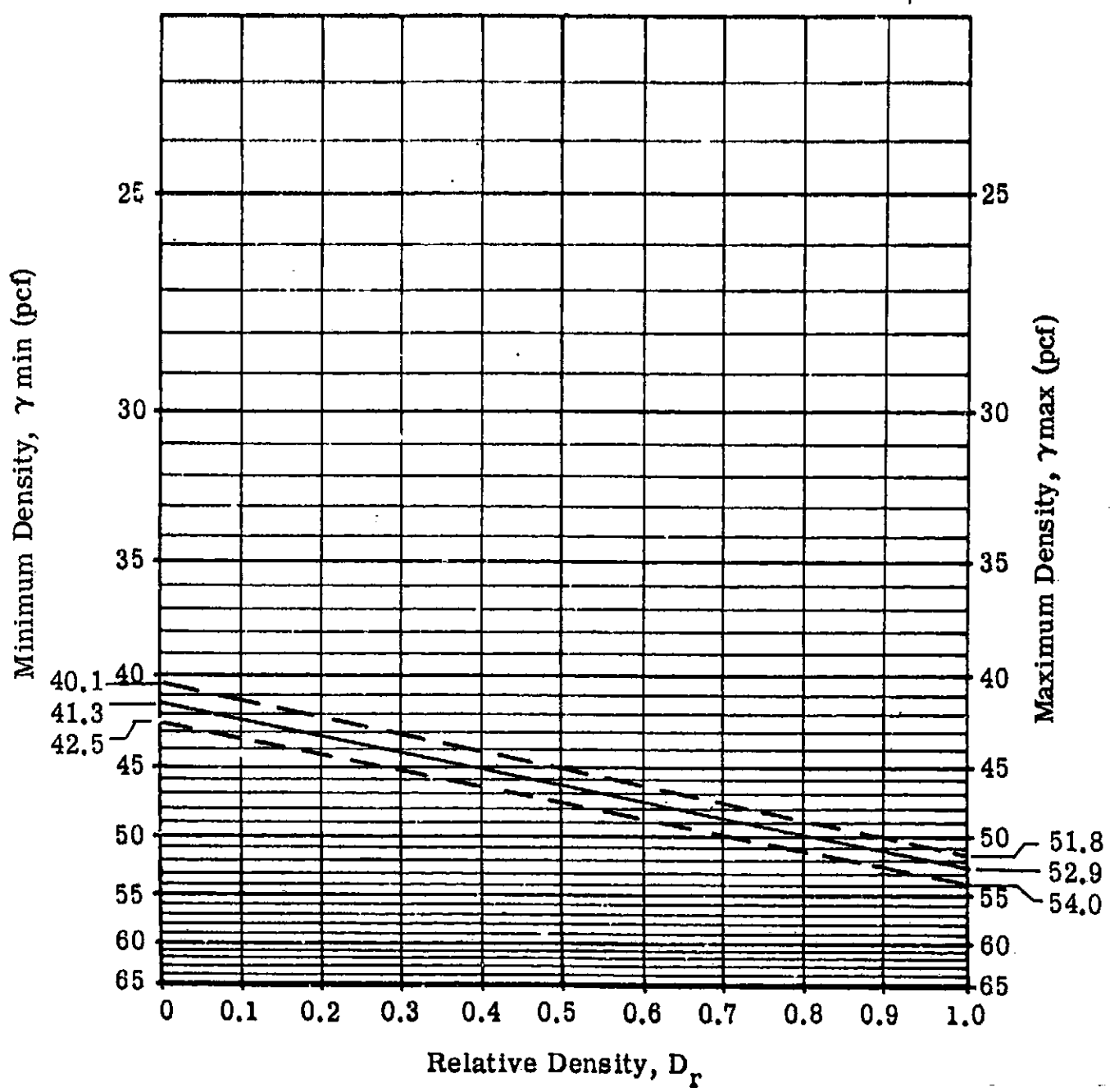
Figure A-11. Density Versus Relative Density for RS Soil
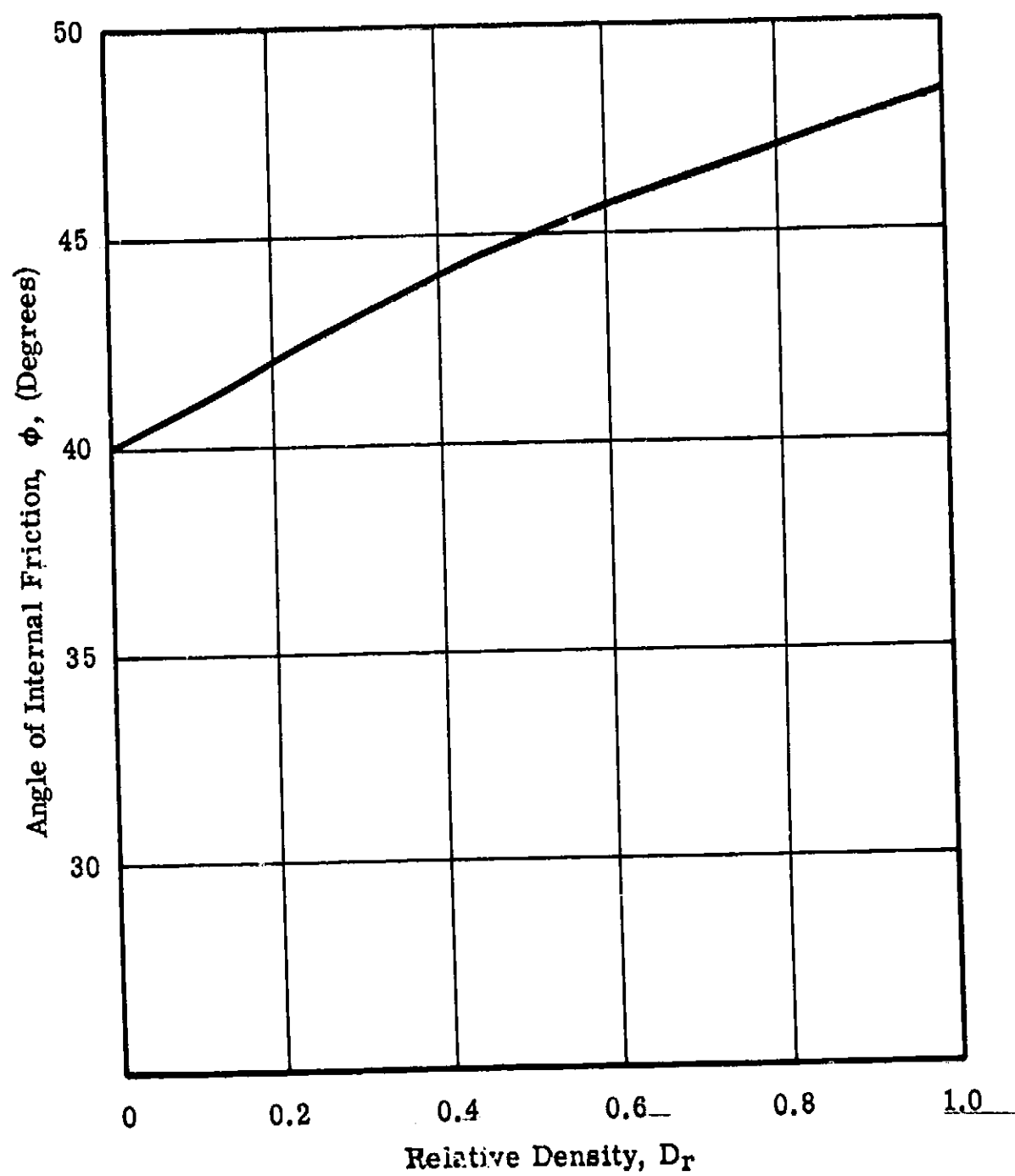
Figure A-12. Angle of Internal Friction (as determined by the direct shear test) Versus Relative Density for RS Soil

13. Soil Test Bed Placement Procedure

Soil No. 3 was placed using a hopper and compacted with 2 passes of a roller.

14. Special Comments

The RS soil is susceptible to particle breakdown or degradation due to handling and testing. Such degradation leads to changes in some soil properties, unit weight in particular. If the handling method is such that this process cannot be prevented, or the soil cannot be replaced when these effects become prominent, periodic sampling of the soil test bed should be made in order that the effects be known quantitatively.

A-24

LM SOIL MECHANICS STUDY

SPECIFICATION FOR SOIL NO. 4

1. Bendix Designation: RS, Dense

2. Description: Red narrowly-graded crushed andesitic volcanic scoria (volcanic cinders).

3. Source: Cinder Products Company
3450 Lakeshore Avenue, Oakland, California 94610

4. Source Name: Volcalite

5. Chemical Analysis:

		Volcalite*	Hypersthene Andesite (a, pp. 456-466)
Silica	(SiO_2)	54.22	56.88
Aluminum Oxide	(Al_2O_3)	25.04	18.25
Ferric Oxide	(Fe_2O_3)	4.28	2.35
Calcium Oxide	(CaO)	8.11	7.53
Magnesium Oxide	(MgO)	5.58	4.07
Sodium Oxide	(NaO)	1.61	3.29
Potassium Oxide	(K_2O)	0.41	1.42
		99.25	

*Chemical analysis provided by producer.

6.___Petrological Description

Highly porous volcanic (extrusive) rock of "basic" composition, commonly termed volcanic scoria. A comparison of the chemical analysis provided by the producer with other published analyses (a, pp. 456-466; b, pp. 126-131) indicates that the rock type is an andesite. Figure A-13 is a photomicrograph of the RS soil.

7. Mineralogical Description

No mineralogic analysis of the test soil has been done, but a normative analysis of the hypersthene andesite reported by Clarke (a, p. 458) gives the following:

Quartz	9.1%
Orthoclase	8.3%
Albite	27.8%
Anorthite	30.9%
Diopside	5.3%
Hypersthene	13.2%
Magnetite	3.5%
Ilmenite	0.8%

The reddish color of the RS soil would indicate that this material contains iron hydroxides (e.g., limonite) rather than the magnetite and ilmenite referred to in the norm and probably constitutes a larger percentage of the RS material than the iron minerals used in the example.

Decomposition due to weathering tends to decrease the percentage of silica, calcium oxide and sodium oxide and increase the percentage of ferric oxides and aluminum oxide (leaching, chloritization and kaolinization). The iron oxides (e.g., magnetite, ilmenite) tend to form iron hydroxides (e.g., limonite); the femic minerals (e.g., hypersthene) to form chlorite (chloritization); and the feldspars (e.g. orthoclase, albite) to

A-26

Scale Graduated In
1/32 Inch Increments

Figure A-13. Photomicrograph RS Soil

form clays (kaolinization). The chemical analyses exhibit these trends indicating that some decomposition due to weathering has occurred.

8. Moisture Content

All tests were run on air-dried material. Oven-drying of the air-dried soil at 230°F yielded moisture contents commonly in the range of 0.2 to 0.6% (percent of dry weight of soil).

9. Grain Size Distribution

Figure A-14 shows the range and average grain size distribution of this soil. The table on this figure lists some of the grain size parameters investigated in this study. All data shown is for unused, undegraded material.

10. Density and Relative Density

The average relative density of Soil No. 4 is about 0.8. Figure A-15 shows the relationship between soil unit weight (density) and relative density for the RS soil as determined by the method of test suggested by D. M. Burmister (c, pp. 175-177). The solid line represents the average of several tests on unused, undegraded soil, and the dashed lines indicate the 95% confidence limits for the data.

11. Direct Shear Test Results

Figure A-16 shows the relationship between angle of internal friction and relative density obtained from the direct shear tests.

This figure indicates that the angle of internal friction for Soil No. 4 is about 47.9°.

The complete data obtained from the direct shear tests is given in Appendix C.

12. Sonic Velocity Test

The values of initial tangent modulus yielded for Soil No. 4 by this test is about 10,900 psi at a confining pressure of 4 psi (no correction made for Poisson's Ratio). A detailed description of the test apparatus and procedures is given in Appendix B.

A-28

GRAIN SIZE ANALYSIS CURVES – LM SMS

Grain Size Parameters		Value	
Name	Symbol	Average	Range
Mean Size	D50	2.2mm	2.1-2.3mm
Effective Diameter	D10	1.3mm	1.2-1.4mm
Coefficient of Uniformity (D60/D10)	Cu	1.7	---
Coarseness	D95	2.8mm	2.8-3.0mm

ASEE Class:	Fine	Medium	Coarse	Fine
SILT (Nonplastic)		SAND		GRAVEL
CLAY (Plastic)				

Grain Size – mm

Percent Finer Than By Weight

U.S. Std. Sieve No.
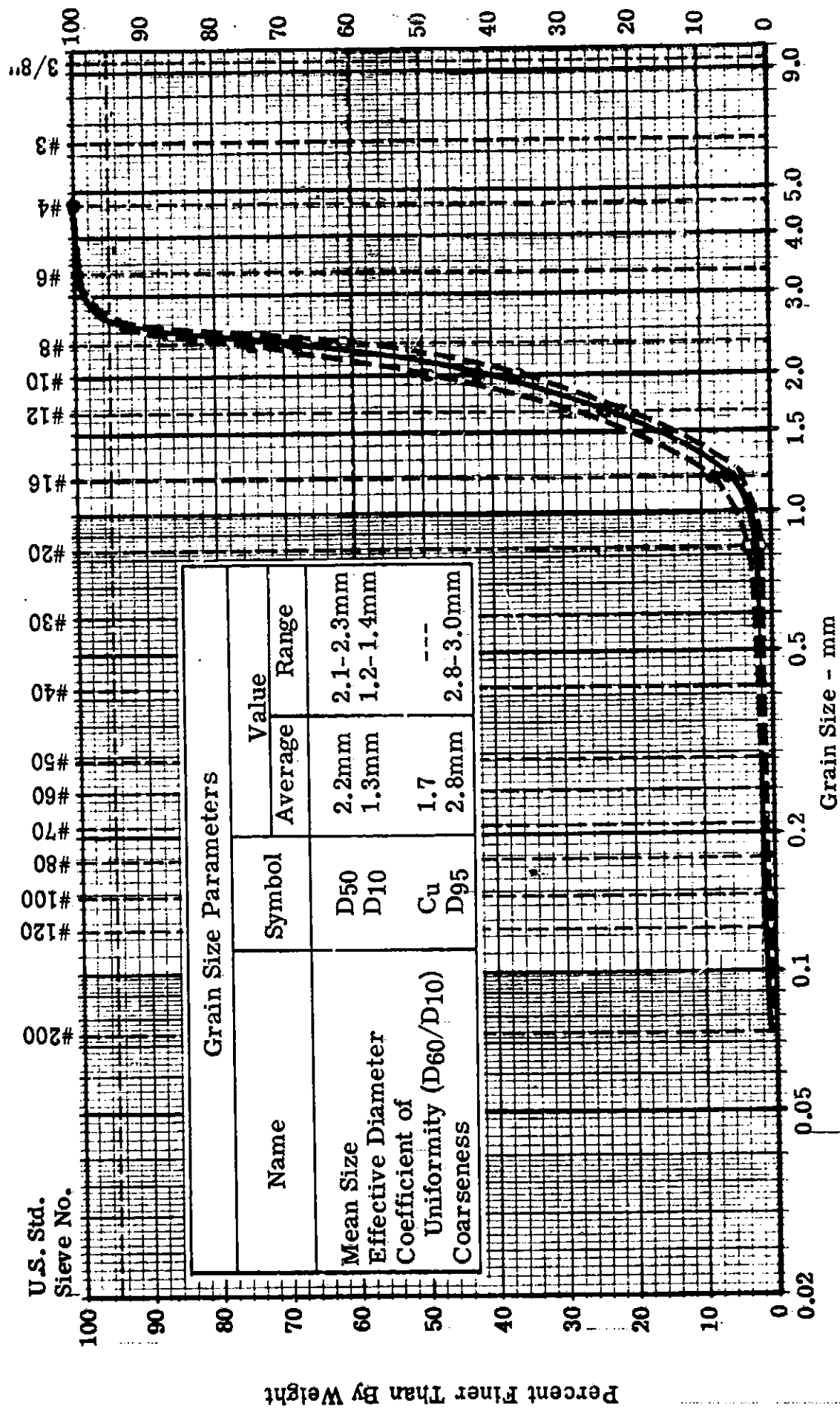
Figure A-14. Average and Range of Three Examples of Unused RS Soil

A-29
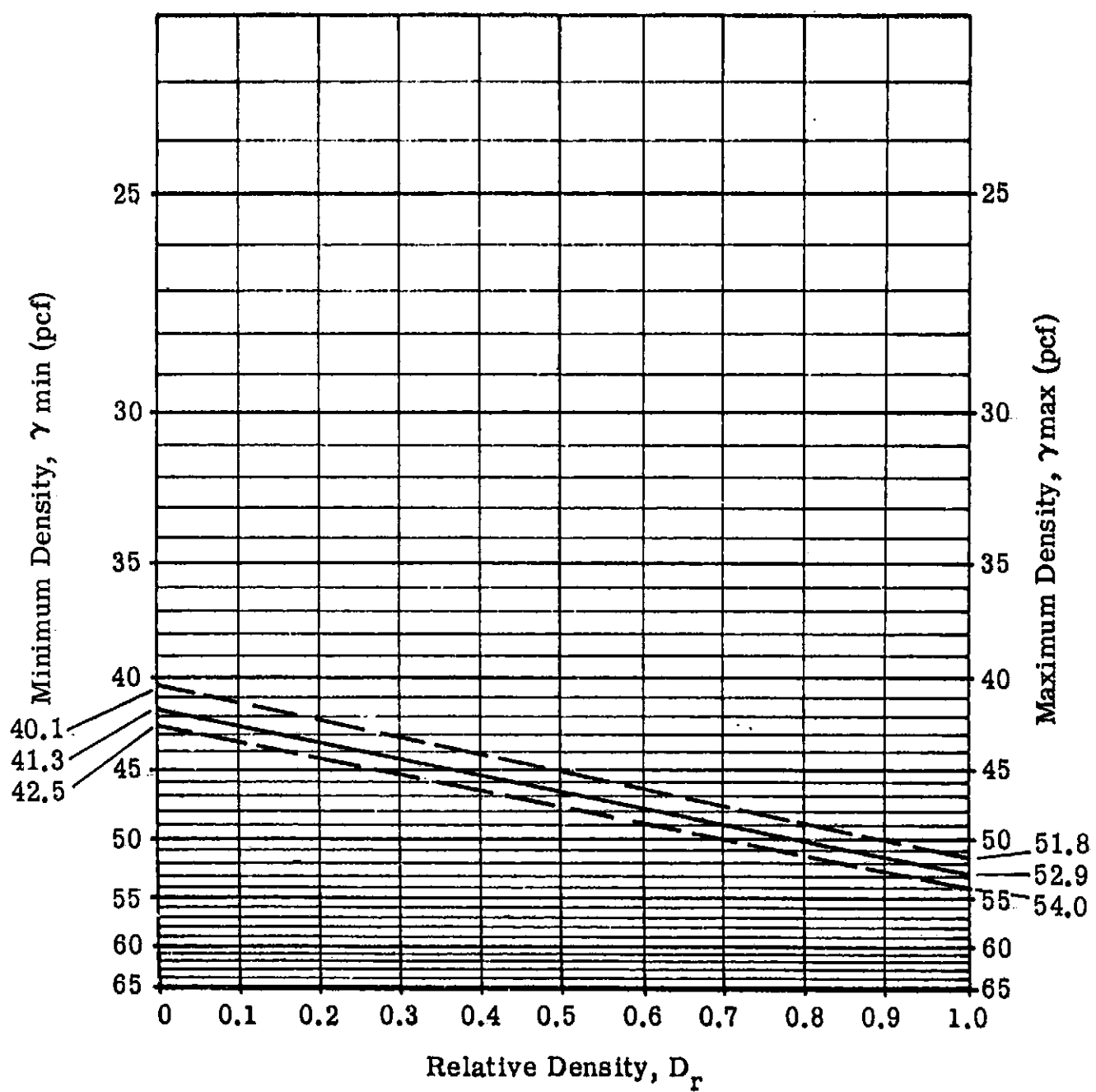
Figure A-15. Density Versus Relative Density for RS Soil
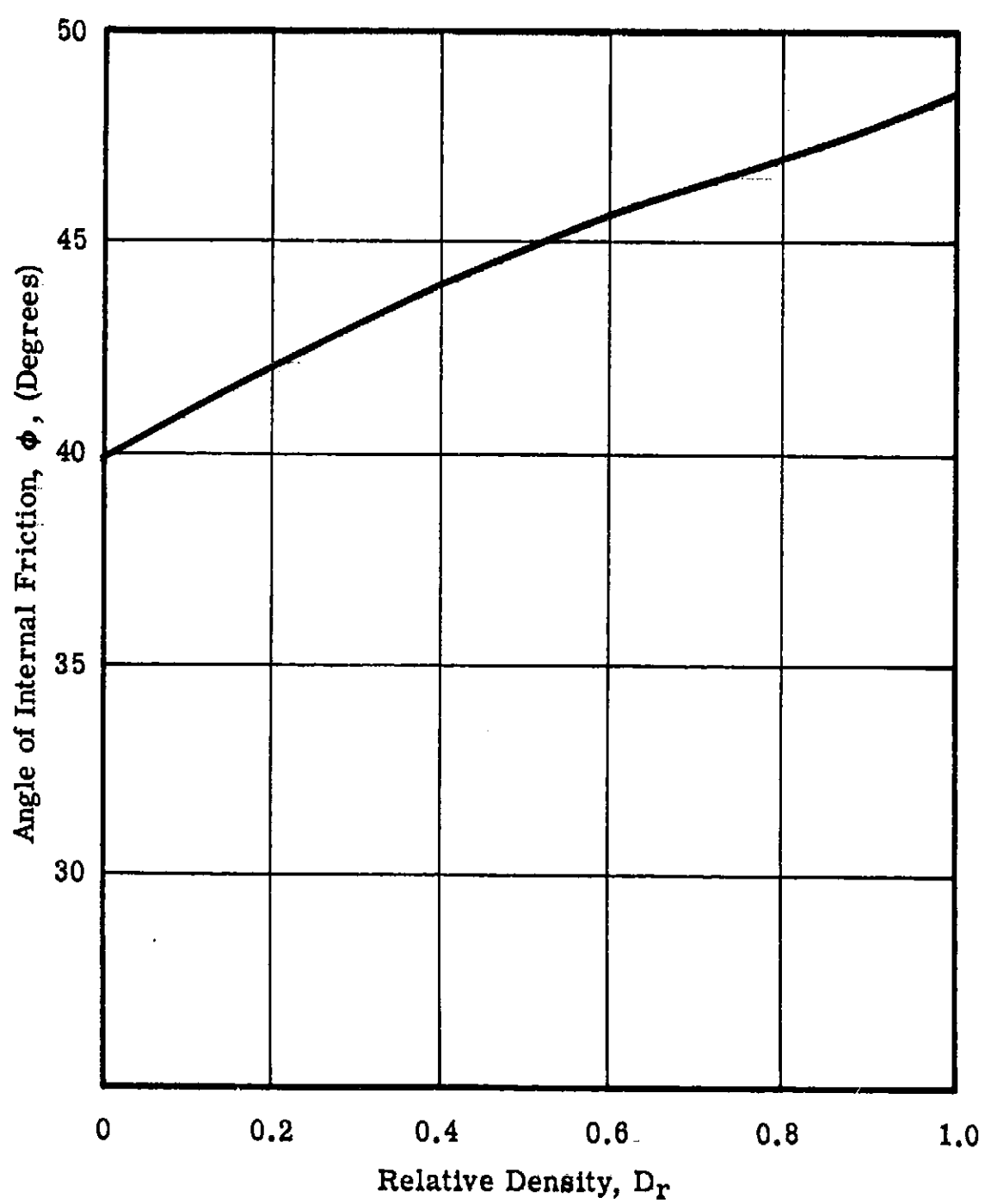
Figure A-16. Angle of Internal Friction (as determined by the direct shear test) Versus Relative Density for RS Soil

13. Soil Test Bed Placement Procedure

Soil No. 4 was placed using a hopper and compacted with 16 passes of a roller.

14. Special Comments

The RS soil is susceptible to particle breakdown or degradation due to handling and testing. Such degradation leads to changes in some soil properties, unit weight in particular. If the handling method is such that this process cannot be prevented, or the soil cannot be replaced when these effects become prominent, periodic sampling of the soil test bed should be made in order that the effects be known quantitatively.

LM SOIL MECHANICS STUDY

SPECIFICATION FOR SOIL NO. 5

1.   Bendix Designation: RSM - a Loose.

2.   Description: Mixture of red narrowly-graded crushed andesitic volcanic scoria
     (volcanic cinders) and white narrowly-graded crushed marble.

3.   Source:

     (a) Volcanic Cinders
          Cinder Products Company
          3450 Lakeshore Avenue, Oakland, California 94610

     (b) Crushed Marble
          Terrazzo Marble Supply
          5700 S. Hamilton Street, Chicago, Illinois 60636

4.   Source Name:

     (a) Volcanic Cinders - Volcalite

     (b) Crushed Marble - #10 Georgia special white marble chips

5.   Chemical Analysis:

     (a) Volcanic Cinders

		Volcalite*	Hypersthene andesite (a, pp. 456-466)
Silica	(SiO_2)	54.22	56.88
Aluminum Oxide	(Al_2O_3)	25.04	18.25
Ferric Oxide	(Fe_2O_3)	4.28	2.35
Calcium Oxide	(CaO)	8.11	7.53
Magnesium Oxide	(MgO)	5.58	4.07
Sodium Oxide	(NaO)	1.61	3.29
Potassium Oxide	(K_2O)	0.41	1.42
		99.25	

(b) Crushed Marble. No chemical analysis available but it is primarily calcium carbonate $(CaCO_3)$.

6. Petrological Description

(a) Volcanic Cinders.

Highly porous volcanic (extrusive) rock of "basic" composition. Commonly termed volcanic scoria. A comparison of the chemical analysis provided by the producer with other published analyses (a, pp. 456-466; b, pp. 126-131) indicates that the rock type is an andesite.

(b) Crushed Marble.

Marble is a crystaline compact variety of metamorphosed sedimentary limestone.

The volcanic cinders and crushed marble are mixed in the ratio of 5:7, respectively, by weight. Figure A-17 is a photomicrograph of the resulting RSM soil.

---

*Chemical analysis supplied by producer.

Scale Graduated In
1/32 Inch Increments

Figure A-17. Photomicrograph RSM Soil

7. Mineralogical Description

    (a) Volcanic Cinders.

        No mineralogic analysis of the test soil has been done, but a normative ana-
lysis of the hypersthene andesite reported by Clarke (a, p. 458) gives the
following:

Quartz	9.1%
Orthoclase	8.3%
Albite	27.8%
Anorthite	30.9%
Diopside	5.3%
Hypersthene	13.2%
Magnetite	3.5%
Ilmenite	0.8%

The reddish color of the RS soil would indicate that this material contains iron hydrox-
ides (e.g., limonite) rather than the magnetite and ilmenite referred to in the norm
and probably constitutes a larger percentage of the RS material than the iron minerals
used in the example.

Decomposition due to weathering tends to decrease the percentage of silica, calcium
oxide and sodium oxide and increase the percentage of ferric oxides and aluminum oxide
(leaching, chloritization and kaolinization). The iron oxides (e.g. magnetite, ilmenite)
tend to form iron hydroxides (e.g., limonite); the femic minerals (e.g., hypersthene)
to form chlorite (chloritization); and the feldspars (e.g., orthoclase, albite) to form
clays (kaolinization). The chemical analyses exhibit these trends indicating that some
decomposition due to weathering has occurred.

(b) Crushed Marble.

No mineralogic analysis of the marble was done but it consists primarily of calcite.

8. Moisture Content

All tests were run on air-dried material. Oven-drying of the air-dried soil at 230°F yielded moisture contents commonly in the range of 0.2 to 0.6% (percent of dry weight of soil).

9. Grain Size Distribution

Figure A-18 shows the range and average grain size distribution of this soil. The table on this figure lists some of the grain size parameters investigated in this study. All data shown is for unused, undegraded material.

10. Density and Relative Density

The average relative density of Soil No. 5 is about zero. Figure A-19 shows the relationship between soil unit weight (density) and relative density for the RSM - a soil as determined by the method of test suggested by D. M. Burmister (c, pp. 175-177).

The solid line represents the average of several tests on unused, undegraded soil, and the dashed lines indicate the 95% confidence limits for the data.

11. Direct Shear Test Results

Figure A-20 shows the relationship between angle of internal friction and relative density obtained from the direct shear tests.

This figure indicates that the angle of internal friction for Soil No. 5 is about 37°. The complete data obtained from the direct shear tests is given in Appendix C.

GRAIN SIZE ANALYSIS CURVES - LM SMS

Grain Size Parameters		Value	
Name	Symbol	Average	Range
Mean Size	D50	2.4mm	2.3-2.4mm
Effective Diameter	D10	1.5mm	1.4-1.6mm
Coefficient of Uniformity (D60/D10)	Cu	1.6	---
Coarseness	D95	2.7mm	2.7-2.8mm

U.S. Std. Sieve No.

Percent Finer Than By Weight

Grain Size – mm

	Fine	Medium	Coarse	Fine
ASEE	SILT (Nonplastic)	SAND		GRAVEL
Class.	CLAY (Plastic)			
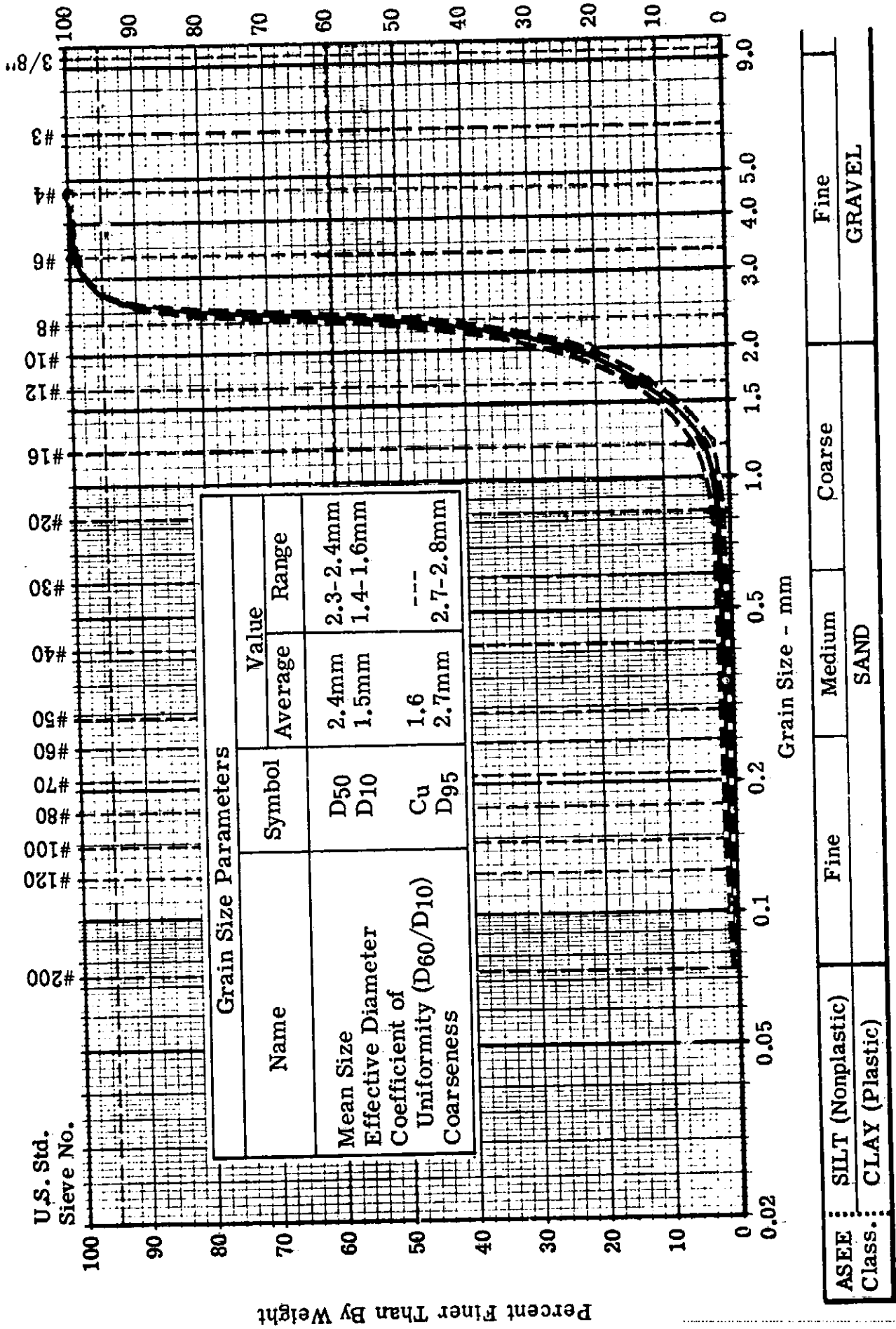
Figure A-18. Average and Range of Three Samples of Unused RSM Soil
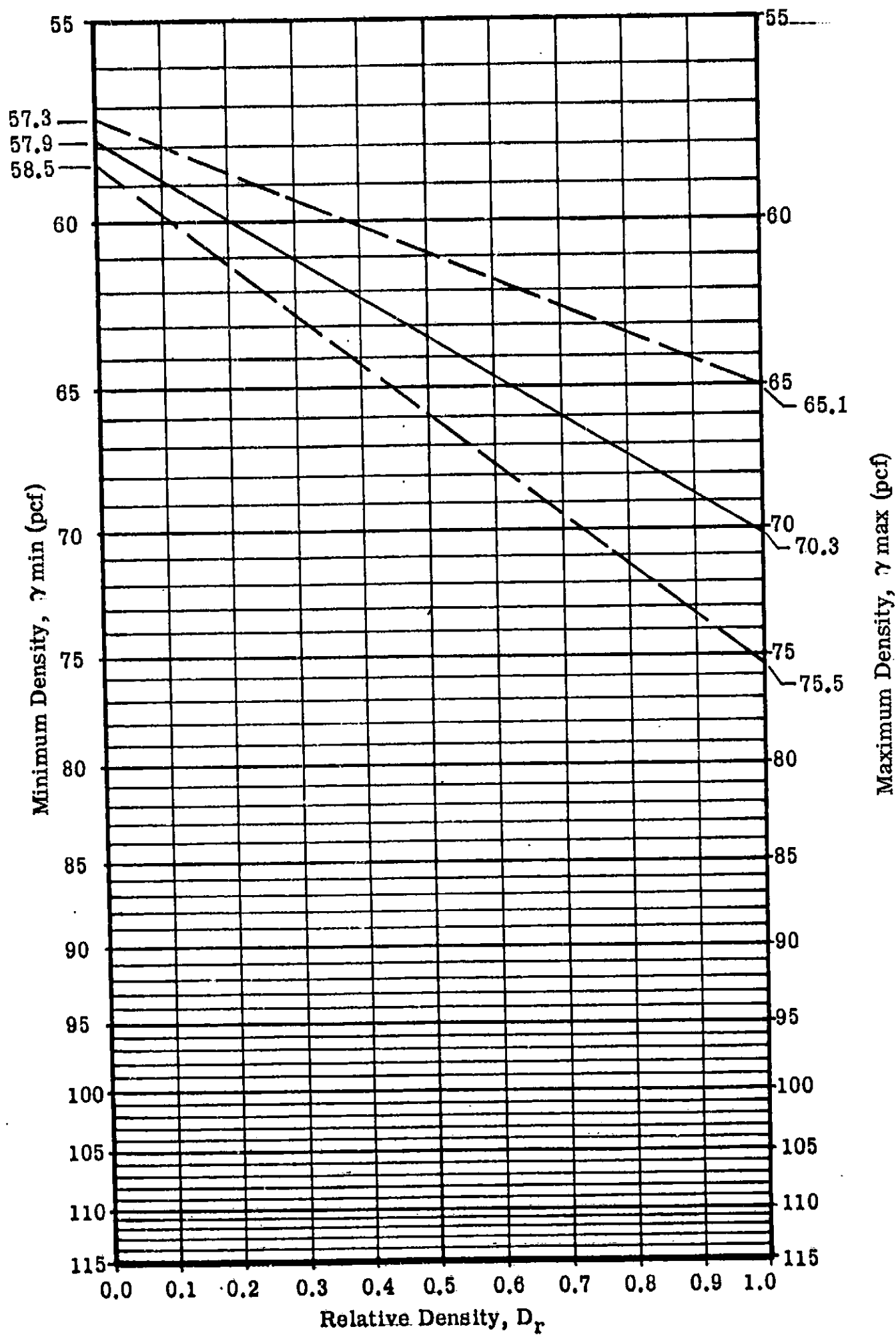
Figure A-19. Density Versus Relative Density for RSM Soil
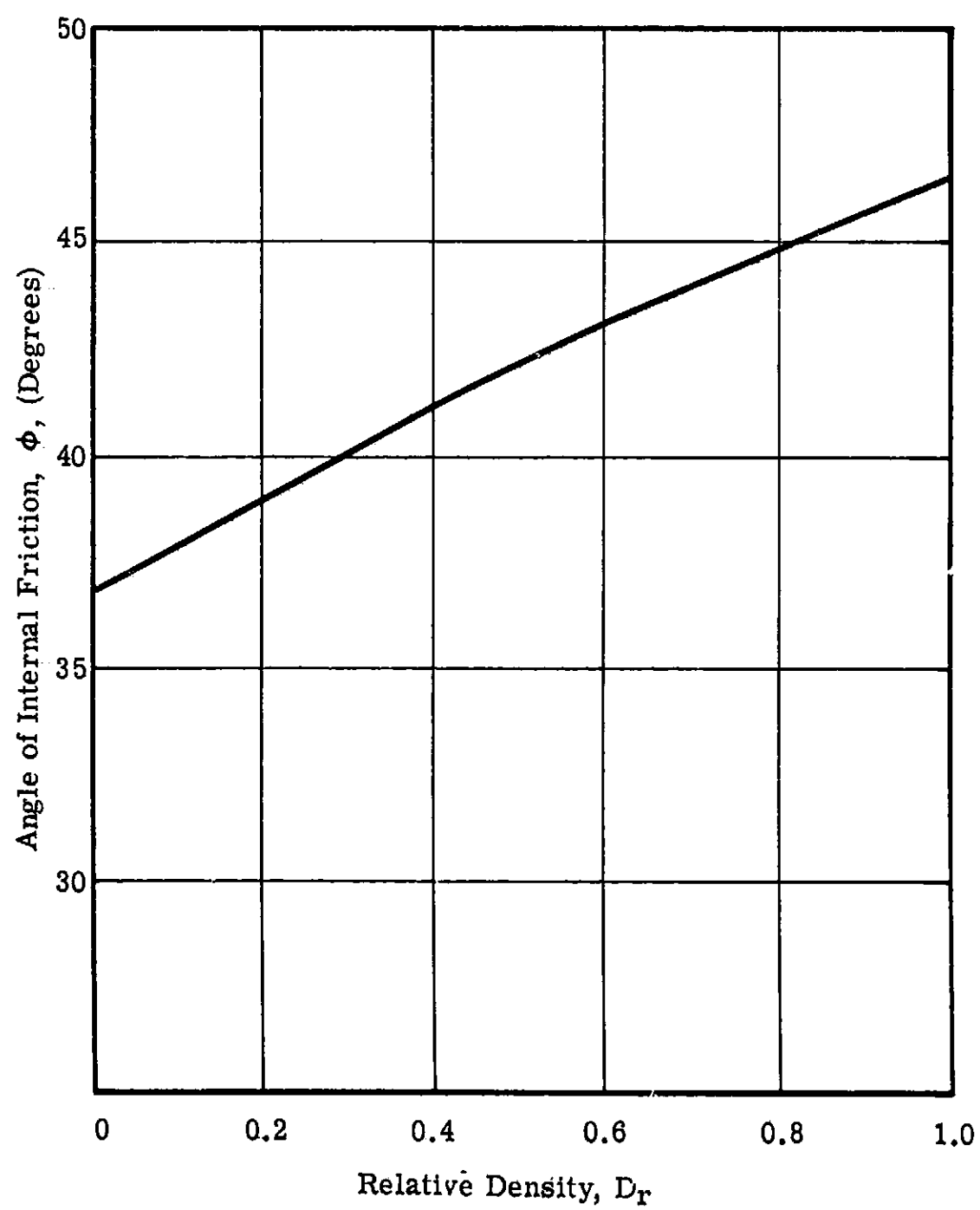
Figure A-20. Angle of Internal Friction (as determined by the direct shear test)
Versus Relative Density for RSM Soil

12. Sonic Velocity Test

No determination of initial tangent modulus was made for Soil No. 5. However, based on data for the other soils the sonic modulus at 4 psi confining pressure is estimated to be 7800 psi.

13. Soil Test Bed Placement Procedure

Soil No. 5 was placed using the hopper method.

14. Special Comments

The RSM - a soil is susceptible to particle breakdown or degradation due to handling and testing. Such degradation leads to changes in some soil properties, unit weight in particular. If the handling method is such that this process cannot be prevented, or the soil cannot be replaced when these effects become prominent, periodic sampling of the soil bed should be made in order that the effects be known quantitatively.

LM SOIL MECHANICS STUDY

SPECIFICATION FOR SOIL NO. 6

1. Bendix Designation: RC2 Loose

2. Description: Red broadly-graded crushed andesitic volcanic scoria (volcanic cinders)

3. Source: Cinder Products Company
            3450 Lakeshore Avenue, Oakland, California 94610

4. Source Name: Volcalite

5. Chemical Analysis:

		Volcalite*	Hypersthene Andesite (a, pp. 456-466)
Silica	(SiO_2)	54.22	56.88
Aluminum Oxide	(Al_2O_3)	25.04	18.25
Ferric Oxide	(Fe_2O_3)	4.28	2.35
Calcium Oxide	(CaO)	8.11	7.53
Magnesium Oxide	(MgO)	5.58	4.07
Sodium Oxide	(NaO)	1.61	3.29
Potassium Oxide	(K_2O)	0.41	1.42
		99.25	

*Chemical analysis provided by producer.

A-42

6.   Petrological Description

Highly porous volcanic (extrusive) rock of "basic" composition, commonly termed volcanic scoria. A comparison of the chemical analysis provided by the producer with other published analyses indicates that the rock type is an andesite. Figure A-21 is a photomicrograph of the RC2 soil.

7.   Mineralogical Description

No mineralogic analysis of the test soil has been done, but a normative analysis of the hypersthene andesite reported by Clarke (a, p. 458) gives the following:

Quartz	9.1%
Orthoclase	8.3%
Albite	27.8%
Anorthite	30.9%
Diopside	5.3%
Hypersthene	13.2%
Magnetite	3.5%
Ilmenite	0.8%

The reddish color of the RS soil would indicate that this material contains iron hydroxides (e.g., limonite) rather than the magnetite and ilmenite referred to in the norm and probably constitutes a larger percentage of the RS material than the iron minerals used in the example.

Decomposition due to weathering tends to decrease the percentage of silica, calcium oxide and sodium oxide and increase the percentage of ferric oxides and aluminum oxide (leaching, chloritization and kaolinization). The iron oxides (e.g., magnetite, ilmenite) tend to form iron hydroxides (e.g., limonite); the femic minerals (e.g. hypersthene) to form chlorite (chloritization); and the feldspars (e.g., orthoclase, albite) to form clays (kaolinization). The chemical analyses exhibit these trends indicating that some decomposition due to weathering has occurred.

A-43

Scale Graduated In
1/32 Inch Increments

Figure A-21. Photomicrograph RC Soil

8.   Moisture Contents

All tests were run on air-dried material. Oven-drying of the air-dried soil at 230°F yielded moisture contents commonly in the range of 0.2 to 0.6% (percent of dry weight of soil).

9.   Grain Size Distribution

Figure A-22 shows the range and average grain size distribution of this soil. The table on this figure lists some of the grain size parameters investigated in this study.

10.   Density and Relative Density

The average relative density of Soil No. 6 is about zero. Figure A-23 shows the relationship between soil unit weight (density) and relative density for the RC2 soil, as determined by the method of test suggested by D. M. Burmister (c, pp. 175-177). The solid line represents the average of several tests on unused, undegraded soil, and the dashed lines indicate the 95% confidence limits for the data.

11.   Direct Shear Test Results

Figure A-24 shows the relationship between angle of internal friction and relative density obtained from the direct shear tests.

The figure indicates that the angle of internal friction for Soil No. 6 is about 43°. The complete data obtained from the direct shear tests is given in Appendix C.

12.   Sonic Velocity Test

The values of initial tangent modulus yielded for Soil No. 6 by this test is about 8000 psi at a confining pressure of 4 psi (no correction made for Poisson's Ratio).

A detailed description of the test apparatus and procedures is given in Appendix B.

13.   Soil Test Bed Placement Procedure

Soil No. 6 was placed using the hopper method. However, the soil handling was done by shovel rather than the vacuum system.

GRAIN SIZE ANALYSIS CURVES - LM SMS

Grain Size Parameters		Value	
Name	Symbol	Average	Range
Mean Size	D50	1.1mm	0.9-2.5mm
Effective Diameter	D10	0.07mm	0.06-0.1mm
Coefficient of Uniformity (D60/D10)	Cu	2 5	15-25
Coarseness	D95	5.0mm	4.1-5.5mm

U.S. Std. Sieve No.

Percent Finer Than By Weight

Grain Size - mm

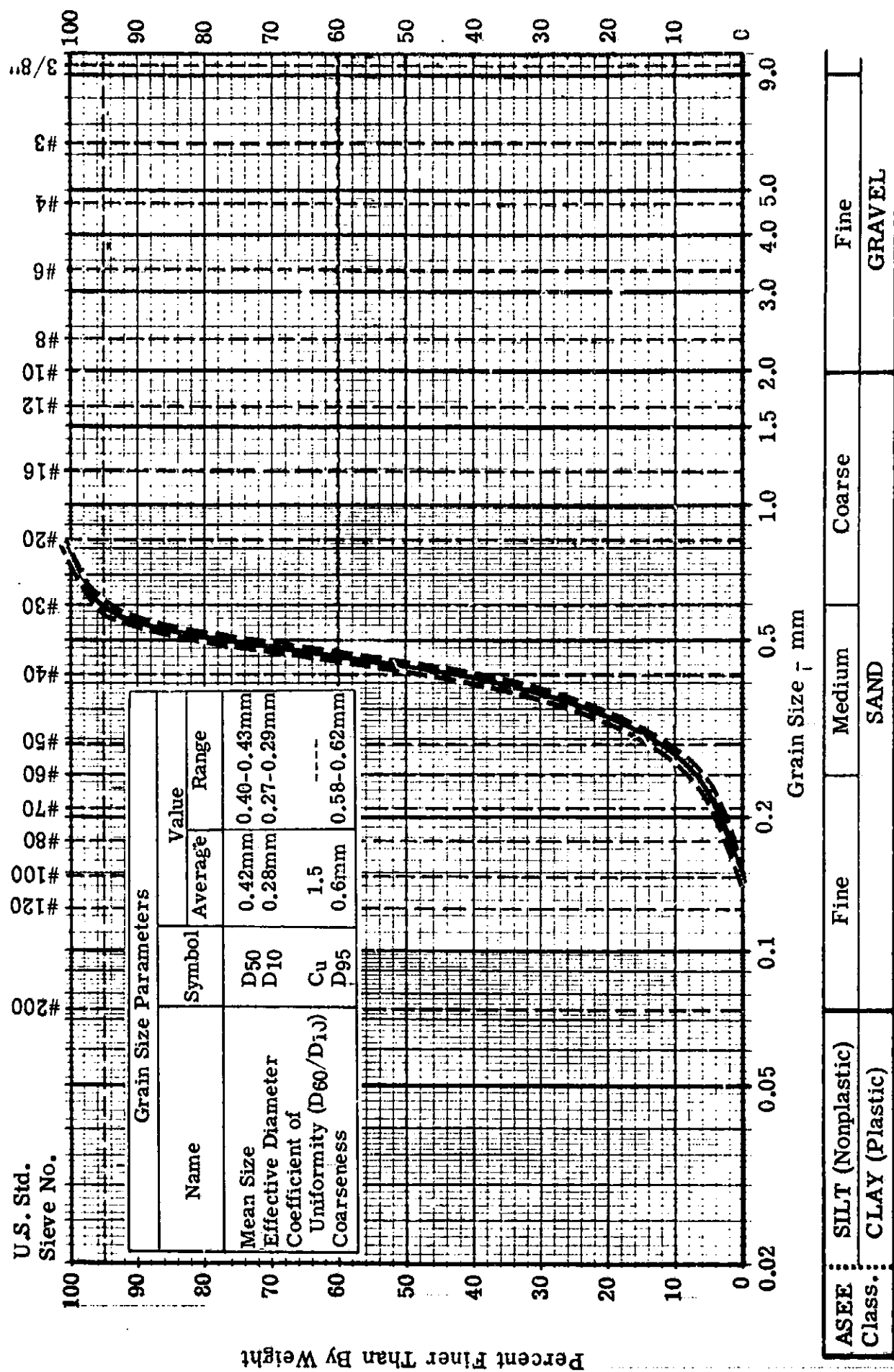| ASEE	SILT (Nonplastic)	Fine	Medium	Coarse	Fine
Class.	CLAY (Plastic)		SAND		GRAVEL
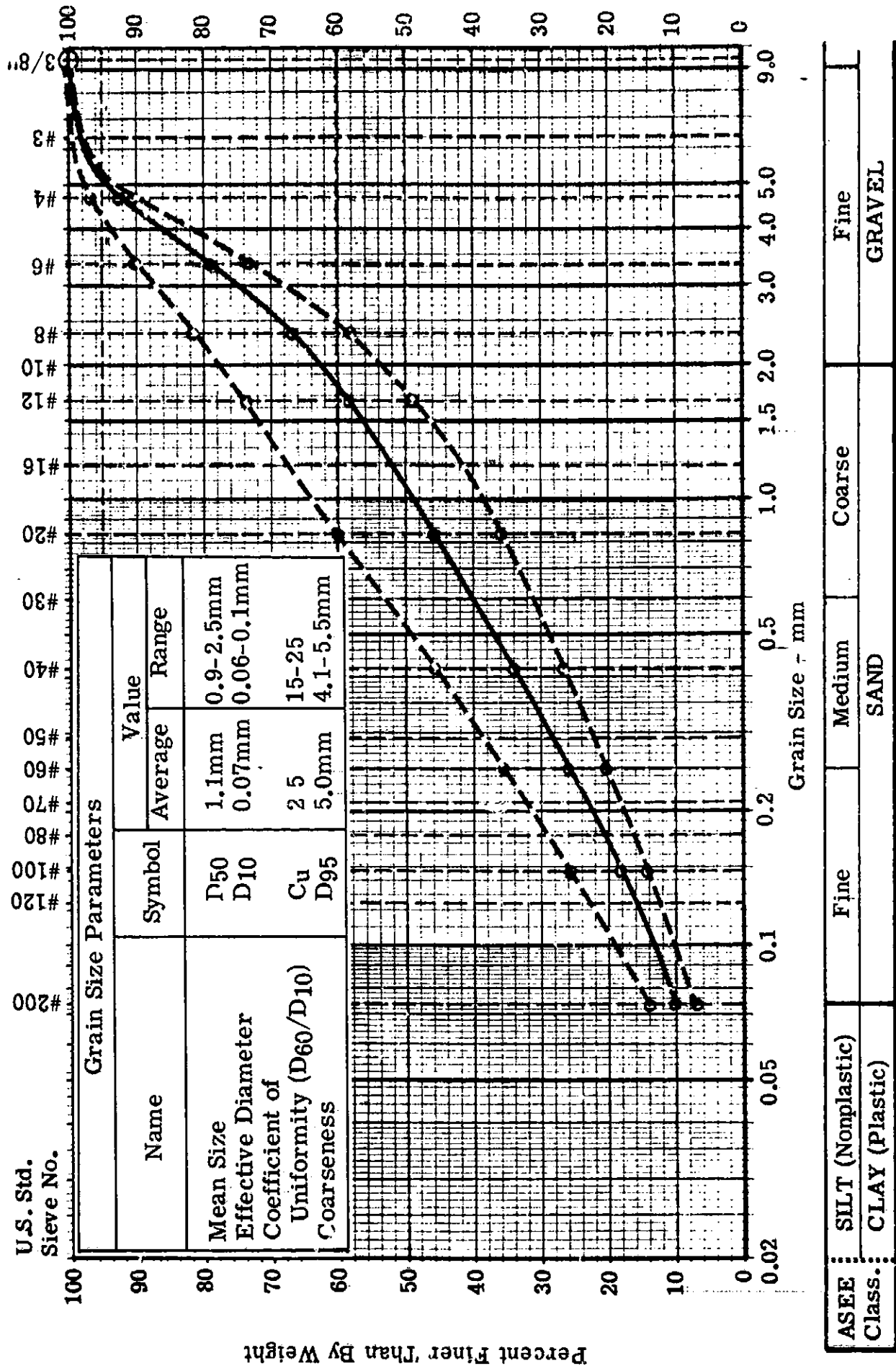
Figure A-22. Average and Range of Six Samples of RC2 Soil
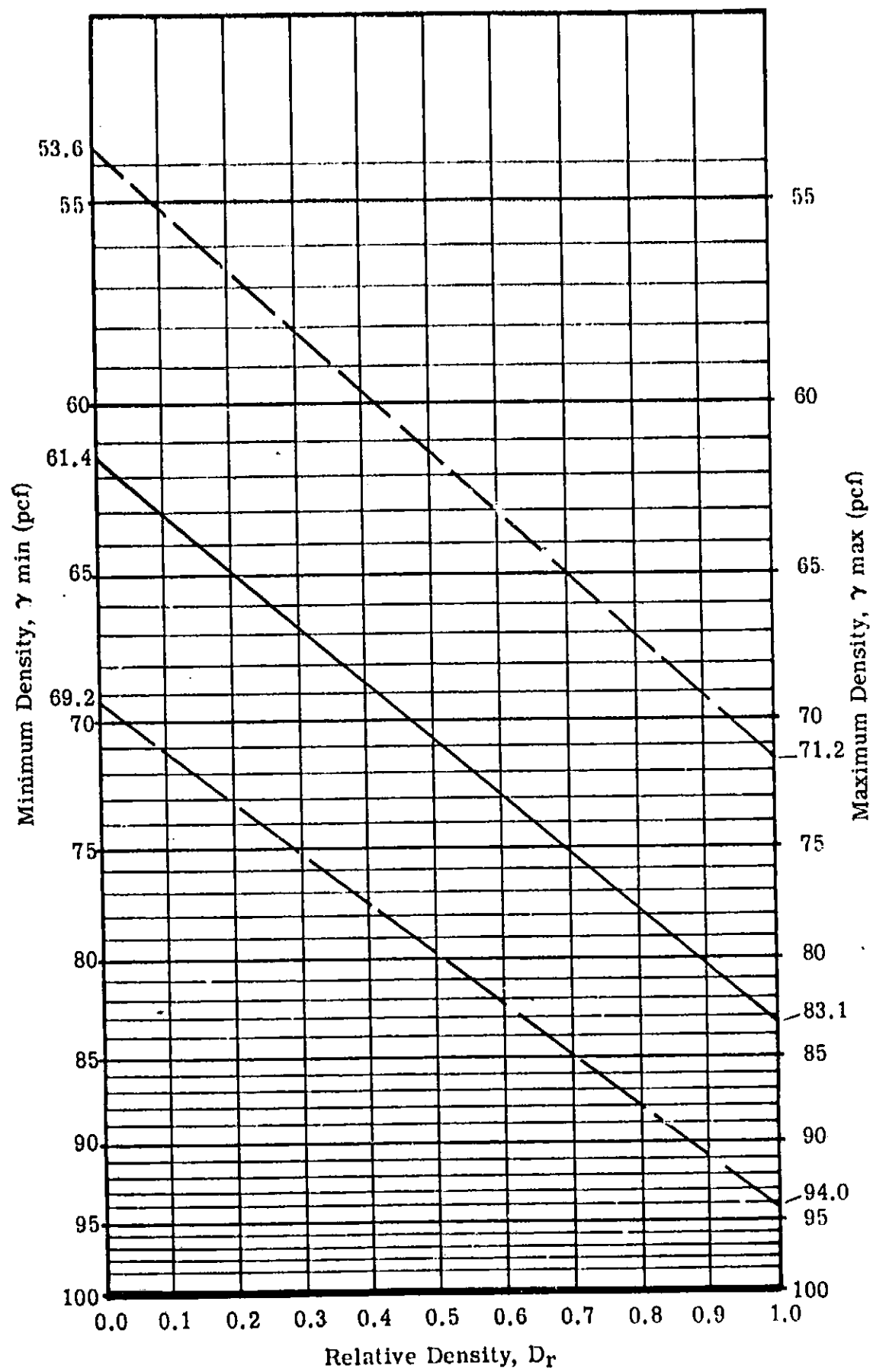
Figure A-23. Density Versus Relative Density for RC2 Soil
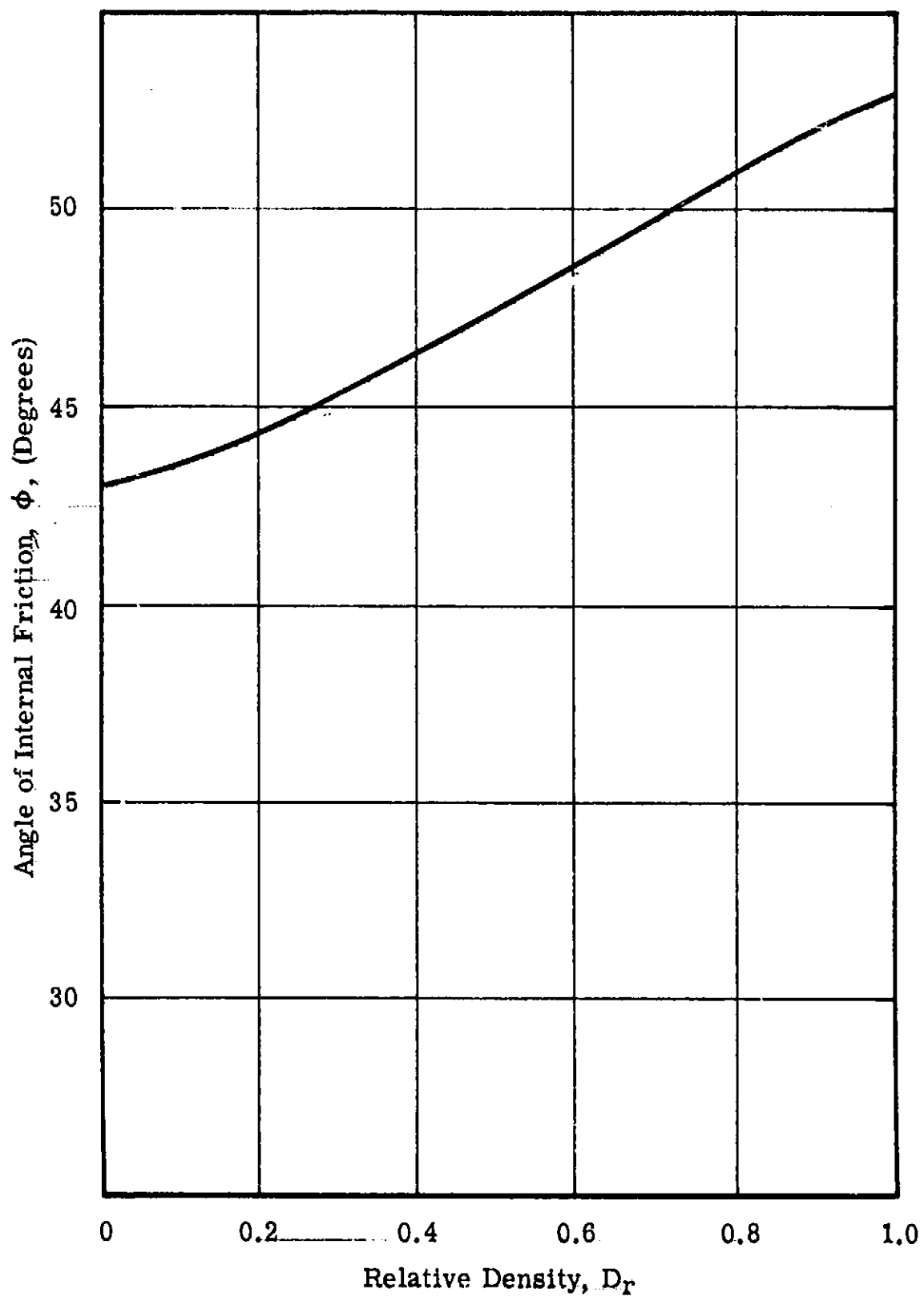
Figure A-24. Angle of Internal Friction (as determined by the direct shear test) Versus Relative Density for the RC2 Soil

14. Special Comments

The average curves in Figures A-22 and A-23 are combined values of used and unused soil. Since the soil was not handled using the vacuum system, no appreciable degradation effects were noted. The greatest variation in soil properties (e.g., grain size distribution and unit weight) was due primarily to unavoidable segregation of particle sizes (i.e., nonuniform grain size distribution with a soil bed and from test bed to test bed). This variation accounts for the wide range and confidence limits exhibited by this soil in Figures A-22 and A-23.

LM SOIL MECHANICS STUDY

SPECIFICATION FOR SOIL NO. 7

1. Bendix Designation: SS Loose

2. Description: White narrowly-graded silica sand.

3. Source: Wedron Silica Company
    135 S. LaSalle Street, Chicago, Illinois 60603

4. Source Name: Wedron 4040 sand.

5. Chemical Analysis: *

Silica	(S_iO_2)	99.9%
Ferric	(Fe_2O_3)	Trace
Aluminum Oxide	(Al_2O_3)	0.1%
Titanium Oxide	(TiO_2)	Trace
Calcium Oxide	(CaO)	Trace
Magnesium Oxide	(MgO)	Trace

6. Petrological Description

Essentially pure quartz (silica) sand grains, rounded to subangular. It is mined from
the St. Peter Sandstone formation in Wedron, Illinois._____   _____

Figure A-25 is a photomicrograph of the SS soil.

*Provided by supplier.
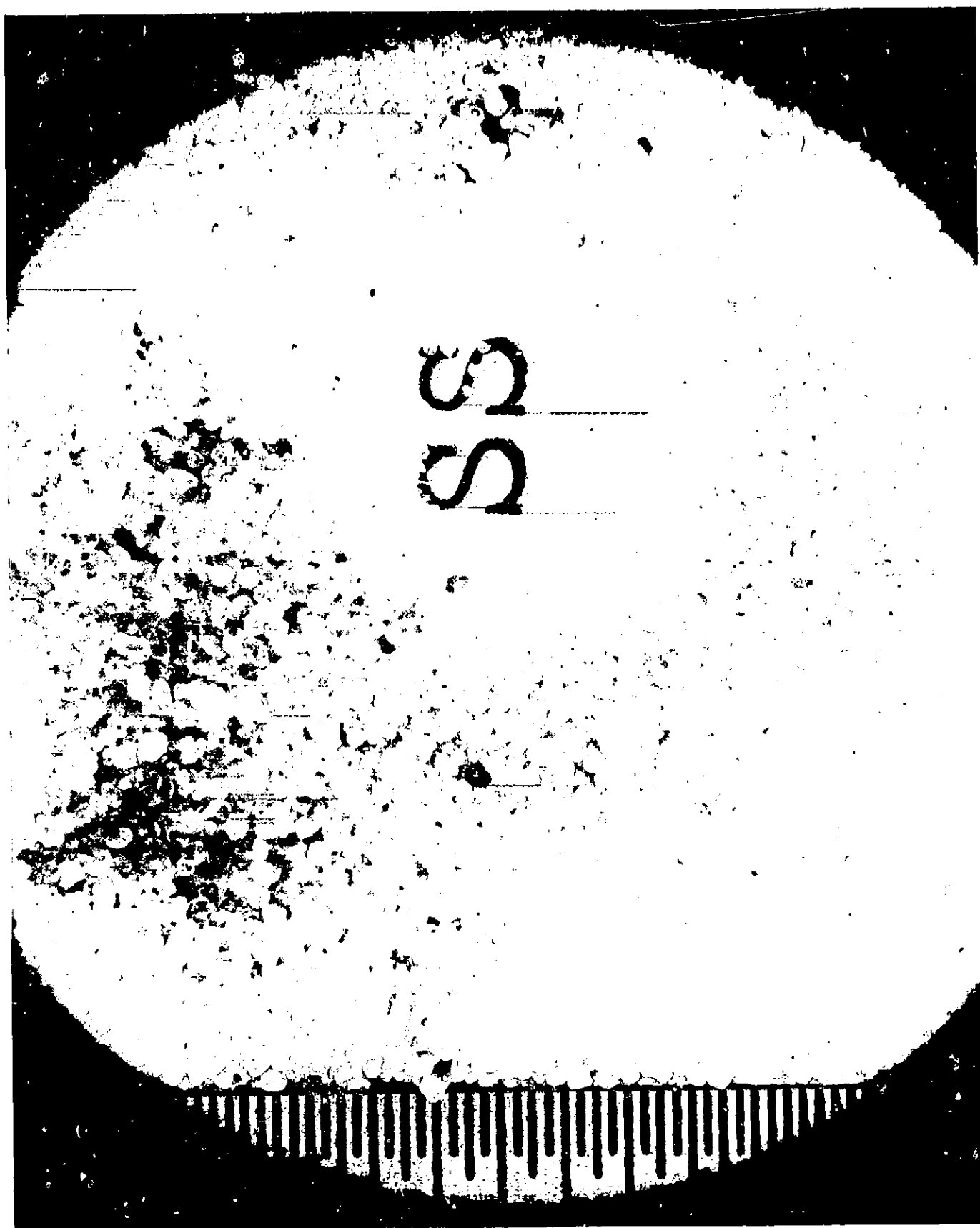
Scale Graduated In
1/32 Inch Increments
Figure A-25. Photomicrograph SS Soil

7.　Mineralogical Description

Essentially the only mineral present in this soil is quartz (silica).

8.　Moisture Content

All tests were run on air-dried material. Oven-drying of the air-dried soil at 230°F yielded moisture contents commonly in the range of 0.2 to 0.6% (percent of dry weight of soil).

9.　Grain Size Distribution

Figure A-26 shows the range and average grain size distribution of this soil. The table on this figure lists some of the grain size parameters investigated in this study.

10.　Density and Relative Density

The average relative density of Soil No. 7 is about zero. Figure A-27 shows the relationship between soil unit weight (density) and relative density for the SS soil as determined by the method of test suggested by D. M. Burmister (c, pp. 175-177). The solid line represents the average of several tests and the dashed lines indicate the 95% confidence limits for the data.

11.　Direct Shear Test Results.

Figure A-28 shows the relationship between angle of internal friction and relative density obtained from the direct shear tests. This figure indicates that the angle of internal friction for Soil No. 7 is about 29.8°. The complete data obtained from the direct shear tests is given in Appendix C.

12.　Sonic Velocity Test

The values of initial tangent modulus yielded for Soil No. 7 by this test is about 10,000 psi at a confining pressure of 4 psi (no correction made for Poisson's Ratio). A detailed description of the test apparatus and procedures is given in Appendix B.

A-52

GRAIN SIZE ANALYSIS CURVES - LM SMS

Grain Size Parameters			
Name	Symbol	Value	
		Average	Range
Mean Size	D50	0.42mm	0.40-0.43mm
Effective Diameter	D10	0.28mm	0.27-0.29mm
Coefficient of Uniformity (D_{60}/D_{10})	Cu	1.5	----
Coarseness	D95	0.6mm	0.58-0.62mm

Percent Finer Than By Weight

Grain Size ~ mm

U.S. Std. Sieve No.

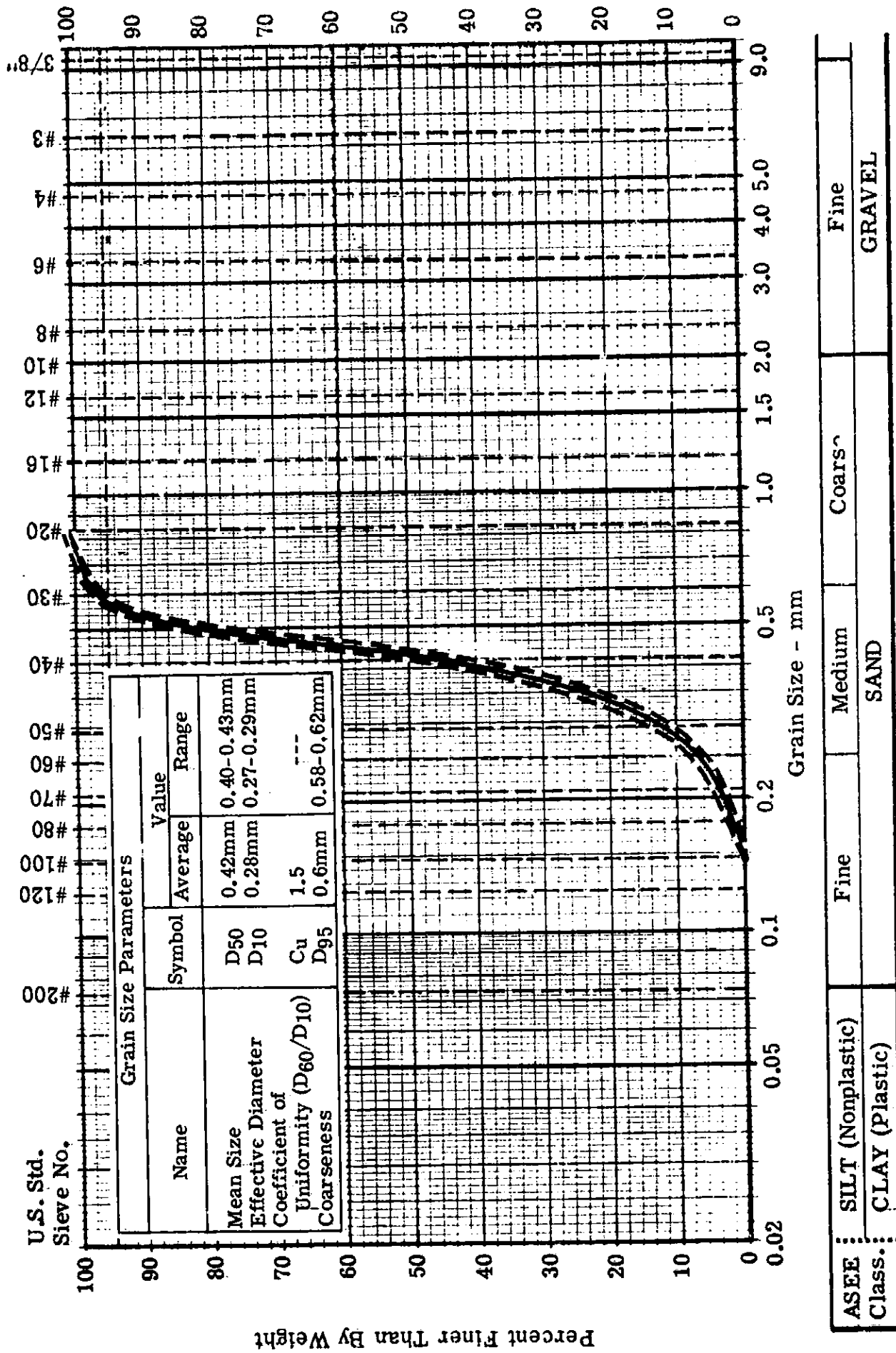| ASEE	SILT (Nonplastic)	Fine	Medium	Coarse	Fine
Class.	CLAY (Plastic)		SAND		GRAVEL

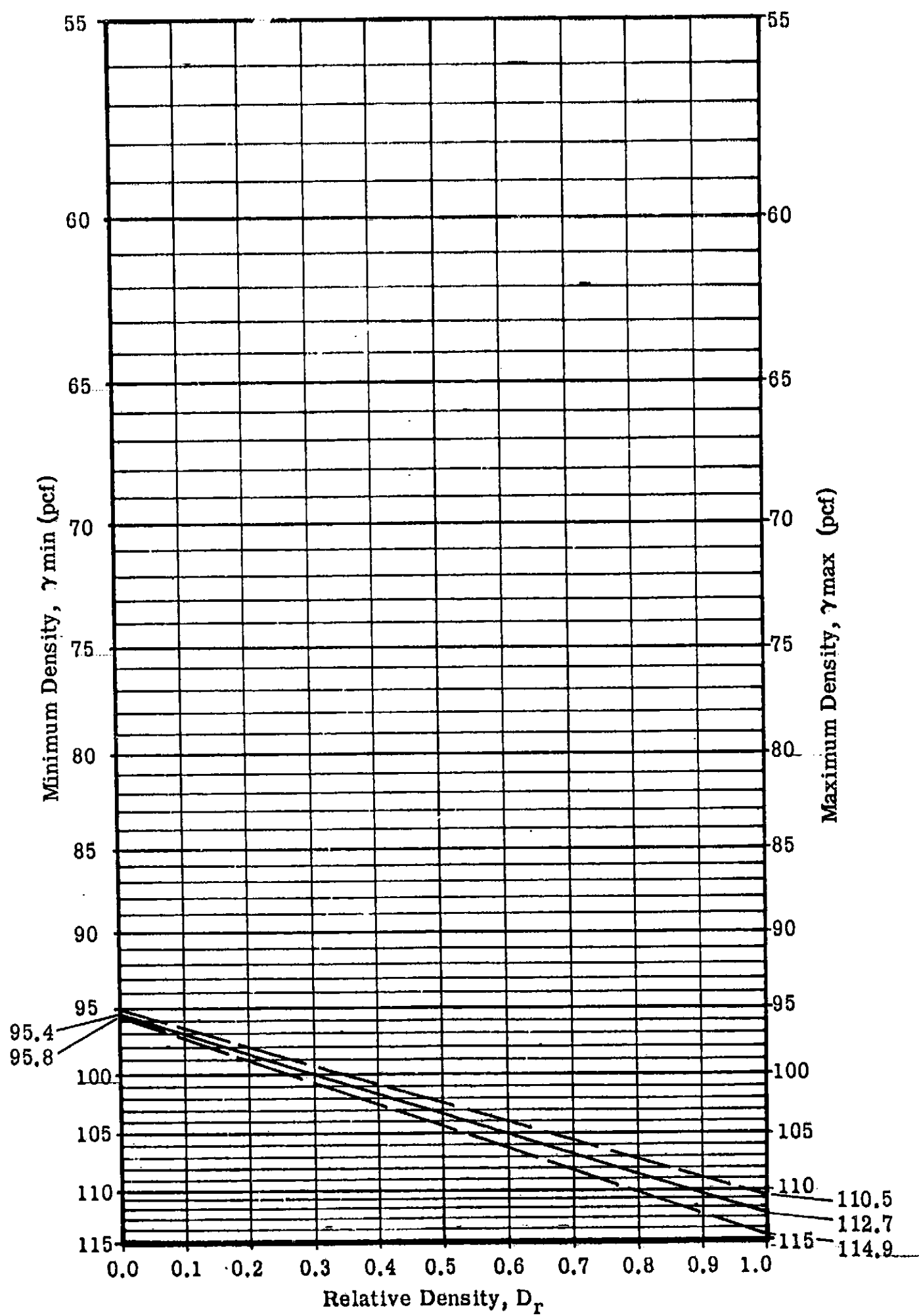Figure A-26. Average and Range of Five Samples of SS Soil

A-53
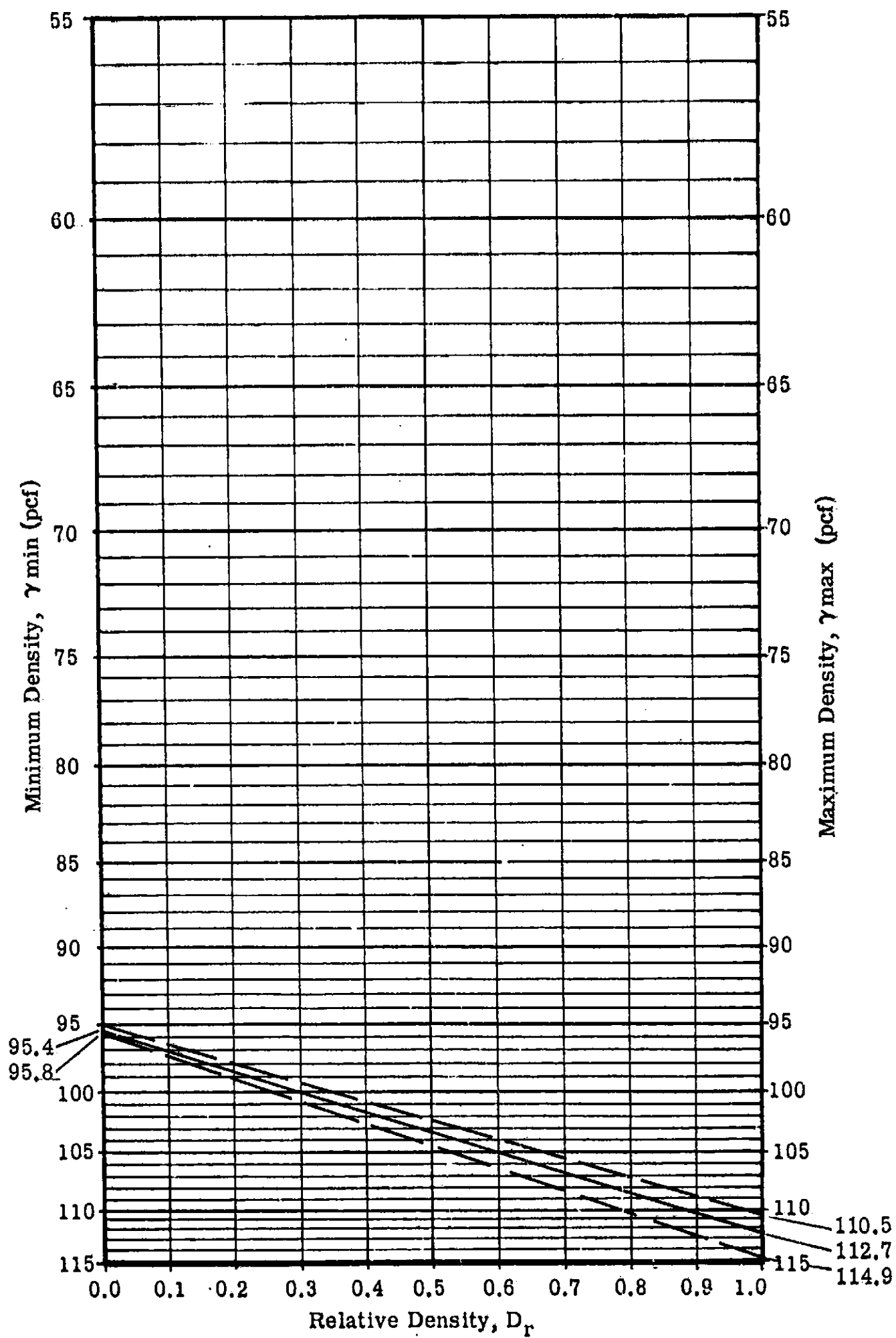
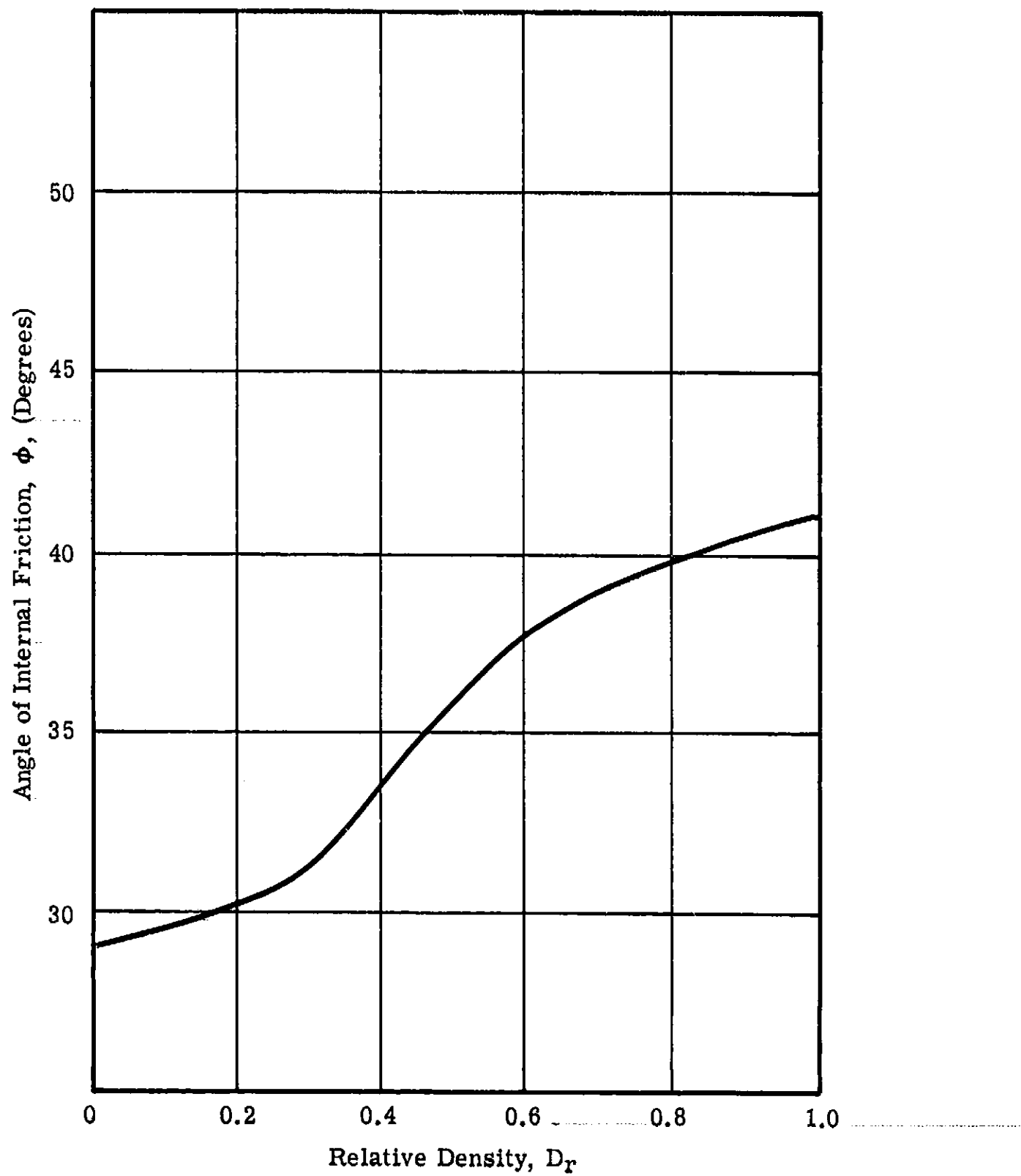Figure A-27. Density Versus Relative Density for SS Soil
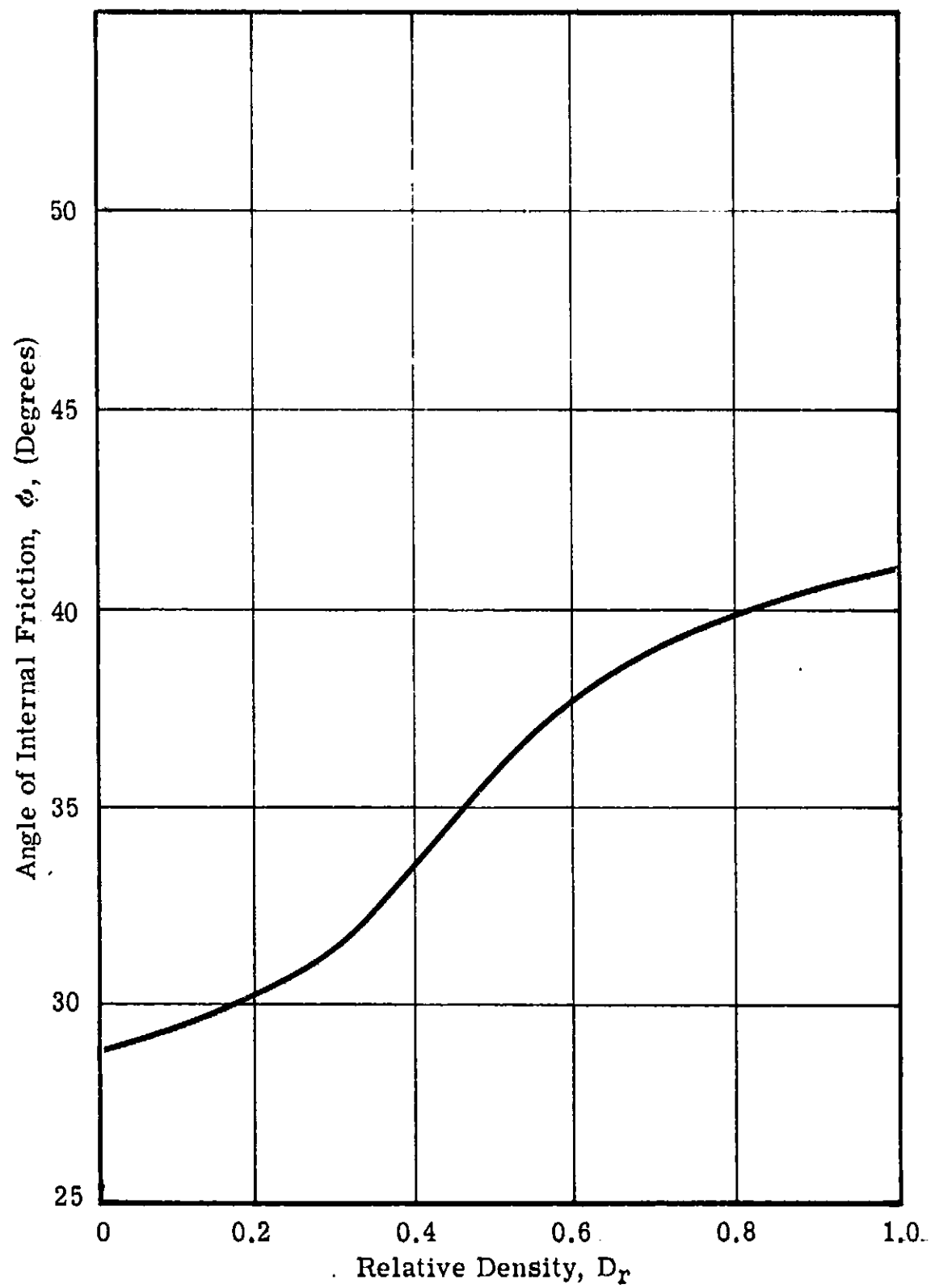
Figure A-28. Angle of Internal Friction (as determined by the direct shear test) Versus Relative Density for SS Soil

13. Soil Test Bed Placement Procedure

Soil No. 7 was placed using the hopper method.

14. Special Conditions

This soil was not appreciably altered by degradation effects created by testing or handling with the vacuum system.

LM SOIL MECHANICS STUDY

SPECIFICATION FOR SOIL NO. 8

1. Bendix Designation: SS Intermediate

2. Description: White narrowly-graded silica sand.

3. Source: Wedron Silica Company
   135 S. LaSalle Street, Chicago, Illinois 60603

4. Source Name: Wedron 4040 Sand.

5. Chemical Analysis:*

Silica	(SiO_2)	99.9%
Ferric Oxide	(Fe_2O_3)	Trace
Aluminum	(Al_2O_3)	0.1%
Titanium Oxide	(TiO_2)	Trace
Calcium Oxide	(CaO)	Trace
Magnesium Oxide	(MgO)	Trace

6. Petrological Description

Essentially pure quartz (silica) sand grains, rounded to subangular. It is mined from the St. Peter Sandstone formation in Wedron, Illinois. Figure A-29 is a photomicrograph of the SS soil.

*Provided by supplier.
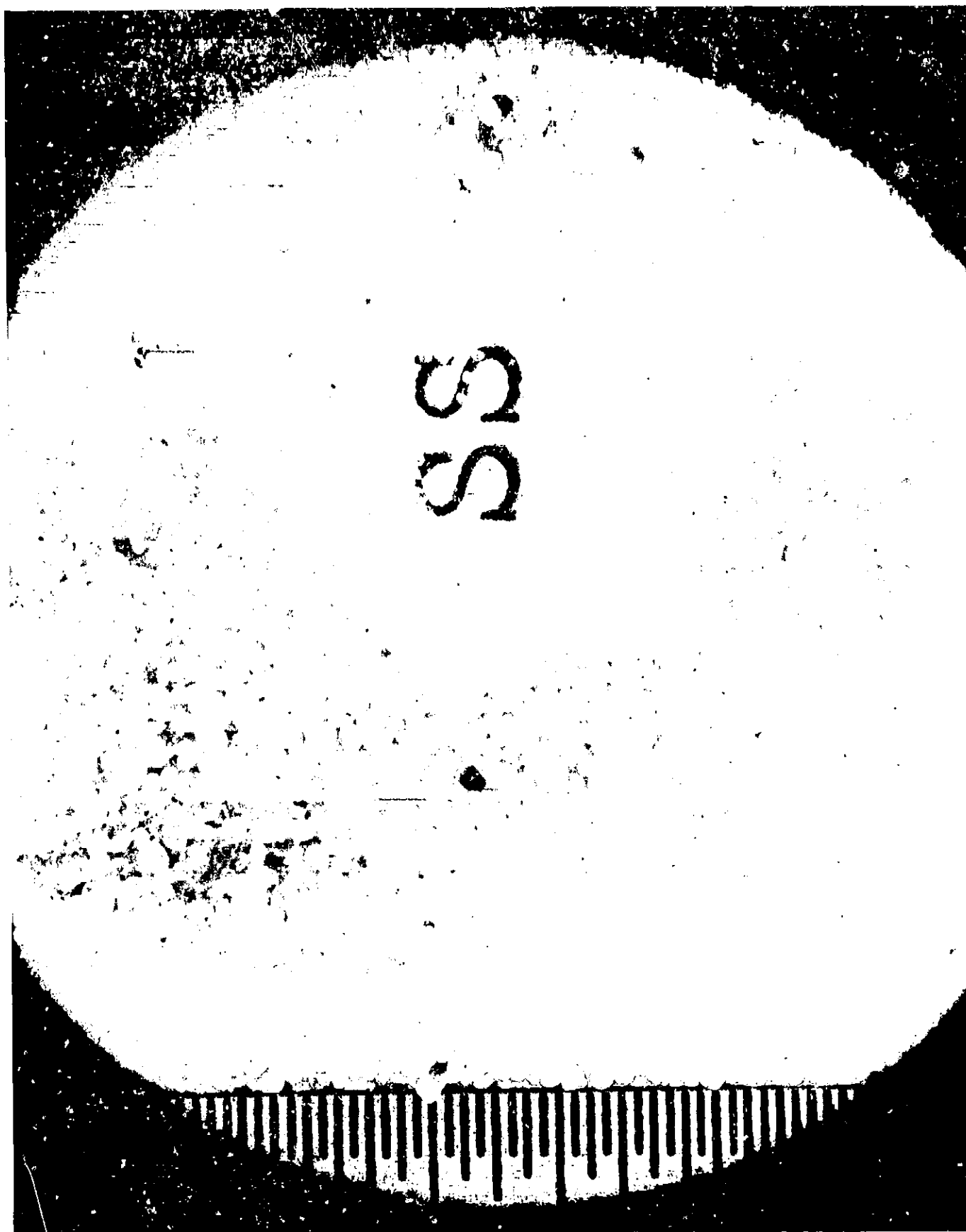
Scale Graduated In
1/32 Inch Increments
Figure A-29. Photomicrograph SS Soil

7. Mineralogical Description

Essentially the only mineral present in this soil is quartz (silica).

8. Moisture Content

All tests were run on air-dried material. Oven-drying of the air-dried soil at 230°F yielded moisture contents commonly in the range of 0.2 to 0.6% (percent of dry weight of soil).

9. Grain Size Distribution

Figure A-30 shows the range and average grain size distribution of this soil. The table on this figure lists some of the grain size parameters investigated in this study.

10. Density and Relative Density

The average relative density of Soil No. 8 is about 0.53. Figure A-31 shows the relationship between soil unit weight (density) and relative density for the SS soil as determined by the method of test suggested by D. M. Burmister (c, pp. 175-177). The solid line represents the average of several tests and the dashed lines indicate the 95% confidence limits for the data.

11. Direct Shear Test Results

Figure A-32 shows the relationship between angle of internal friction and relative density obtained from the direct shear tests.

This figure indicates that the angle of internal friction for Soil No. 8 is about 36.8°. The complete data obtained from the direct shear tests is given in Appendix C.

12. Sonic Velocity Test

The value of initial tangent modulus yielded for Soil No. 8 by this test is about 18,000 psi at a confining pressure of 4 psi (no correction made for Poisson's Ratio). A detailed description of the test apparatus and procedures is given in Appendix B.

GRAIN SIZE ANALYSIS CURVES - LM SMS

Grain Size Parameters

Name	Symbol	Value Average	Range
Mean Size	D50	0.42mm	0.40-0.43mm
Effective Diameter	D10	0.28mm	0.27-0.29mm
Coefficient of Uniformity (D_{60}/D_{10})	Cu	1.5	---
Coarseness	D95	0.6mm	0.58-0.62mm

U.S. Std. Sieve No.

Percent Finer Than By Weight

Grain Size - mm

ASEE	SILT (Nonplastic)	Fine	Medium	Coars^	Fine
Class.	CLAY (Plastic)		SAND		GRAVEL

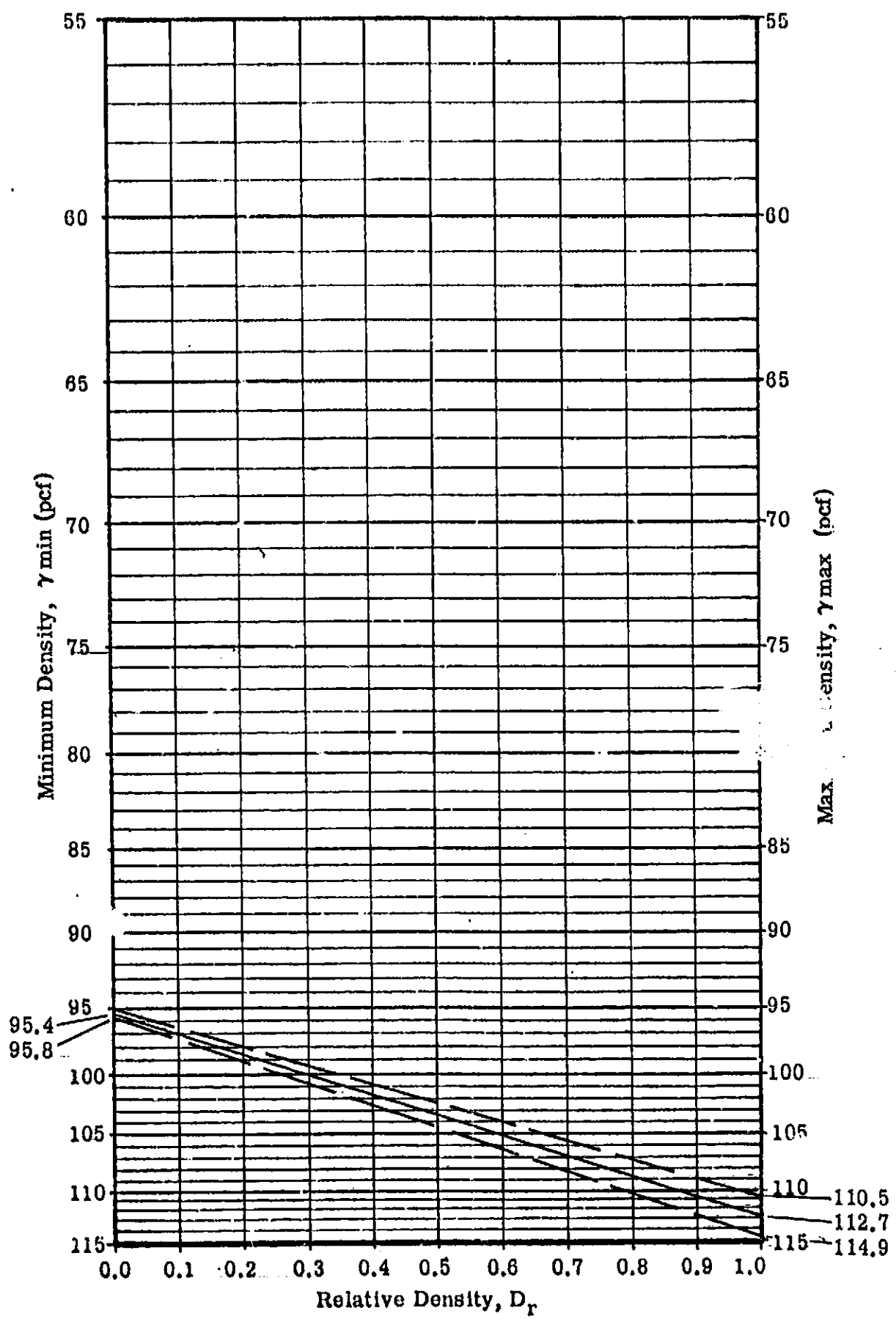Figure A-30. Average and Range of Five Samples of SS Soil

Figure A-31. Density Versus Relative Density for SS Soil
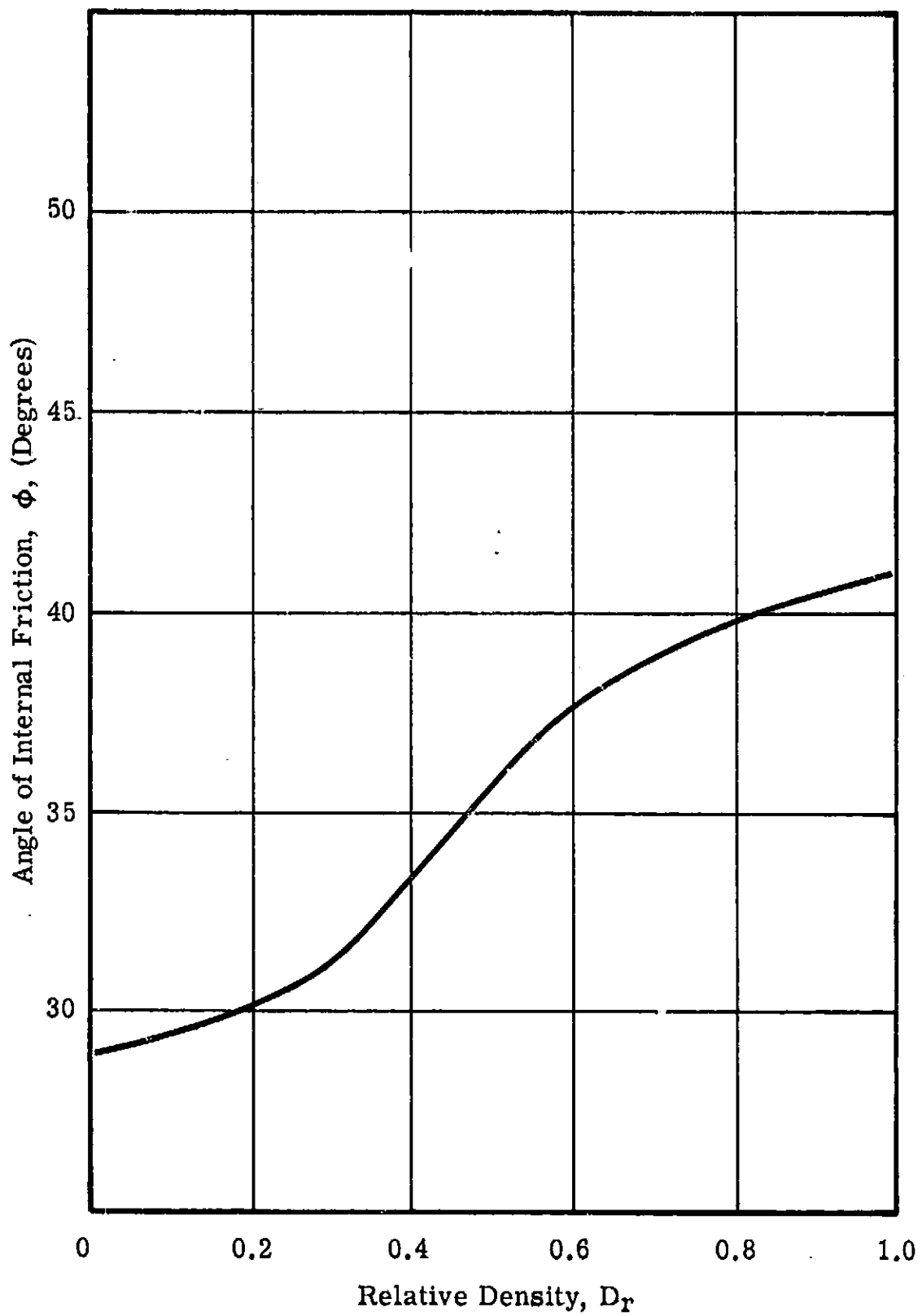
Figure A-32. Angle of Internal Friction (as determined by the direct shear test) Versus Relative Density for SS Soil

13. Soil Test Bed Placement Procedure

Soil No. 8 was placed with a hopper and compacted with 8 passes of a roller.

14. Special Conditions

This soil was not appreciably altered by degradation effects created by testing or handling with the vacuum system.

A-63

LM SOIL MECHANICS STUDY

SPECIFICATION FOR SOIL NO. 9

1.   Bendix Designation: SS Dense

2.   Description: White narrowly-graded silica sand.

3.   Source: Wedron Silica Company
            135 S. LaSalle Street, Chicago, Illinois   60603

4.   Source Name: Wedron 4040 Sand.

5.   Chemical Analysis:*

Silica	(SiO_2)	99.9%
Ferric Oxide	(Fe_2O_3)	Trace
Aluminum Oxide	(Al_2O_3)	0.1%
Titanium Oxide	(TiO_2)	Trace
Calcium Oxide	(CaO)	Trace
Magnesium Oxide	(MgO)	Trace

6.   Petrological Description

Essentially pure quartz (silica) sand grains, rounded to subangular. It is mined from the St. Peter Sandstone formation in Wedron, Illinois. Figure A-33 is a photomicrograph of the SS soil.

*Provided by supplier.

A-64
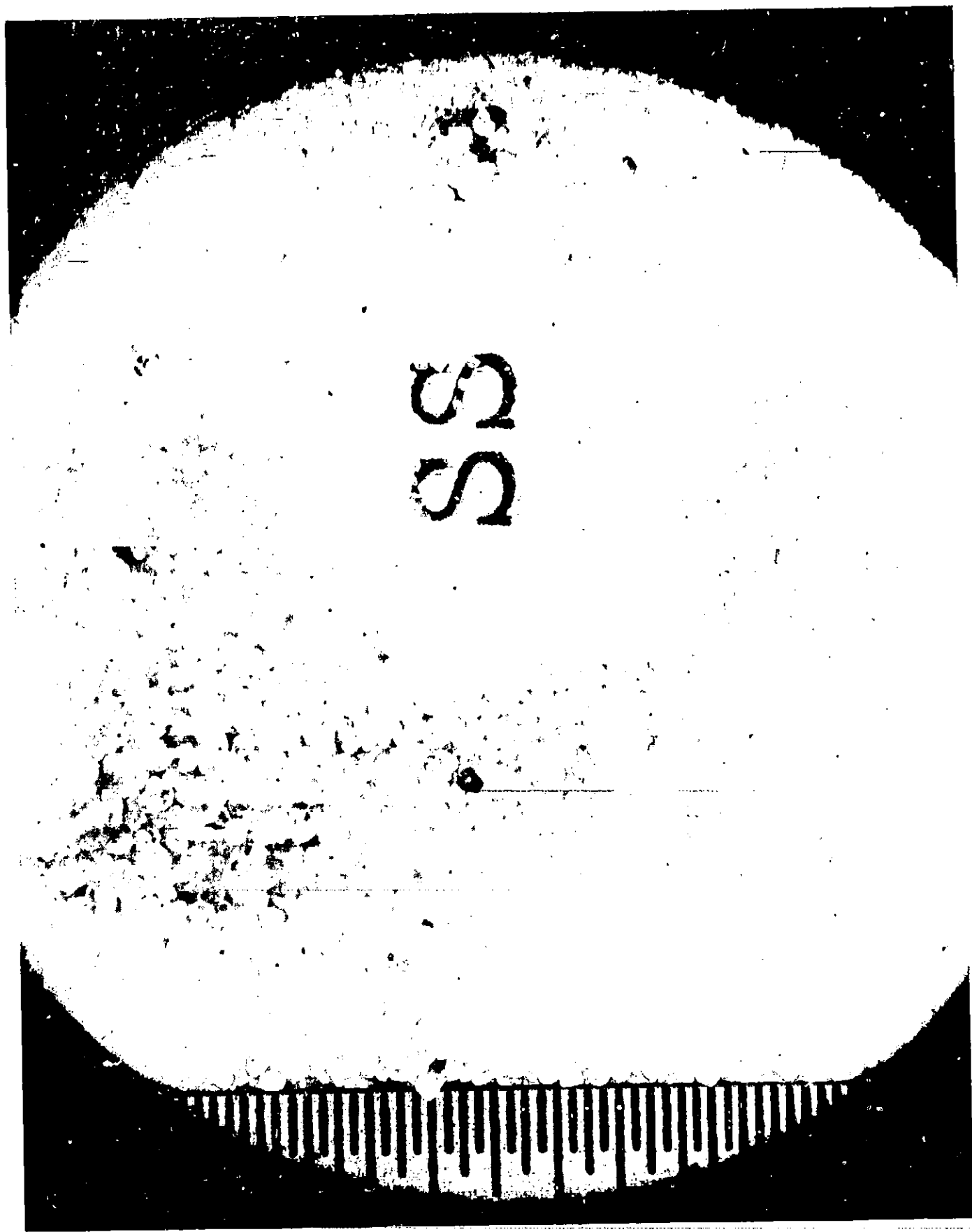
Scale Graduated In
1/32 Inch Increments

Figure A-33. Photomicrograph SS Soil

7. Mineralogical Description

Essentially the only mineral present in this soil is quartz (silica).

8. Moisture Content

All tests were run on air-dried material. Oven-drying of the air-dried soil at 230°F yielded moisture contents commonly in the range of 0.2 to 0.6% (percent of dry weight of soil).

9. Grain Size Distribution

Figure A-34 shows the range and average grain size distribution of this soil. The table on this figure lists some of the grain size parameters investigated in this study.

10. Density and Relative Density

The average relative density of Soil No. 9 is about 0.69. Figure A-35 shows the relationship between soil unit weight (density) and relative density for the SS soil as determined by the method of test suggested by D. M. Burmister (c, pp. 175-177). The solid line represents the average of several tests and the dashed lines indicate the 95% confidence limits for the data.

11. Direct Shear Test Results.

Figure A-36 shows the relationship between angle of internal friction and relative density obtained from the direct shear tests. This figure indicates that the angle of internal friction for Soil No. 9 is about 39°. The complete data obtained from the direct shear tests is given in Appendix C.

12. Sonic Velocity Test

The values of initial tangent modulus yielded for Soil No. 9 by this test is about 24,000 psi at a confining pressure of 4 psi (no correction made for Poisson's Ratio). A detailed description of the test apparatus and procedures is given in Appendix B.

A-66

GRAIN SIZE ANALYSIS CURVES - LM SMS

U.S. Std. Sieve No.

Percent Finer Than By Weight

3/8" #3 #4 #6 #8 #10 #12 #16 #20 #30 #40 #50 #60 #70 #80 #100 #120 #200

Grain Size – mm

9.0 5.0 4.0 3.0 2.0 1.5 1.0 0.5 0.2 0.1 0.05 0.02

Grain Size Parameters

Name	Symbol	Value	
		Average	Range
Mean Size	D_{50}	0.42mm	0.40-0.43mm
Effective Diameter	D_{10}	0.28mm	0.27-0.29mm
Coefficient of Uniformity (D_{60}/D_{10})	C_u	1.5	----
Coarseness	D_{95}	0.6mm	0.58-0.62mm
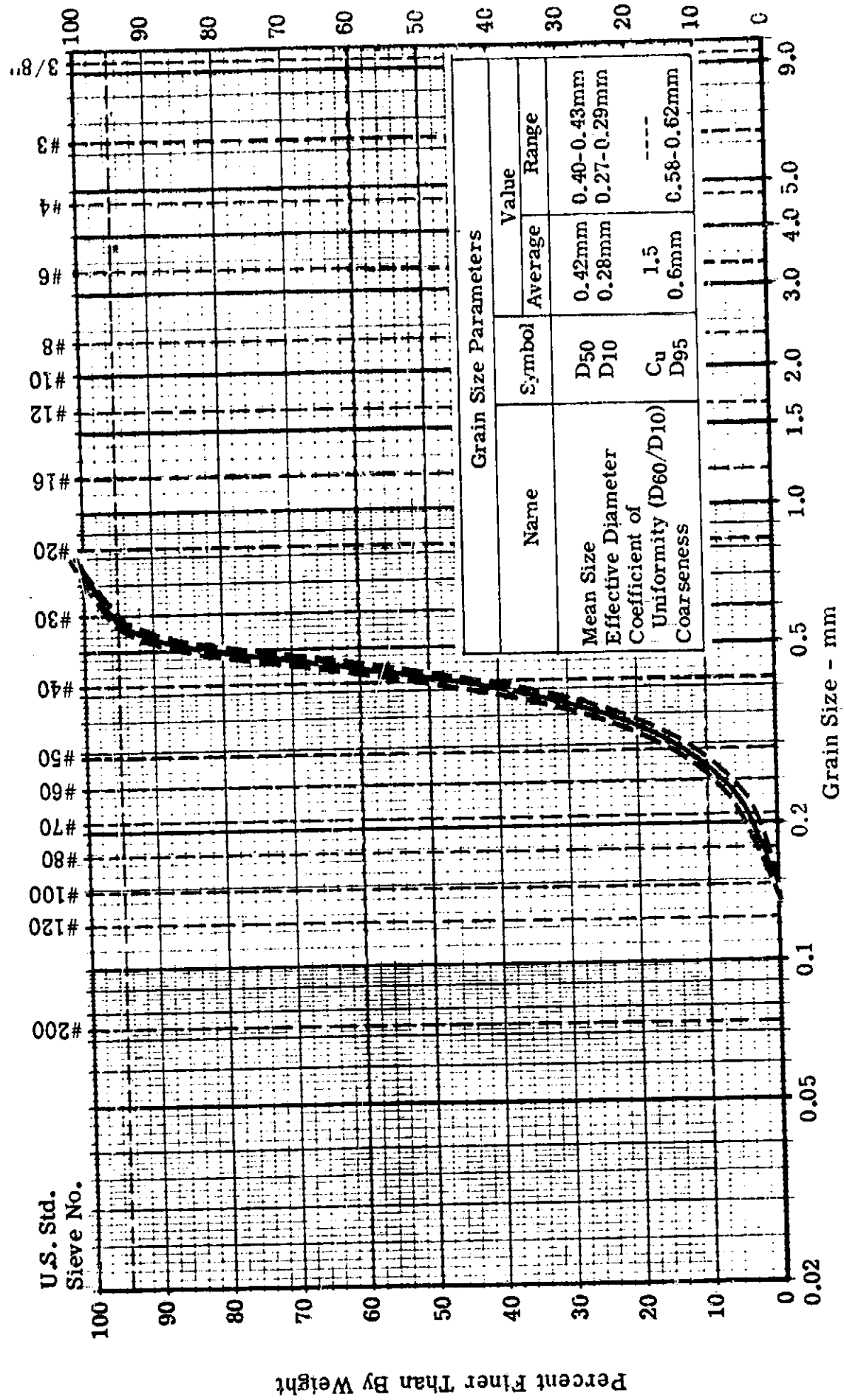
ASEE	SILT (Nonplastic)	Fine	Medium	Coarse	Fine
Class.	CLAY (Plastic)		SAND		GRAVEL

Figure A-34. Average and Range of Five Samples of SS Soil

Figure A-35. Density Versus Relative Density for SS Soil

Figure A-36. Angle of Internal Friction (as determined by the direct shear test) Versus Relative Density for SS Soil

13. Soil Test Bed Placement Procedure

Soil No. 9 was placed by a hopper and compacted with 24 passes of a roller.

14. Special Conditions

This soil was not appreciably altered by degradation effects created by testing or handling with the vacuum system.

LM SOIL MECHANICS STUDY

SPECIFICATION FOR SOIL NO. 10

1. <u>Bendix Designation:</u> LSM intermediate

2. <u>Description:</u> Mixture of red broadly-graded crushed andesitic volcanic scoria (volcanic cinders) and light gray kaolin-type clay.

3. <u>Source:</u>

    (a) Volcanic cinders-   Cinder Products Company

                                  3450 Lakeshore Avenue, Oakland, California 94610

    (b) Clay-   Cedar Heights Clay Company

                                  50 Portsmouth Road, Oak Hill, Ohio

4. <u>Source Name:</u>

    (a) Volcanic cinders - Volcalite

    (b) Clay - Cedar Heights Airfloated Bonding Clay

5. <u>Chemical Analysis:</u>

    (a) Volcanic cinders.

		Volcalite*	Hypersthene Andesite (a, p. 458)
Silica	(SiO_2)	54.22	56.88
Aluminum Oxide	(Al_2O_3)	25.04	18.25

*Chemical analysis provided by supplier.

(a) Volcanic cinders (Continued)

		Volcalite*	Hypersthene Andesite (a, p. 458)
Ferric Oxide	(Fe$_2$O$_3$)	4.28	2.35
Calcium Oxide	(CaO)	5.58	4.07
Sodium Oxide	(NaO)	1.61	3.29
Potassium Oxide	(K$_2$O)	0.41	1.42
		99.25	

(b) Clay

Ignition loss	9.4%
Silica	57.3%
Alumina	28.5%
Iron Oxide	1.1%
Titania	2.0%
Lime	0.1%
Magnesia	0.2%
Alkalies	1.2%
Sulphur	0.2%
Total	100.0%

6. Petrological Description

(a) Volcanic cinders.

   Highly porous volcanic (extrusive) rock of "basic" composition commonly
   termed volcanic scoria. A comparison of the chemical analysis provided
   by the producer with other published analyses (a, pp. 456-466; (b, pp. 126-131)
   indicates that the rock type is an andesite.

_____

*Chemical analysis provided by supplier.

(b) Clay.

The supplier reports that this material is essentially a kaolin-type clay.

The volcanic cinders (RC2 type) and clay are mixed 1:1 (by weight) to produce the LSM soil. Figure A-37 is a photomicrograph of the LSM soil.

7. Mineralogical Description

(a) Volcanic cinders.

No mineralogic analysis of the test soil has been done, but a normative analysis of the hypersthene andesite reported by Clarke (a, p. 458) gives the following:

Quartz	9.1%
Orthoclase	8.3%
Albite	27.8%
Anorthite	30.9%
Diopside	5.3%
Hypersthene	13.2%
Magnetite	3.5%
Ilmenite	0.8%

The reddish color of the RC soil would indicate that this material contains iron hydroxides (e.g., limonite) rather than the magnetite and ilmenite referred to in the norm and probably constitutes a larger percentage of the RC material than the iron minerals used in the example.

Decomposition due to weathering tends to decrease the percentage of silica, calcium oxide and sodium oxide and increase the percentage of ferric oxides and aluminum oxide (leaching, chloritization and kaolinization). The iron oxides (e.g., magnetite, ilmenite) tend to form iron hydroxides (e.g., limonite); the femic minerals (e.g., hypersthene) to

Scale Graduated In
1/32 Inch Increments

Figure A-37. Photomicrograph LSM Soil

form chlorite (chloritization); and the feldspars (e.g., orthoclase, albite) to form clays (kaolinization). The chemical analyses exhibit these trends indicating that some decomposition due to weathering has occurred.

(b) Clay

No mineralogic analysis of the clay was done but the supplier reports that the major component of the clay is kaolin.

8. Moisture Content

All test were run on air-dried material. Oven-drying of the air-dried soil at 230° F yielded moisture contents commonly in the range of 0.2 to 0.6% (percent of dry weight of soil).

9. Grain Size Distribution

Figure A-38 shows the range and average grain size distribution of this soil. The table on this figure lists some of the grain size parameters investigated in this study.

10. Density and Relative Density

The average relative density of Soil No. 10 is about 0.5. Figure A-39 shows the relationship between soil unit weight (density) and relative density for the LSM soil as determined by the method of test suggested by D. M. Burmister (c, pp. 175-177). The solid line represents the average of several tests, and the dashed lines indicate the 95% confidence limits for the data.

11. Direct Shear Test Results

Figure A-40 shows the relationship between angle of internal friction and relative density obtained from the direct shear tests. This figure indicates that the angle of internal friction for Soil No. 10 is about 42°. The complete data obtained from the direct shear tests is given in Appendix C.

GRAIN SIZE ANALYSIS CURVES - LM SMS

U.S. Std. Sieve No.

Percent Finer Than By Weight

Grain Size – mm

Grain Size Parameters

Name	Symbol	Value — Average	Value — Range
Mean Size	D50	0.07mm	0.06-0.08mm
Effective Diameter	D10	Small	----
Coefficient of Uniformity (D60/D10)	Cu	Large 4.1mm	----
Coarseness	D95		4.0-4.2mm

ASEE	SILT (Nonplastic)	Fine	Medium	Coarse	Fine
Class.	CLAY (Plastic)		SAND		GRAVEL
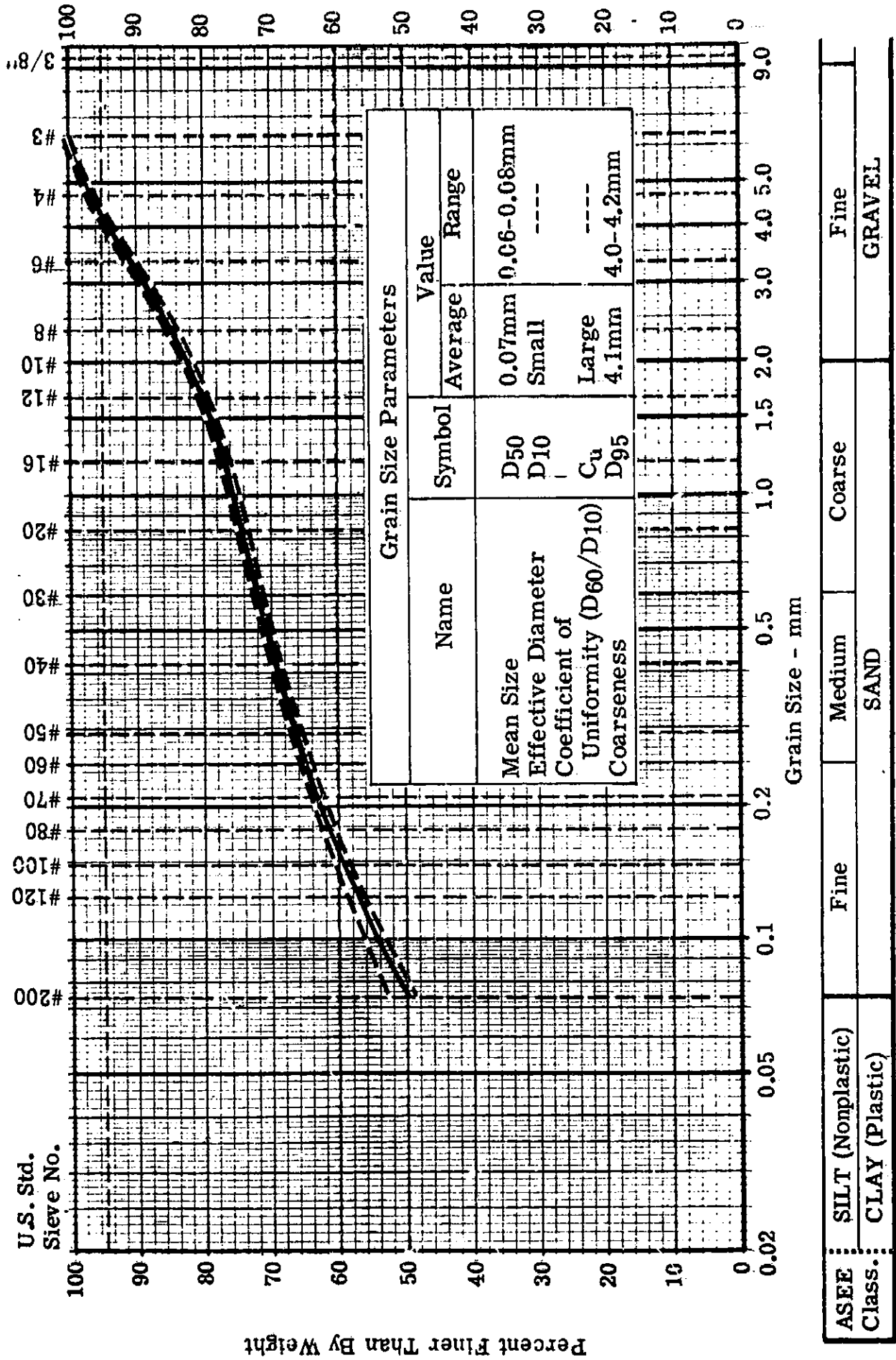
Figure A-38. Average and Range of Seven Samples of LSM

A-76
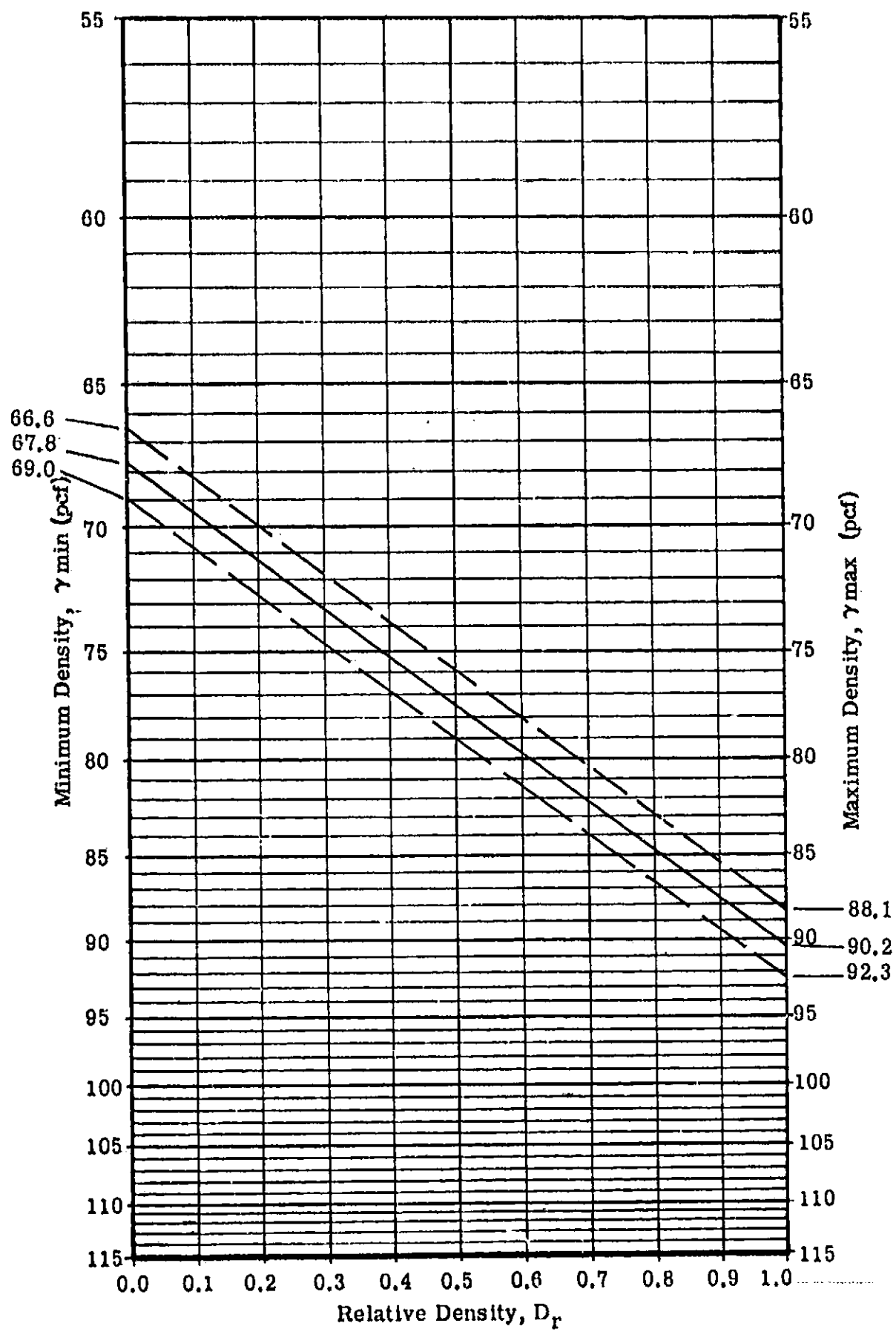
Figure A-39. Density versus Relative Density for LSM Soil
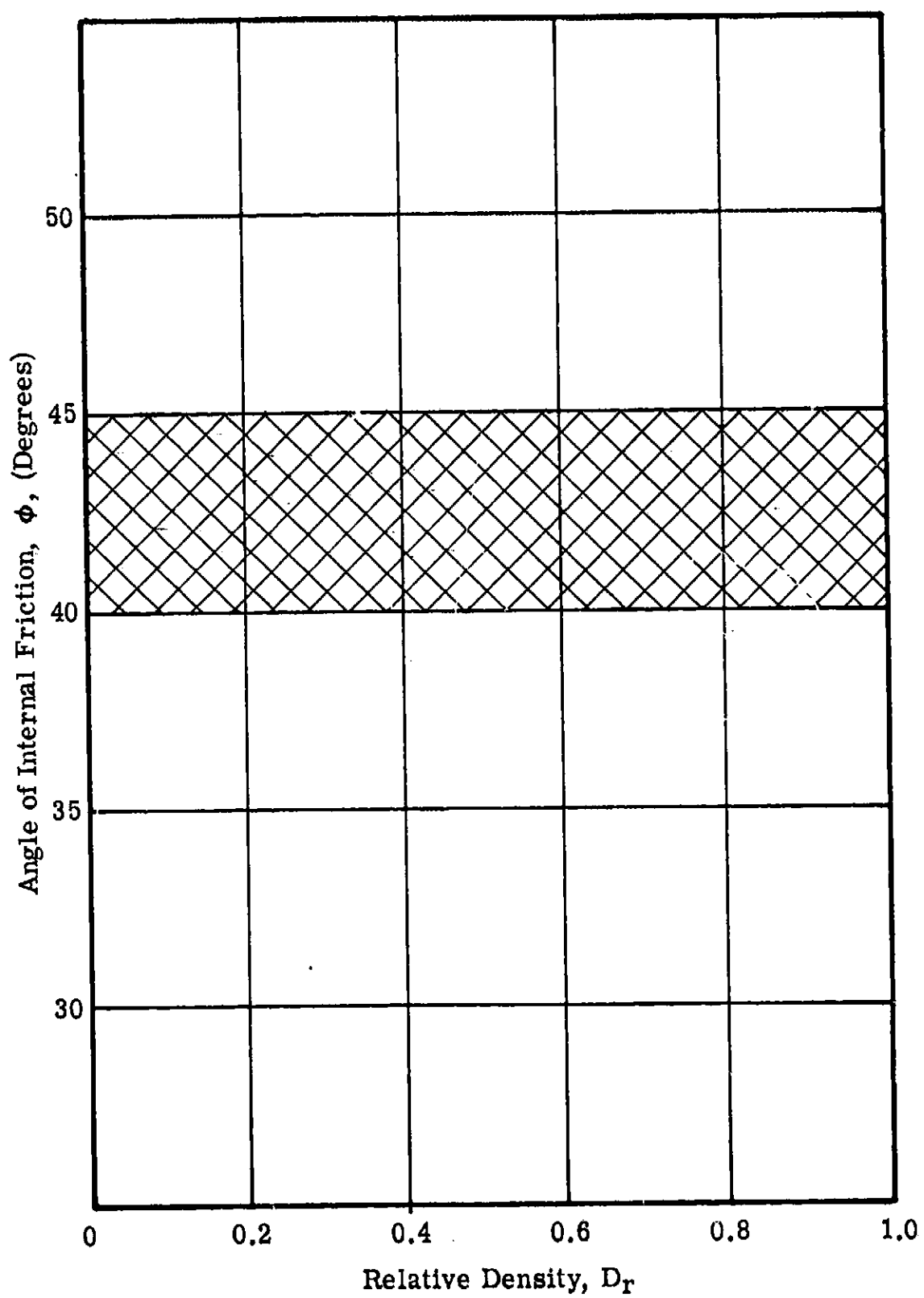
Figure A-40. Angle of Internal Friction (as determined by the direct shear test) Versus Relative Density for LSM Soil

A-78

12.   Sonic Velocity Test

The value of initial tangent modulus was not obtained for Soil No. 10. Tests on LSM soil with D_r = 0.77 gave values of initial tange~ ^{t} modulus between 5,000 and 6,000 psi at a confining pressure of 4 psi (no correction made for Poisson's Ratio). The estimated initial tangent modulus for this soil is 4000 psi. A detailed description of the test apparatus and procedures is given in Appendix B.

13.   Soil Test Bed Placement Procedure

Soil No. 10 was placed with a hopper but was handled by shovel rather than the vacuum system. Each layer (covered with a strip of cardboard) was rolled two times (one pass back and forth in the bin).

14.   Special Conditions

The values of angle of internal friction obtained for the loose and dense LSM soil in the direct shear test were essentially the same - about 40° to 45°. This was due to the fact that the loose soil tended to densify upon application of the normal load.

For this reason it was not possible to construct a ϕ vs. D_r curve. The scatter band shown in Figure A-40 is the estimated range of ϕ for D_r values ranging from .40 to 1.00 based on examination of the direct shear test results.

LM SOIL MECHANICS STUDY

SPECIFICATION FOR SOIL NO. 11

1. <u>Bendix Designation</u>: LSM Dense

2. <u>Description</u>: Mixture of red broadly-graded crushed andesitic (volcanic cinders) and light gray kaolin-type clay.

3. <u>Source</u>:

    (a) Volcanic cinders -   Cinder Products Company
                               3450 Lakeshore Avenue, Oakland, California 94610

    (b) Clay -   Cedar Heights Clay Company
                               50 Portsmouth Road, Oak Hill, Ohio

4. <u>Source Name</u>:

    (a) Volcanic cinders - Volcalite

    (b) Clay - Cedar Heights Airfloated Bonding Clay.

5. <u>Chemical Analysis</u>

    (a) Volcanic cinders

		Volcalite*	Hypersthene Andesite (a, p. 458)
Silica	(SiO_2)	54.22	56.88
Aluminum Oxide	(Al_2O_3)	25.04	18.25

---

*Chemical analysis provided by supplier.

A-80

(a) Volcanic cinders (Continued)

		Volcalite*	Hypersthene Andesite (a, p. 458)
Ferric Oxide	(Fe_2O_3)	4.28	2.35
Calcium Oxide	(CaO)	8.11	7.53
Magnesium Oxide	(MgO)	1.81	3.29
Potassium Oxide	(K_2O)	0.41	1.42
		99.25	

(b) Clay

Ignition loss	9.4%
Silica	57.3%
Alumina	28.5%
Iron Oxide	1.2%
Titania	2.0%
Lime	0.1%
Magnesia	0.2%
Alkalies	1.2%
Sulphur	0.2%
Total	100.0%

6. Petrological Description

(a) Volcanic cinders

Highly porous volcanic (extrusive) rock of "basic" composition termed vol-
canic scoria. A comparison of the chemical analysis provider by the pro-
ducer with other published analyses (a, pp. 456-466; b, pp. 126-131) indicates
that the rock type is an andesite.

*Chemical analysis provided by supplier.

(b) Clay

The supplier reports that this material is essentially a kaolin-type clay.

The volcanic cinders (RC2 type) and clay are mixed 1:1 (by weight) to produce the LSM soil. Figure A-41 is a photomicrograph of the LSM soil.

7.   Mineralogical Description

(a) Volcanic cinders

No mineralogic analysis of the test soil has been done, but a normative analysis of the hypersthene andesite reported by Clarke (a, p. 458) gives the following:

Quartz	9.1%
Orthoclase	8.3%
Albite	27.8%
Anorthite	30.9%
Diopside	5.3%
Hypersthene	13.2%
Magnetite	3.5%
Ilmenite	0.8%

The reddish color of the RC soil would indicate that this material contains iron hydroxides (e.g., limonite) rather than the magnetite and ilmenite referred to in the norm and probably constitutes a larger percentage of the RC material than the iron minerals used in the example.

Decomposition due to weathering tends to decrease the percentage of silica, calcium oxide and sodium oxide and increase the percentage of ferric oxides and aluminum oxide (leaching, chloritization and kaolinization). The iron oxides (e.g., magnetite, ilmenite) tend to form iron hydroxides (e.g., limonite); the femic minerals (e.g., hypersthene)

A-82

Scale Graduated In
1/32 Inch Increments
Figure A-41. Photomicrograph LSM Soil

to form chlorite (chloritization); and the feldspars (e.g., orthoclase, albite) to form clays (kaolinization). The chemical analyses exhibit these trends indicating that some decomposition due to weathering has occurred.

(b) Clay

No mineralogic analysis of the clay was done but the supplier reports that the major component of the clay is kaolin.

8. Moisture Content

All tests were run on air-dried material. Oven-drying of the air-dried soil at 230°F yielded moisture contents commonly in the range of 0.2 to 0.6% (percent of dry weight of soil).

9. Grain Size Distribution

Figure A-42 shows the range and average grain size distribution of this soil. The table on this figure lists some of the grain size parameters investigated in this study.

10. Density and Relative Density

The average relative density of Soil No. 11 is about 0.70. Figure A-43 shows the relationship between soil unit weight (density) and relative density for the LSM soil as determined by the method of test suggested by D. M. Burmister (c, pp. 175-177). The solid line represents the average of several tests and the dashed lines indicate the 95% confidence limits for the data.

11. Direct Shear Test Results

Figure A-44 shows the relationship between angle of internal friction and relative density obtained from the direct shear tests. This figure indicates that the angle of internal friction for Soil No. 11 is about 38.3°. The complete data obtained from the direct shear tests is given in Appendix C.

A-84

GRAIN SIZE ANALYSIS CURVES – LM SMS

Percent Finer By Weight

U.S. Std.
Sieve No.

3/8" #3 #4 #6 #8 #10 #12 #16 #20 #30 #40 #50 #60 #70 #80 #100 #120 #200

Grain Size – mm

Grain Size Parameters			
Name	Symbol	Value	
		Average	Range
Mean Size	D_{50}	0.07mm	0.06-0.08mm
Effective Diameter	D_{10}	Small	---
Coefficient of Uniformity (D_{60}/D_{10})	C_u	Large	---
Coarseness	D_{95}	4.1mm	4.0-4.2mm

ASEE	SILT (Nonplastic)	Fine	Medium	Coarse	Fine
Class.	CLAY (Plastic)		SAND		GRAVEL
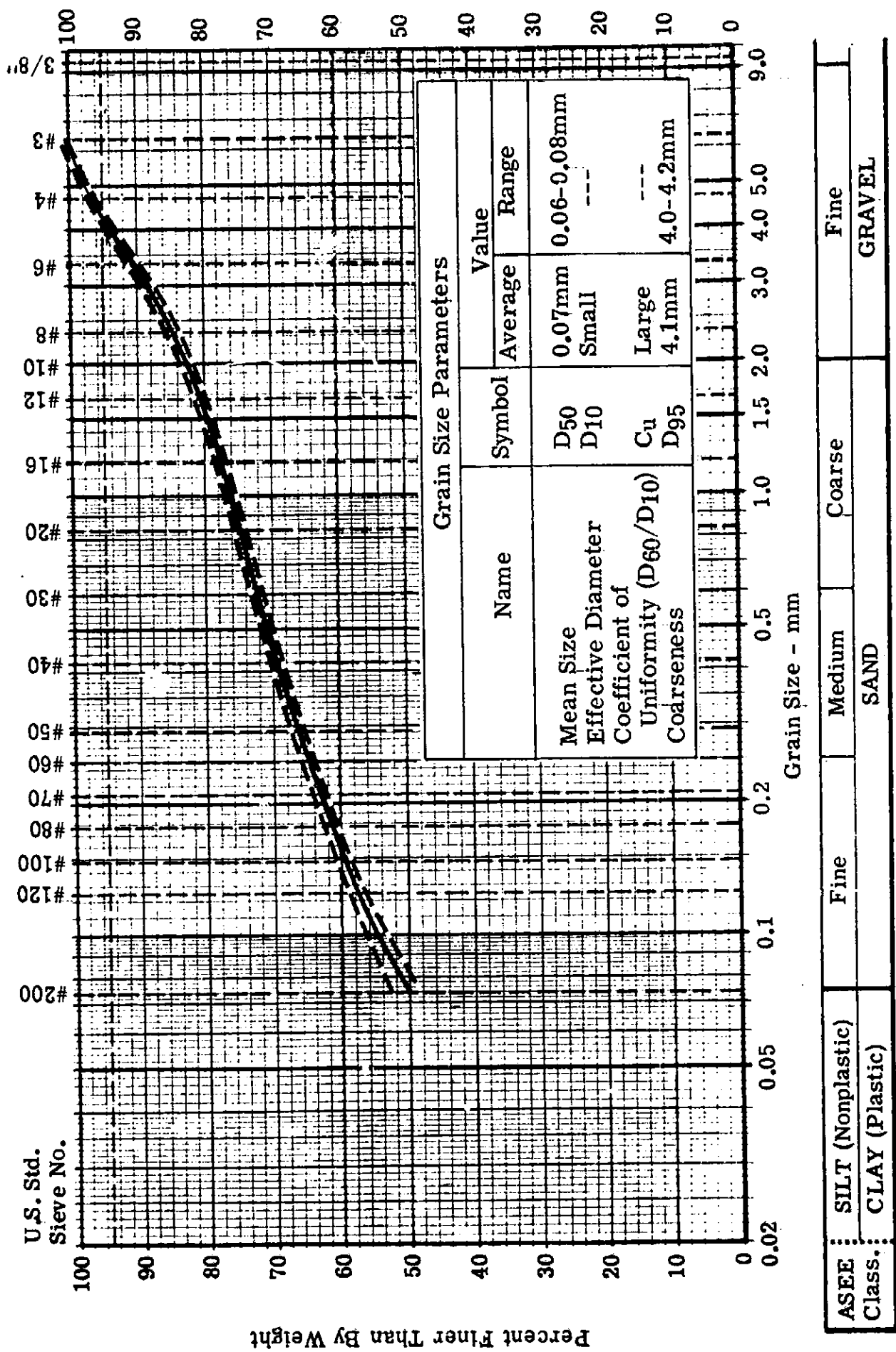
Figure A-42. Average and Range of Seven Samples of LSM Soil

A-85
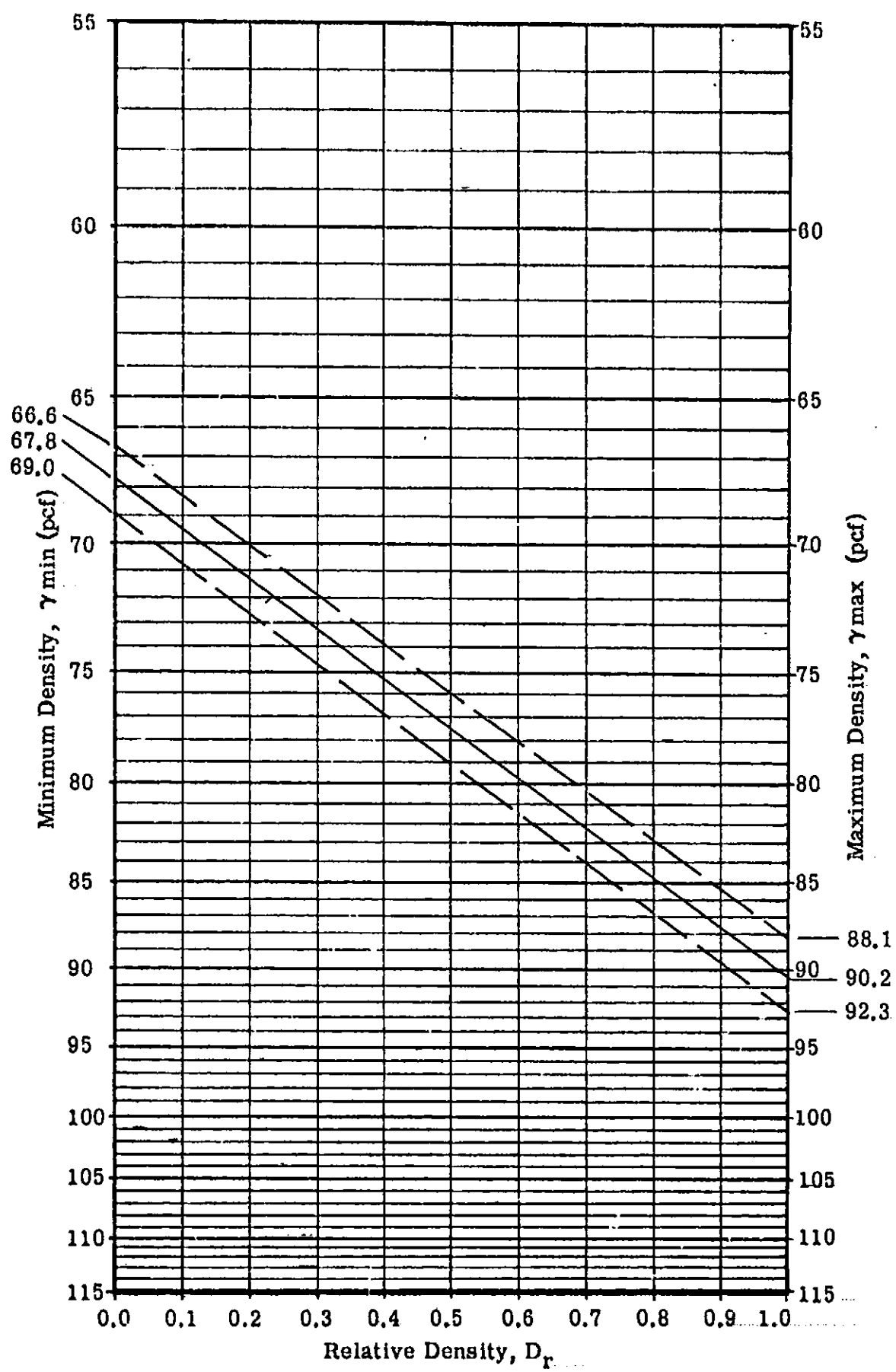
Figure A-43. Density Versus Relative Density for LSM Soil
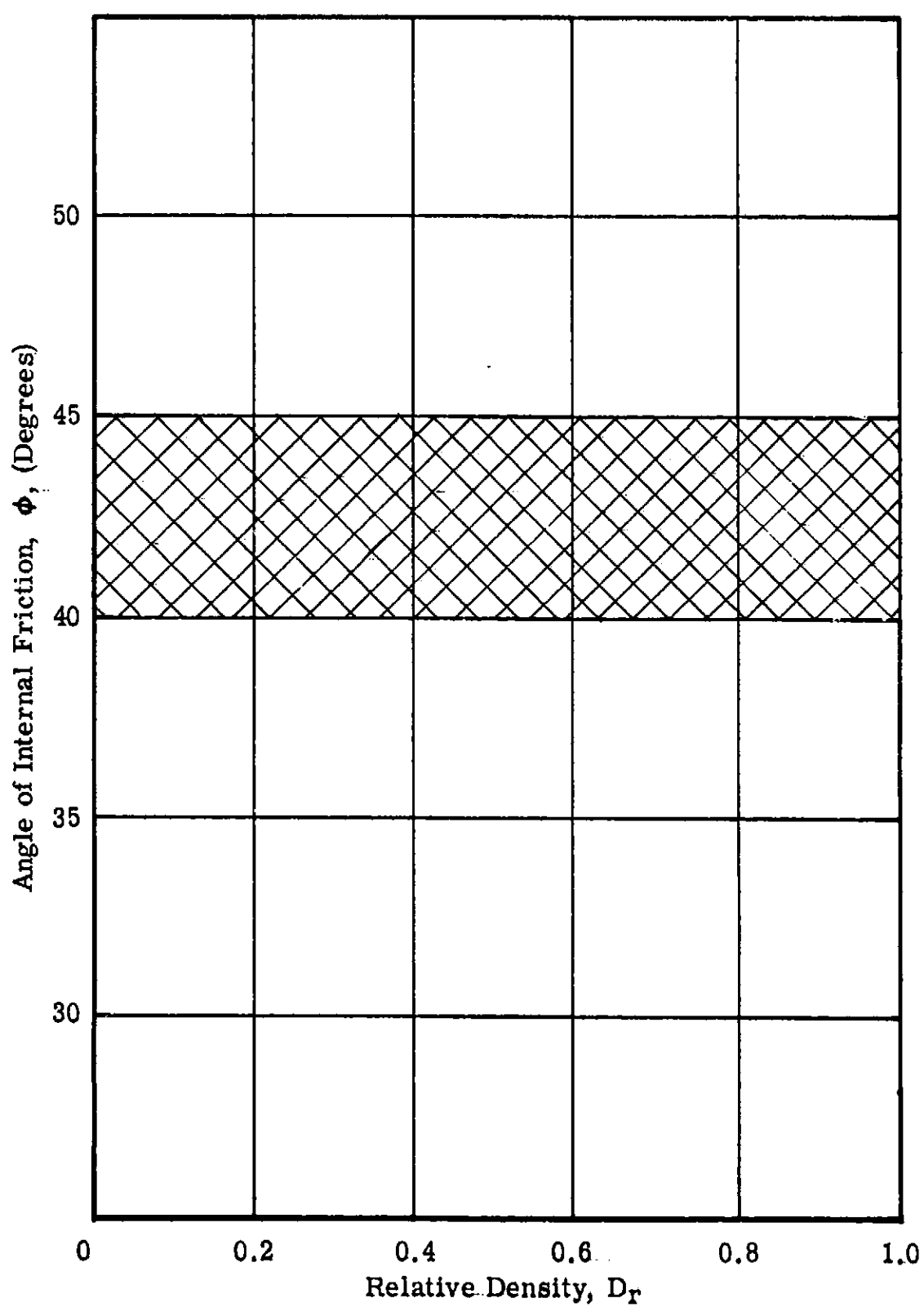
Figure A-44. Angle of Internal Friction (as determined by the direct shear test) Versus Relative Density for LSM Soil

12. Sonic Velocity Test

The values of initial tangent modulus for Soil No. 11 by this test 6,000 psi at a confining pressure of 4 psi (no correction made for Poisson's Ratio). A detailed description of the test apparatus and procedures is given in Appendix B.

13. Soil Test Bed Placement Procedure

Soil No. 11 was placed with a hopper but was handled by shovel rather than the vacuum system. Each layer (covered with a strip of cardboard) was rolled six times (three passes back and forth in the bin).

14. Special Conditions

The values of angle of internal friction obtained for the loose and dense LSM soil in the direct shear were essentially the same - about 40° to 45°. This was due to the fact that the loose soil tended to densify upon application of the normal load.

For this reason it was not possible to construct a ϕ vs. D_r curve. The scatter band shown in Figure A-44 is the estimated range of ϕ for D_r values ranging from .40 to 1.00 based on examination of the direct shear test results.

LM SOIL MECHANICS STUDY

SPECIFICATION FOR SOIL NO. 12

1. <u>Bendix Designation:</u> RSM-b Dense.

2. <u>Description:</u> Mixture of red narrowly-graded crushed andesitic volcanic scoria (volcanic cinders) and white narrowly-graded crushed marble.

3. <u>Source:</u>

   (a) Volcanic Cinders- Cinder Products Company
   3450 Lakeshore Avenue, Oakland, California 94610

   (b) Crushed Marble- Terrazzo Marble Supply
   5700 S. Hamilton Street
   Chicago, Illinois 60636

4. <u>Source Name:</u>

   (a) Volcanic Cinders-Volcalite

   (b) Crushed Marble - #10 Georgia special white marble chips

5. <u>Chemical Analysis:</u>

   (a) Volcalite Cinders

		Volcalite*	Hypersthene Andesite (a, pp. 459-466)
Silica	(SiO_2)	54.22	56.88
Aluminum Oxide	(Al_2O_3)	25.04	18.25
Ferric Oxide	(Fe_2O_3)	4.28	2.35

*Chemical analysis supplied by producer.

A-89

(a) Volcanic Cinders. (Continued)

		Volcalite*	Hypersthene Andesite (a, pp. 456-466)
Calcium Oxide	(CaO)	8.11	7.53
Magnesium Oxide	(MgO)	5.58	4.07
Sodium Oxide	(NaO)	1.61	3.29
Potassium Oxide	(K$_2$O)	0.41	1.42
		99.25	

(b) Crushed Marble:

No chemical analysis available but primarily calcium carbonate (CaCO$_3$).

6. Petrological Description

(a) Volcanic Cinders.

Highly porous volcanic (extrusive) rock of "basic" composition. Commonly termed volcanic scoria. A comparison of the chemical analysis provided by the producer with other published analyses (a, pp. 456-466; b, pp. 126-131) indicates that the rock type is an andesite.

(b) Crushed Marble.

Marble is a crystaline compact variety of metamorphosed sedimentary limestone.

The volcanic cinders and crushed marble are mixed in the ratio of 1:3, respectively, by weight. Figure A-45 is a photomicrograph of the resulting RSM.

7. Mineralogical Description

(a) Volcanic Cinders.

---

*Chemical analysis supplied by producer.
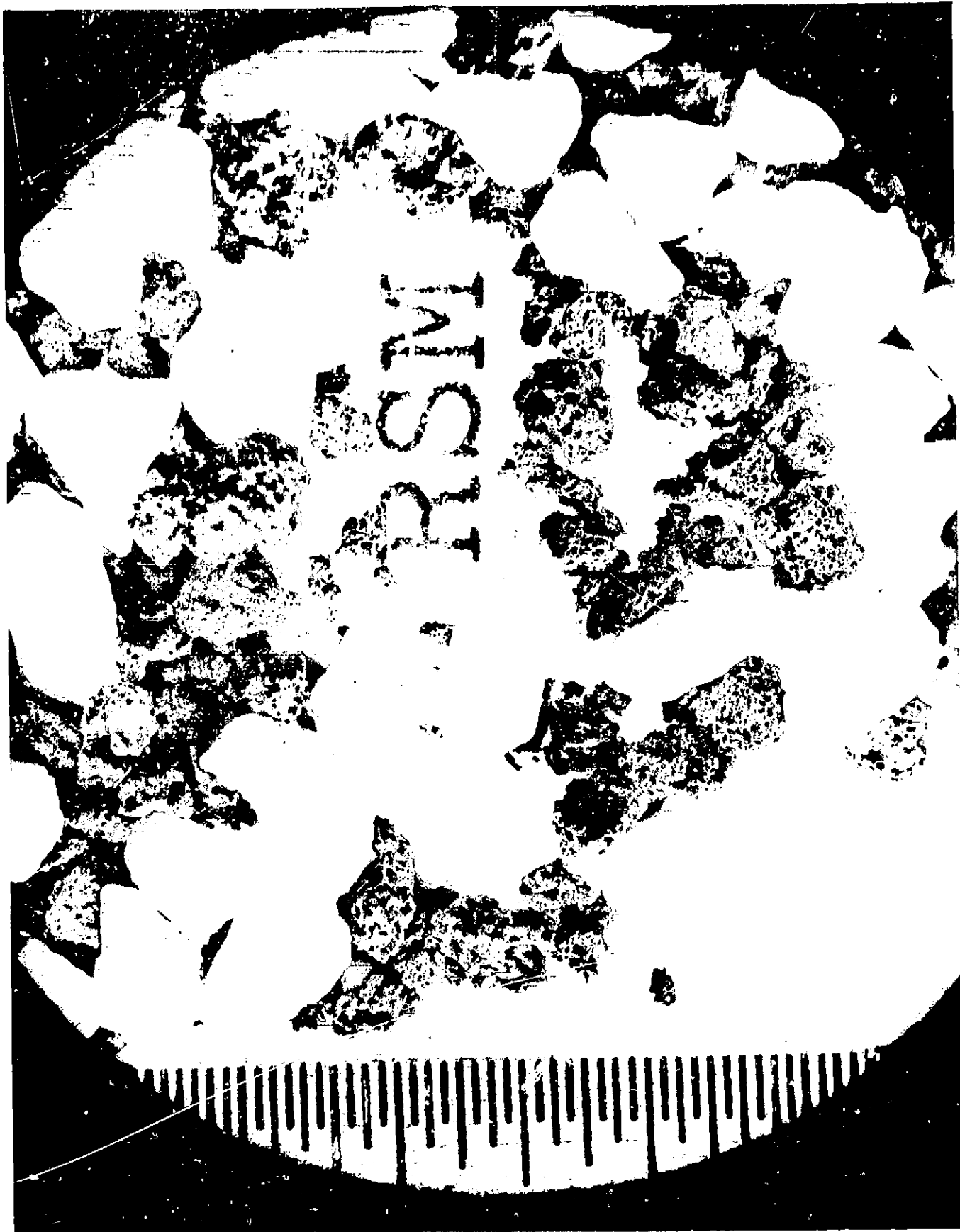
Scale Graduated In
1/32 Inch Increments

Figure A-45. Photomicrograph RSM Soil

No mineralogic analysis of the test soil has been done, but a normative
analysis of the hypersthene andesite reported by Clarke (a, p. 458) gives
the following:

Quartz	9.1%
Orthoclase	8.3%
Albite	27.8%
Anorthite	30.9%
Diopside	5.3%
Hypersthene	13.2%
Magnetite	3.5%
Ilmenite	0.8%

The reddish color of the RS soil would indicate that this material contains iron hydrox-
ides (e.g., limonite) rather than the magnetite and ilmenite referred to in the norm
and probably constitutes a larger percentage of the RS material than the iron minerals
used in the example.

Decomposition due to weathering tends to decrease the percentage of silica, calcium
oxide and sodium oxide and increase the percentage of ferric oxides and aluminum oxide
(leaching, chloritization and kaolinization). The iron oxides (e.g., magnetite, ilmenite)
tend to form iron hydroxides (e.g., limonite); the femic minerals (e.g., hypersthene) to
form chlorite (chloritization); and the feldspars (e.g., orthoclase, albite) to form clays
(kaolinization). The chemical analyses exhibit these trends indicating that some decom-
position due to weathering has occurred.

(b) Crushed Marble.

No mineralogic analysis of the marble was done but it consists primarily of
calcite.

8. Moisture Content

All tests were run on air-dried material. Oven-drying of the air-dried soil at 230°F yielded moisture contents commonly in the range of 0.2 to 0.6% (percent of dry weight of soil).

9. Grain Size Distribution

Figure A-46 shows the range and average grain size distribution of this soil. The table on this figure lists some of the grain size parameters investigated in this study. All data shown is for unused, undegraded material.

10. Density and Relative Density

The average relative density of Soil No. 12 is about 0.75. Figure A-47 shows the relationship between soil unit weight (density) and relative density for the RSM soil as determined by the method of test suggested by D. M. Burmister (c, pp. 175-177).

11. Direct Shear Test Results

Figure A-48 shows the relationship between angle of internal friction and relative density obtained from the direct shear tests.

This figure indicates that the angle of internal friction for Soil No. 12 is about 37°.

The complete data obtained from the direct shear tests is given in Appendix C.

12. Sonic Velocity Test

No determination of initial tangent modulus was made for Soil No. 12. Based on the results of tests with other soils the modulus is estimated to be in the vicinity of 20,000 psi.

13. Soil Test Bed Placement Procedure

Soil No. 12 was placed by shovel and rolled with 10 passes per two inch layer using the lawn roller equipment.

GRAIN SIZE ANALYSIS CURVES - LM SMS

Grain Size Parameters				
			Value	
Name	Symbol	Average	Range	
Mean Size	D_{50}	2.15	2.1-2.2	
Effective Diameter	D_{10}	1.23	1.2-1.3	
Coefficient of Uniformity (D_{60}/D_{10})	C_u	1.87	---	
Coarseness	D_{95}	2.9	2.9	

ASEE	Fine	Medium	Coarse	Fine
Class.	SILT (Nonplastic)	SAND		GRAVEL
	CLAY (Plastic)			
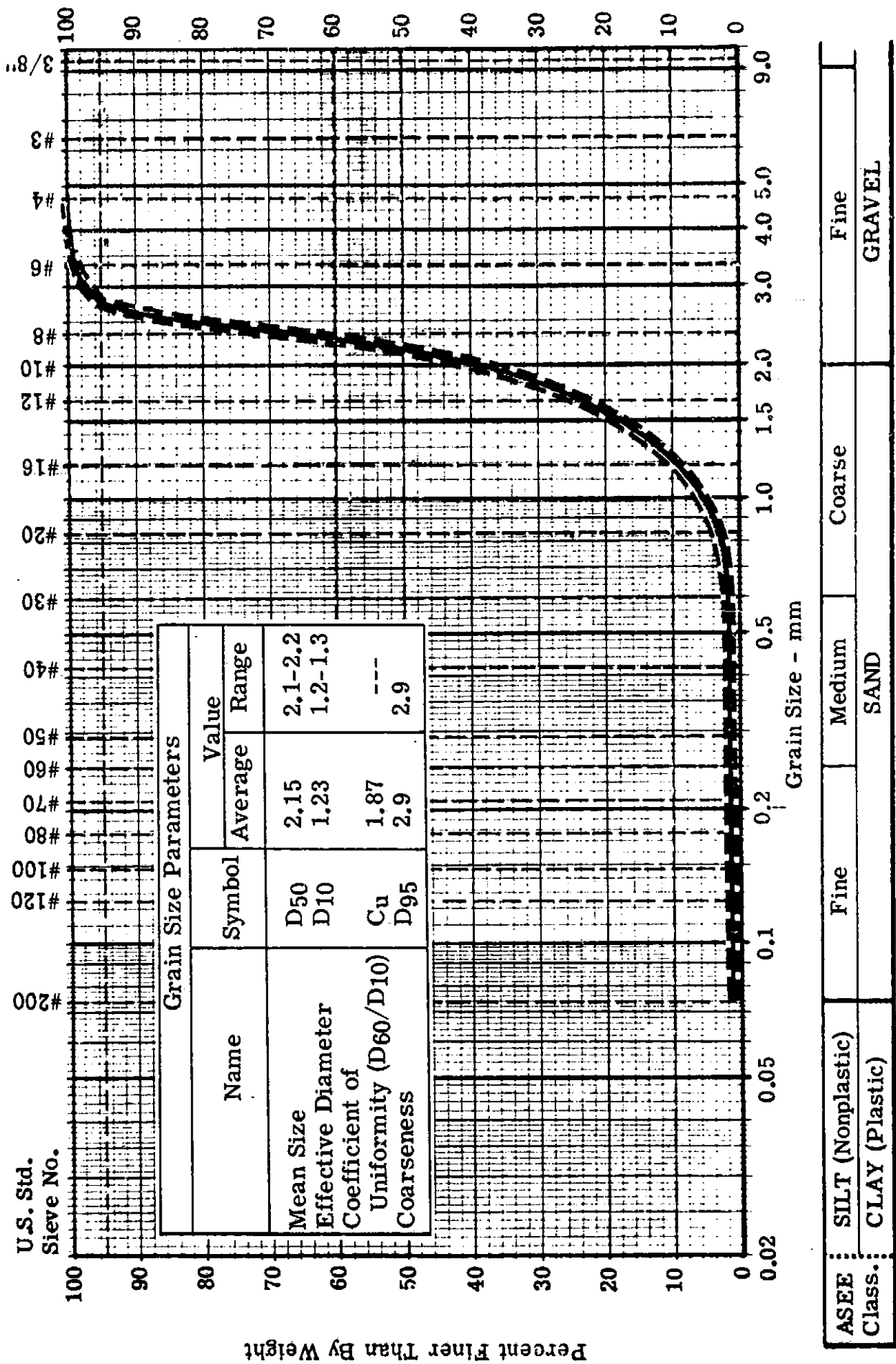
Figure A-46. Average and Range of Sample of Unused RSM-b Soil
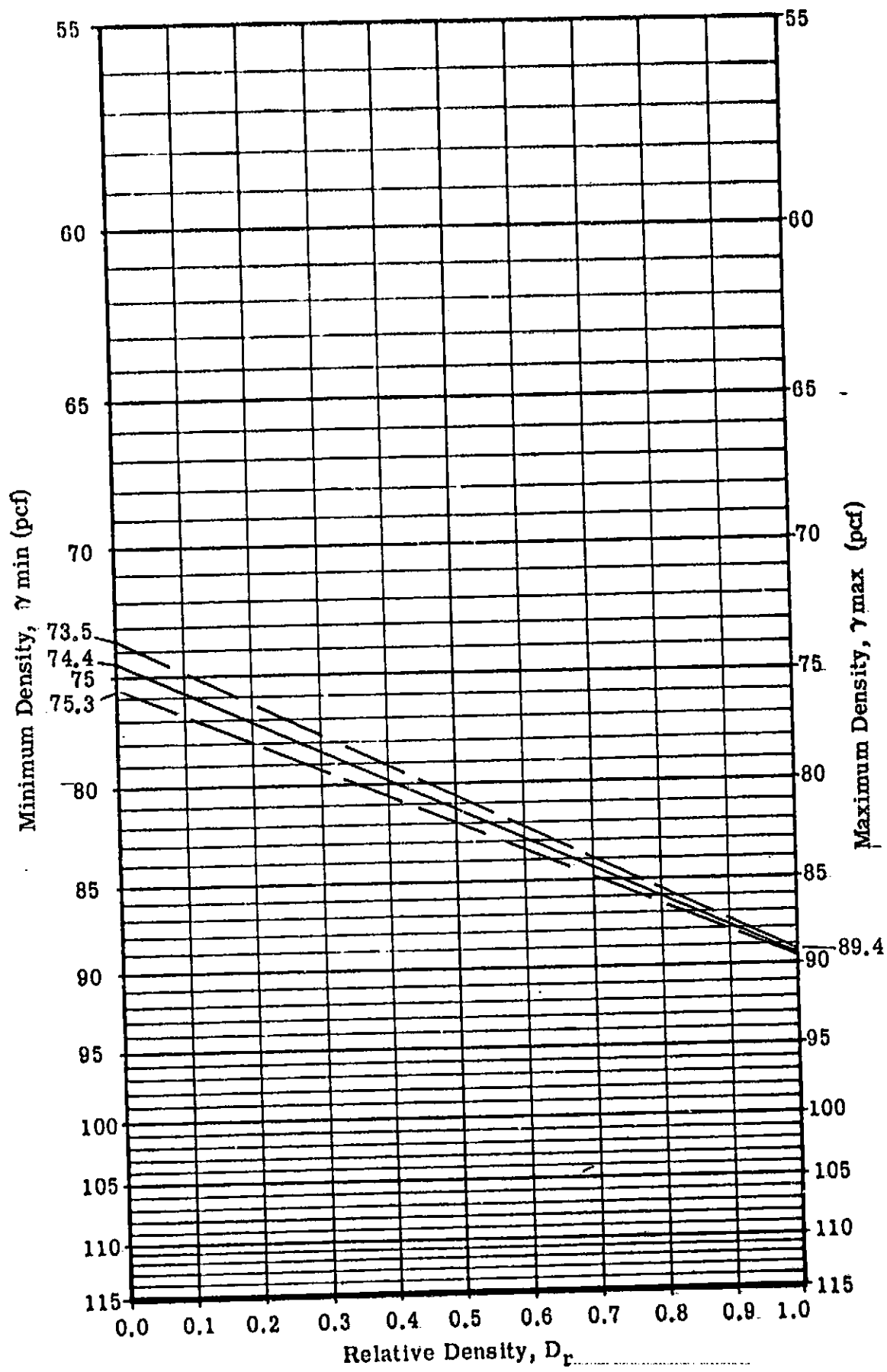
Figure A-47. Density Versus Relative Density for RSM Soil
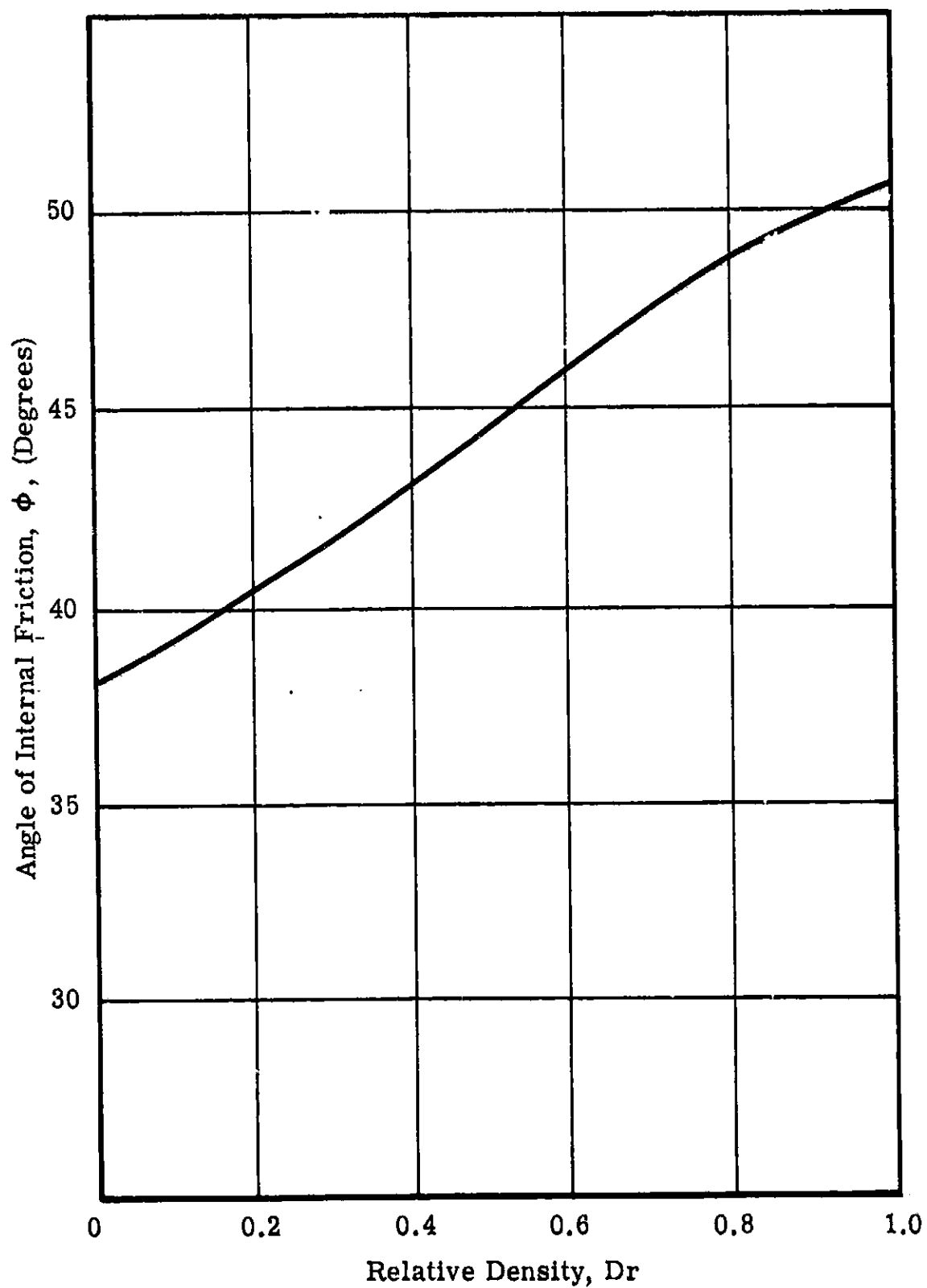
Figure A-48. Angle of Internal Friction (as determined by the direct shear test) Versus Relative Density for RSM Soil

14. Special Comments

The RSM-b soil is susceptible to particle breakdown or degradation due to handling and testing. Such degradation leads to changes in some soil properties, unit weight in particular. If the handling method is such that this process cannot be prevented, or the soil cannot be replaced when these effects become prominent, periodic sampling of the soil bed should be made in order that the effects be known quantitatively.

APPENDIX B

The determination of the sonic modulus of the test soils was subcontracted
by Bendix to the IIT Research Institute at Chicago, Illinois. Appendix B
is a complete reproduction of the final report prepared by IITRI, which
explains the test equipment and procedures used and the results obtained.

IITRI Final Report M6175
P.O. No. 5800191M

DETERMINATION OF THE

INITIAL TANGENT   MODULUS
for
Bendix Products Aerospace Division
The Bendix Corporation
South Bend, Indiana

January, 1967

IIT RESEARCH INSTITUTE
Technology Center
Chicago, Illinois 60616

Report No. M6175
(Final Report)

DETERMINATION OF THE INITIAL TANGENT MODULUS

P. O. No. 5800191M
November 9, 1966 to January 6, 1967

by

J. D. Nelson

for
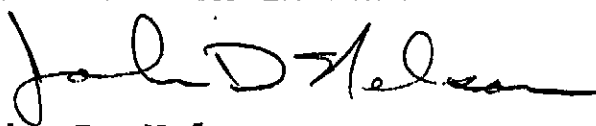
Bendix Products Aerospace Division
The Bendix Corporation
South, Bend, Indiana

January, 1967
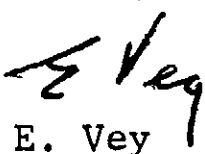
FOREWORD

This report represents the final report on IIT Research Institute Project No. M6175 for Bendix Products Aerospace Division under P. O. No. 5800191M. The work reported herein was performed during the period November 9, 1966 to January 6, 1967. Persons who contributed to this work are J. D. Nelson, R. D. Rowe and E. Vey.

Respectfully submitted,
IIT RESEARCH INSTITUTE

John D. Nelson
Research Engineer

APPROVED:

E. Vey
Assistant Director of Research
Mechanics Research Division

JDN:is

TABLE OF CONTENTS

IIT RESEARCH INSTITUTE

DETERMINATION OF THE INITIAL TANGENT MODULUS

A. INTRODUCTION

The measured initial tangent modulus of soil is highly dependent on the manner in which it is measured. Values measured directly by static triaxial compression tests will generally differ by an order of magnitude from those obtained indirectly by the measurement of stress wave propagation velocities. Furthermore, the determination of the stress-strain curve under dynamic loading[1] yields values of the modulus that may differ by as much as a factor of 4 from those computed from the velocity of wave propagation.

It is difficult, therefore, to ascertain the actual value of the initial tangent modulus for soil, but it is generally believed that the value computed from the stress wave velocity represents most closely the actual value.

This report describes experiments in which a stress wave was passed along a triaxial soil specimen and the wave velocity measured by stress gages located at each end of the sample. The initial tangent modulus was then computed from the measured velocity.

B. APPARATUS AND EXPERIMENTAL PROCEDURE

The apparatus used in this investigation[2] is shown in Fig. 1. The stress wave was generated by a shock tube using compressed air. The time required for the wave to traverse the specimen was determined by displaying the output of stress gages on an oscilloscope and measuring the difference between arrival

---

[1] Vey, E. and L. Strauss, "Stress-Strain Relationships in Clay Due to Propagating Stress Waves", to be published.

[2] Selig, E. T. and E. Vey, "Shock-Induced Stress Wave Propagation in Sand", J. Soil Mech. and Found. Div., ASCE, Vol. 91, No. SM3, Proc. Paper 4332, May 1965, pp. 19-49.

times at each position. Piezoelectric stress gages were mounted at each end of the specimen. The one at the forward end was cemented to the outside of the sample (Fig. 2) and the one at the reaction end was mounted on the inside face of the end plate.

The loose samples were prepared by pouring the soil through a funnel with a slotted end. To obtain dense samples the soil was vibrated by means of a small vibrating plate during preparation (Ref. 2).

The confining pressure was applied to the sample by applying a partial vacuum to the sample inside a rubber diaphragm. Several measurements were made on each sample at different confining pressures. The axial stress applied to the specimen was controlled by pressurizing the driver end of the shock tube to the same pressure each time. The peak stress applied to the sample in this way was somewhat less than 2 psi.

C. RESULTS

The initial tangent modulus was computed by the equation

$$E = \rho c^2 \tag{1}$$

where

      E is the initial tangent modulus

      ρ is the mass density

      c is the velocity of stress wave propagation.

The values so determined were plotted as a function of confining pressure, σ_3, and are shown in Fig. 3 through 7 for the different soils.

The results appear quite reasonable and show a decrease in modulus with a decrease in confining pressure and/ or density. The results for the LSM soil may be somewhat questionable because of difficulties encountered in applying a uniform confining pressure along the specimen length. The permeability of this particular soil was quite low and hence,

there appeared to be a pressure gradient from one end of the specimen to the other. For this reason the actual "effective" confining pressure could not be determined.

This problem was not encountered in any of the other soils.

D. DISCUSSION OF RESULTS

The modulus as computed from Eq. (1) neglects lateral effects and is valid only for a soil in which no lateral strain is permitted. For a more general case the wave velocity would be given by the equation

$$E = \rho c^2 \ \frac{(1+\nu)(1-2\nu)}{(1-\nu)} \tag{2}$$

in which ν is Poisson's ratio. The factor

$$f(\nu) = \frac{(1+\nu)(1-2\nu)}{(1-\nu)} \tag{3}$$

was plotted as a function of ν in Fig. 8. It can be seen that for values of ν less than 0.20 the error introduced by neglecting this term is less than 10 percent. However, it is recommended that measurements be made of ν for the various soils to determine the extent to which this term would be expected to influence the results.

IIT RESEARCH INSTITUTE
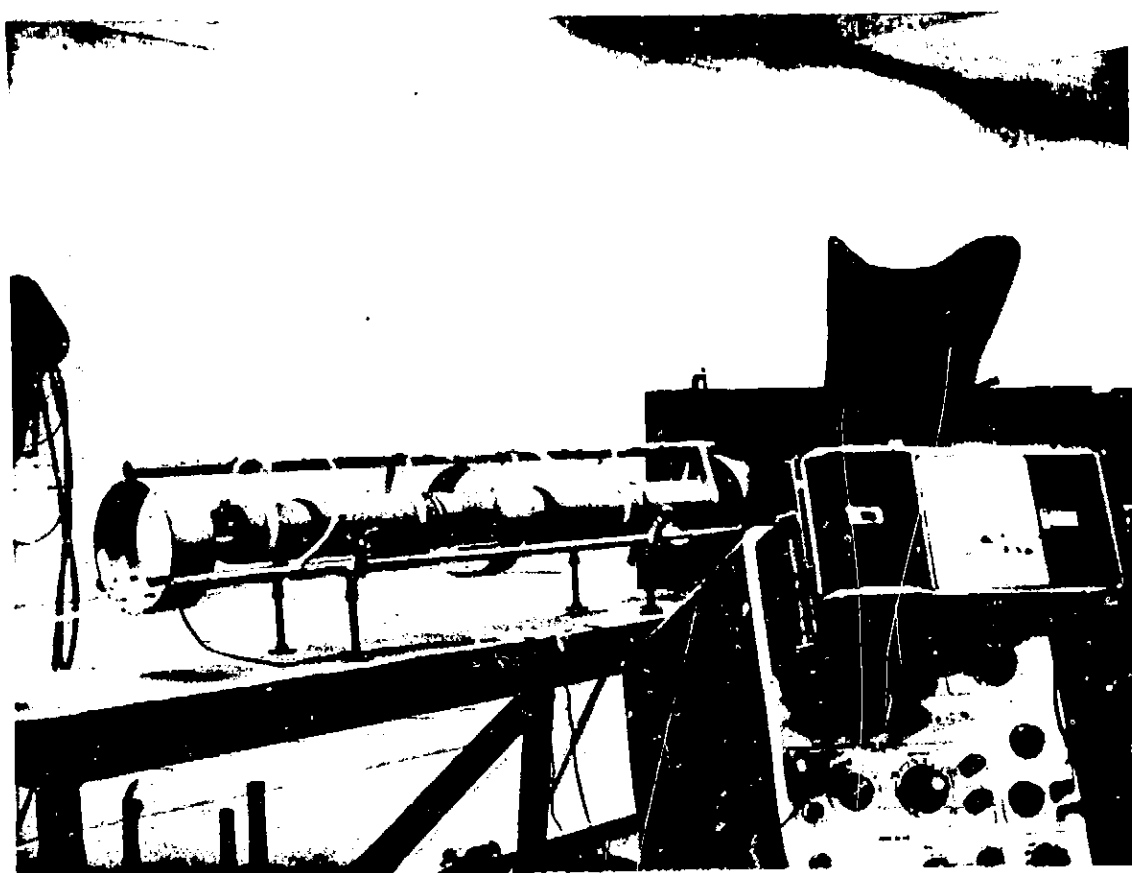
Fig. 1 APPARATUS FOR MEASUREMENT OF
STRESS WAVE VELOCITY
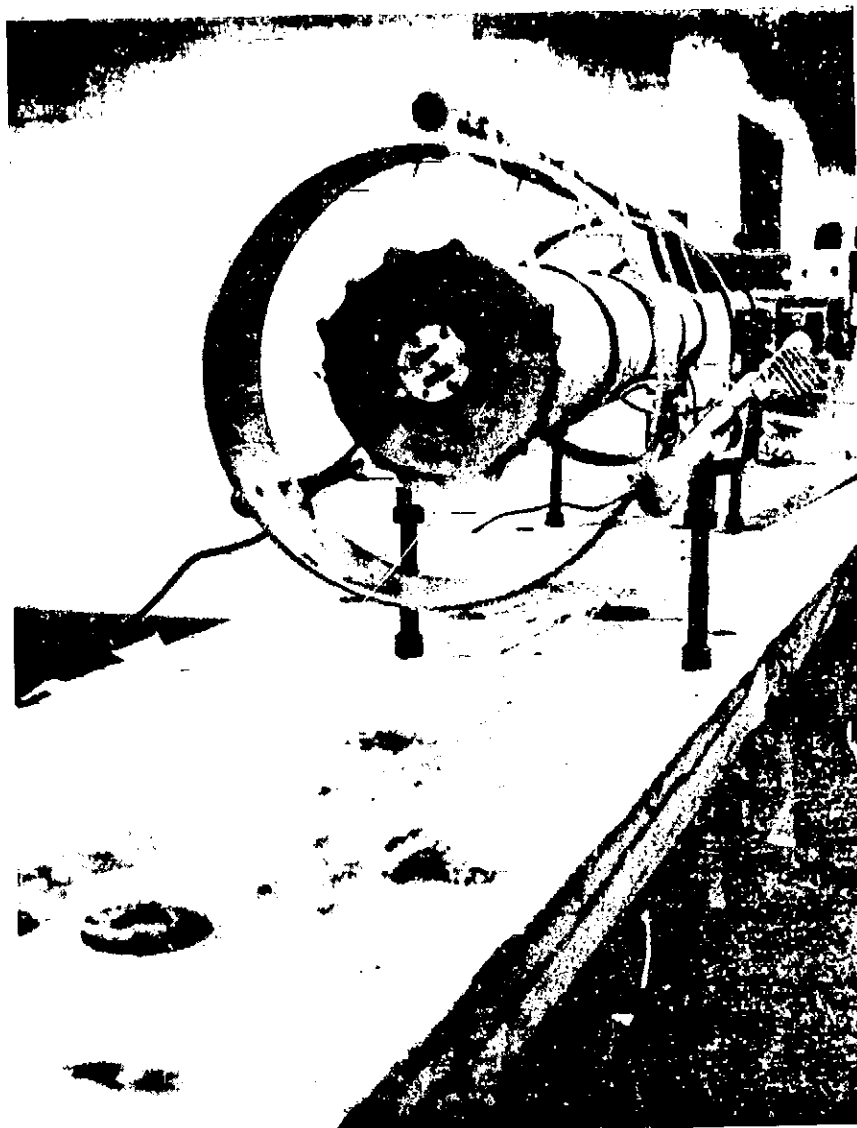
Fig. 2 STRESS GAGE AT FORWARD END
OF SPECIMEN

Fig. 3   E VERSUS σ_3 FOR   RS SOIL

6

Fig. 4 E VERSUS σ_3 FOR PS SOIL

7
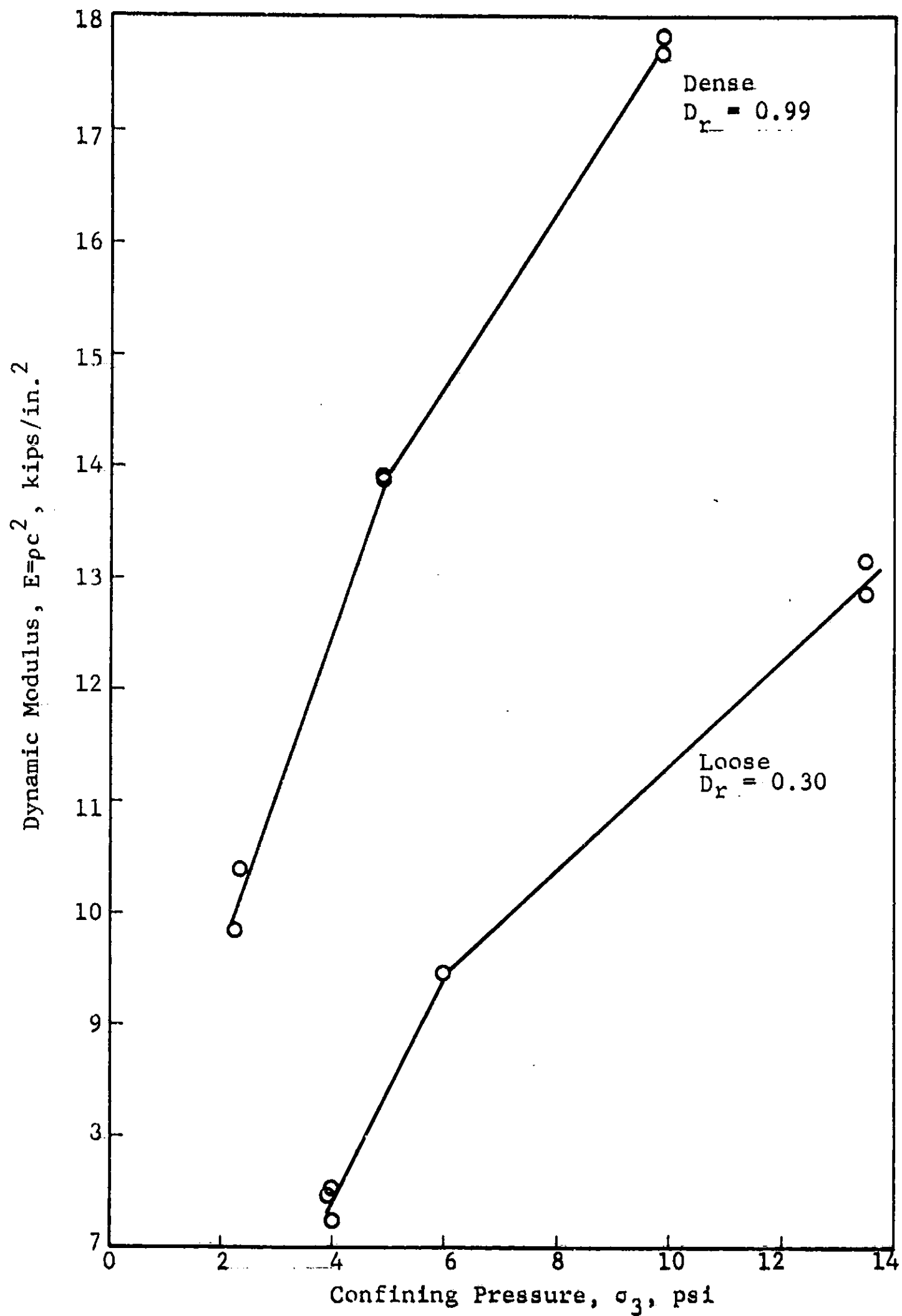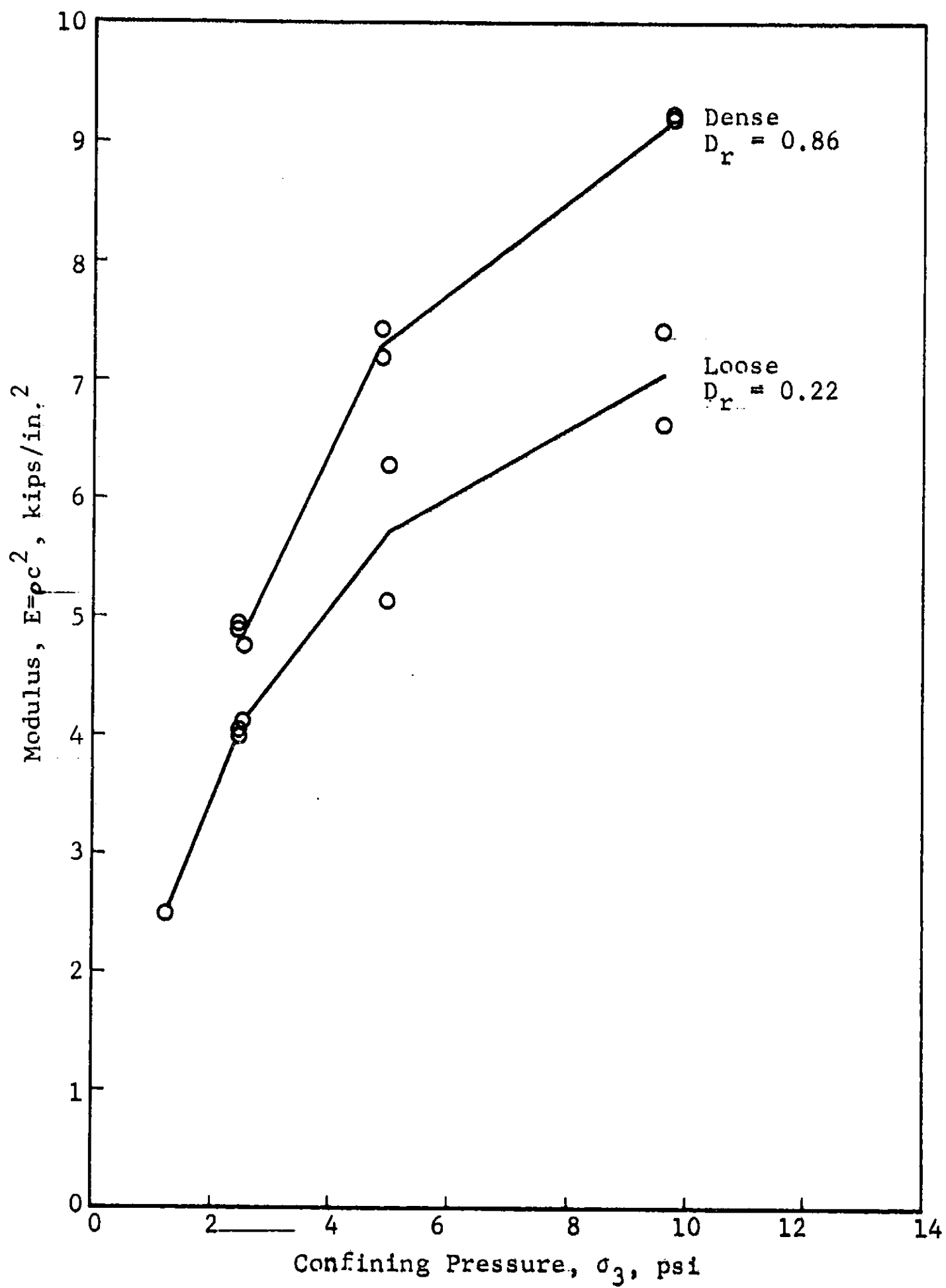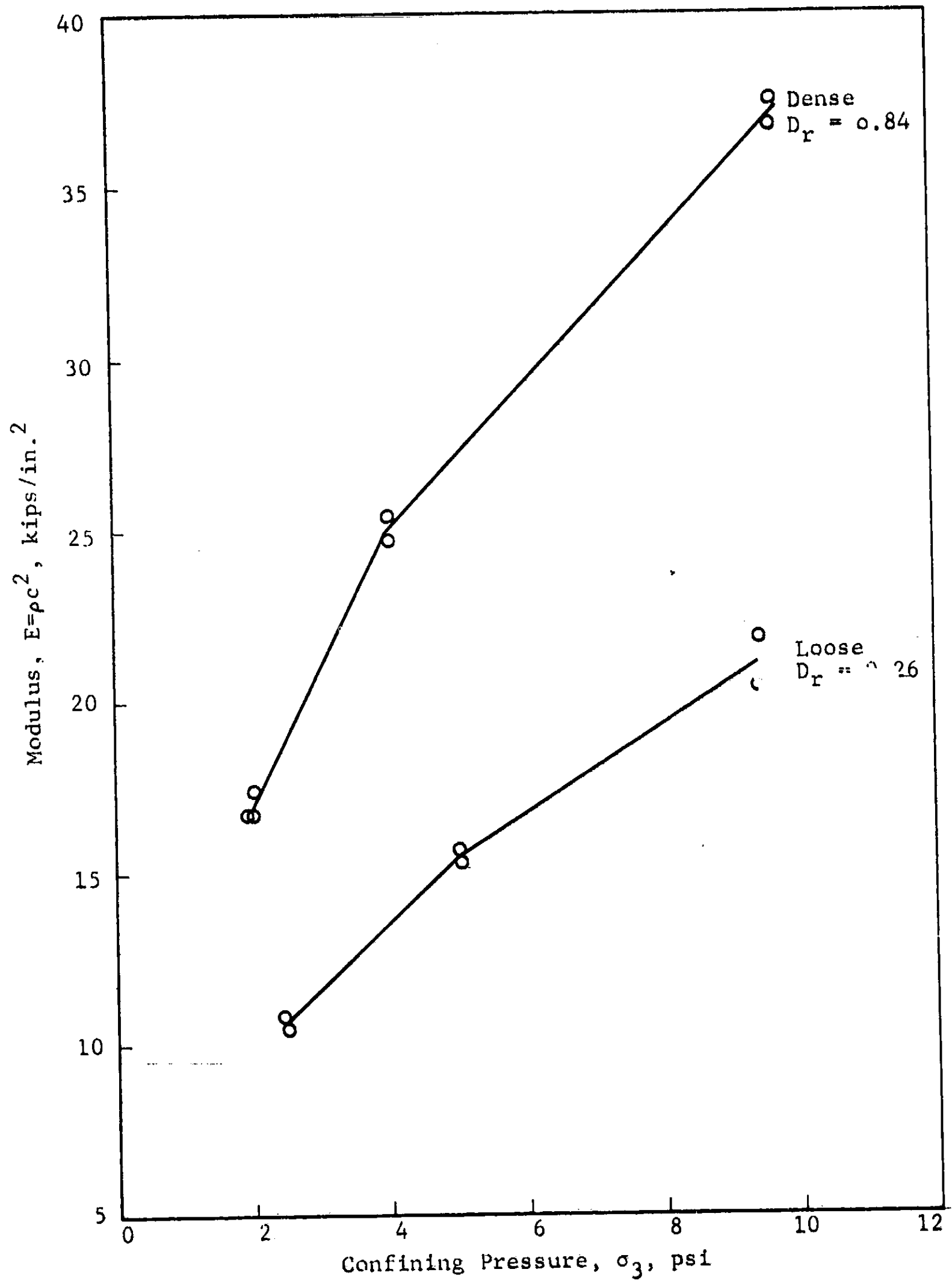
Fig. 5   E VERSUS σ_3 FOR SS SOIL

Fig. 6   E VERSUS σ_3 FOR RC SOIL

9
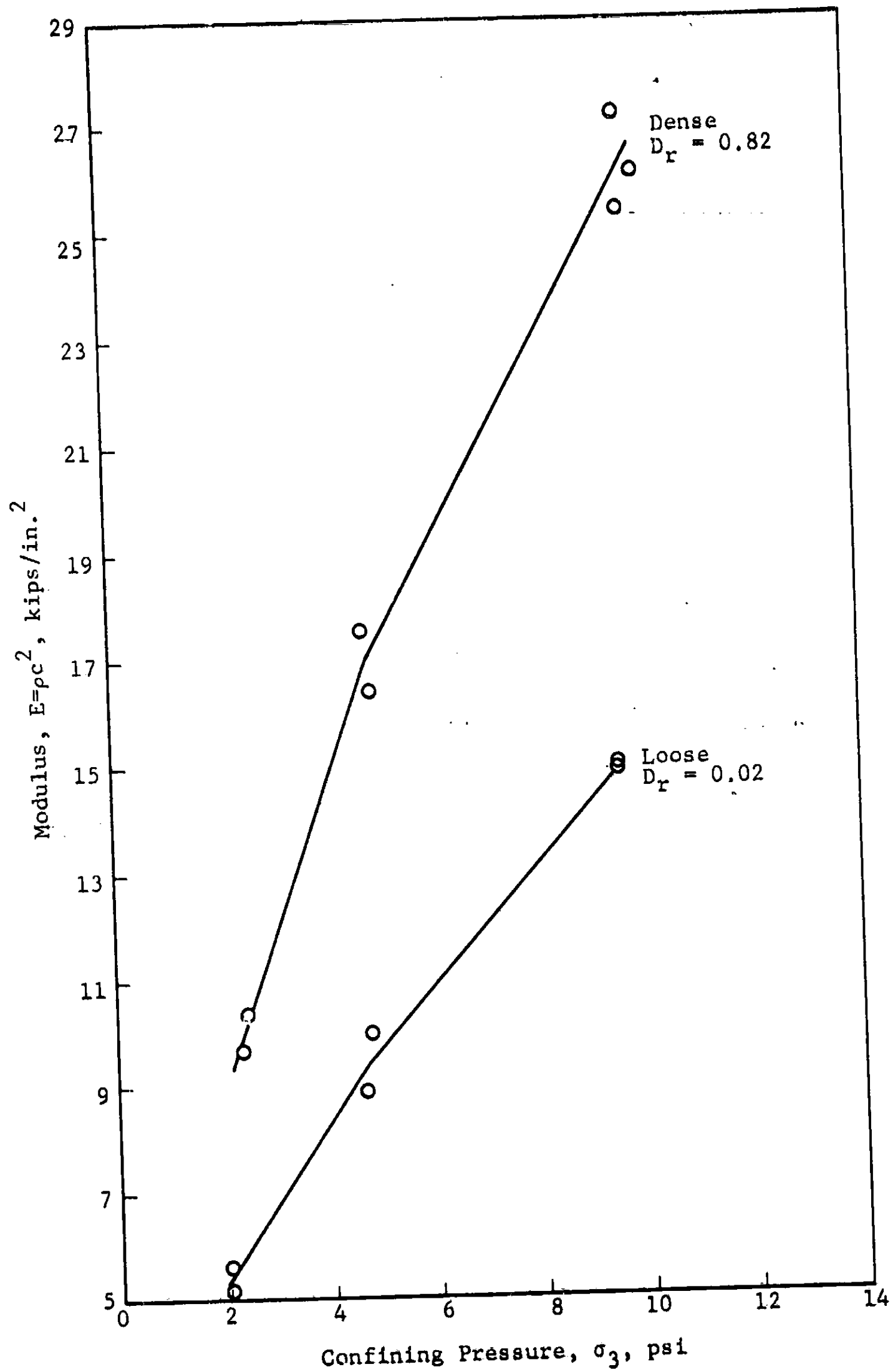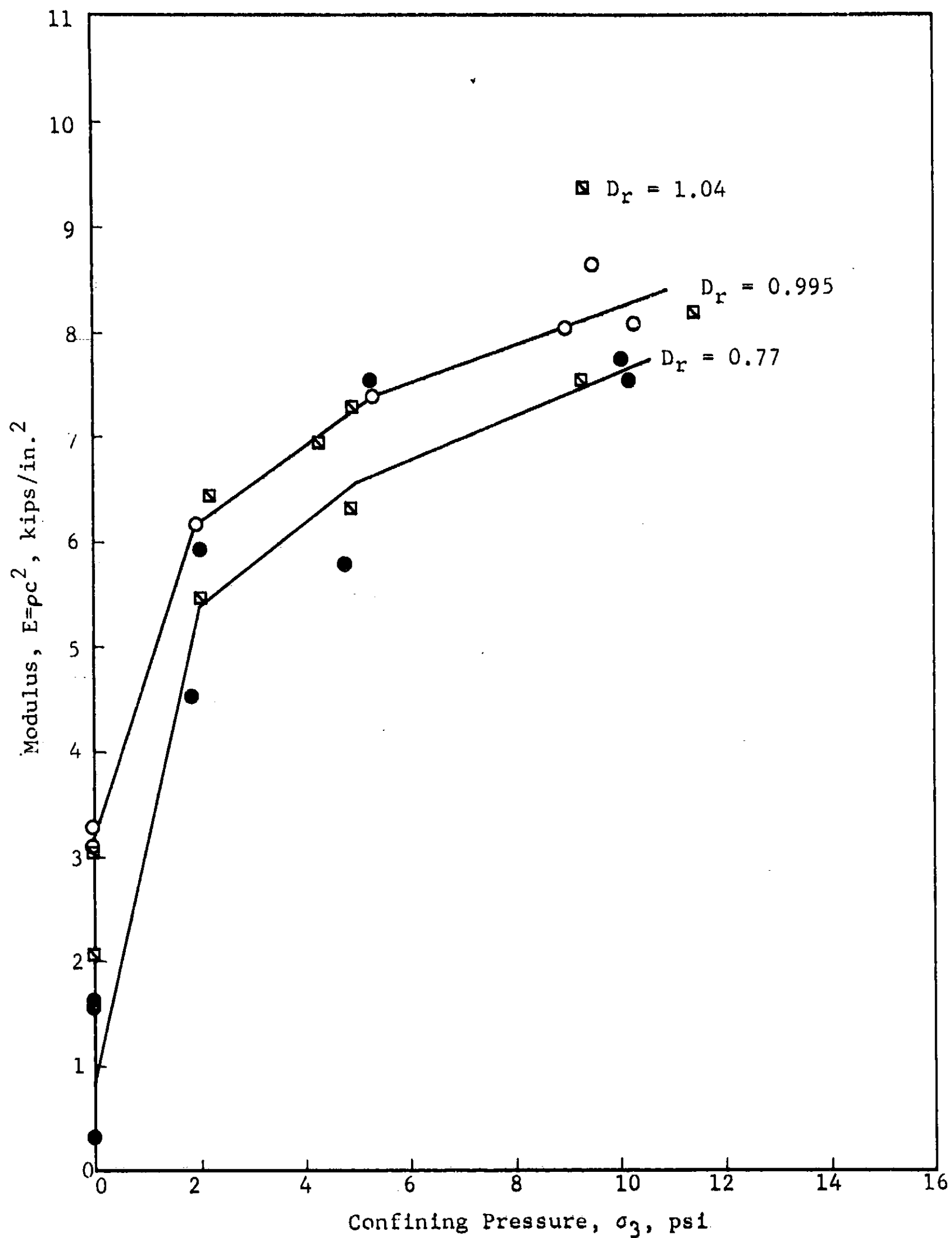
Fig. 7   E VERSUS σ_3 FOR LSM SOIL

Fig. 8 DEPENDENCY OF $f(\nu)$ ON ν $(E=\rho c^2 f(\nu))$

The y-axis is labeled $f(\nu) = \frac{(1+\nu)(1-2\nu)}{(1-\nu)}$

The x-axis is labeled Poisson's Ratio, ν

11
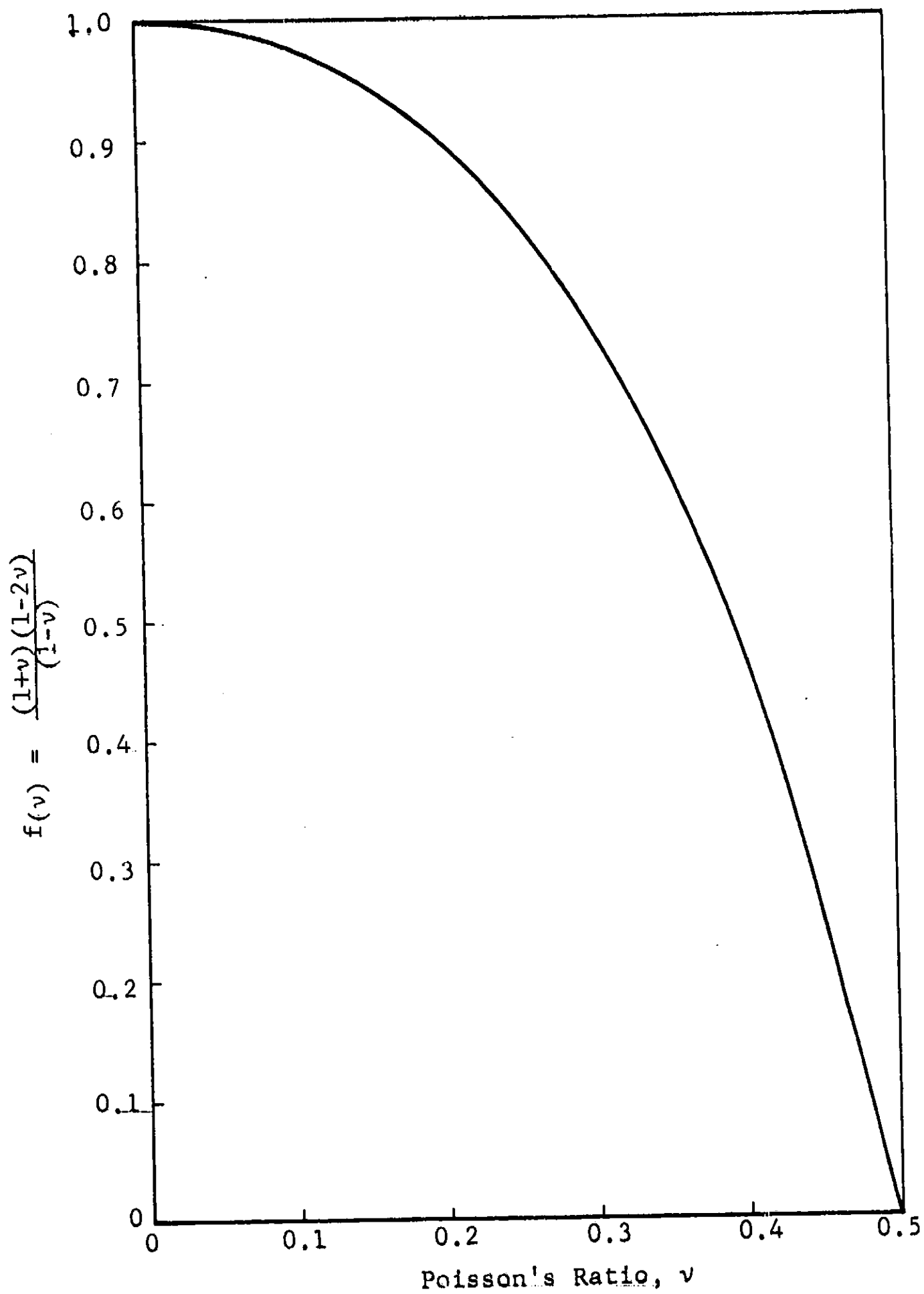
APPENDIX C

DIRECT SHEAR TEST DATA

The direct shear test data presented in this appendix was obtained from tests performed by the Civil Engineering Department of the University of Notre Dame under the supervision of Dr. Bruce B. Schimming, Associate Professor. One exception on Figure C-5A is noted.

Figures C-1A through C-7B are the data sheets and failure envelopes for the original series of tests performed on the test soils. Figures C-8 through C-15 present the failure envelopes plotted by the Univac 1107 computer on a CAL-COMP PLOTTER at Notre Dame. Where more than one series of tests were performed on a given soil, the figures are numbered "A," "B," "C," etc., and the last figure in the series represents a combined plot of all tests.

Finally, Figures C-16 through C-22 show the relationship between angle of internal friction and relative density indicated by the direct shear tests for each soil. Figure C-23 plots the average relationship for all soils except soil number 10.
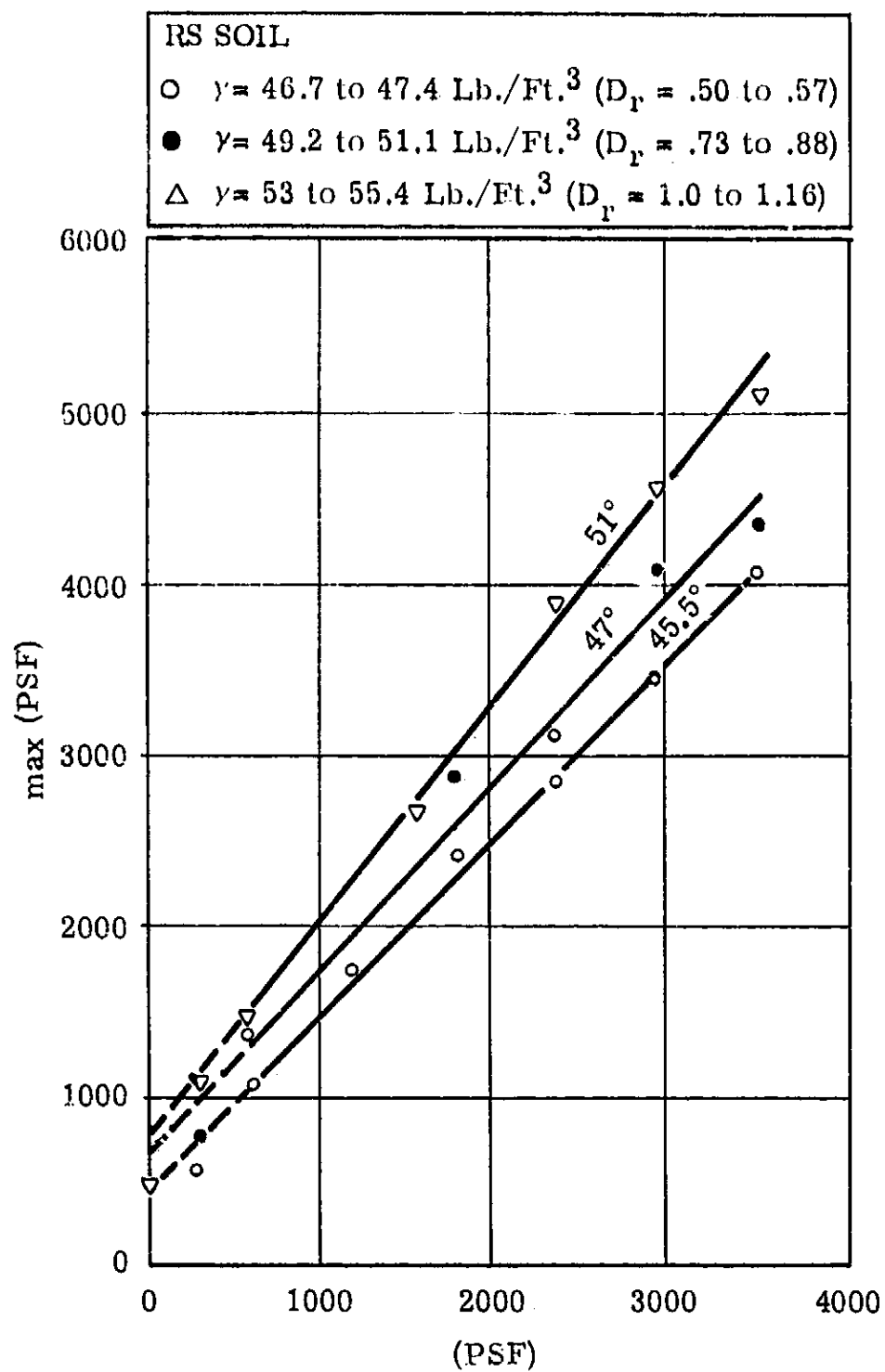
Figure C-1A. Failure Envelopes (Maximum Shear Stress vs. Normal Stress)
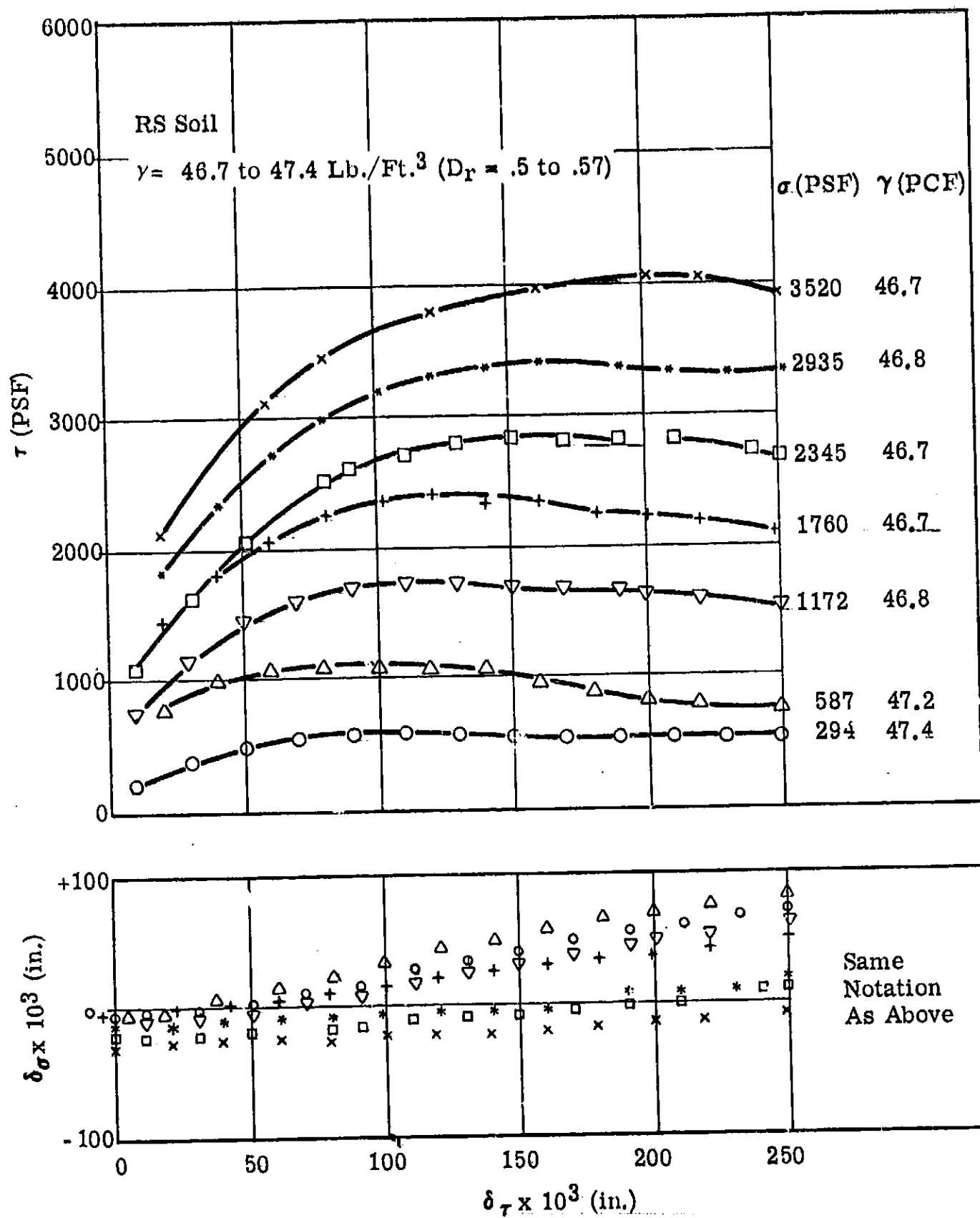
Figure C-1B. Direct Shear Test Data - Shear Stress vs. Shear Displacement
Dilation Displacement vs. Shear Displacement
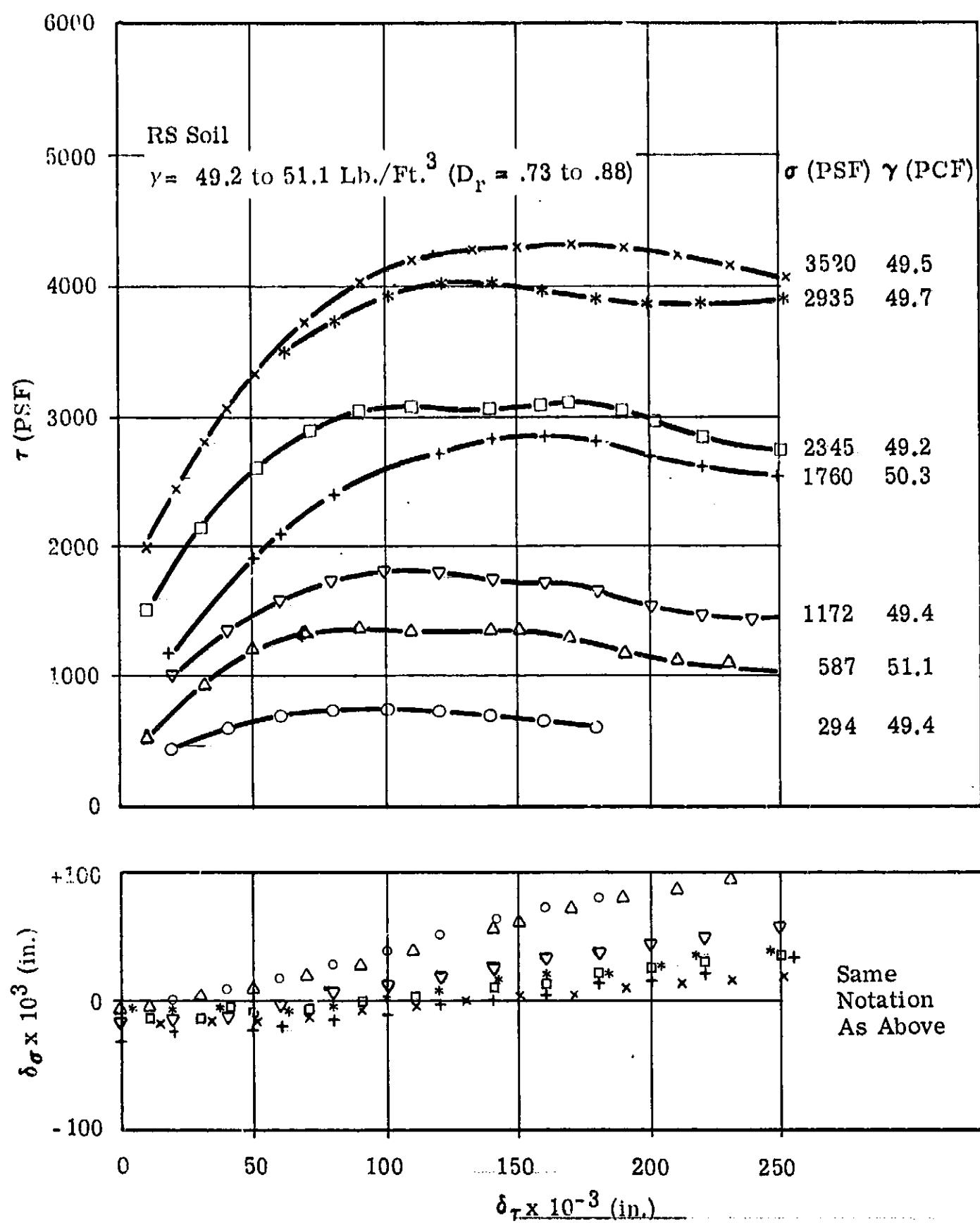
Figure C-1C. Direct Shear Test Data - Shear Stress vs. Shear Displacement
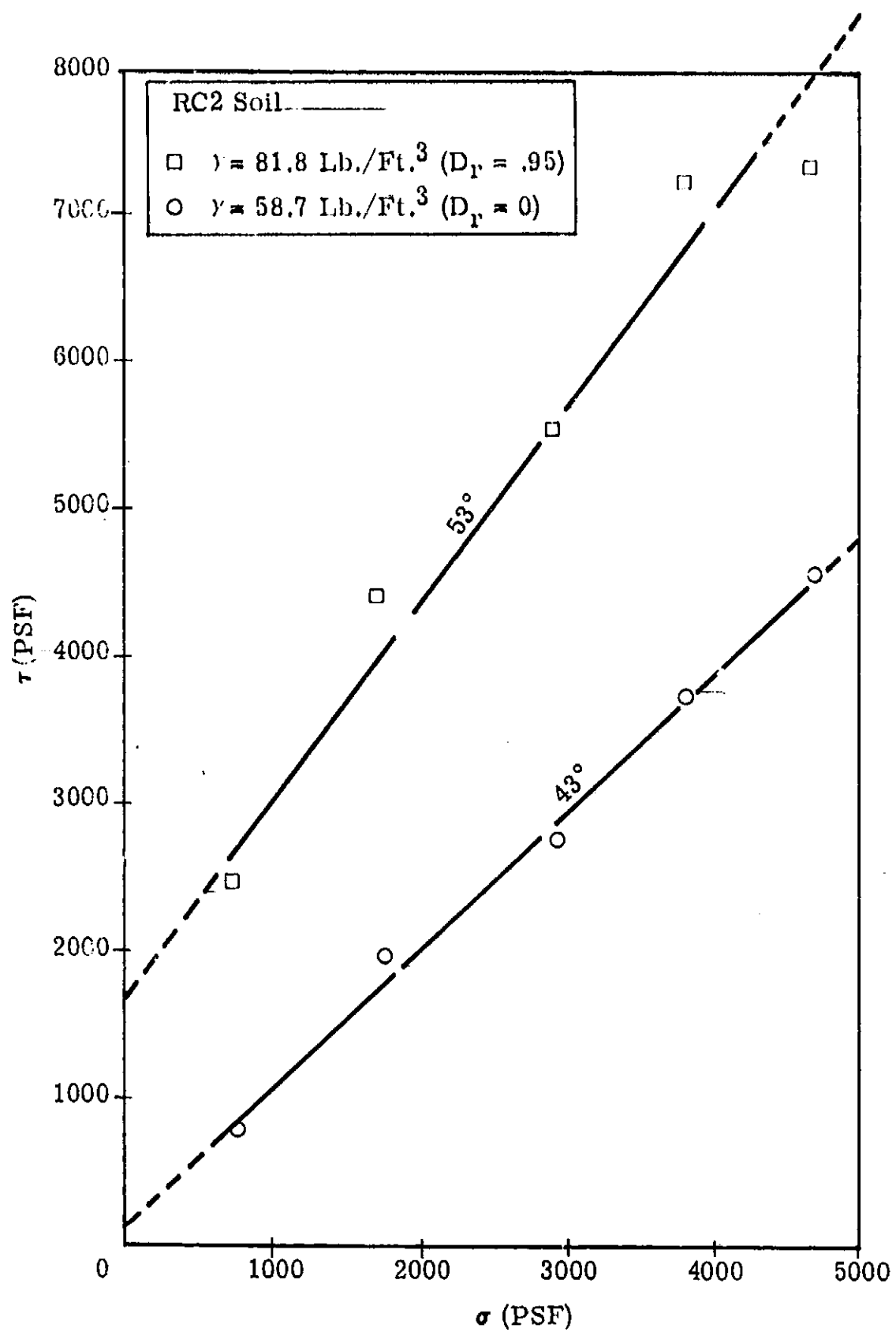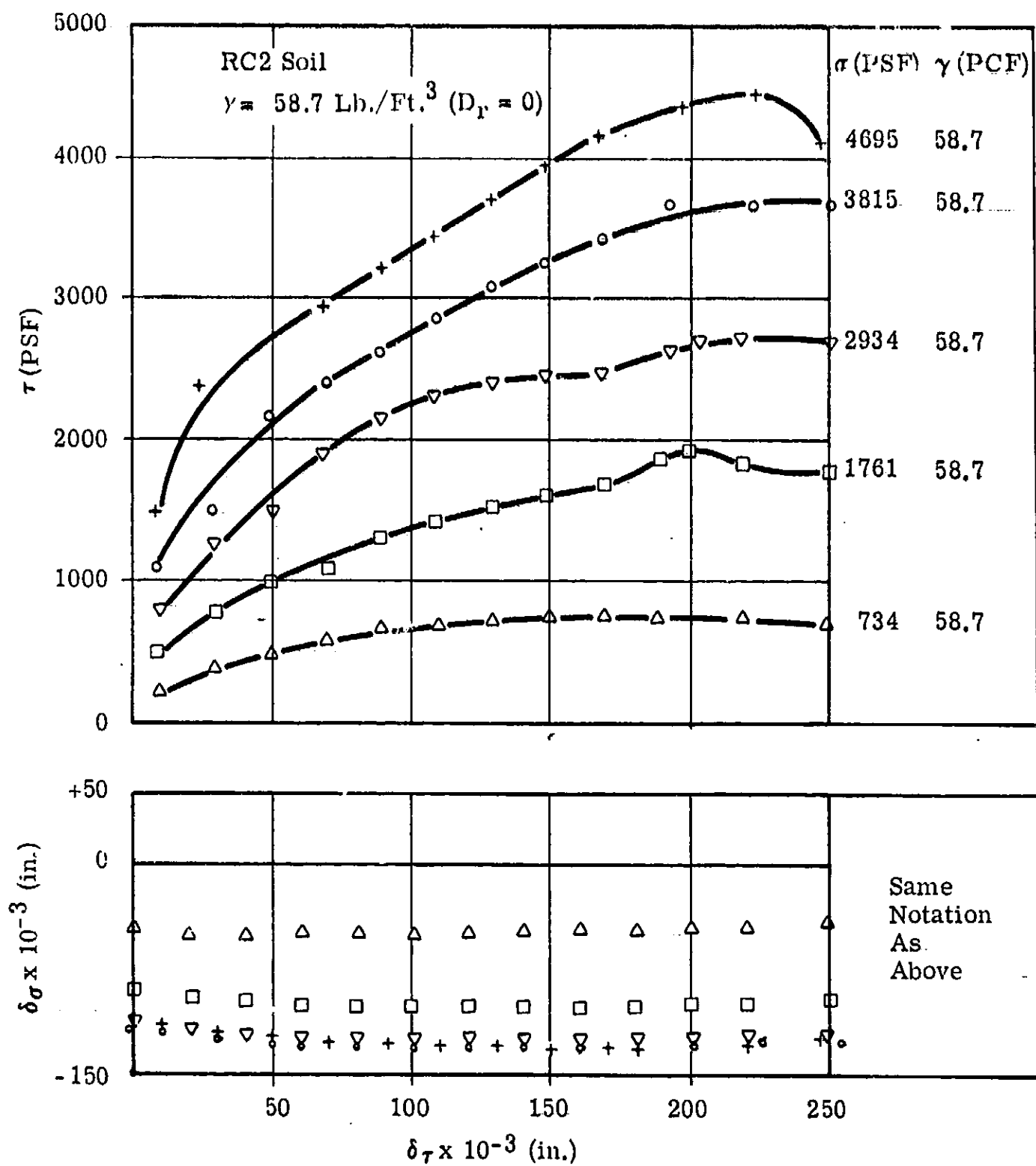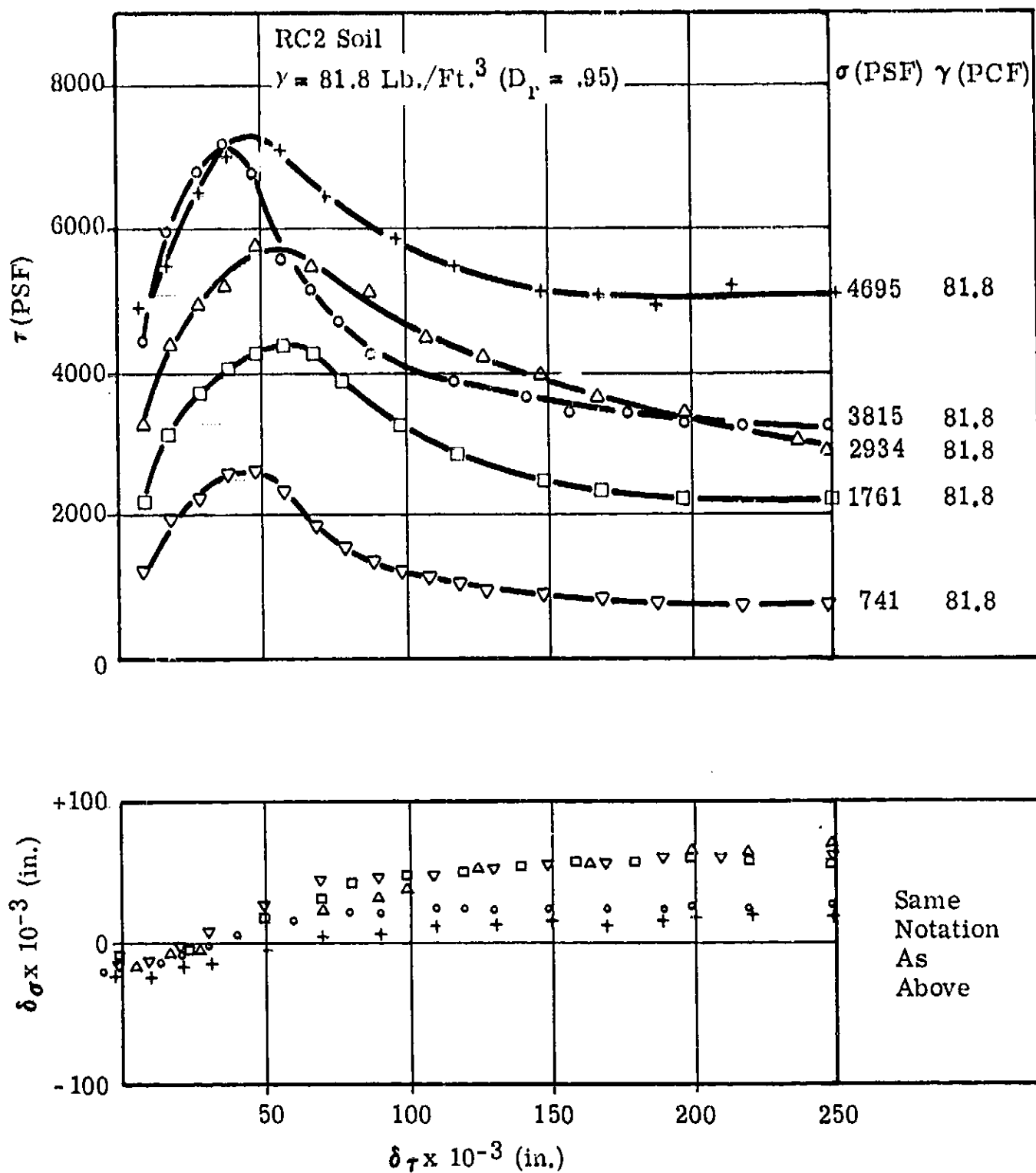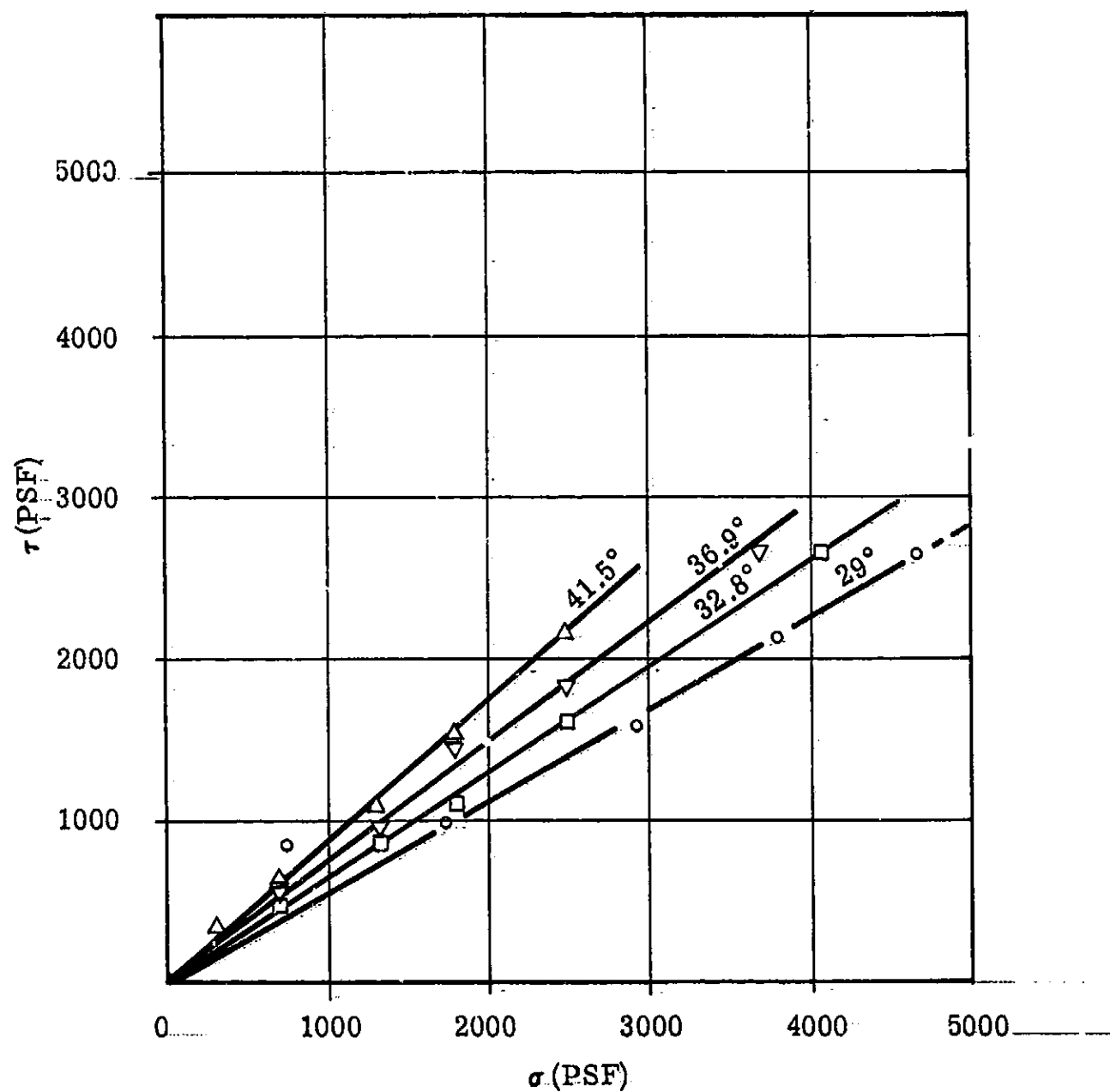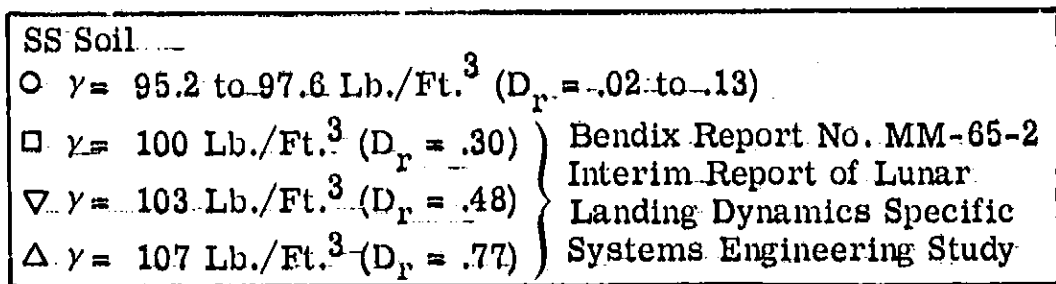Dilation Displacement vs. Shear Displacement
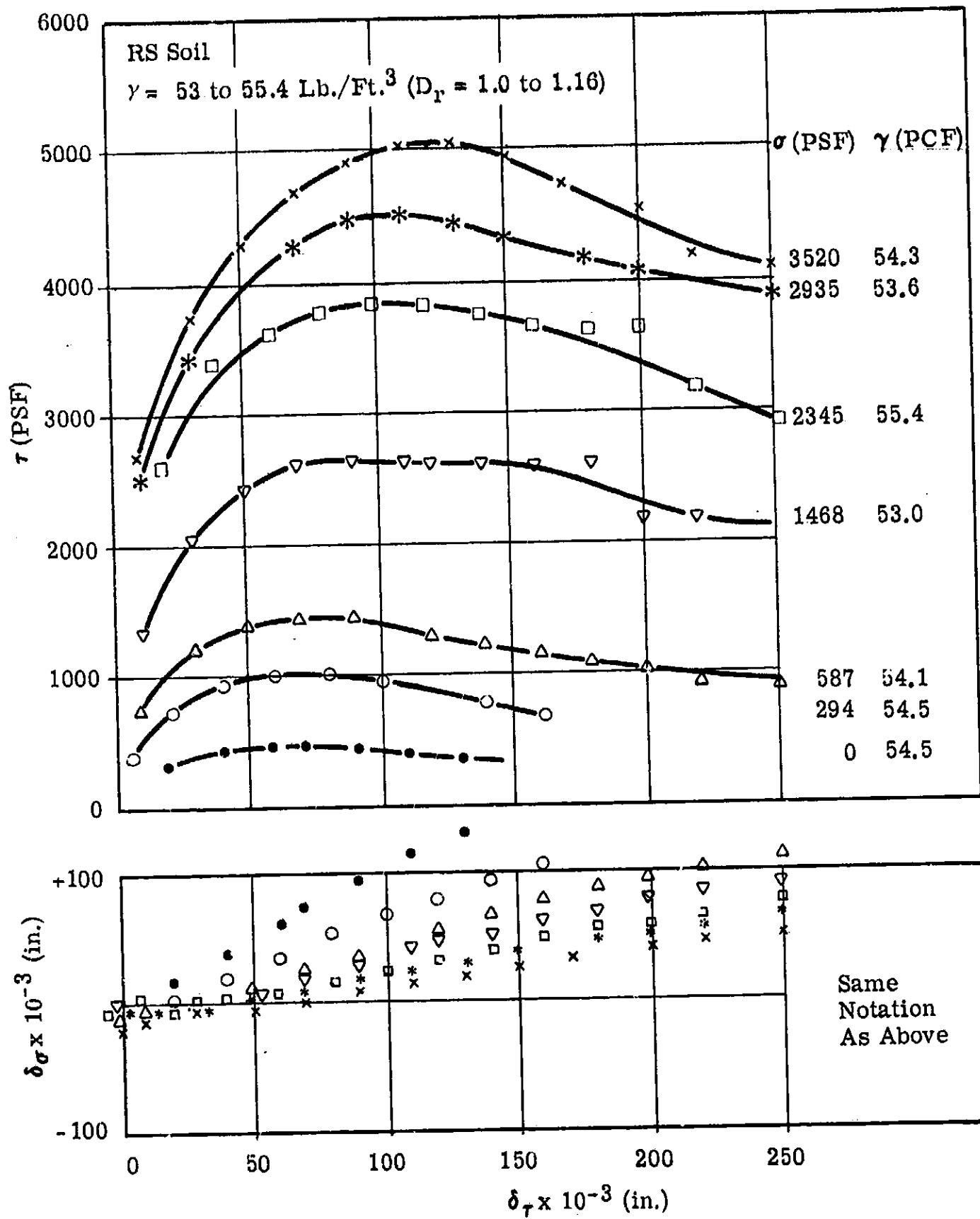
Figure C-1D. Direct Shear Test Data - Shear Stress vs. Shear Displacement
Dilation Displacement vs. Shear Displacement
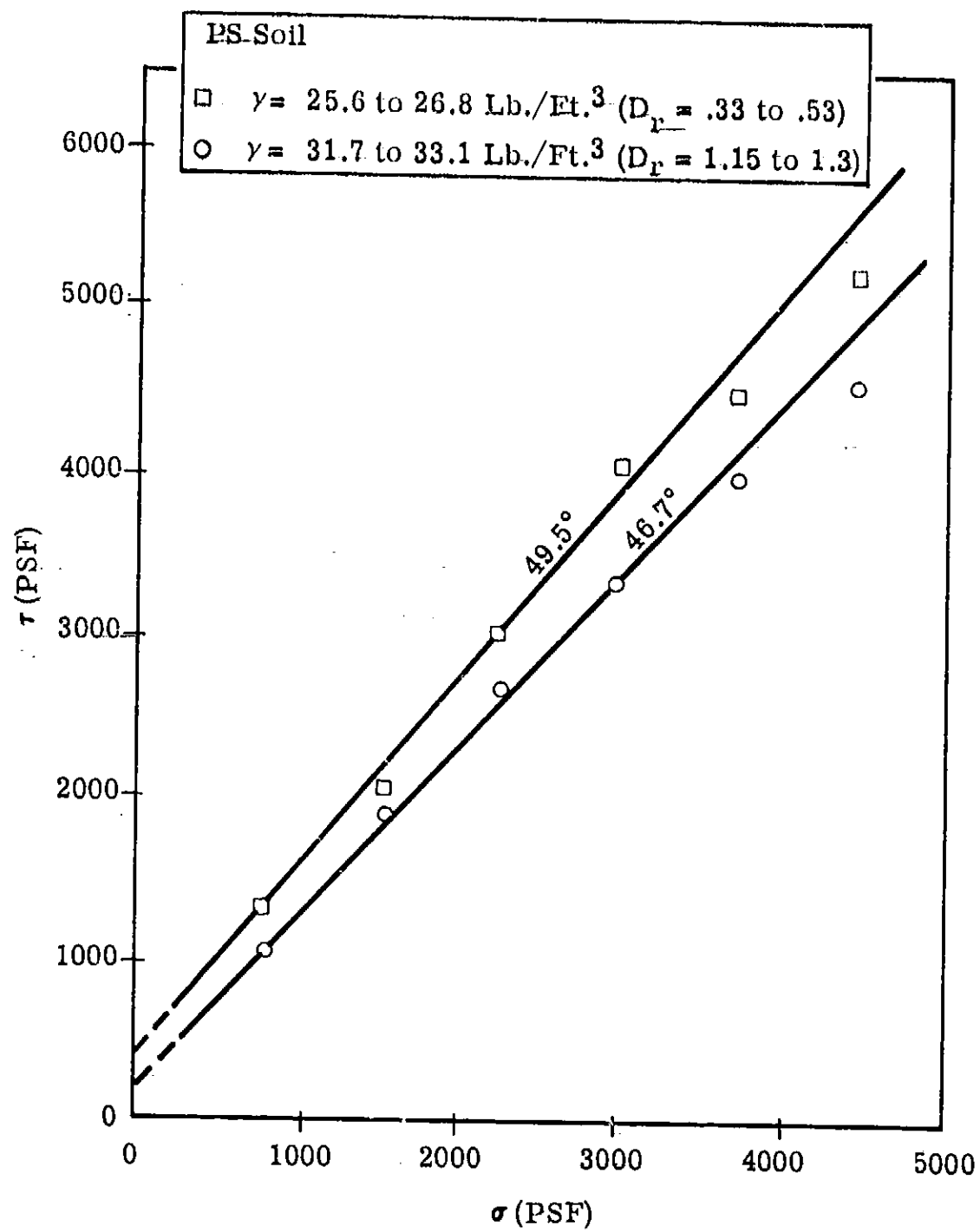
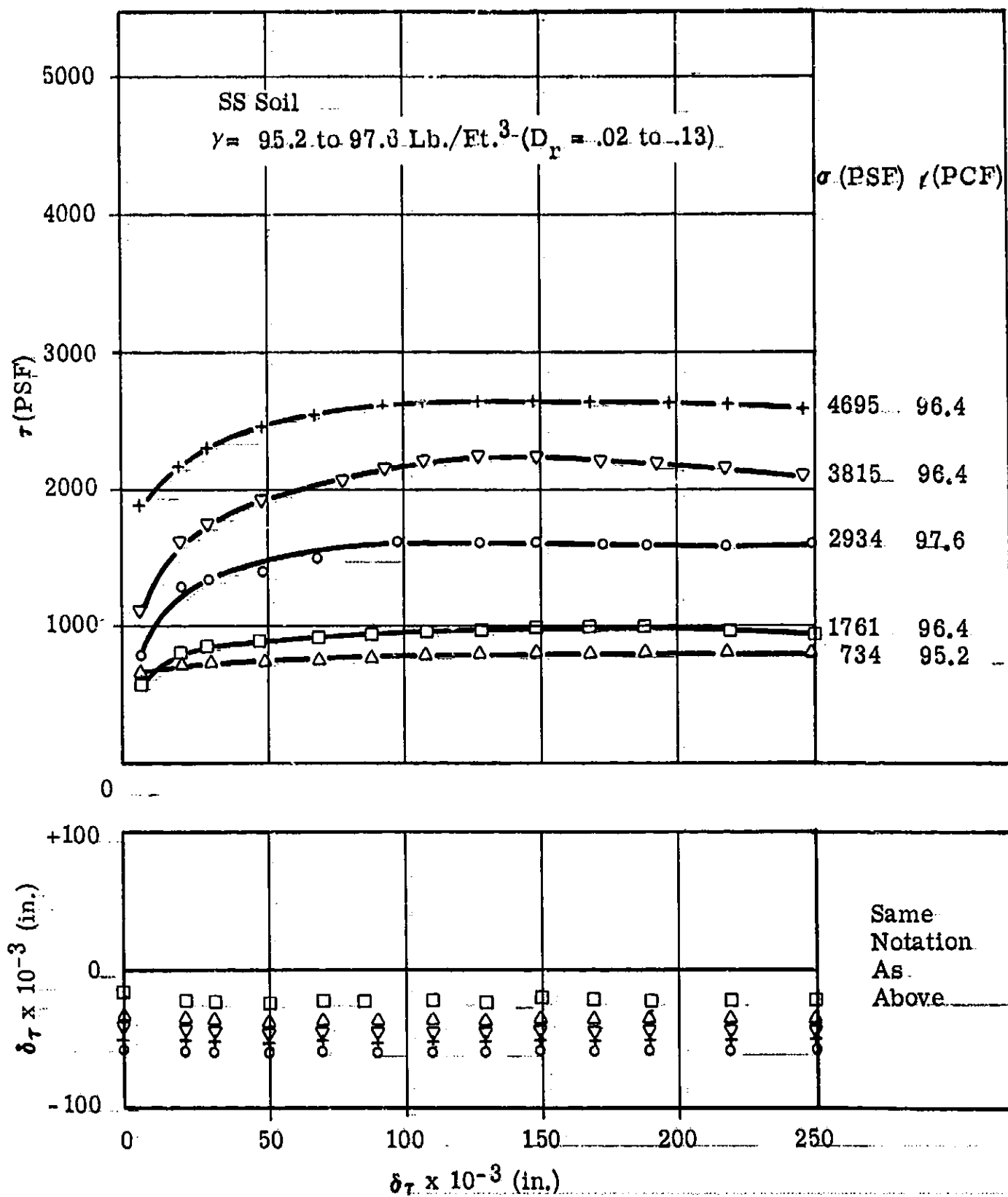Figure C-2A. Failure Envelopes - Maximum Shear Stress vs. Normal Stress

C-6
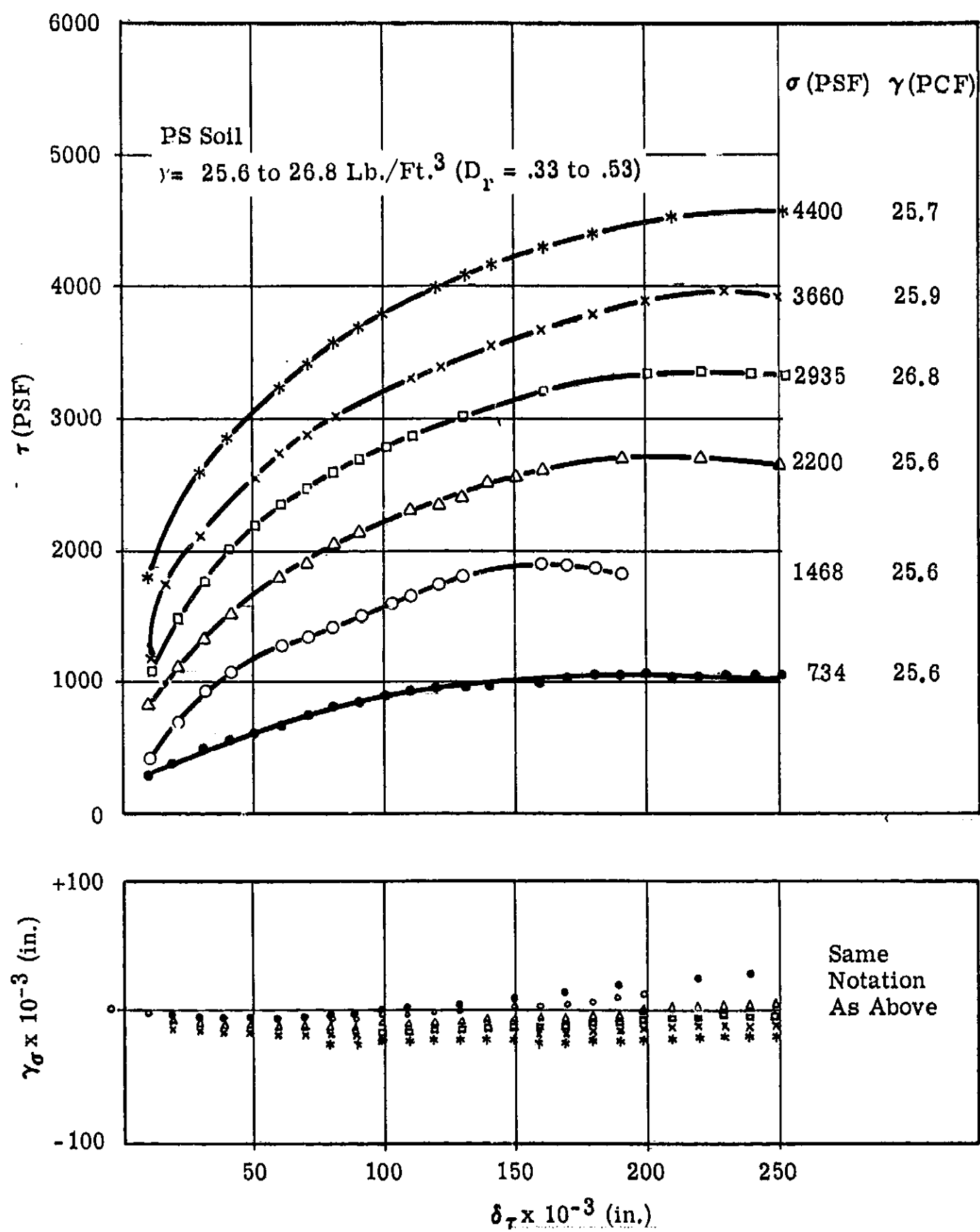
Figure C-2B. Direct Shear Test Data - Shear Stress vs. Shear Displacement
Dilation Displacement vs. Shear Displacement
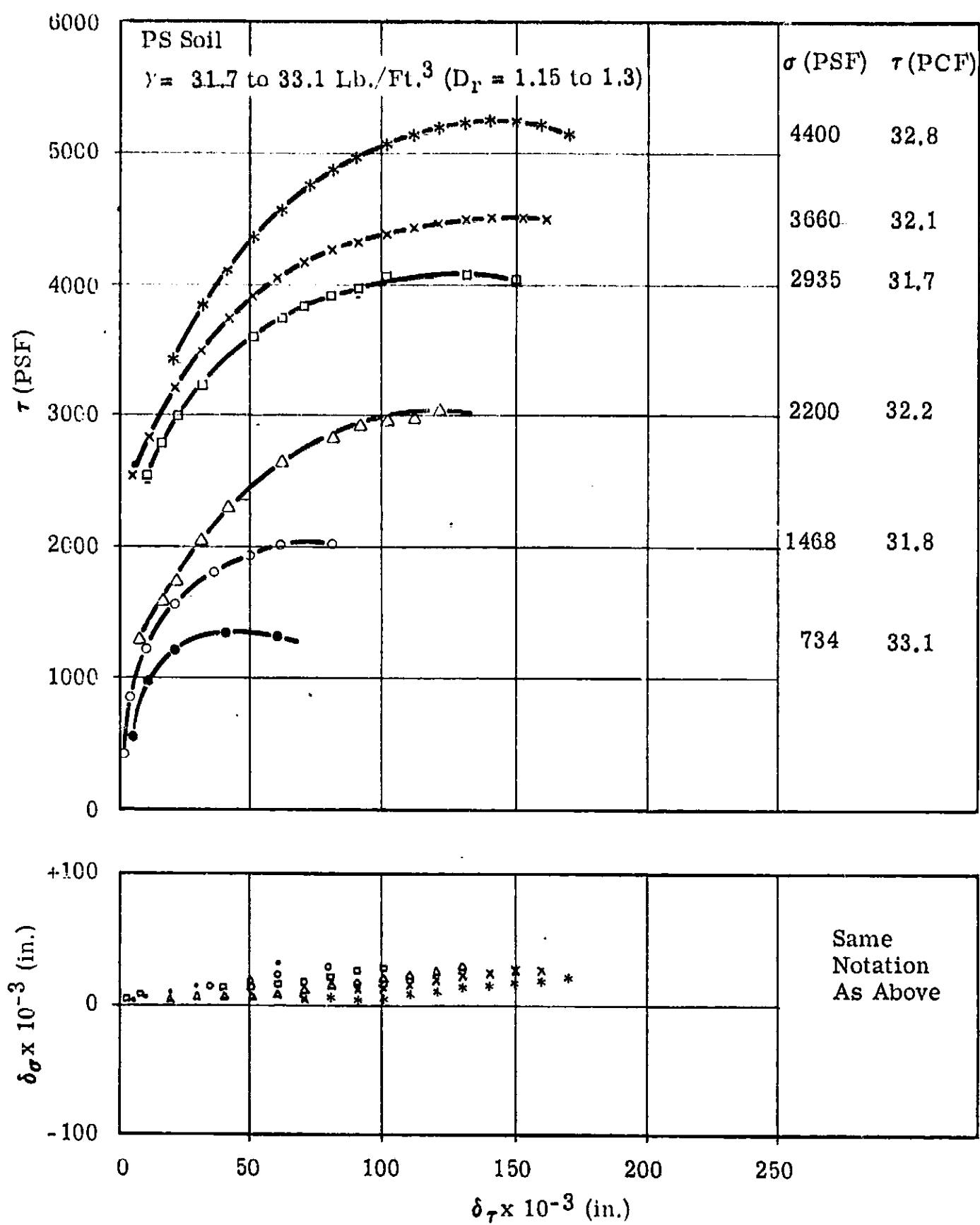
Figure C-2C. Direct Shear Test Data - Shear Stress vs. Shear Displacement
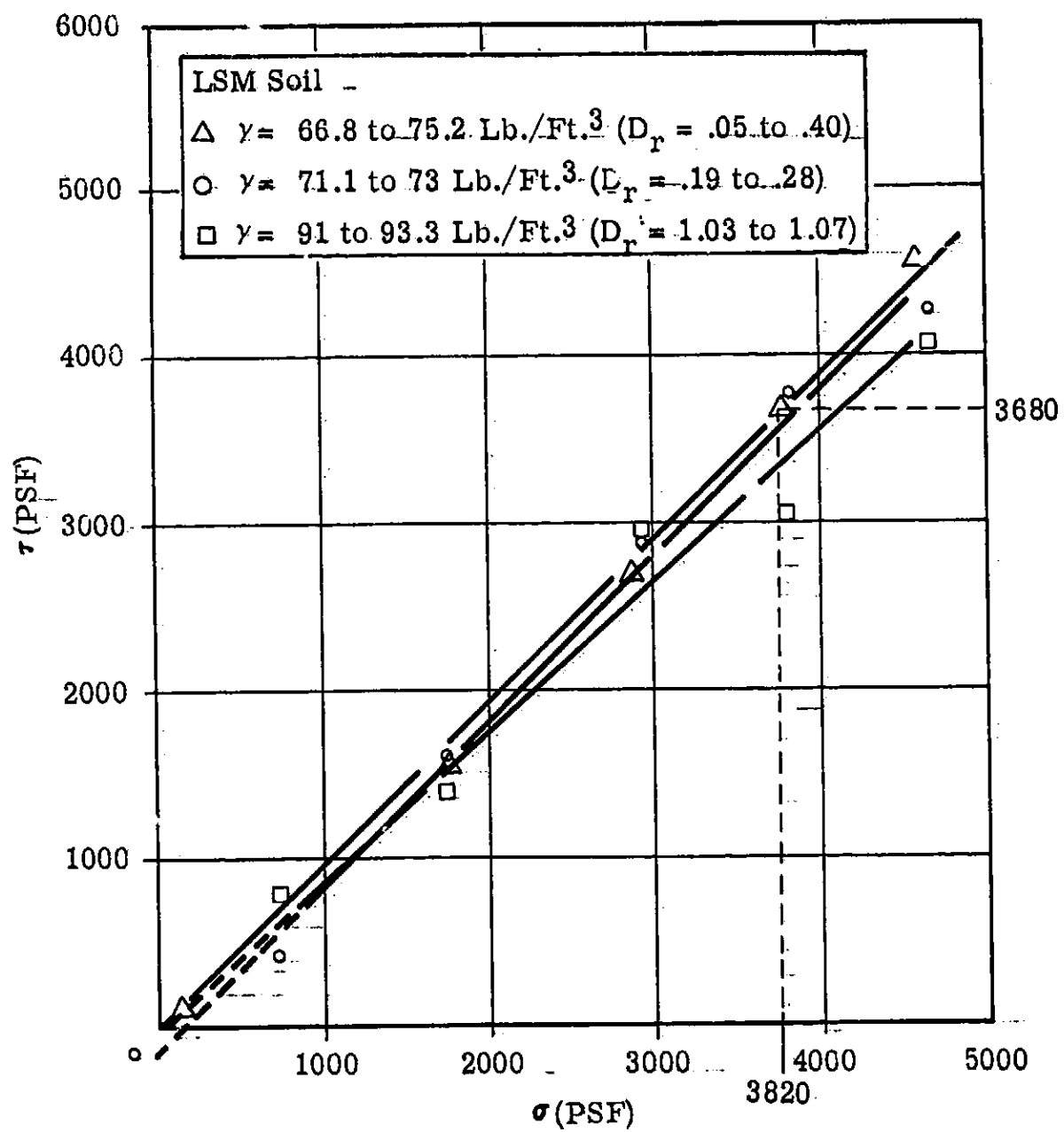Dilation Displacement vs. Shear Displacement
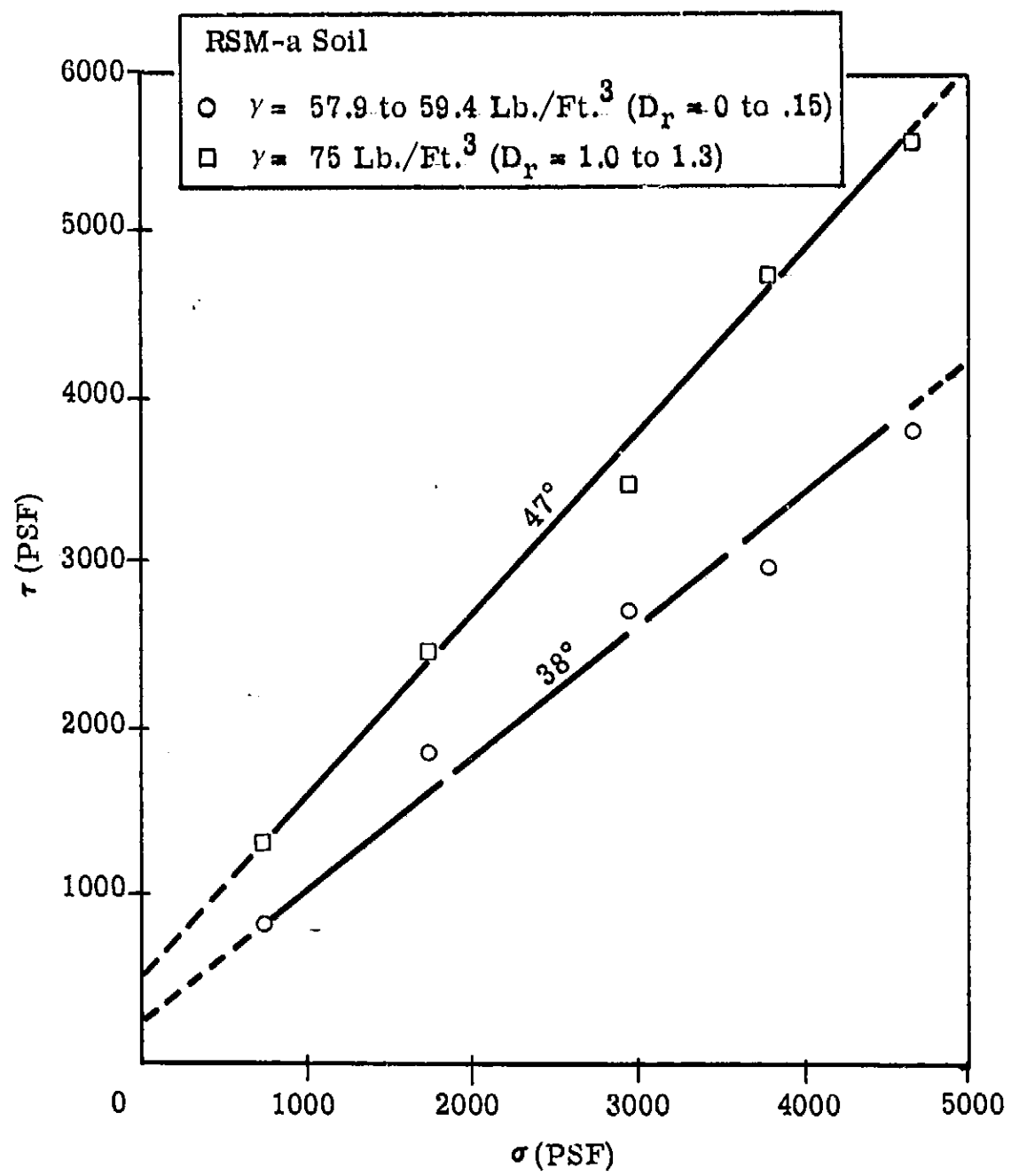
Figure C-3A. Failure Envelopes - Maximum Shear Stress vs. Normal Stress
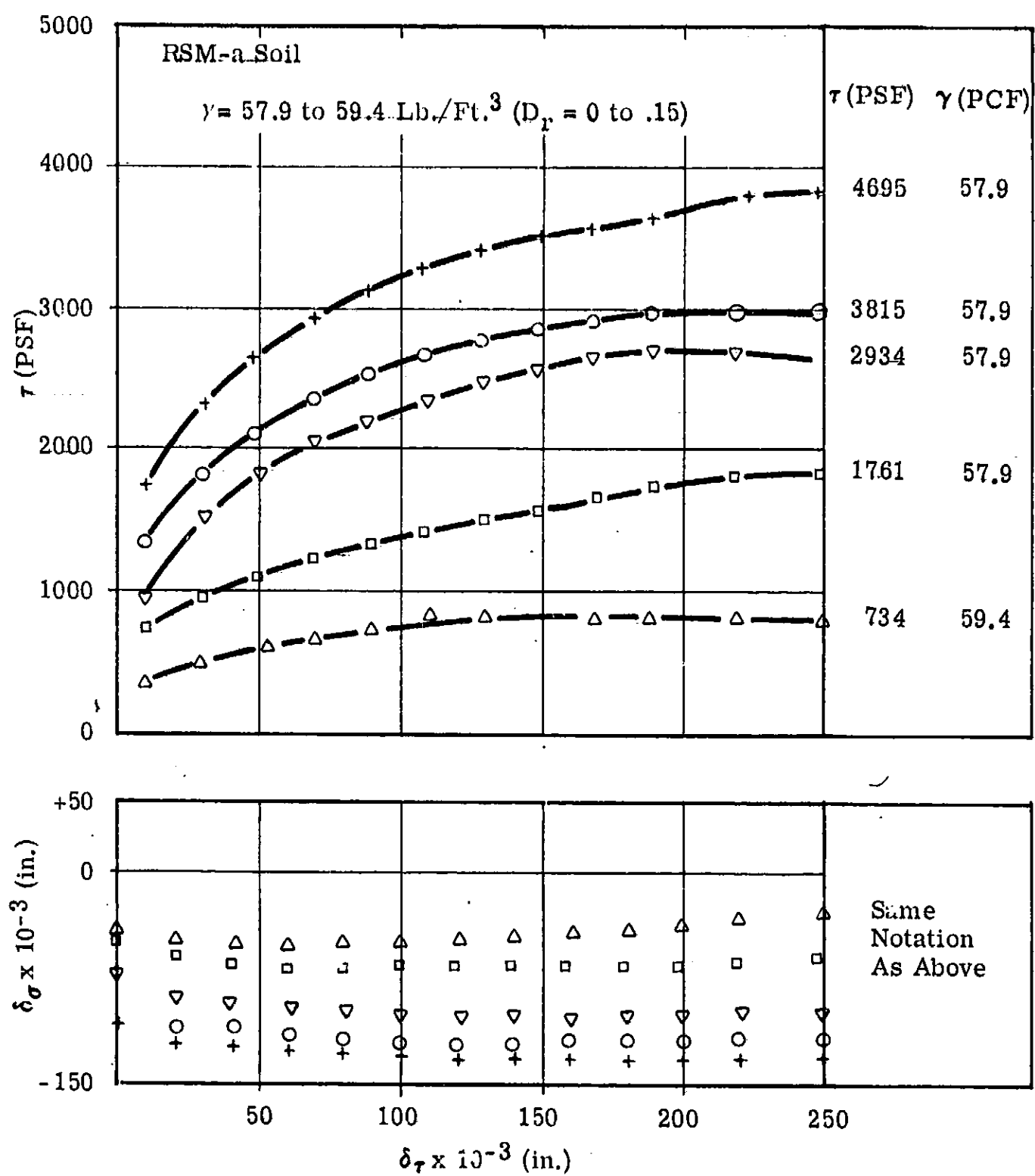
Figure C-3B. Direct Shear Test Data - Shear Stress vs. Shear Displacement
Dilation Displacement vs. Shear Displacement
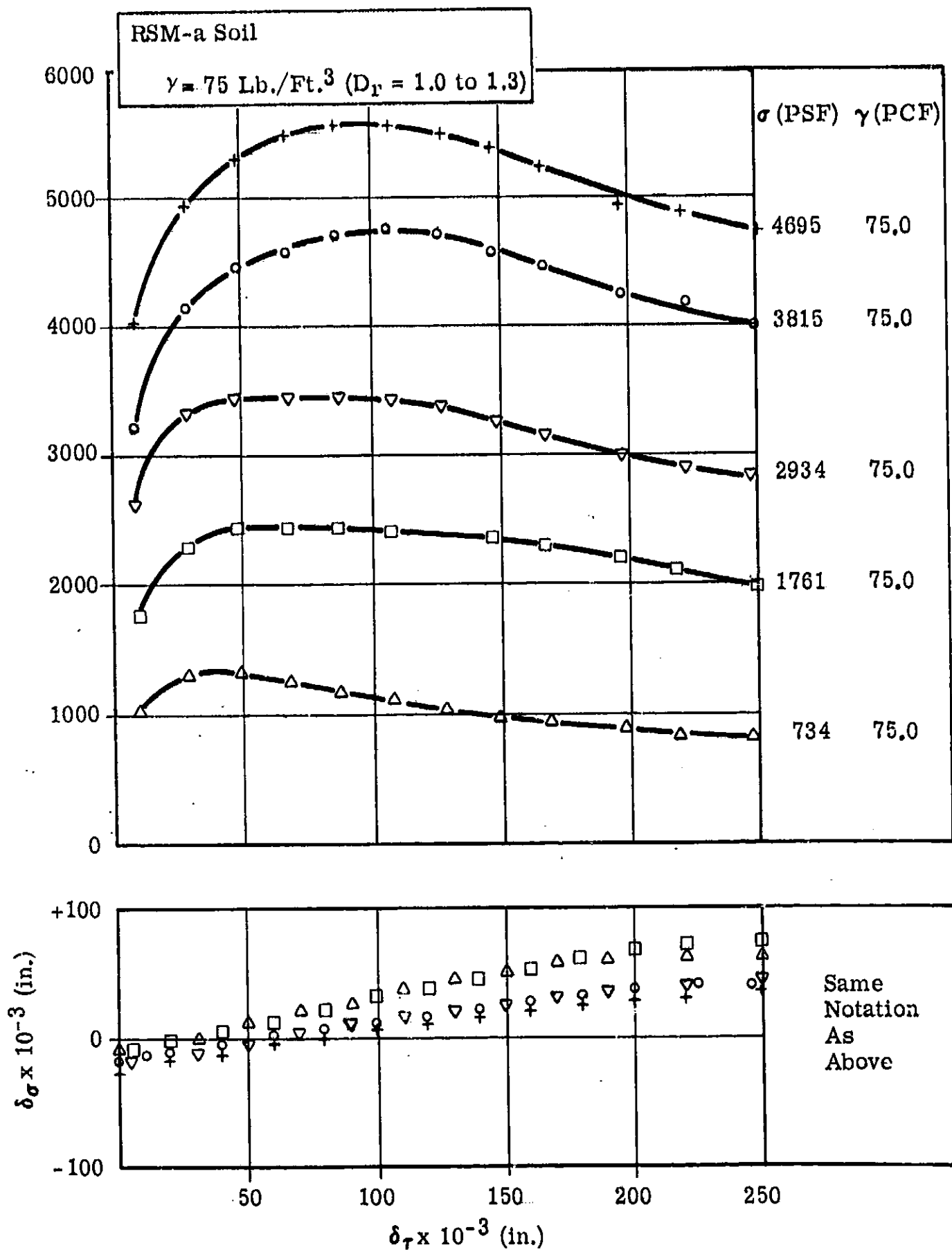
Figure C-3C. Direct Shear Test Data - Shear Stress vs. Shear Displacement
Dilation Displacement vs. Shear Displacement

Figure C-4A. Failure Envelopes - Maximum Shear Stress vs. Normal Stress
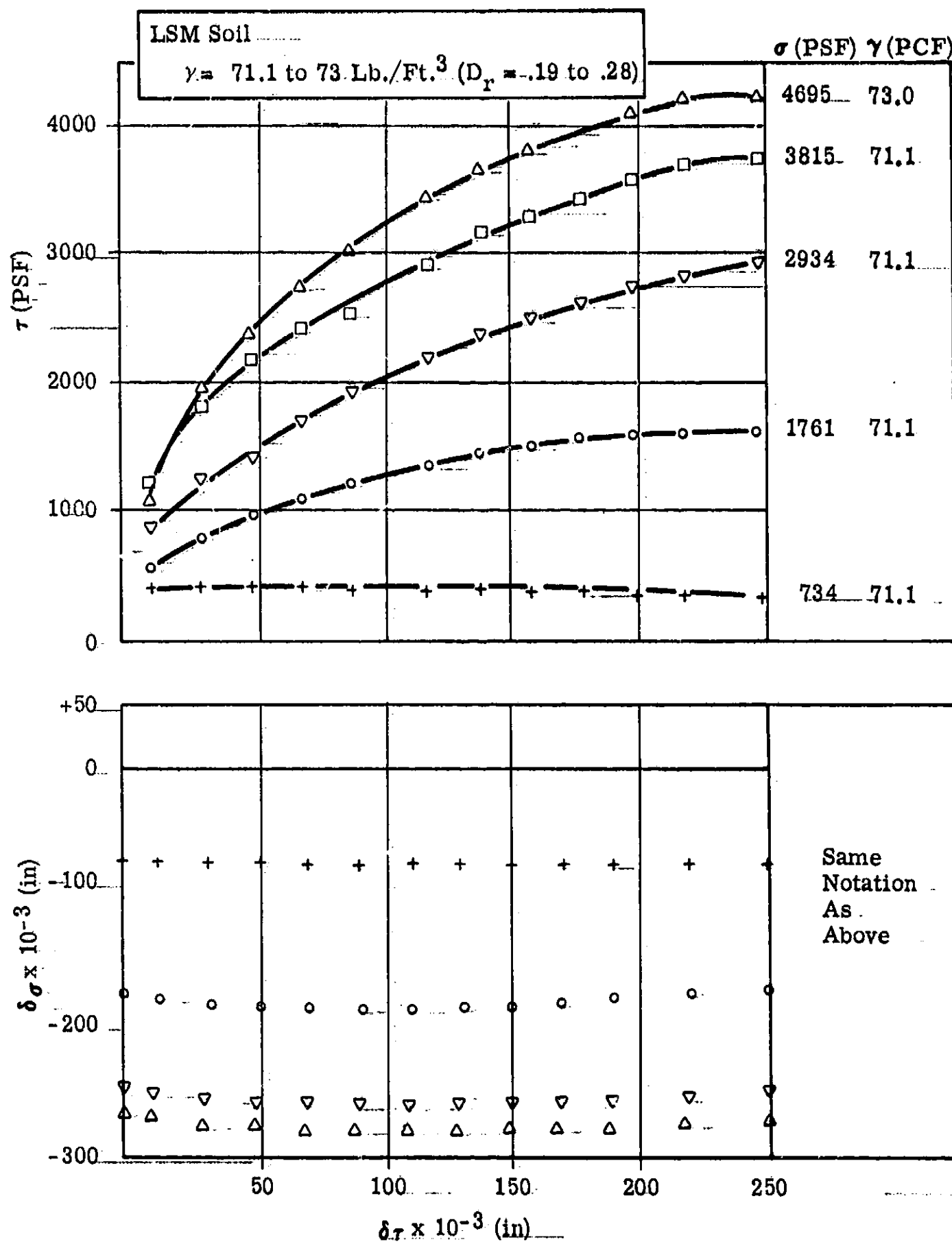
Figure C-4B. Direct Shear Test Data - Shear Stress vs. Shear Displacement
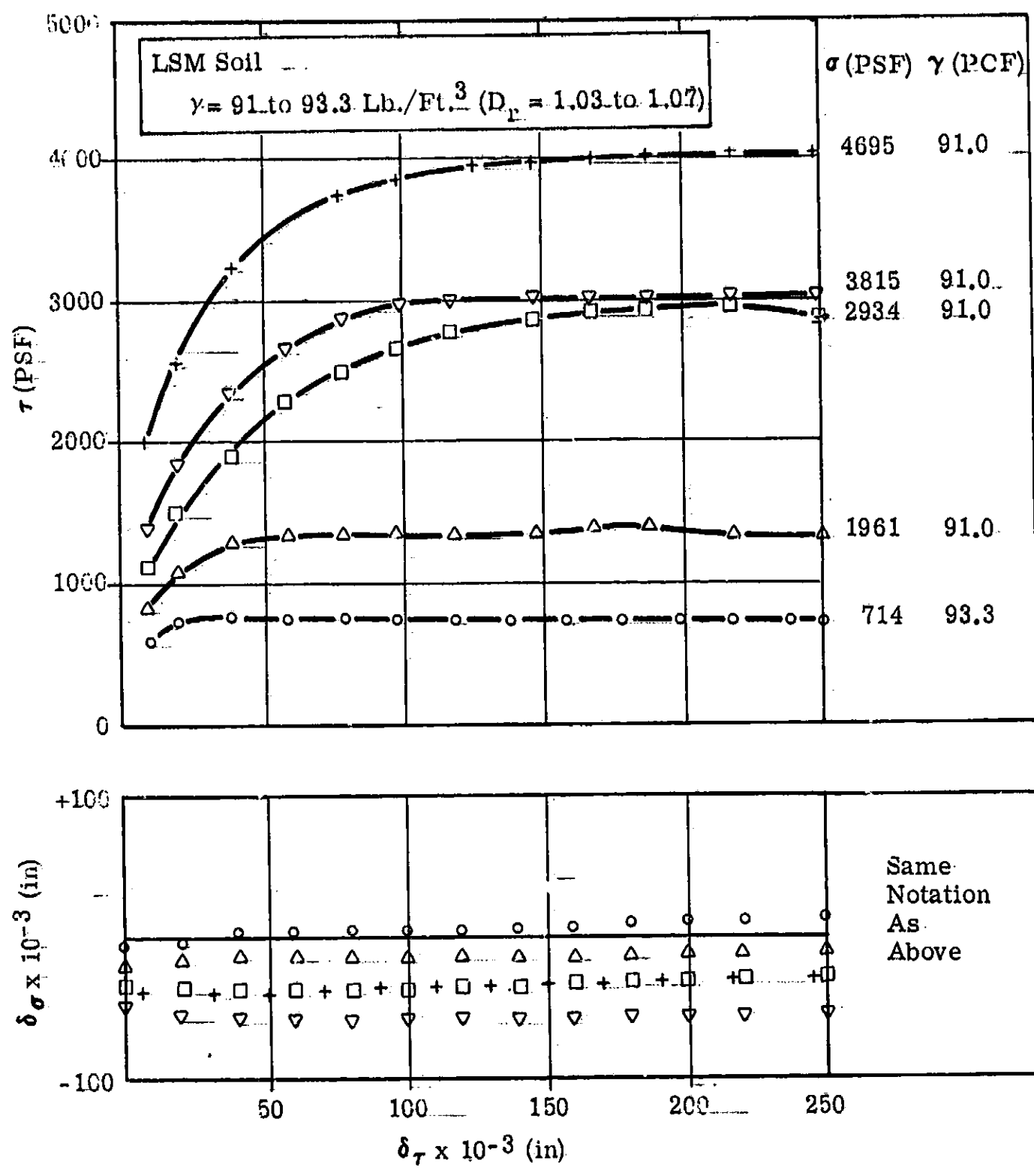Dilation Displacement vs. Shear Displacement

Figure C-4C. Direct Shear Test Data - Shear Stress vs. Shear Displacement
Dilation Displacement vs. Shear Displacement

Figure C-5A. Failure Envelopes —Maximum Shear Stress vs. Normal Stress
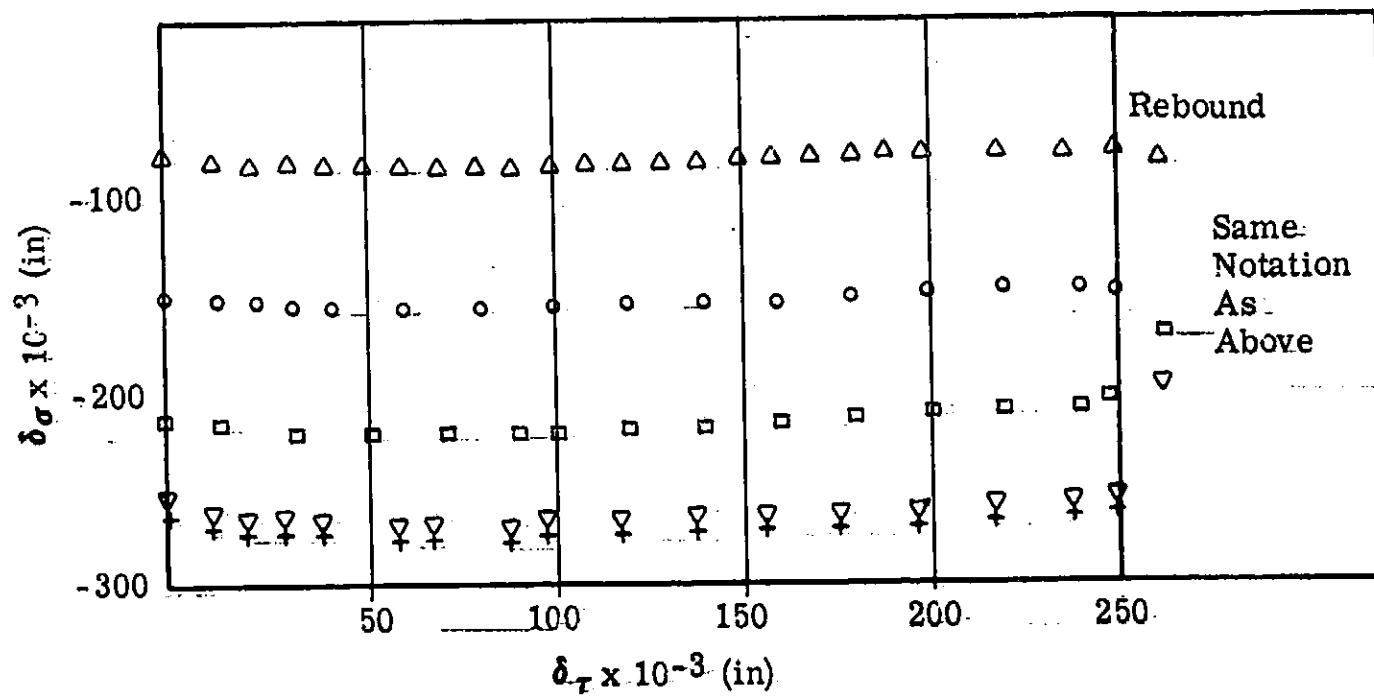
Figure C-5B. Direct Shear Test Data – Shear Stress vs. Shear Displacement Dilation Displacement vs. Shear Displacement

Figure C-6A. Failure Envelopes – Maximum Shear Stress
vs. Normal Stress

C-17

Figure C-6B. Direct Shear Test Data - Shear Stress vs. Shear Displacement
Dilation Displacement vs. Shear Displacement

Figure C-6C. LSM Soil Dense - Shear Stress vs. Shear Displacement
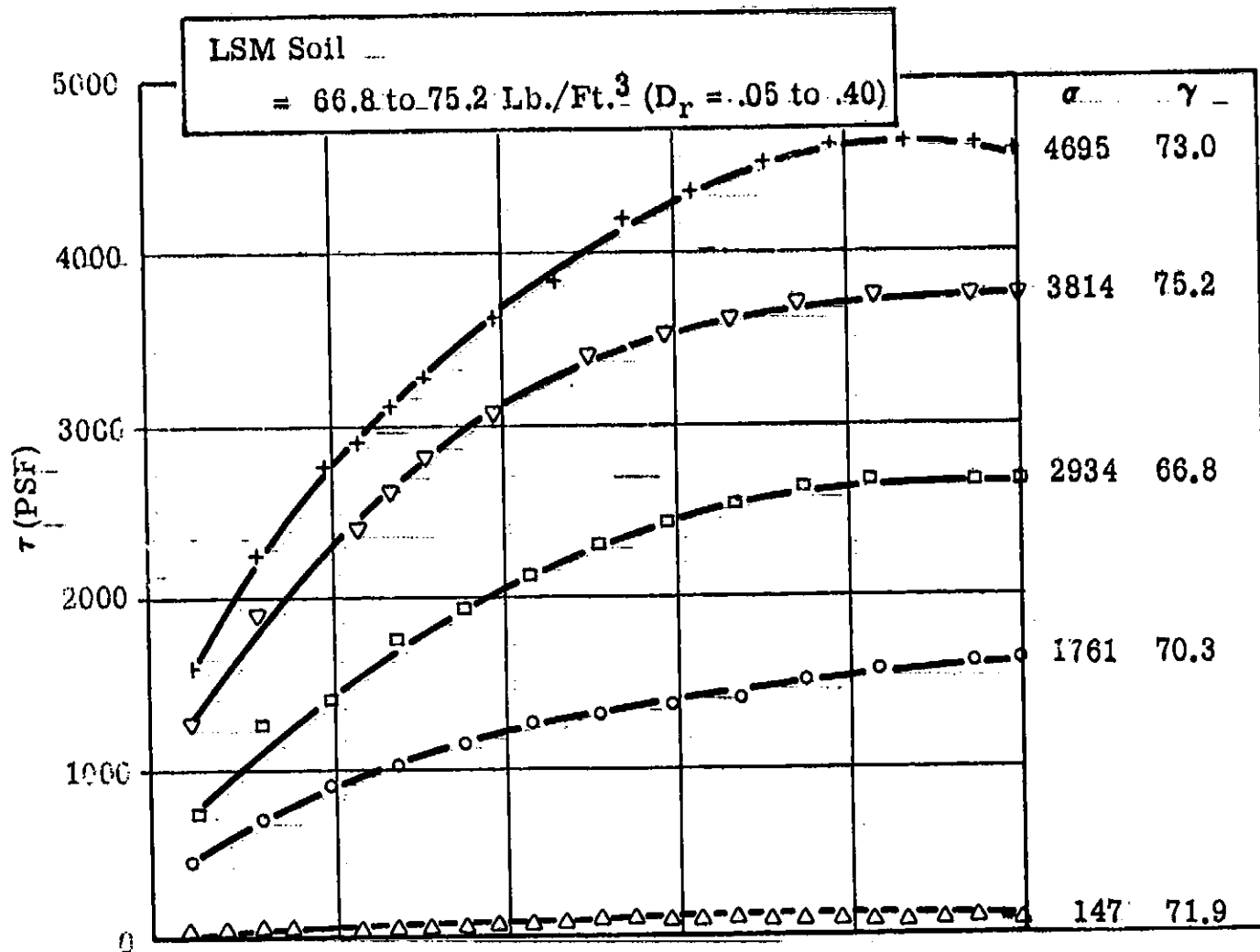Dilation Displacement vs. Shear Displacement

Figure C-6D. Direct Shear Test Data - Shear Stress vs. Shear Displacement
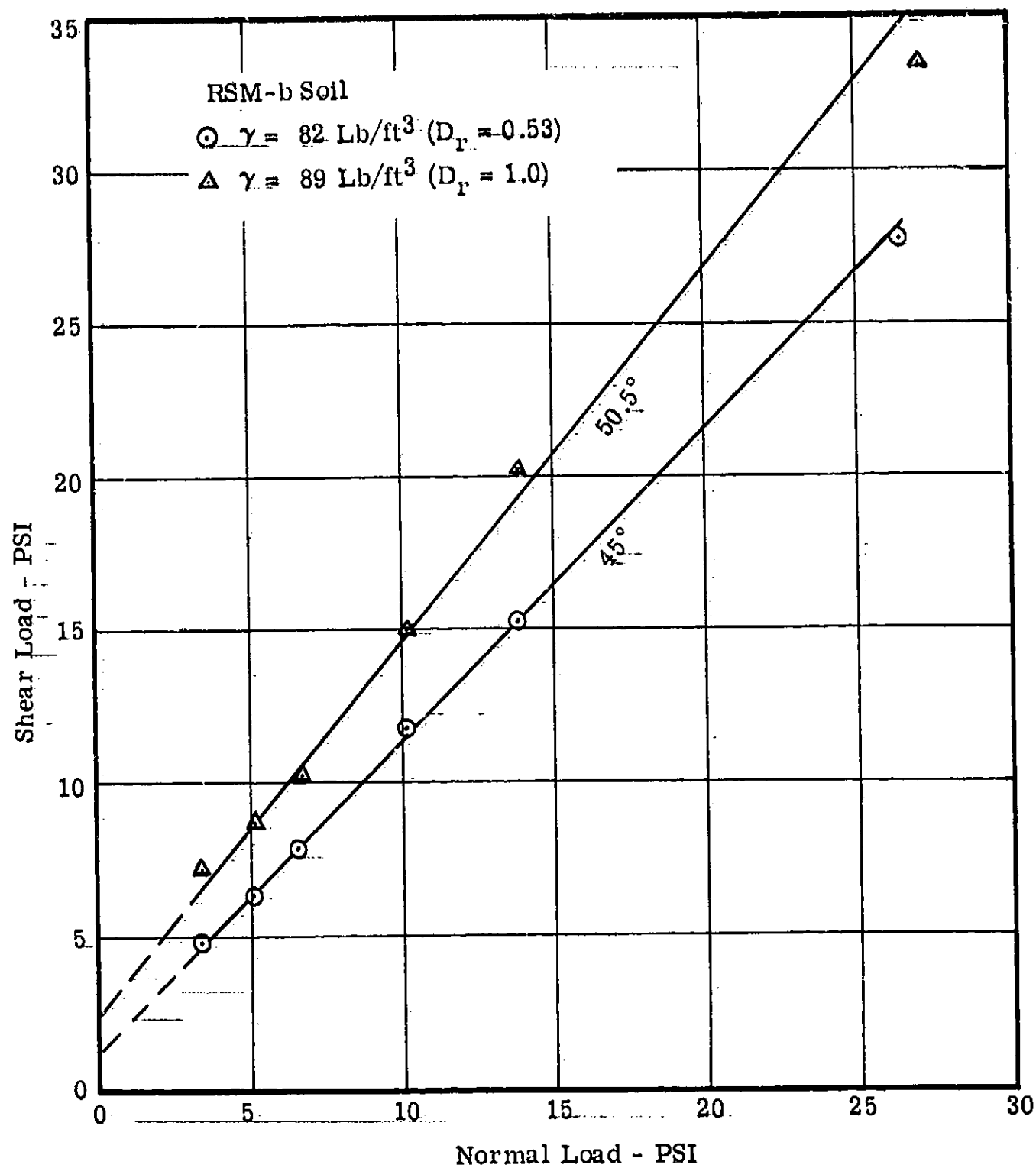Dilation Displacement vs. Shear Displacement

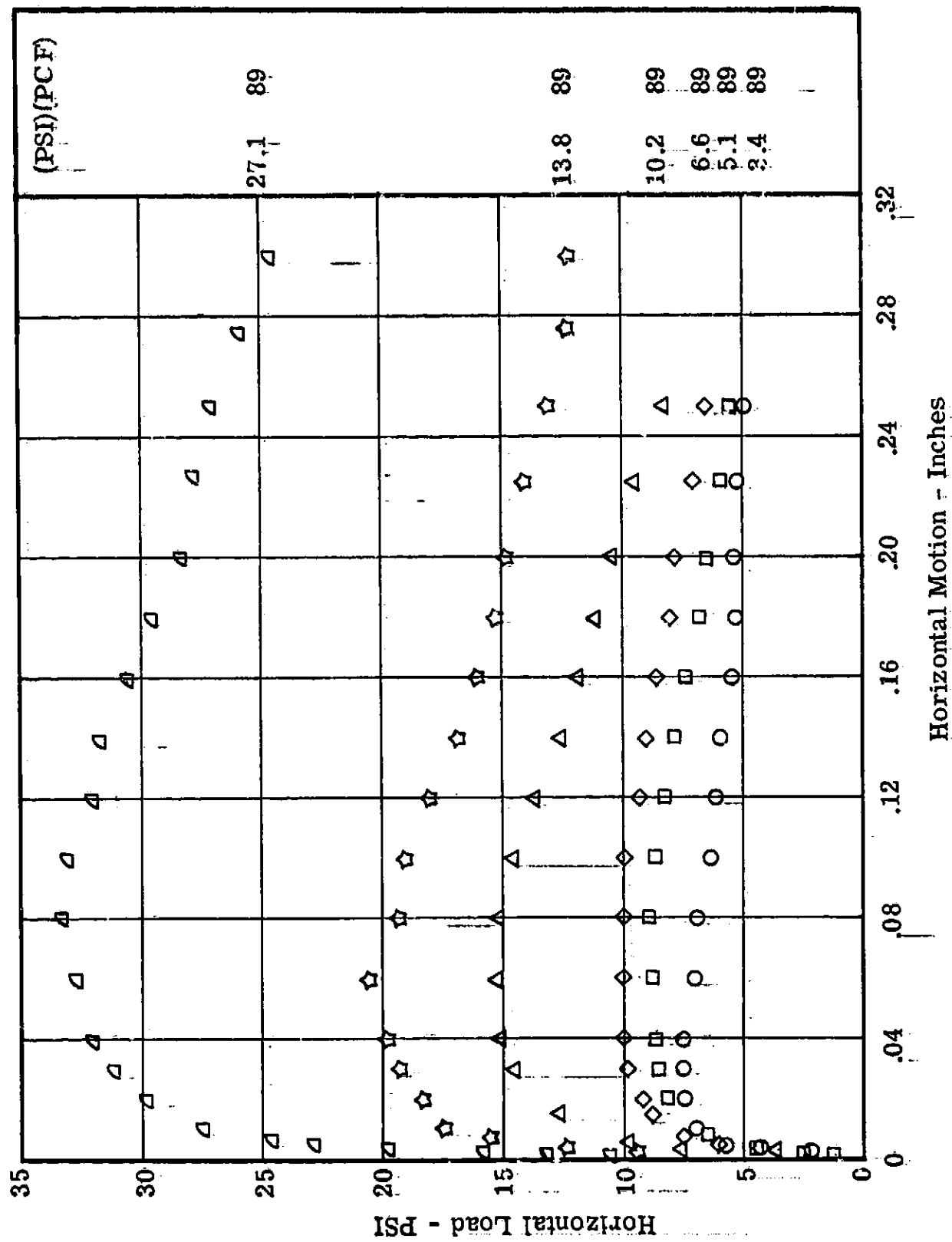Figure C-7A. Failure Envelopes --Maximum Shear Stress vs.
Normal Shear Stress

Figure C-7B. Direct Shear Test Data – Shear Stress vs. Shear Displacement

C-22

(PSI)	(PCF)
26.5	82
13.8	82
10.2	82
6.6	82
5.1	82
3.4	82

Horizontal Motion – Inches
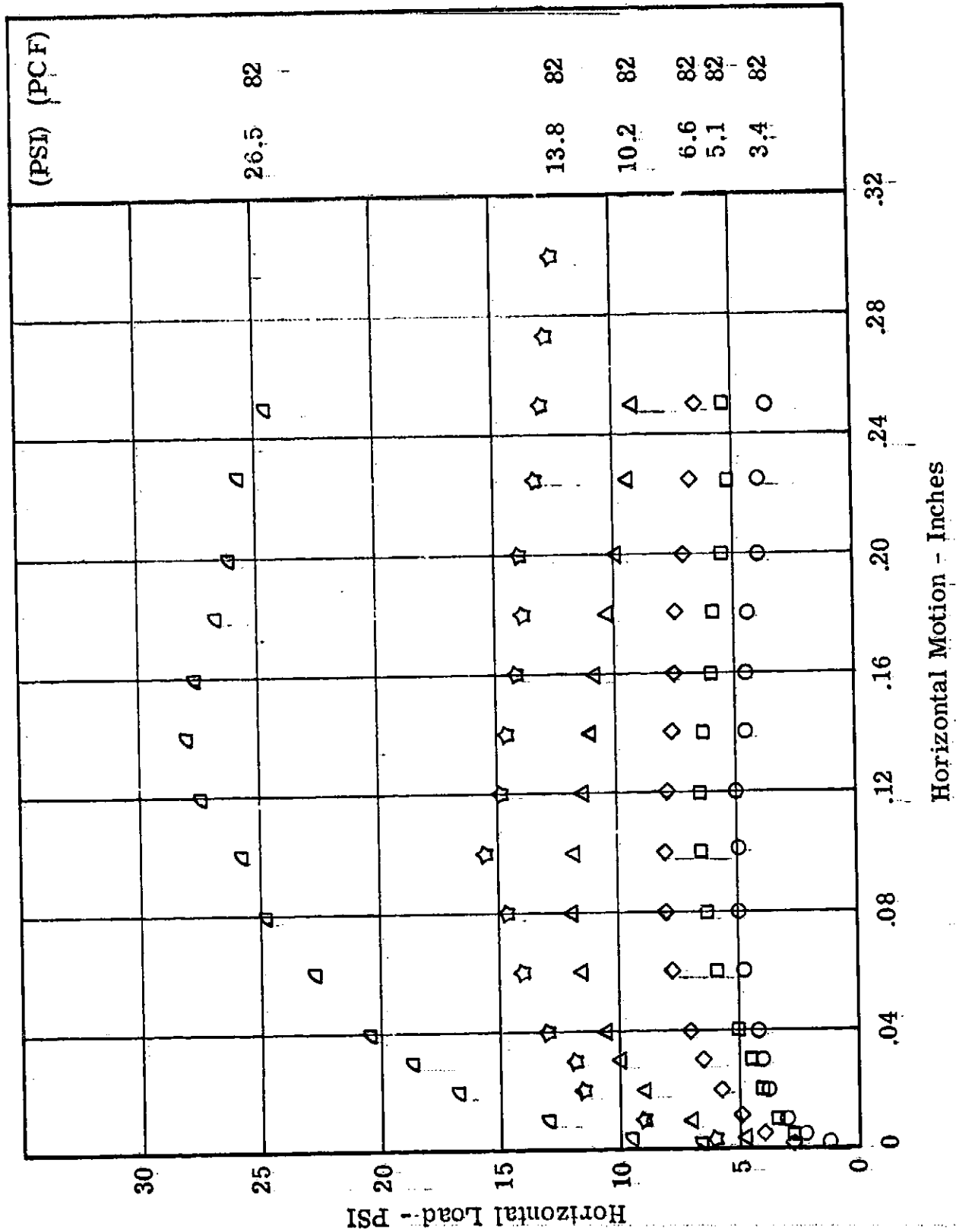
Horizontal Load – PSI
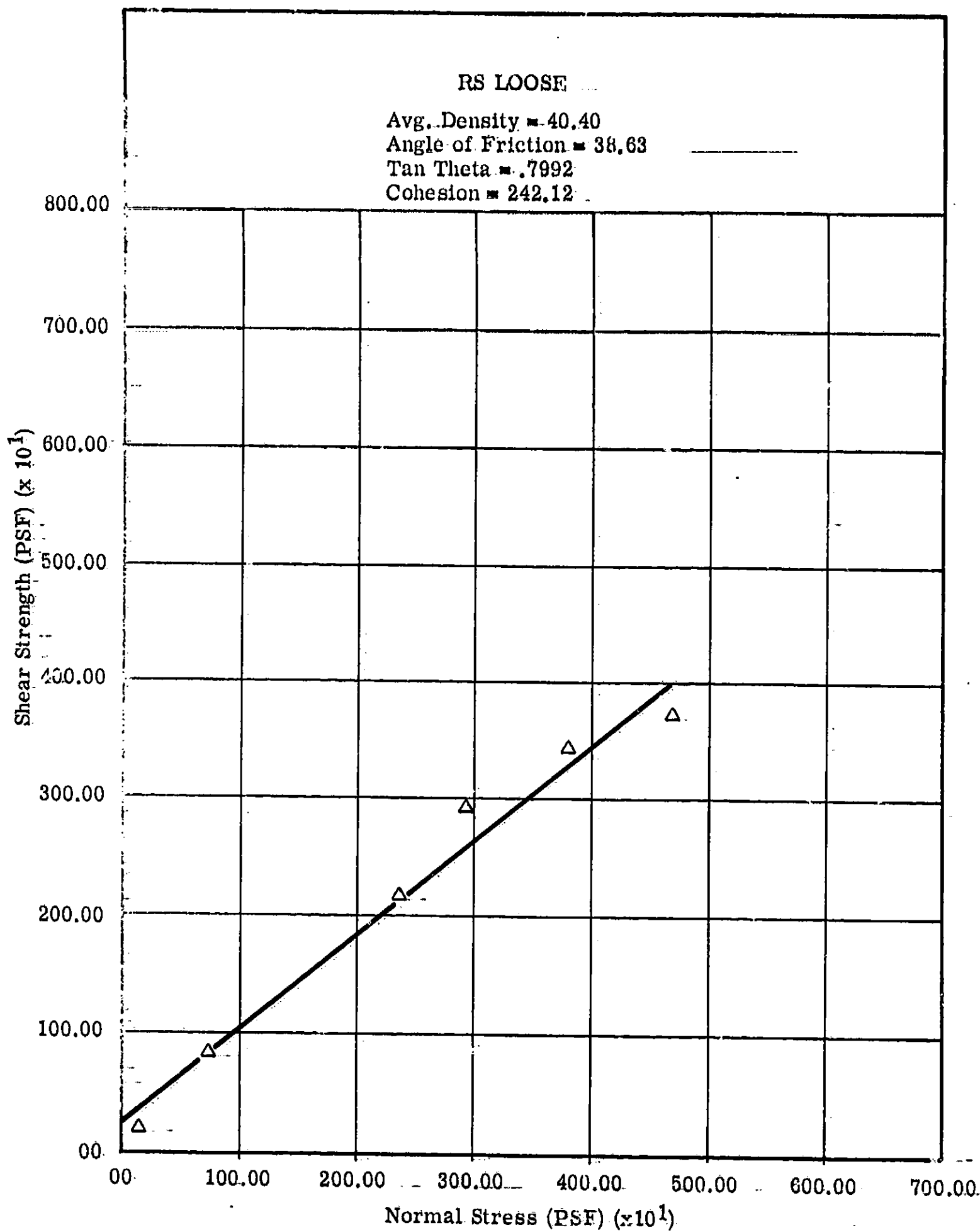
Figure C-7C. Direct Shear Test Data – Shear Stress vs. Shear Displacement

Figure C-8. RS Loose

Figure C-9A. RS Dense

RS DENSE
Avg. Density = 54.40
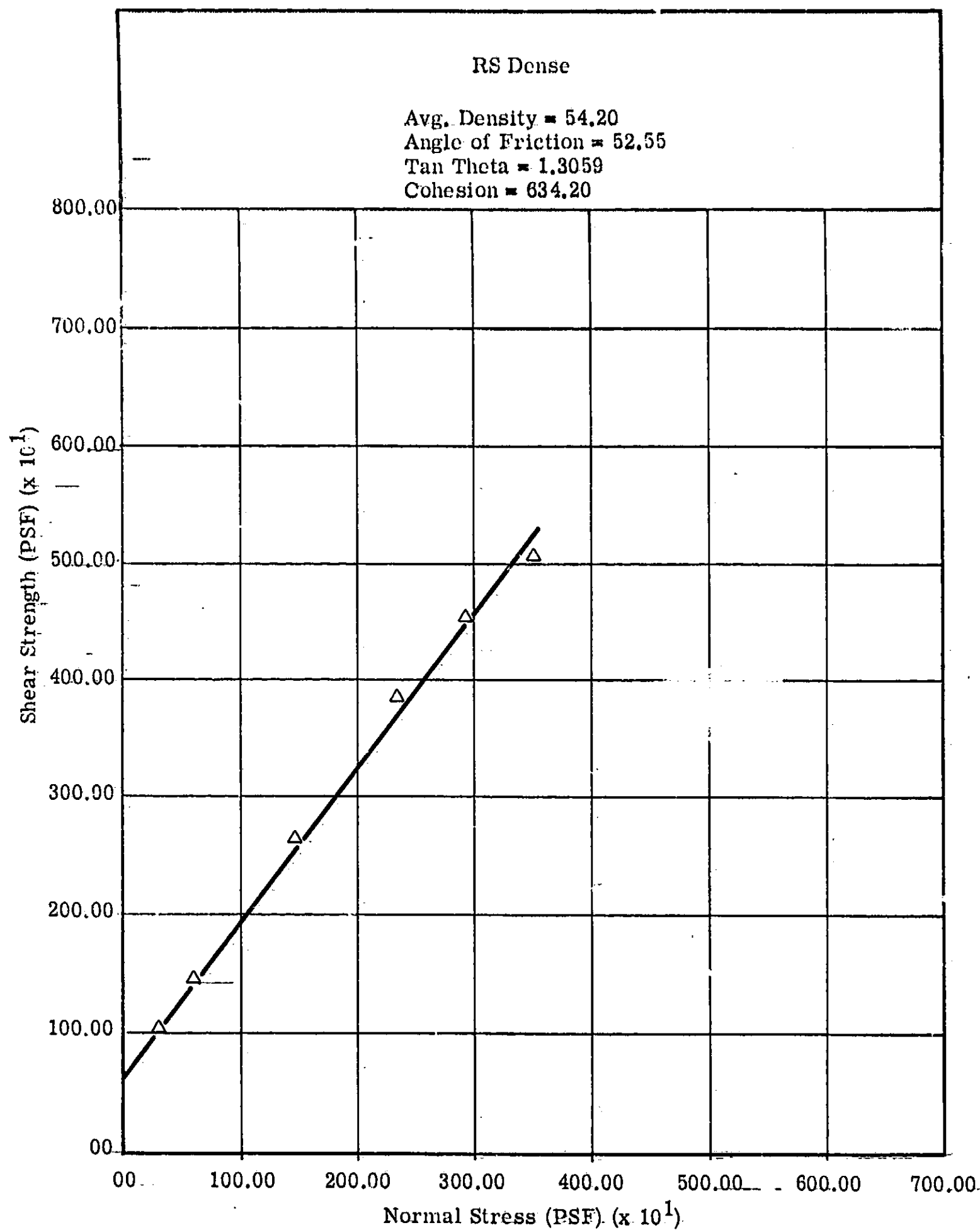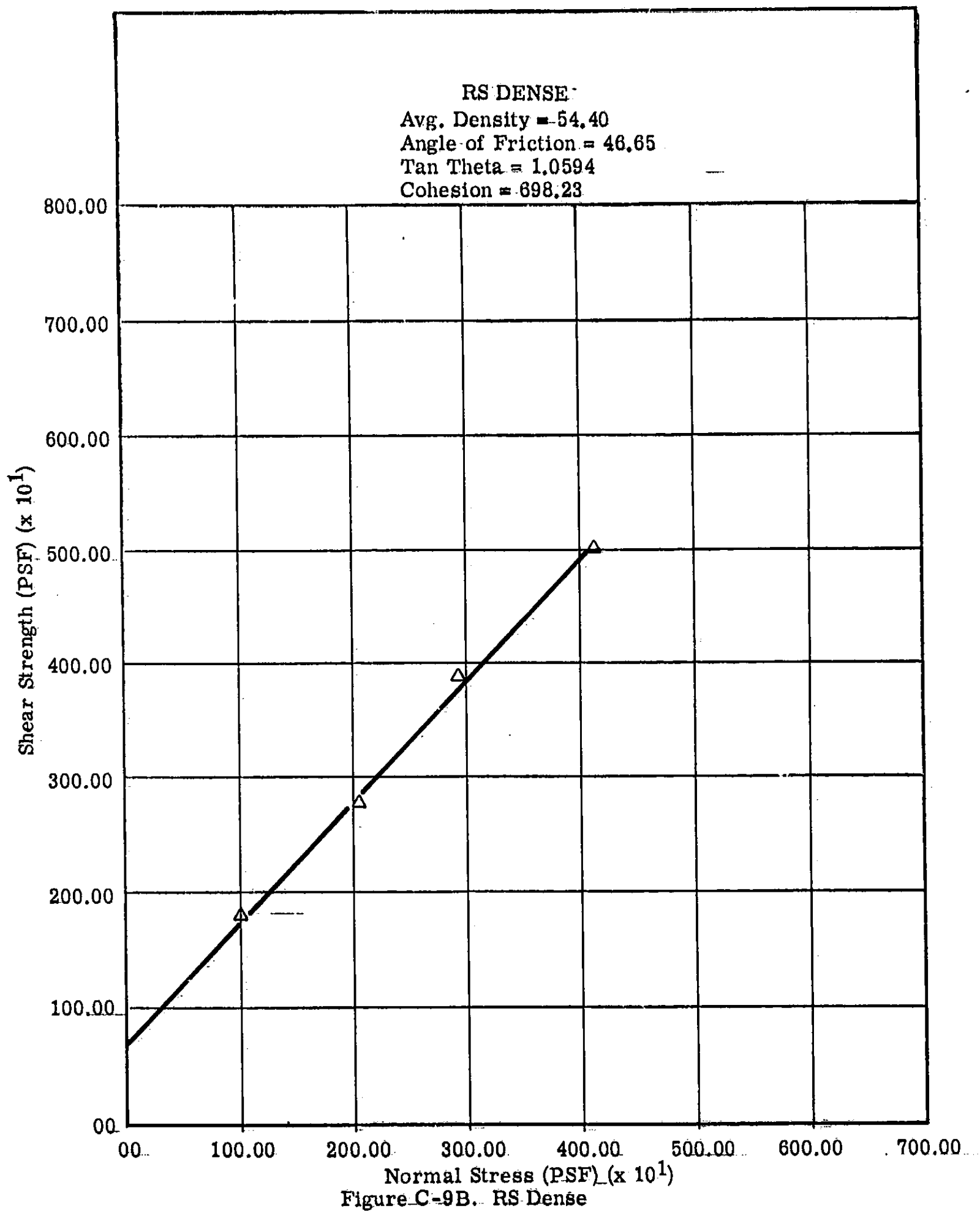Angle of Friction = 46.65
Tan Theta = 1.0594
Cohesion = 698.23

Figure C-9B. RS Dense

C-26

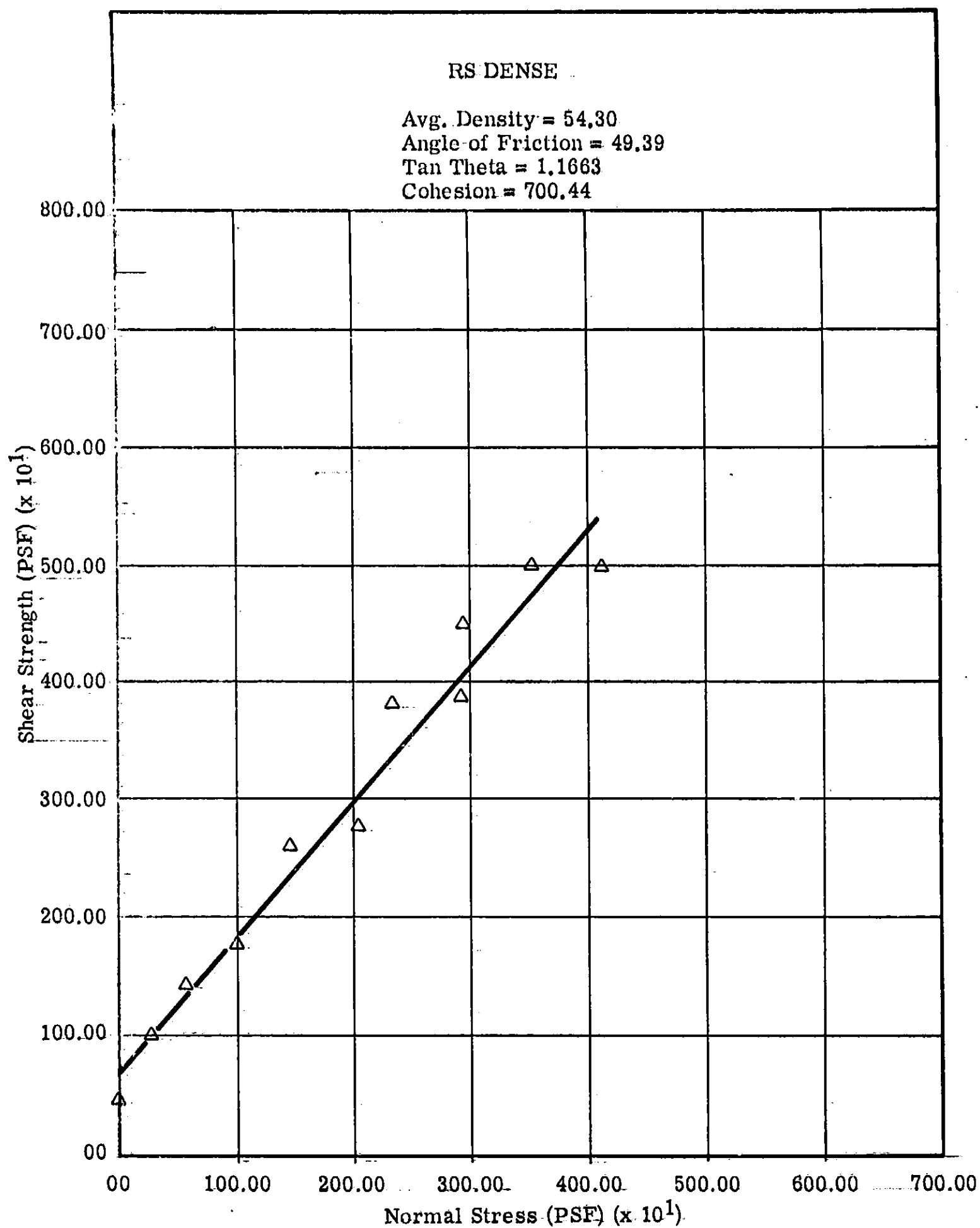Figure C-9C. RS Dense

Figure C-10A. PS Loose
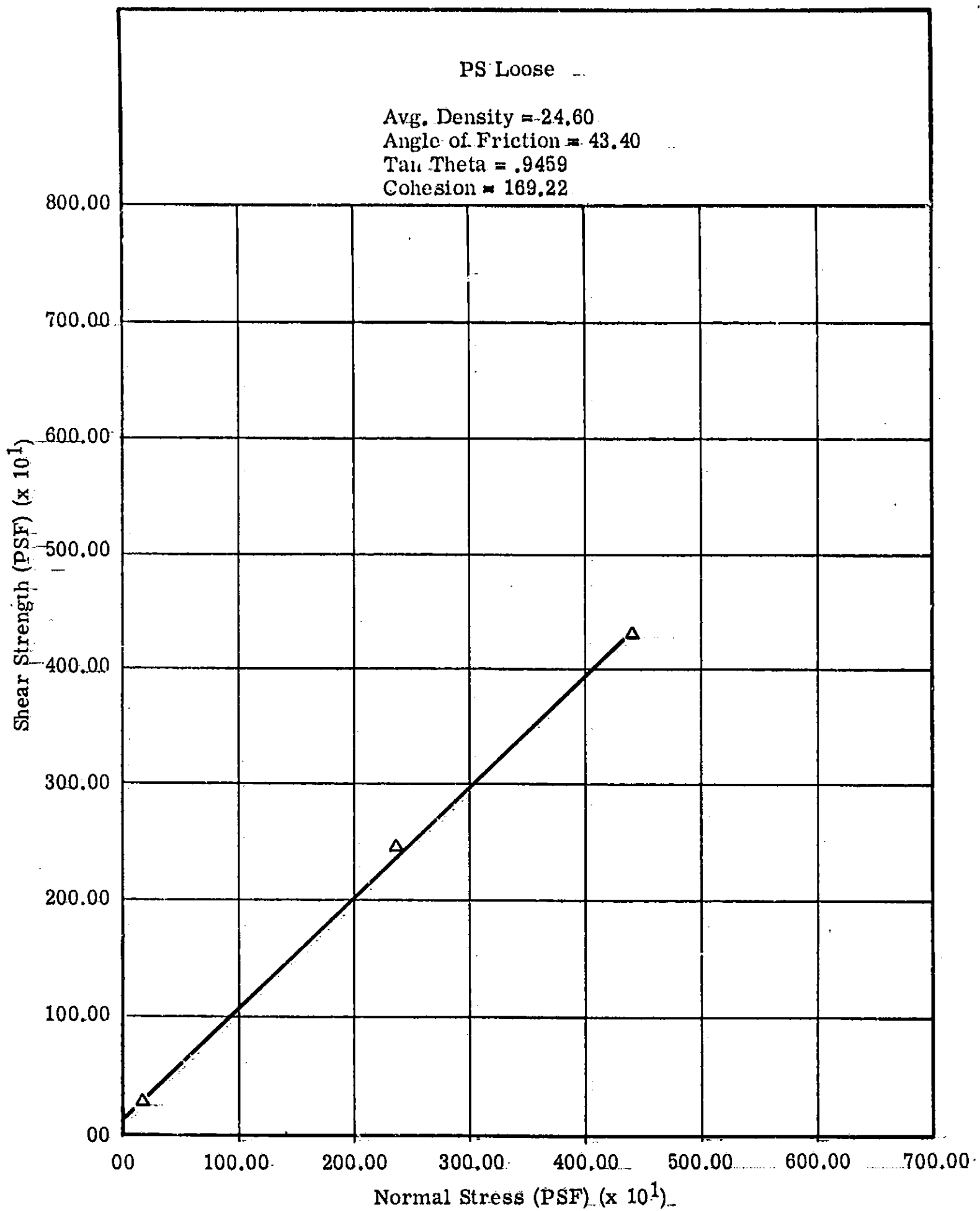
Figure C-10B. PS Loose

Figure C-10C. PS Loose

RSM Loose

Avg. Density = 58.20
Angle of Friction = 35.92
Tan Theta = .7244
Cohesion = 444.69

Shear Strength (PSF) (x 10^1)

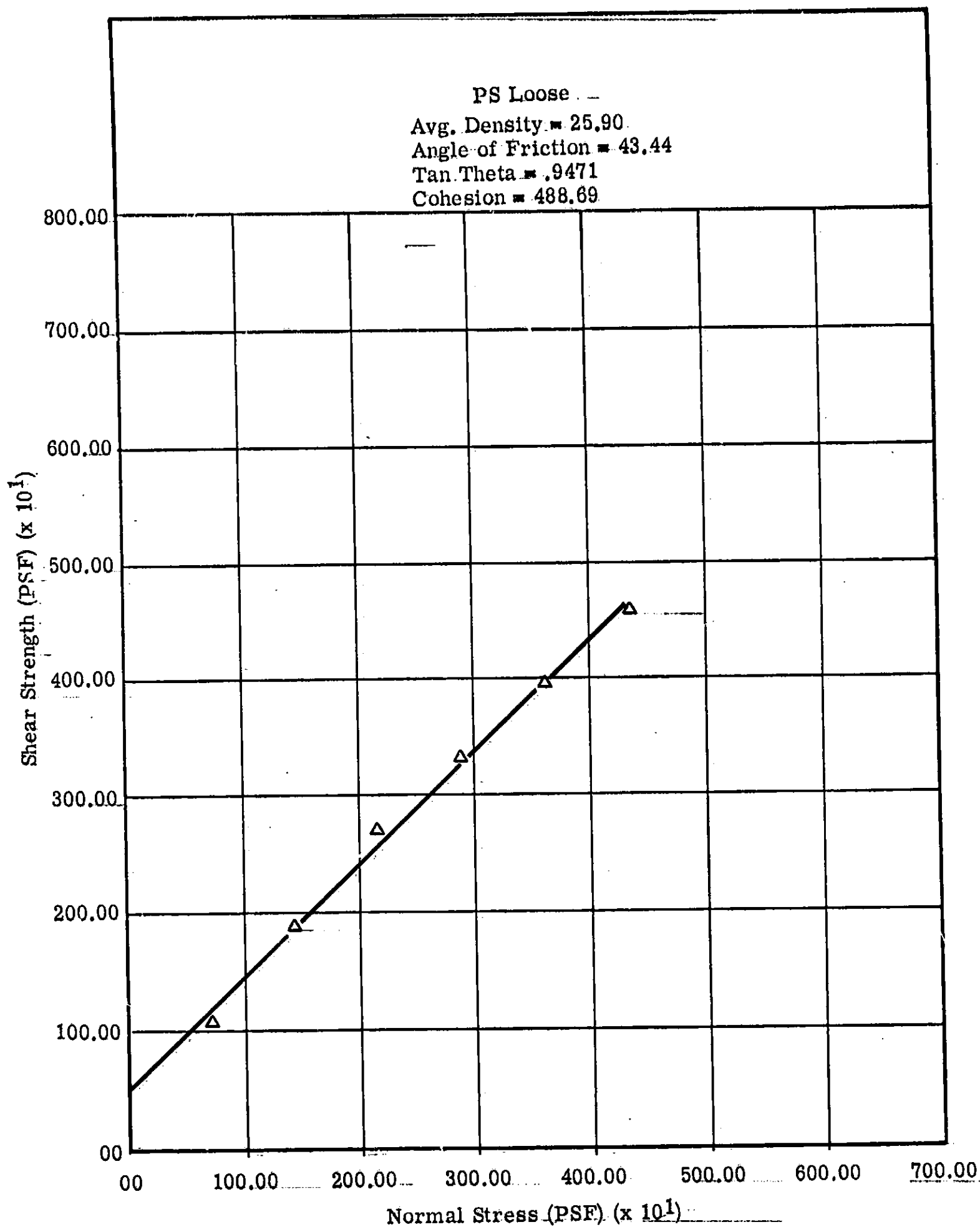Normal Stress (PSF) (x 10^1)
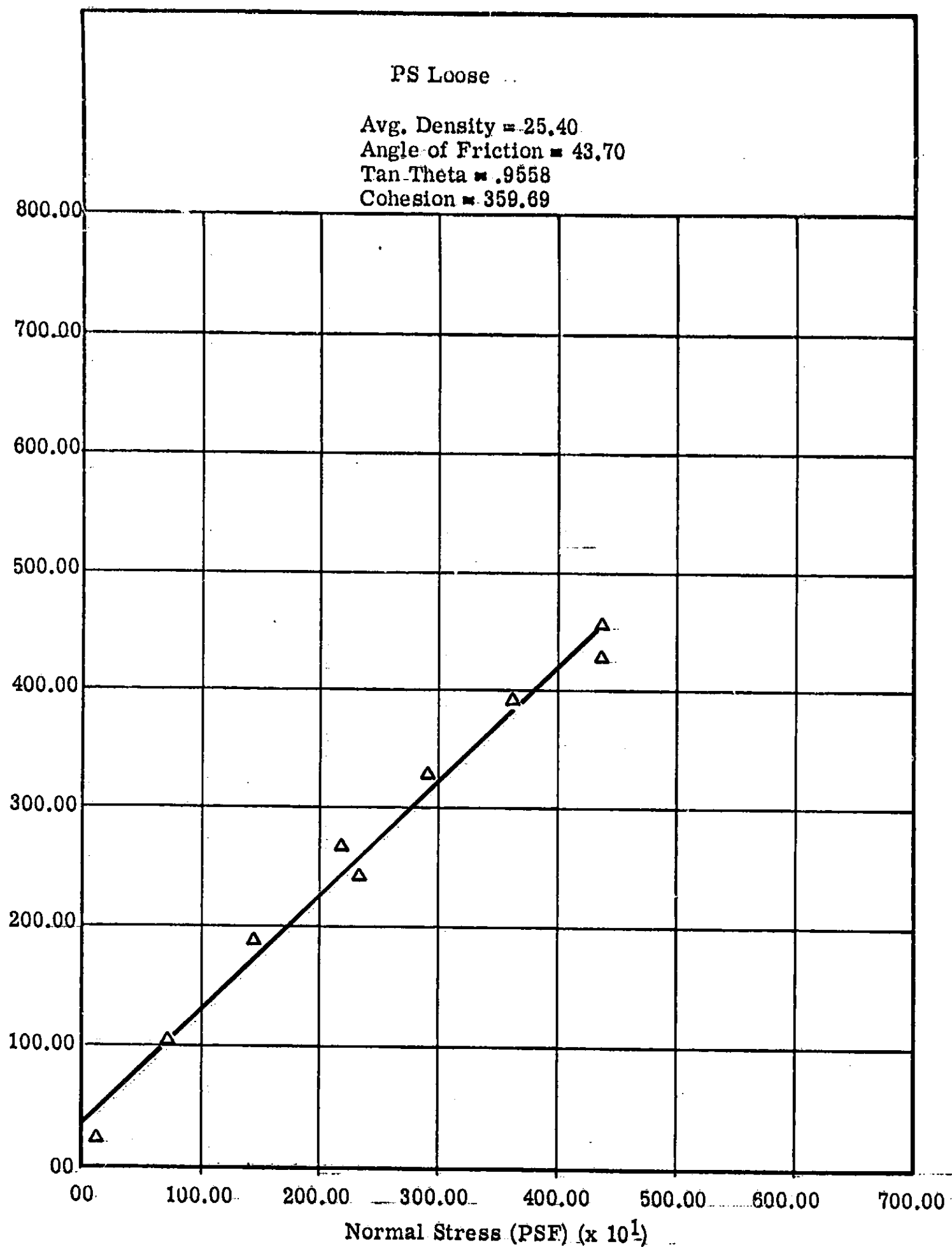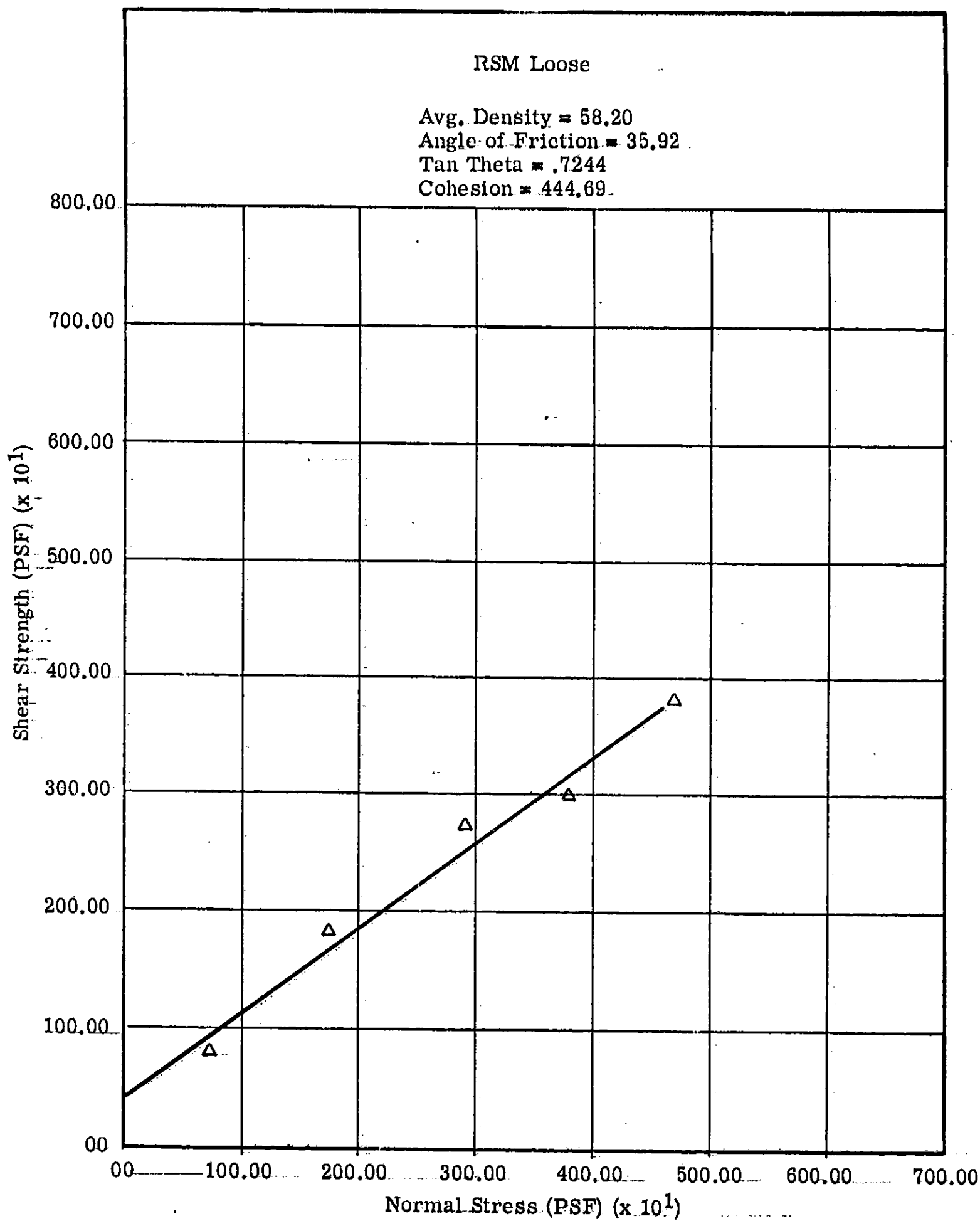
Figure C-11A. RSM Loose.
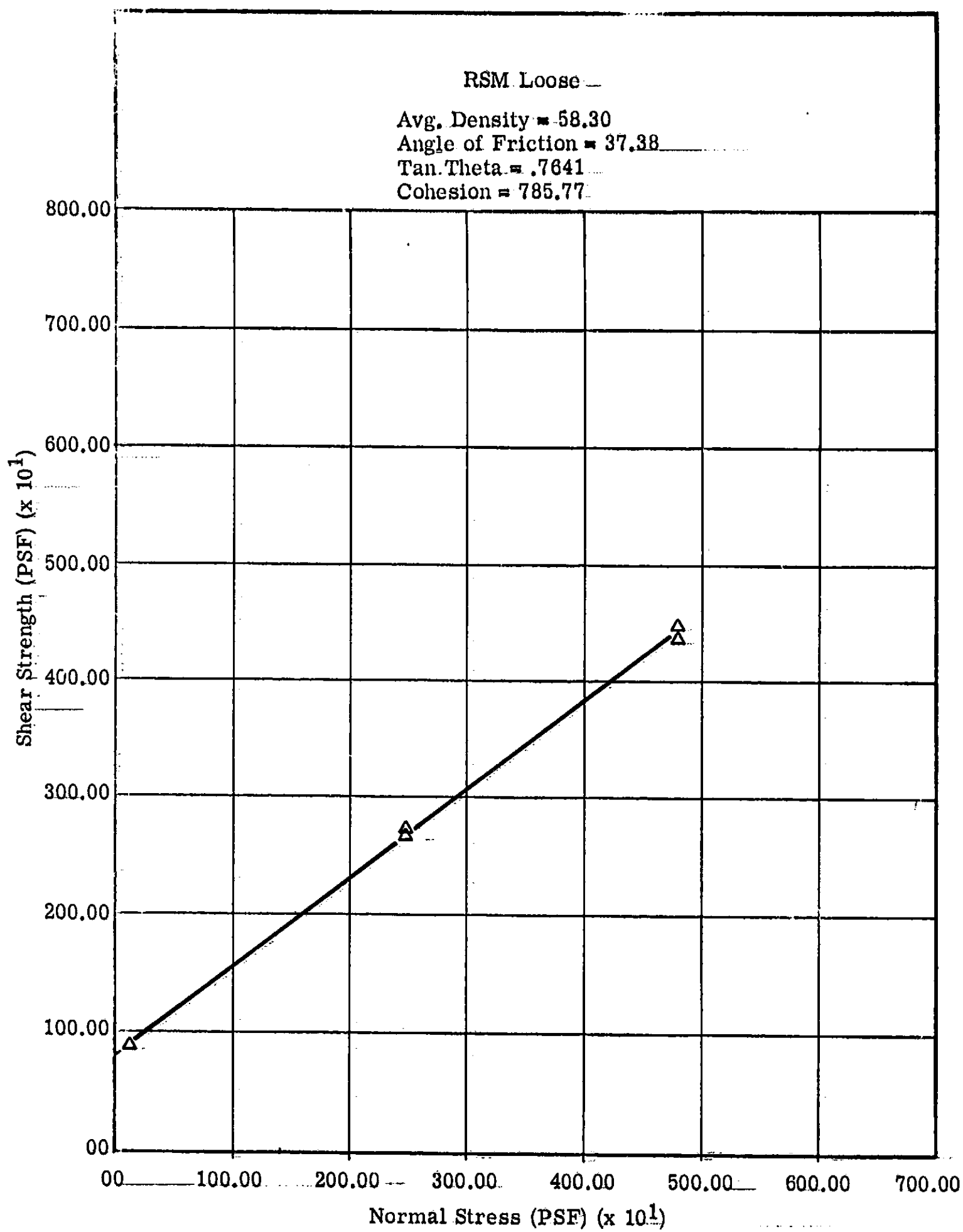
Figure C-11B. RSM Loose
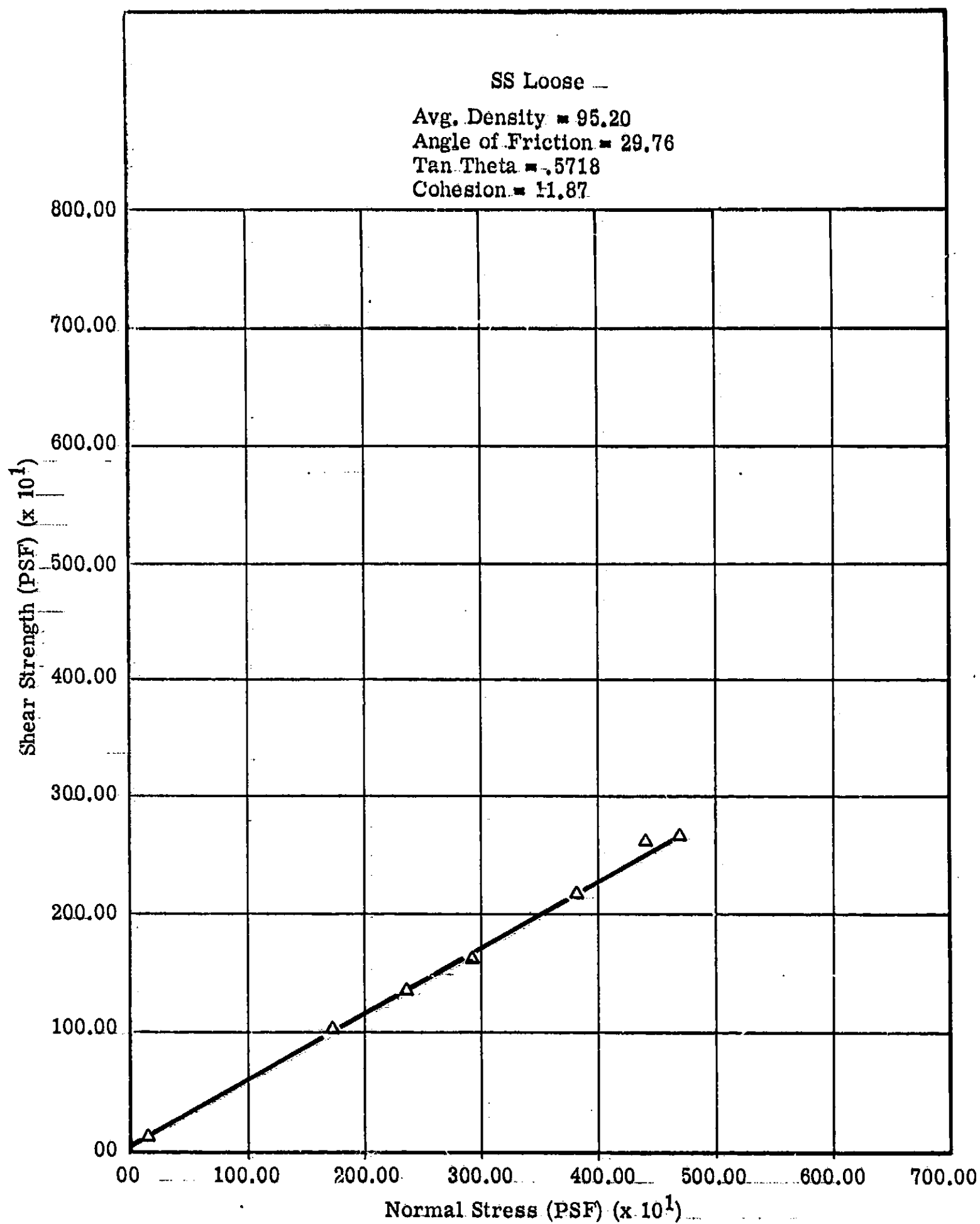
Figure C-13. SS Loose
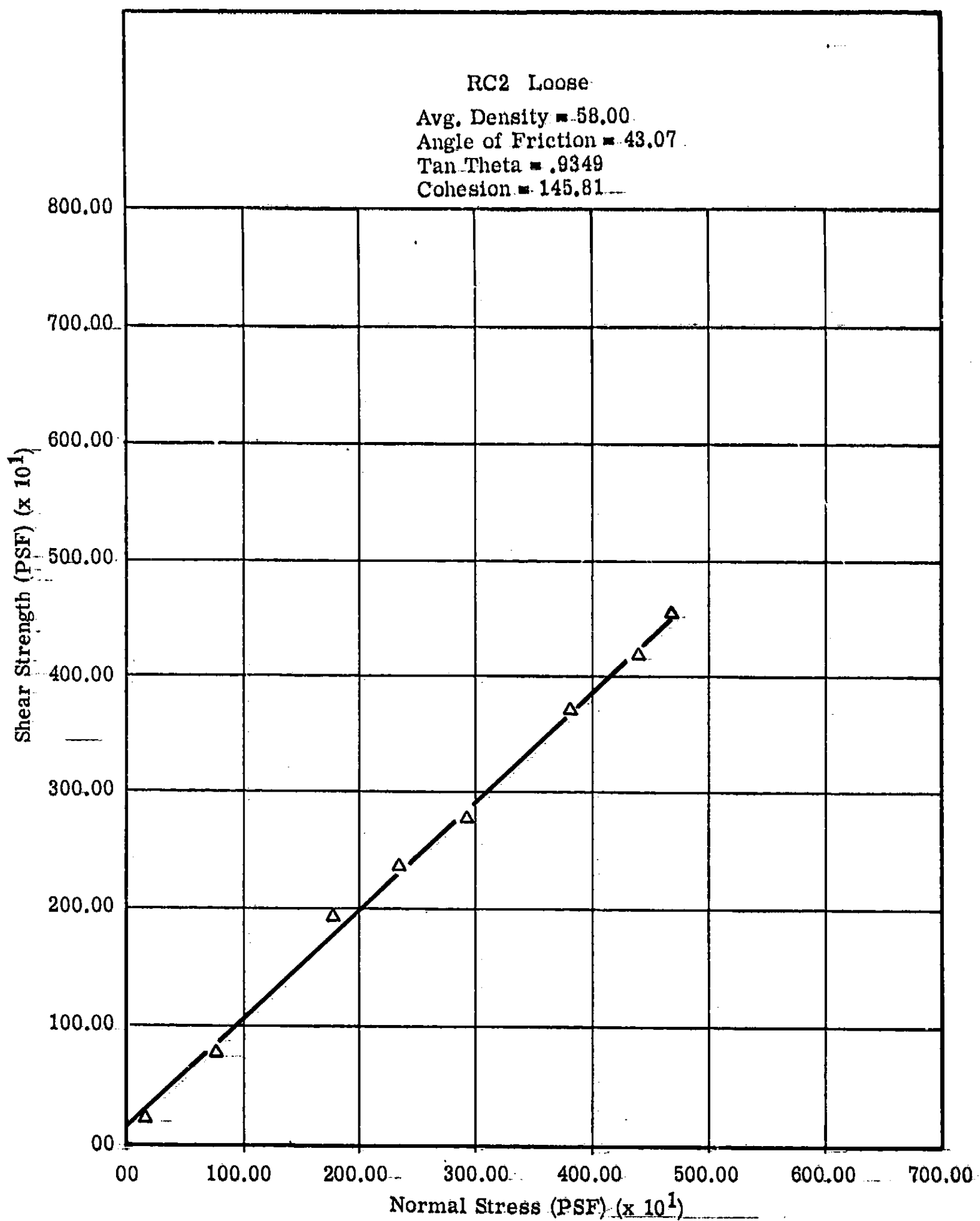
Figure C-12. RC2 Loose
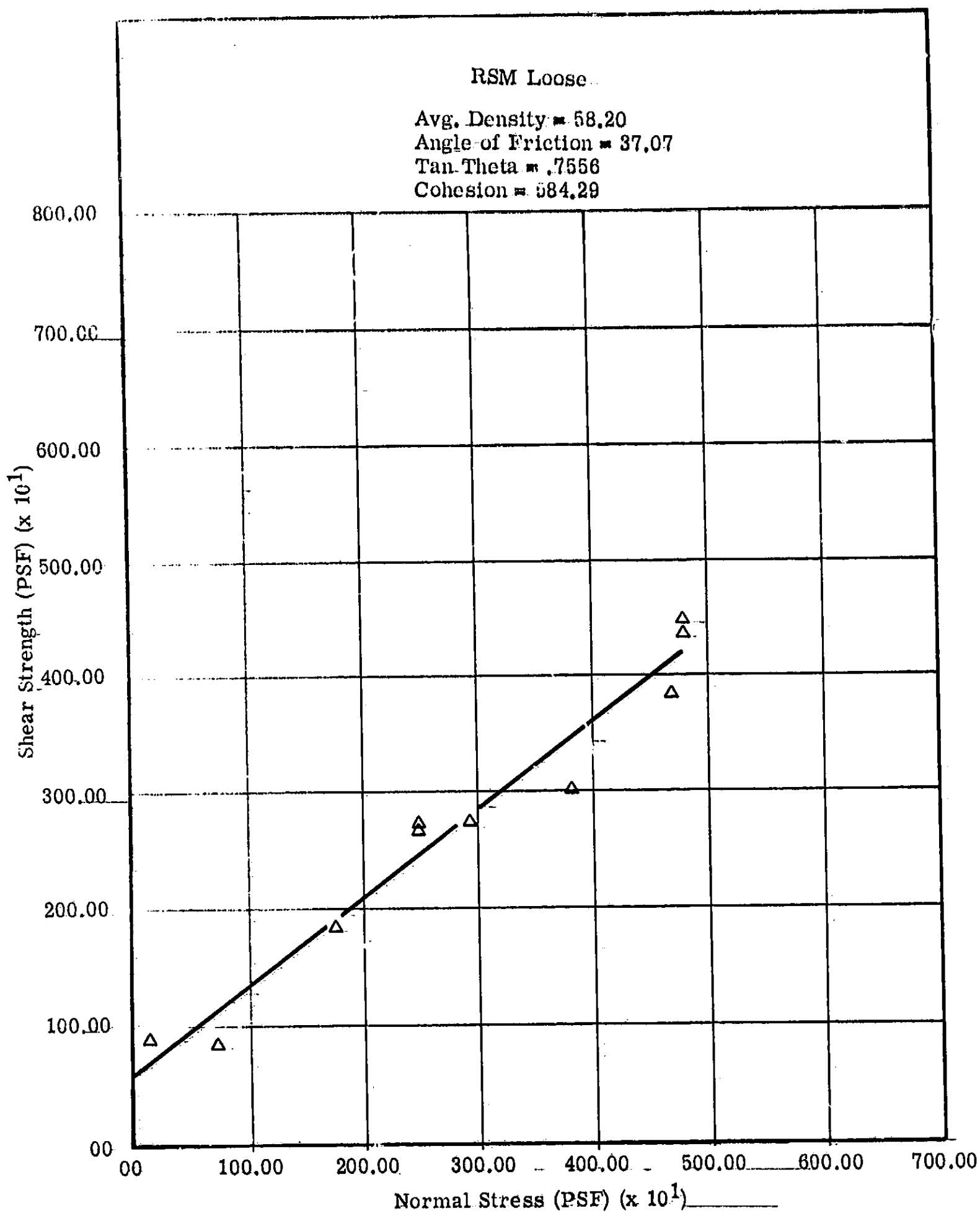
Figure C-11C. RSM Loose
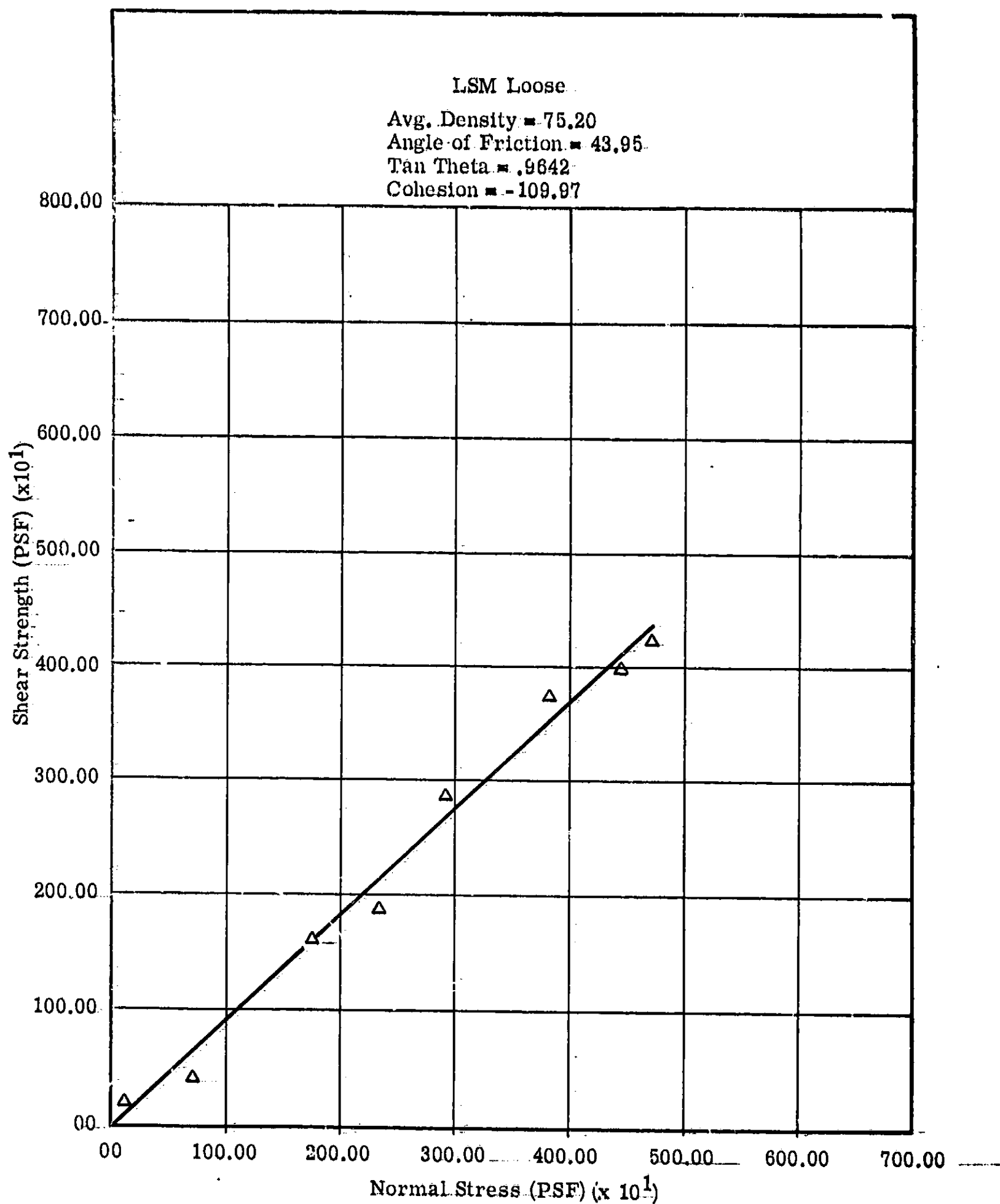
Figure C-14. LSM Loose
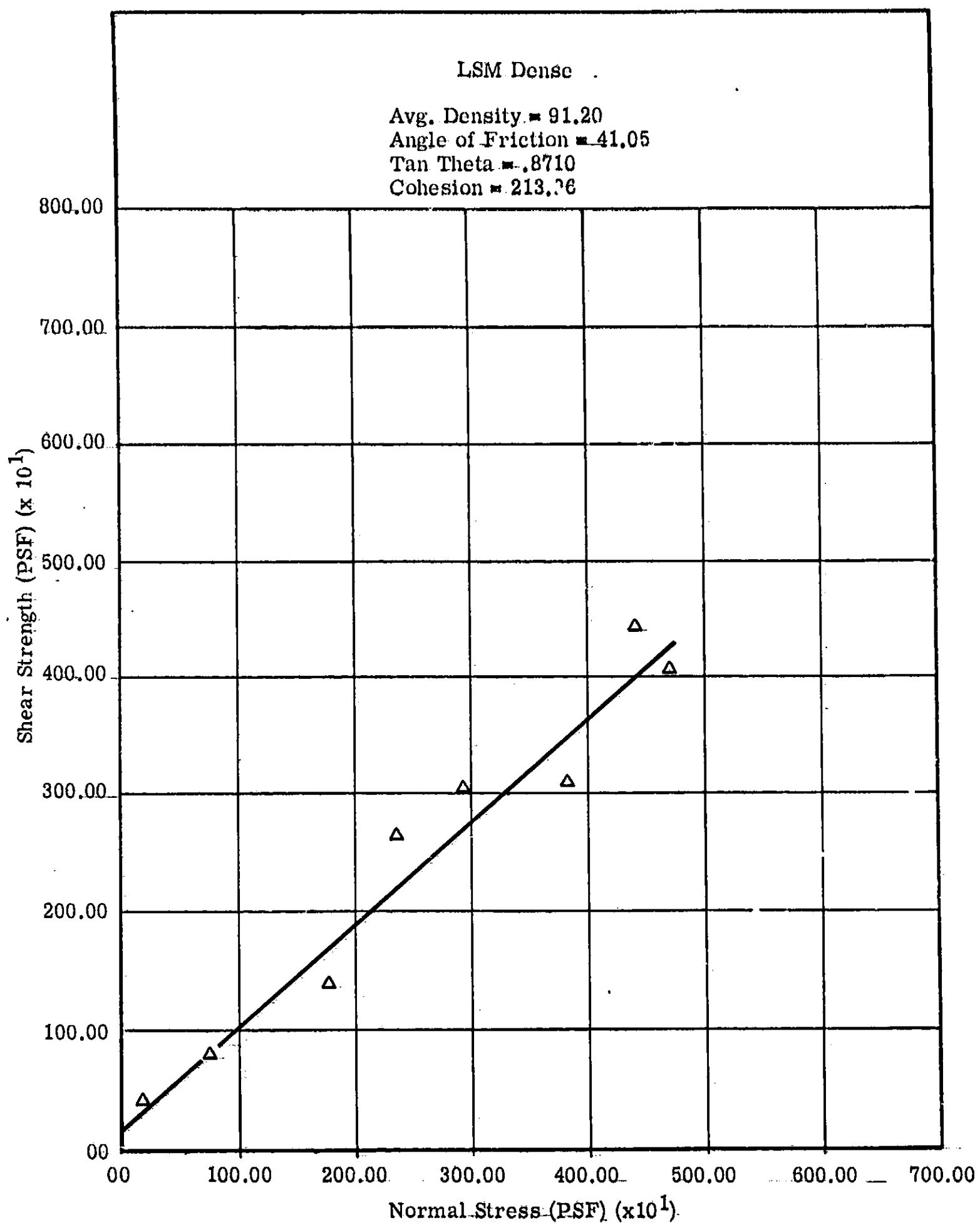
Figure C-15. LSM Dense
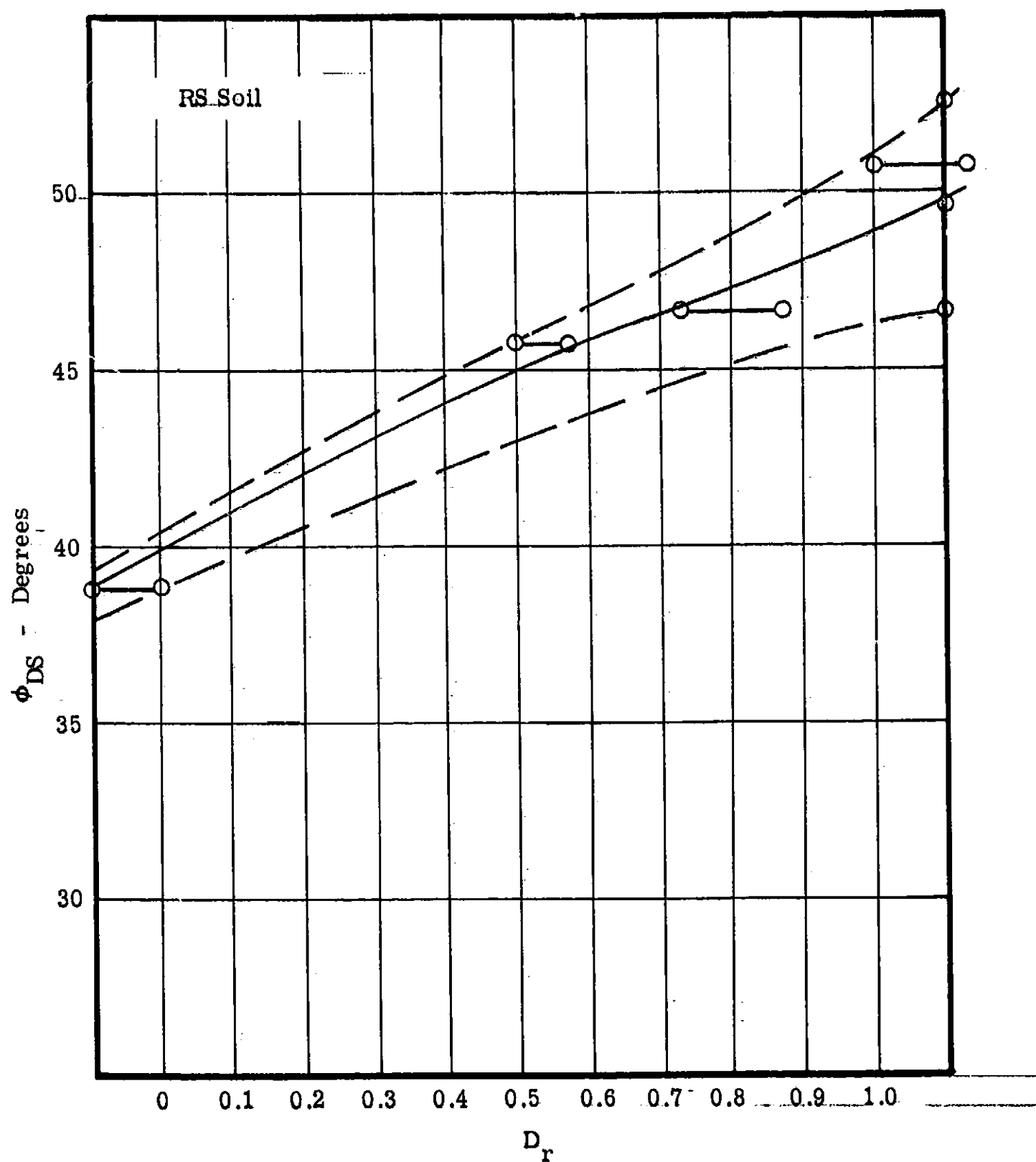
Figure C-16. Angle of Internal Friction vs. Relative Density
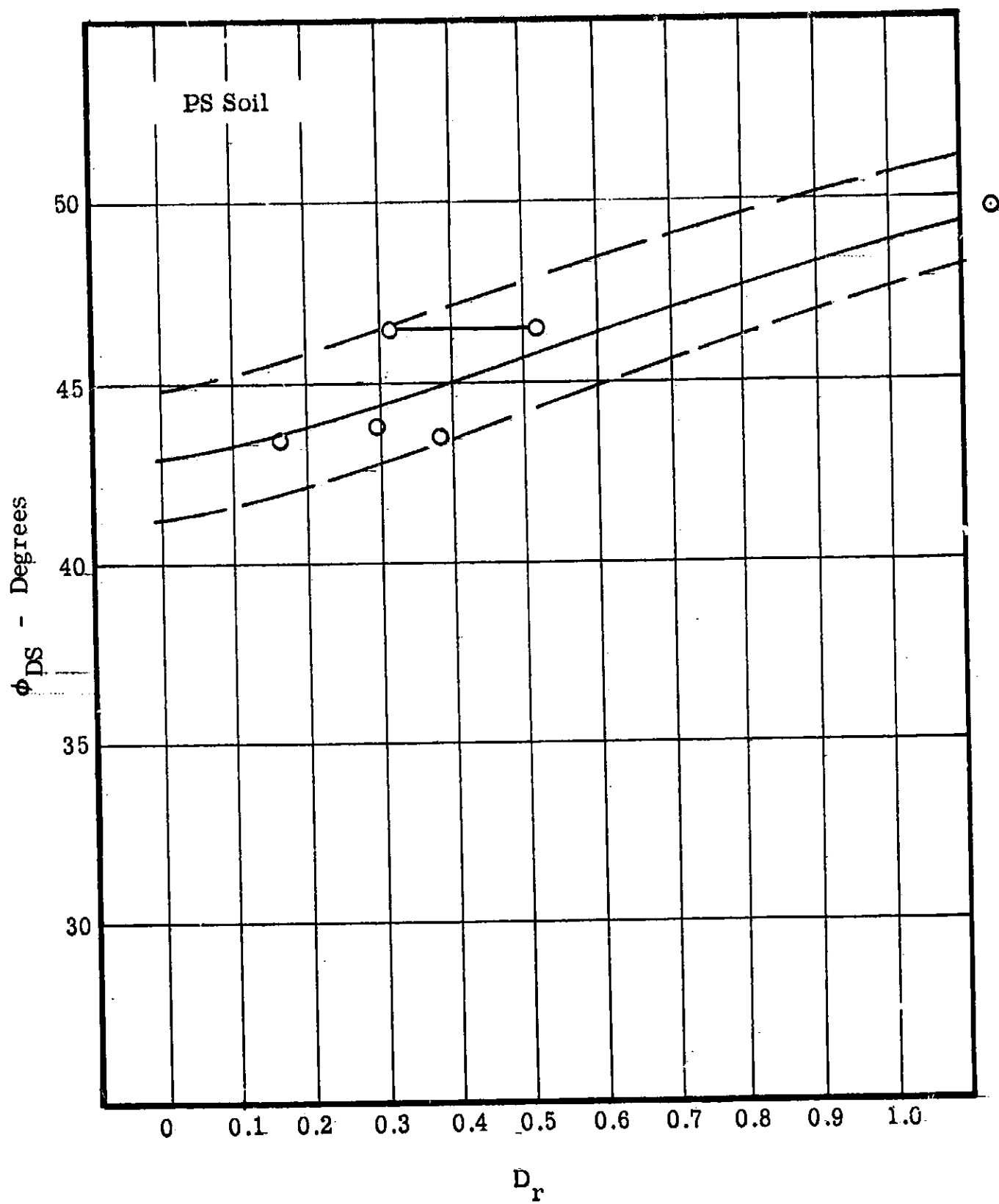
Figure C-17. Angle of Internal Friction vs. Relative Density
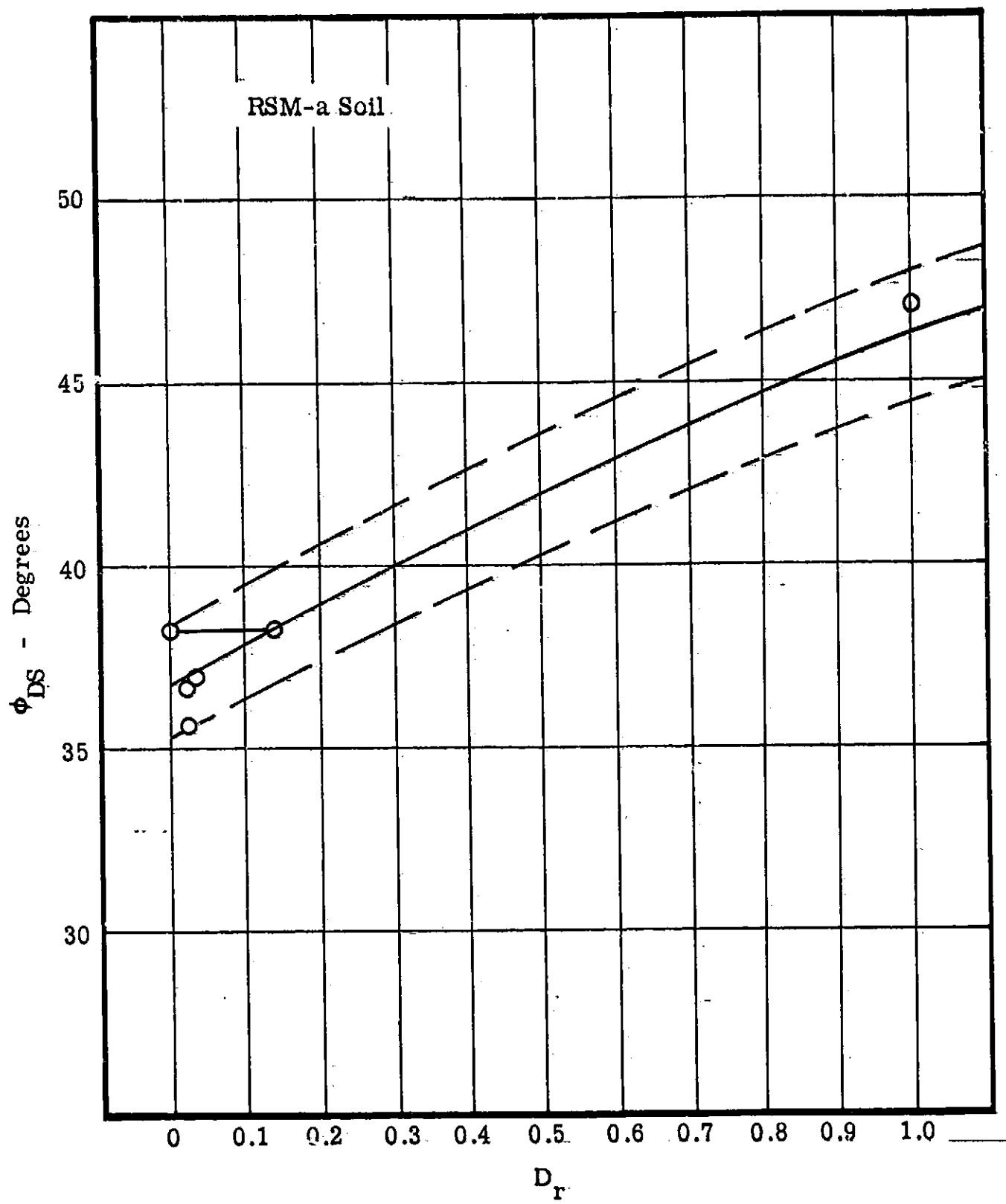
Figure C-18. Angle of Internal Friction vs. Relative Density
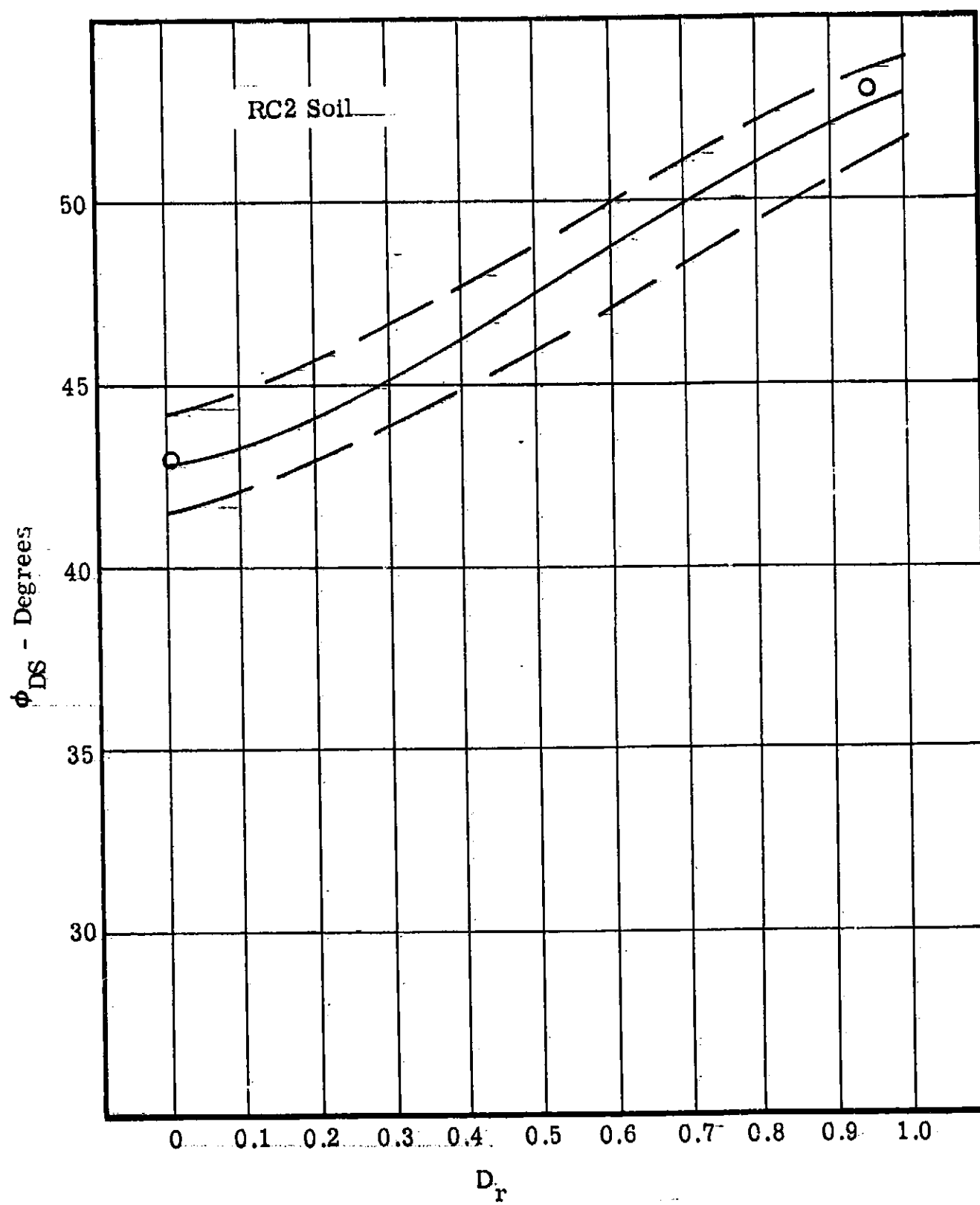
Figure C-19. Angle of Internal Friction vs. Relative Density
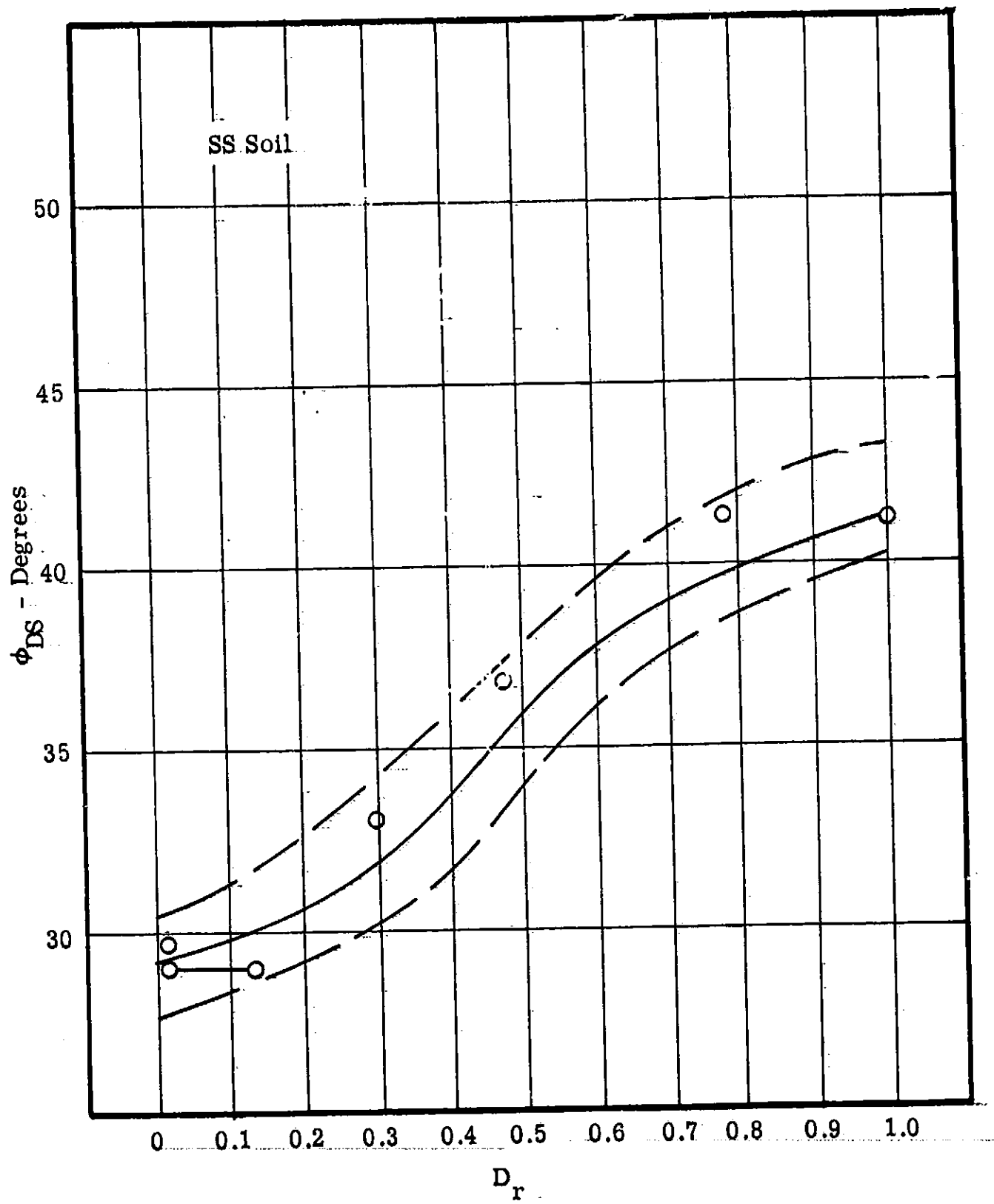
Figure C-20. Angle of Internal Friction vs. Relative Density
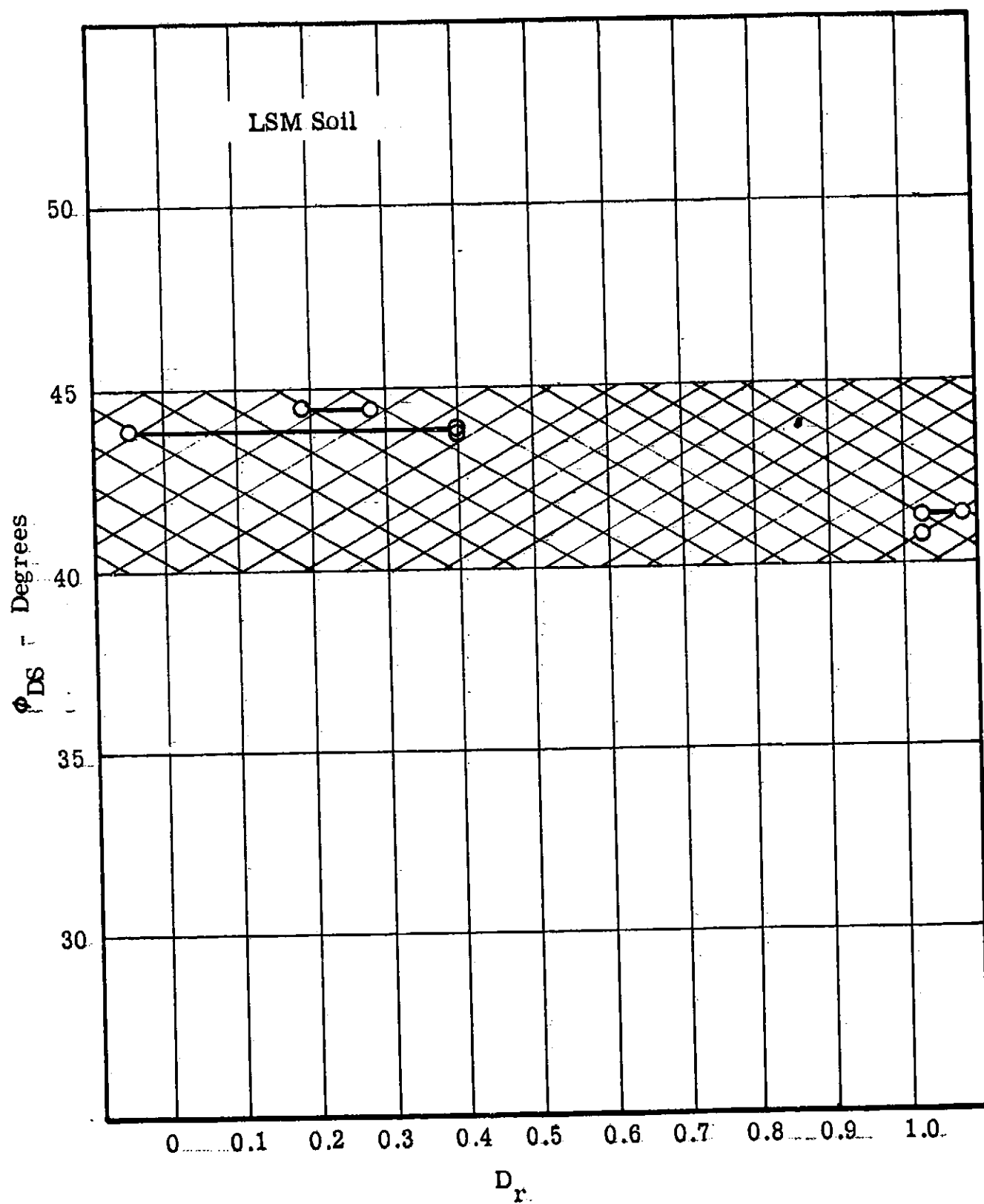
Figure C-21. Angle of Internal Friction vs. Relative Density
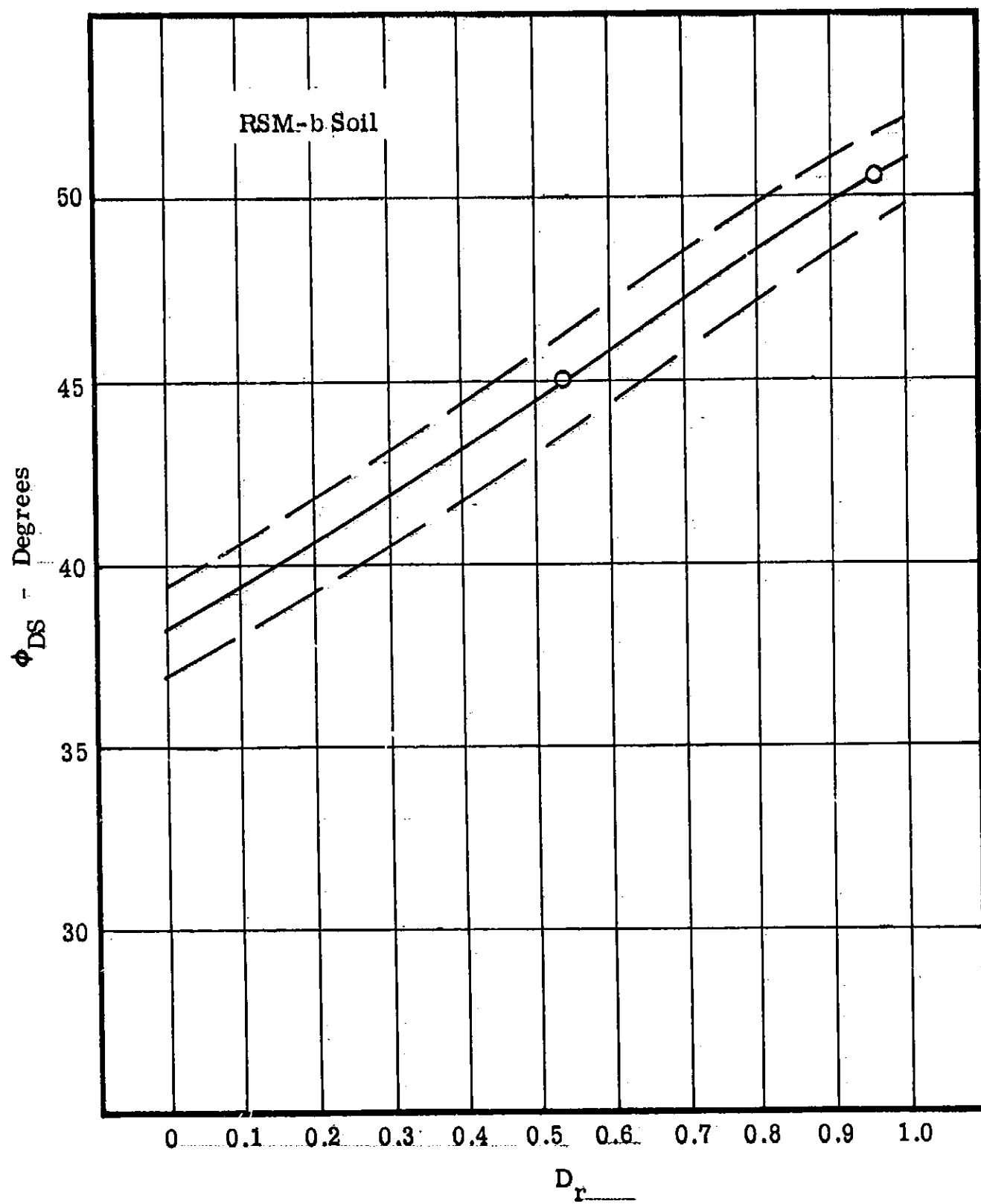
Figure C-22. Angle of Internal Friction vs. Relative Density
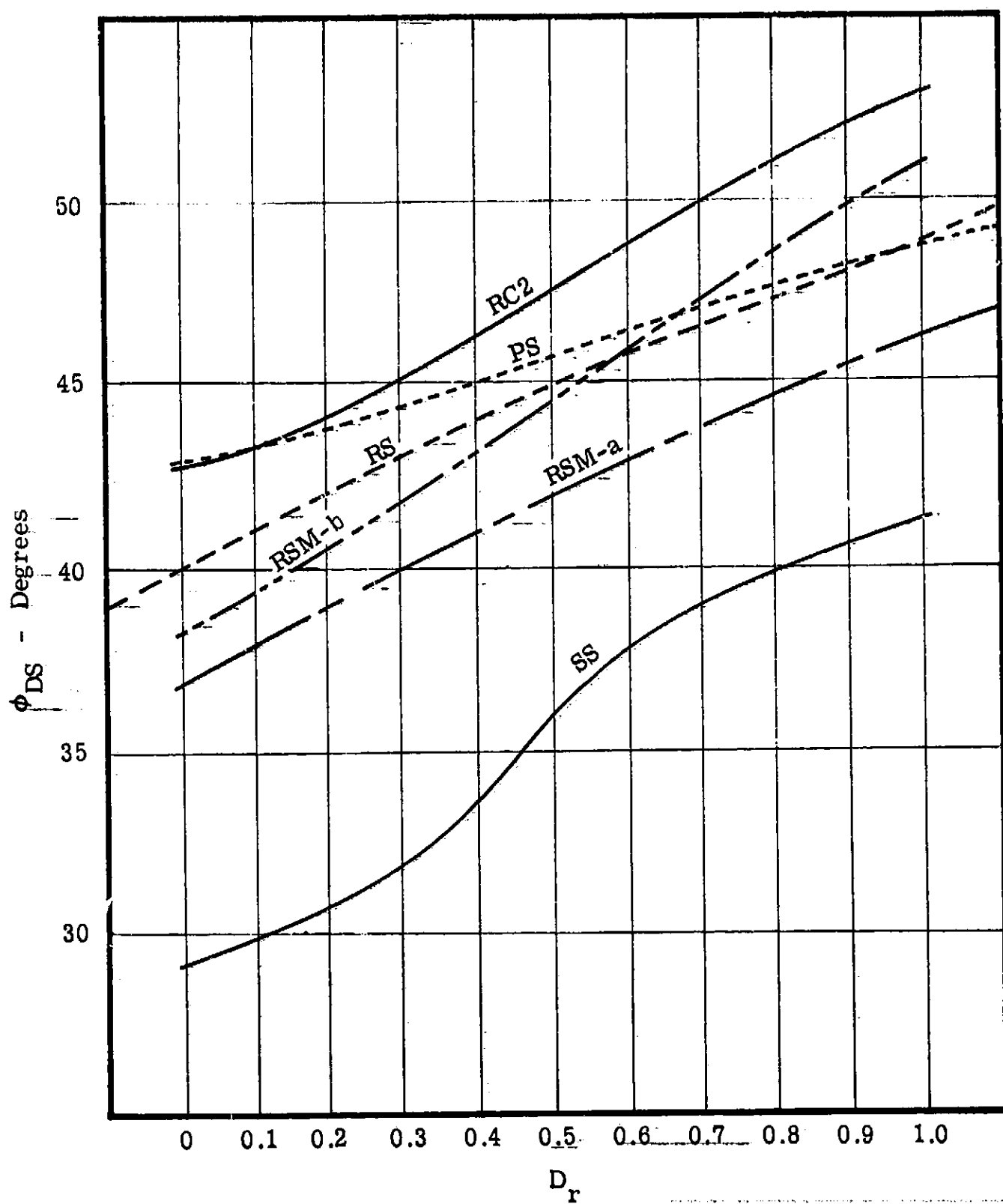
Figure C-23. Angle of Internal Friction Versus Relative Density
(From Direct Shear Test Results)

APPENDIX D

FULL-SCALE LM FOOTPAD DRAG TEST FACILITY DESIGN

D.1 INTRODUCTION

A detail design study was performed for the construction of a large drag test facility to accommodate tests on a full-scale simulated LM footpad in selected soil materials. Because of changes from the original program requirements, this effort was not carried through actual hardware fabrication. However, each of the three basic equipment components was designed to a state that would permit hardware to be procured or fabricated with a minimum of necessary additional design expenditure. This Appendix describes the equipment design that resulted from this study.

The full-scale test facility was intended to complement the subscale drag test equipment used during the program. The requirements included providing the capability for conducting either constant penetration or constant load footpad drag tests at any steady-state velocity between 2 and 15 feet/second, with footpad penetrations up to two feet.

Figure D-1 portrays an artist's impression of the facility installed over a soil test bed. The figure of a six-foot technician permits a realistic evaluation of scale. Floor space requirements are approximately 60 feet by 12 feet, while maximum height required is less than 12 feet. Multiple test stations or additional soil test beds would increase the width requirement proportionally. Figure D-2 is a design layout of this same installation.
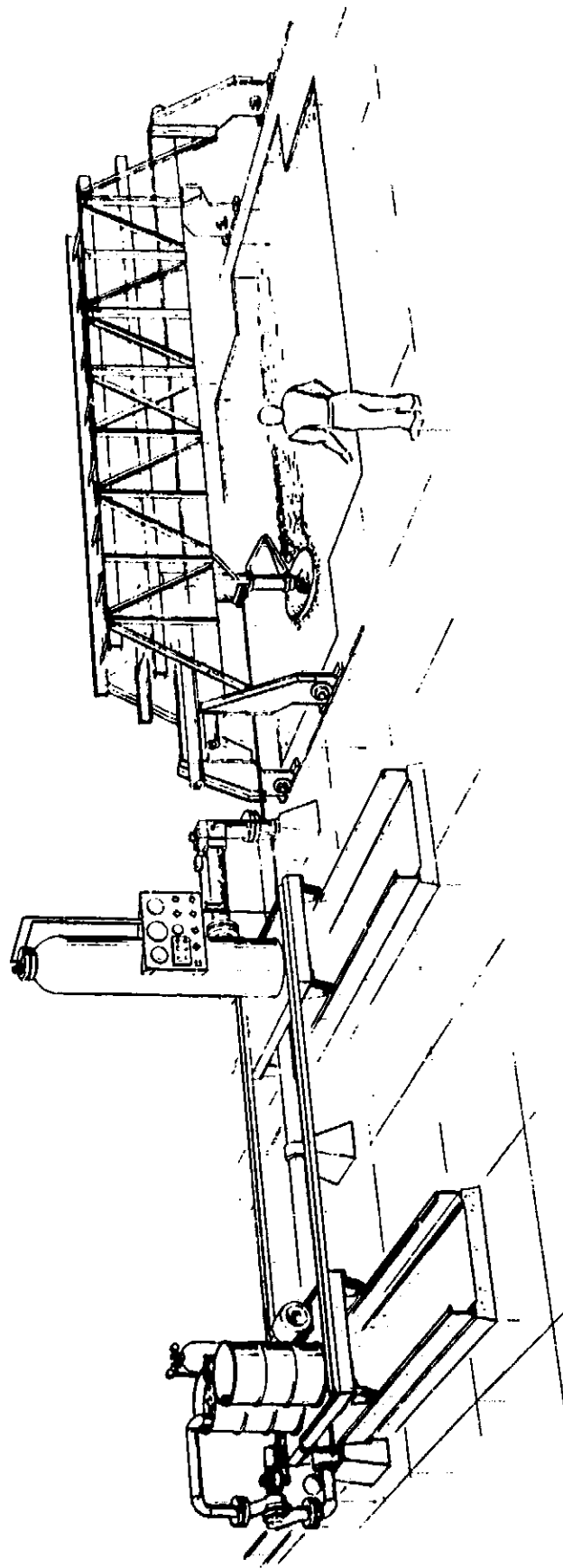
Figure D-1. Perspective View of the Full-scale LM Footpad Drag Test Facility

Figure D-2. General Arrangement of Full-scale LM Footpad Drag Test Facility

The major components of the facility are:

*1. The hydraulic power/control unit including actuator and electrical controls,

2. The carriage and gantry structure to support and guide the instrumented strut and landing pad over the soil test beds, and

3. The instrumented strut and full-scale simulated LM footpad.

The soil bed consists of a rectangular concrete pit approximately 10 feet wide by 24 feet long and 5 feet deep. Massive foundations form the ends and serve as supports for the gantry. Other hardpoints, located in line with the pit, are used to anchor the power cylinder and related control system. For multiple installations, several pits may be individually located adjacent one to another or may be formed from a single wide bed with longitudinal partitions. The pits would be filled to floor level with specific granular materials and renovated or recompacted prior to each test run by means of the appropriate soil bed preparation equipment.

General requirements of strength, rigidity, safety, serviceability, and convenience of operation formed the basis for design of all major components of the facility. In addition, detail requirements were established to govern the design of the power/control unit based on desired test system operational capabilities. Those requirements that reflect the system performance are summarized below.

1. System to be capable of propelling the test carriage horizontally over a prescribed (test run) distance at any desired constant velocity between 2 feet/second and 15 feet/second. The carriage velocity attained during the test run is to be maintained within ±0.1 foot/second.

---

*Design of the Power/Control Unit was accomplished by the Bendix Missile Systems Division, Mishawaka, Indiana, to meet technical requirements established by the Energy Controls Division. This work was performed between June and October 1966, under a working arrangement between the two Bendix Divisions.

2. The steady-state velocity actually attained during any test run is to be within 0.25 foot/second of the velocity desired (programmed).

3. The maximum axial (drawbar) load on the actuator is 7,000 pounds with a superimposed ±10 percent load fluctuation.

4. Total actuator stroke (carriage travel) to be 21 feet. Acceleration and deceleration to be accomplished within the first and last three feet of carriage travel, respectively, with the constant velocity test run using the remaining 15-foot distance.

5. Smooth transition to be effected between acceleration and steady-state velocity conditions.

Although a hydraulic power and control system was originally proposed as a means of propelling the drag test carriage, final choice of this particular method resulted from a feasibility study that also considered various electrical and mechanical drive arrangements. The selection was based chiefly on factors relating to availability and size of hardware to handle the extreme power requirements plus anticipated development problems and their cost in dollars and schedule in view of the velocity control and accuracies desired.

The design of each of the major facility components was carried as far as practical for study purposes and is believed consistent with the scope of effort intended by the NASA Work Statement requirements. Although certain areas of the system require some further definition, this can best be accomplished after installation site and fabrication sources and methods are established. The more significant of these areas are noted in the respective sections.

It should also be noted that during early phases of the full-scale system design, a survey of a number of existing large drag test facilities was made to determine their availability and their adaptability to the full-scale footpad test requirements. Of those contacted, none available could accommodate the specific test requirements without significant modification.

The following paragraphs, D.2, D.3, and D.4 describe each of the three major system components; D.5 describes operating procedures for the equipment and - in particular - the power/control system; D.6 lists design and manufacturing drawings that resulted from the study; and D.7 presents analytical predictions of system performance.

D.2   DESCRIPTION AND OPERATION OF THE POWER/CONTROL UNIT

The hydraulic power/control unit provides and controls the drawbar force that moves the strut/footpad and carriage assembly through the acceleration, constant velocity, and deceleration phases of its transit across the soil bed. The unit consists, essentially, of a 21-foot stroke hydraulic actuator powered by a high pressure oil supply tank with related accessories and flow controls, integrally mounted onto a single mobile framework. The flow controlling elements of the system were developed through analysis to meet the performance requirements summarized in paragraph D.1.

Figure D-3 illustrates the general configuration of the unit. The roller platform arrangement permits precise alignment of the power/control unit and gantry/carriage interface and facilitates repositioning the system to any of several adjacent soil beds. The platform and subframe structure are designed to prevent excessive loading and deflection of the power cylinder and other critical components during movement from one bed to another. During tests the unit is secured in position by anchoring the actuator to the floor at the three saddle supports shown. A fourth anchorage (not shown) would extend horizontally from the end of the power cylinder to restrain the system against the drawbar load.

Except for adjustment of the high pressure nitrogen storage cylinder regulator valve, all operational functions of the system are effected at the main control panel.

The actuator (or power cylinder) is of relatively conventional design except for its length. The steel cylinder provides a 21-foot usable stroke for the five-inch diameter piston, is cushioned at the blind end, and adapted for high flow rate inlet and outlet connections. The piston rod extends through a standard high pressure seal and terminates in a fitting
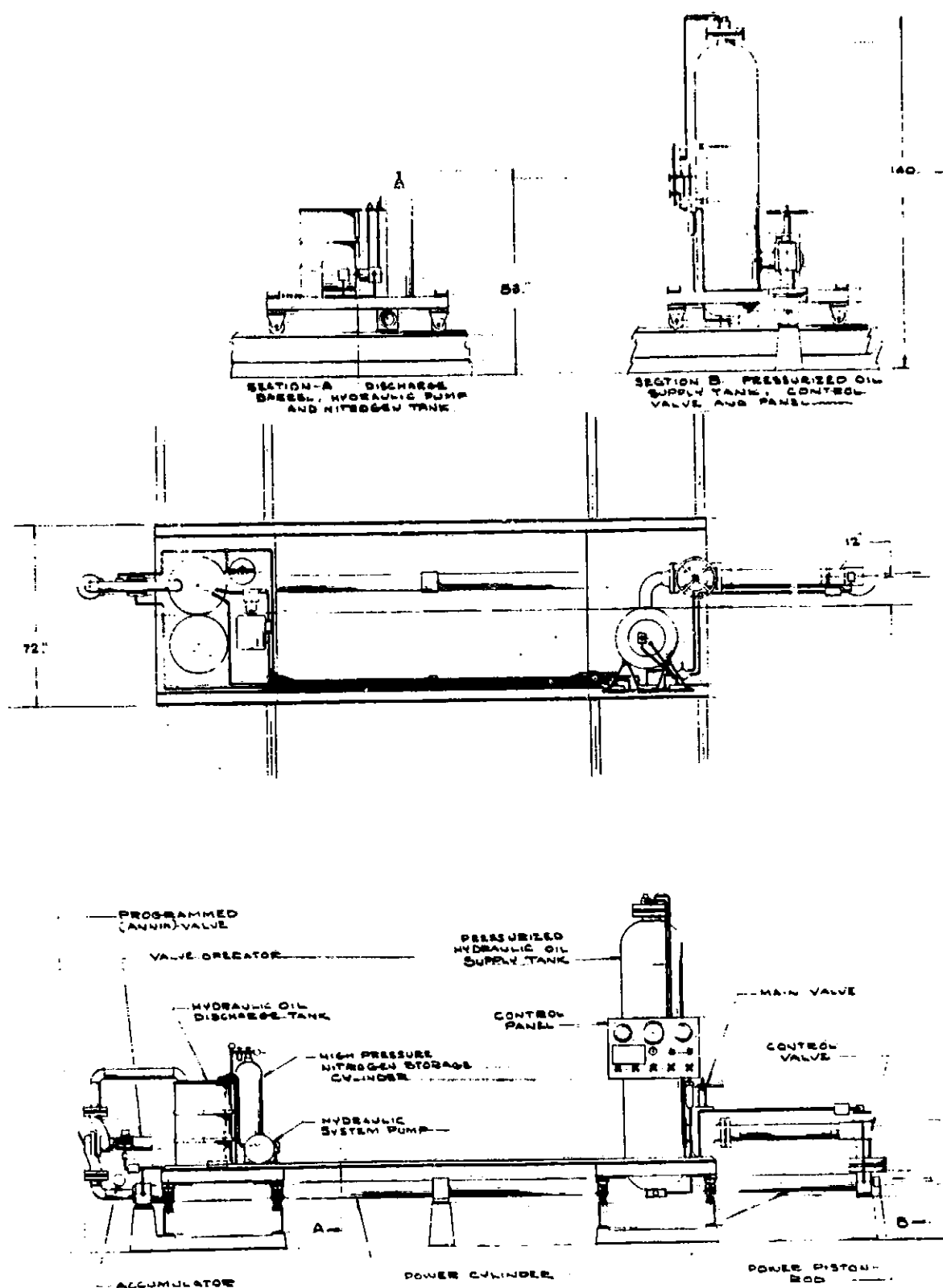
Figure D-3. General Arrangement Hydraulic Power/Control Unit

that allows quick disconnect from the drawbar which is attached to the carriage. After a test run the carriage must be disconnected and manually returned to its starting position, since the actuator is designed to power the system only during its compression stroke.

The power/control system is essentially self-contained with all hardware - including plumbing, gaging, valving and electrical components - mounted on the wheeled support structure. Wherever possible, standard off-the-shelf and commercially available hardware is used to minimize cost, procurement, and servicing problems. All components - whether purchased or designed - conform to industry accepted safety and performance standards or codes, such as API valve and pipe ratings, ASME unfired pressure vessel code, or UL approval on electrical fittings.

A schematic diagram of the power/control unit hydraulic system is shown in Figure D-4. The actuator operating force is generated by compressed nitrogen gas at 2,000 psi acting upon the surface of hydraulic oil within a 20-cubic-foot pressure storage tank (9). During operation, oil flows from the pressure tank through a control valve (6) to the actuator inlet port to power the piston. Displaced oil in the actuator discharges through the "Annin" valve (14) into the supply/discharge tank (1). A 4-gpm electric powered pump (8) draws oil from the discharge tank to extend the piston and refill the pressure storage tank after test. To reduce potential hazard, the hydraulic system is normally kept unpressurized except immediately prior to and during a test run.

The operational phases of actuator piston motion (i.e., acceleration, constant velocity, and deceleration) are governed by two separate - but interdependent - flow control units. Acceleration and deceleration is accomplished by the programmed opening and closing, respectively, of the air operated Annin valve (14). The required footpad velocity versus displacement profile (i.e., steady-state velocity) is achieved by the high-response control valve (6) which programs the rate of oil flow to the actuator. Flow rate is governed by both the control valve pneumatic setting and the metering orifice selection.
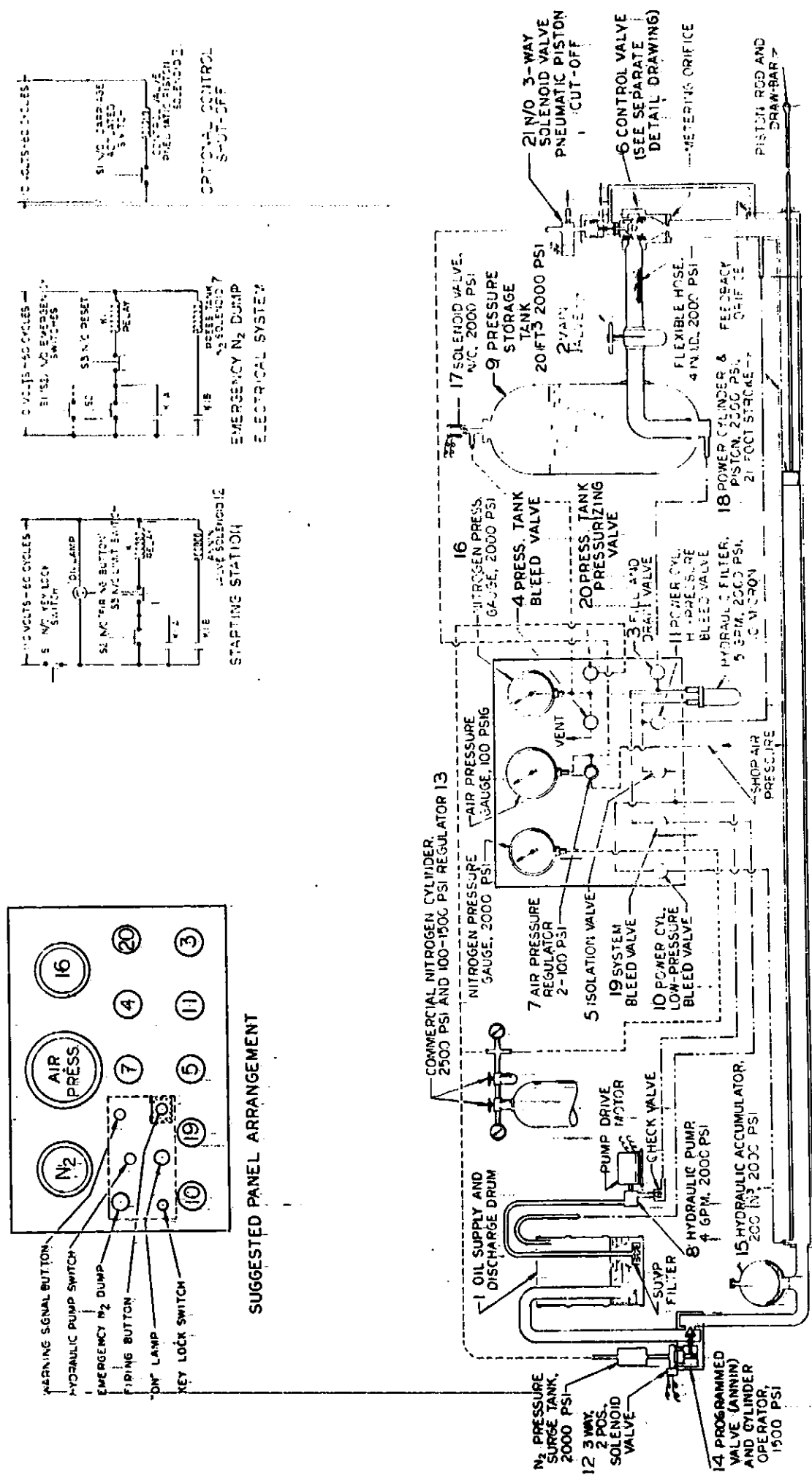
Figure D-4. Schematic Diagram Hydraulic Power/Control Unit

The design of the control valve is based on a previously developed high-response fuel flow regulator that was successfully employed by Bendix in a missile fuel control system. This regulator is too small to accommodate the test facility actuator flow requirements, however, the proven concepts and analysis techniques developed during its design were applicable to the control valve design and to the detailed analytical study of the system.

Although no attempt is made here to describe details of the analytical procedures used, it is noted that both analog and digital computer simulations were employed using a carefully developed mathematical model of the open-loop control system. This analysis was directed toward evaluating the hydraulic system dynamics, predicting system performance, calibration, and optimizing hardware, including critical sizing and arrangement of the control valve components.

The analytical study was carried as far as practical without benefit of experimental results and, as shown in paragraph D.7, provides good indication that the desired performance requirements can be met. However, this can be fully realized only through a subsequent development phase when the actual control valve and other hardware components are made available. At that time, any deviations between hardware test results and characteristics assumed in the mathematical model would be evaluated and incorporated into the model for further detailed analysis. An important output of the final analysis will be the calibration data for use in selecting the proper metering orifice and control valve pneumatic-setting necessary for programming the control valve to accommodate specific test velocity and load requirements.

The control system is essentially open-loop in that there is no direct signal feedback to the valve from the moving carriage. However, closed-loop features are employed from the standpoint that flow to the power cylinder, which is proportional to carriage movement, is sensed and used to regulate the control valve. This approach, followed in the interest of economy and simplicity, appears adequate based on analysis results thus far. If experimental results disagree either of several closed-loop designs could be incorporated without major redesign of the system.

Figure D-5 illustrates the schematic arrangement of the control valve. A functional description of this unit and other active elements of the flow control system can best be presented if a typical test run is assumed. In order to preserve continuity, some redundancy with prior discussions is necessary, and reference is made to both Figures D-4 and D-5.

Immediately prior to test, the entire hydraulic system (Figure D-4) is charged to 2,000 psi by pressurizing the high pressure storage tank (9). At this time the actuator piston is fully extended, the Annin valve (14) is closed, and the control valve ports (Figure D-5) are held open by the regulated air pressure acting on the constant force piston.

The following conditions would exist after pressurization and at any time prior to the moment of actual "firing."

Full hydraulic pressure exists on both faces of the actuator piston (18). Due to the piston rod cross section there is an area differential between the head and rod faces of the piston. This inequality results in a force unbalance across the piston tending to hold it in the extended position (to the right, in Figure D-4).

The control valve (6) is situated between the pressure storage tank and the power cylinder supply port. A fixed metering orifice is located immediately downstream from the control valve. It is one of a set of four which can be selected and assembled into the circuit to meet specific velocity requirements.

The control valve consists of a sliding tubular element with eight identically contoured ports piercing the walls and forming variable orifices in conjunction with the lip of an annular groove inside the valve sleeve. The valve is hydraulically balanced or nonpressure sensitive, since the driving web is perforated to allow pressure equalization.

Two separate control devices serve to position the control valve. The first consists of a constant force pneumatic piston and push rod which tends to hold the valve against its wide open or maximum flow stop. (The air pressure to the constant force piston is set

CONTROL VALVE PISTON

CONSTANT FORCE
PNEUMATIC PISTON
AND PUSH ROD

REGULATED AIR
PRESSURE

OIL FROM
PRESSURE
TANK

VENT

CONTROL VALVE
AND SLEEVE

FLOW STRAIGHTENER

METERING ORIFICE

TO POWER
PISTON

FEEDBACK ORIFICE

PRESSURE CONNECTIONS
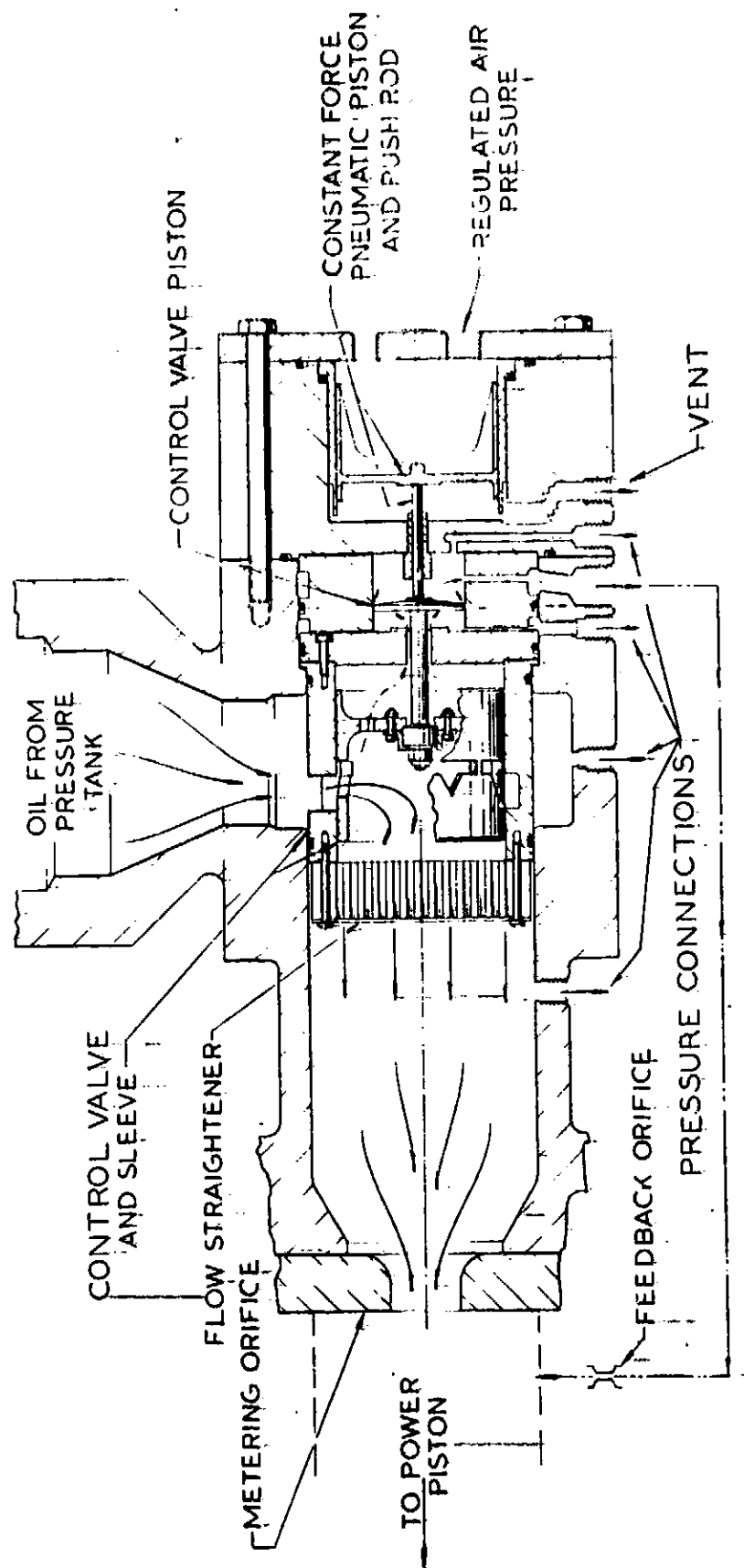
Figure D-5. Schematic Arrangement–Control Valve Assembly

at the air pressure regulator (7) during test preparations and remains constant through-out the run.) The second is a relatively small diameter control valve piston, solidly attached to the control valve. It is sensitive to the differential pressure between the valve chamber upstream of the metering orifice and, through a secondary "feedback orifice," to the conduit below the metering orifice. This pressure differential, modified by the scheduled leakage or circulation past the piston itself, is transmitted as a force tending to modify the control valve position during operation.

Although the control valve is subject to full hydraulic pressure and, in addition, is held in the wide open position by the pneumatic piston prior to "firing," the forces across the control piston are zero since there is neither oil flow nor pressure drop in the circuit.

A pneumatically loaded accumulator (15) and a solenoid actuated, programmed, quick operating (Annin) valve (14) are located beyond the discharge, or retraction end of the power cylinder. This valve is the component which maintains the system under pressure before firing and initiates the entire operational sequence after firing.

The following sequence is initiated immediately upon firing or beginning a drag test "run." (Refer to Figure D-4.)

The solenoid valve (12), activated by the firing circuit, releases high pressure nitrogen to a valve operator cylinder which, in turn, opens the Annin valve (14) through its full scheduled range in a matter of milliseconds. The programmed flow of oil through the valve to the discharge drum (1) results in a rapid pressure reduction in the actuator cylinder below the power piston (18). The differential caused by the deteriorating pressure at the piston face and the sustained high pressure at the rod face causes a force transition across the power piston. As the differential increases, the power piston starts to accelerate toward the retracted end of travel and to draw the gantry carriage and foot-pad across the soil test bed. The power piston acceleration response is slower than the differential pressure rate of change across the piston. To prevent cavitation and resulting instability of the cylinder, the pressure drop is modified by the influx of a measured volume of oil discharged from the pneumatically-loaded accumulator (15).

Initially, the motion of the actuator piston is determined by the programmed opening of the Annin valve (14), but within a few milliseconds the control valve (6) becomes functional and assumes regulation of the steady-state travel phase.

Simultaneously with the start of power piston travel, pressurized oil from the supply tank begins to flow through the control valve and metering orifice toward the actuator supply port. As the rate flow increases, there is a corresponding pressure drop across the metering orifice. Although this decrease in pressure is communicated to the rod face of the power piston, the pressure on the opposite face is decreasing at a still faster rate and the power piston continues to accelerate.

The precise diametrical fit between the control valve piston and its body forms a constant area orifice and leakage path for pressurized oil flowing through the control valve. The oil pressure drops as oil leaks past the piston and continues through the feedback orifice to discharge into the lower pressure flow of the main conduit below the metering orifice. The pressure drop across the control piston applies a closing force to the control valve opposing the opening force exerted by the constant-force pneumatic piston. Thus, as oil flow through the control valve increases to accelerate the power piston, the control valve piston tends to reduce the valve opening (and retard the flow) to approach a steady-state rate of actuator piston travel.

The transition of flow control from Annin valve to control valve occurs during the initial two or three feet of acceleration after which the control valve maintains the carriage and footpad at a constant rate of transit as programmed by the metering orifice selection and the constant-force pneumatic piston pressure setting.

At the termination of 15 feet of piston-carriage steady-state travel (18 feet of total travel), the moving components are decelerated following a sequence in the reverse order of acceleration, as described below.

As the gantry carriage passes the 18-foot total travel position, it breaks an electrical circuit to the programmed (Annin) valve solenoid. The scheduled rate of valve closure

causes the pressure to rise ahead of the moving power piston, tending to decrease the differential pressure across the piston.

Rate of oil flow through the metering orifice and control valve decreases as the power piston decelerates. The control valve senses the reduced drop across the metering orifice and moves toward its open position to maintain the rate of oil flow. Since the rate of pressure increase ahead of the power piston is higher than the capability of the control piston to increase the flow behind the piston, the differential pressure continues to approach zero and to further decelerate the moving components.

The rising pressure between the actuator piston and closing Annin valve diverts a portion of the oil volume to the accumulator to minimize hydraulic shock.

Differential pressure degradation, friction, and drag loads combine to bring the system to a full stop in less than three feet of decelerated travel. For additonal safety other hydraulic and/or mechanical damping devices would also be installed on the gantry or at end of the soil bed to assist deceleration and limit the travel of the carriage.

During the constant velocity phase of carriage motion the steady-state velocity control is effected as follows.

Load fluctuations on the moving footpad are transferred as velocity variation impulses to the actuator piston, with increased drag loads momentarily decreasing the piston velocity. This results in a slight decrease in pressure differential across the metering orifice which is sensed by the control valve piston. The piston moves toward its open position to increase control valve flow and, correspondingly, to increase and restore the actuator piston velocity toward its previous steady-state value.

The increased flow results in proportionate increase in pressure differential across the metering orifice with a corresponding closing movement of the control valve piston to stabilize the oil flow at its programmed value.

D-15

Paragraph D.5 of this Appendix describes the procedures for activating and operating the power/control system based on the system description given. Paragraph D.7 presents results of analytical studies that predict system performance, however, as noted earlier, further development of the system is necessary before actual performance to the design requirements can be assured. Control valve and other system hardware should be procured, tested and experimental results used to refine the computer analysis. Further analytical studies could then be directed toward determining actual performance characteristics, system optimization, and final sizing of hardware.

D.3   THE CARRIAGE AND GANTRY STRUCTURE

The gantry, shown in Figure D-6, is a mobile structural bridge which spans the soil test beds and provides a sturdy track and sliding carriage to support and guide the strut and footpad during test operations. A 31-foot long structure is required to accommodate a 24-foot soil test bed which allows 21-foot maximum transit for the footpad.

Each of the two main side frames of the gantry is made up of three longitudinal steel beams. The upper and middle elements have an angle cross section and are 3-1/2 inches wide by 5 inches deep while the lower element has a channel cross section and is 3 inches wide by 12 inches deep to insure a rigid support for the guide rail. The rail consists of a 31-foot long, 5-inch diameter seamless steel tube bolted through "T" section stand-offs to the channel inner surface. A system of vertical and diagonal three-inch steel angles complete the truss.

The side frames are spaced 36 inches apart and are joined by a horizontal truss system of three-inch angles at the middle channel to insure lateral stiffness. The top channels are connected by a series of two-inch diameter pipes incorporating welded one-inch diameter threaded studs projecting from either end. Double nuts on the studs permit the introduction of sufficient deflection into the side trusses to establish a 27-inch mean center-line spacing between the guide rails. This verniering capability during fabrication will enable rail alignment to insure free passage for the carriage.
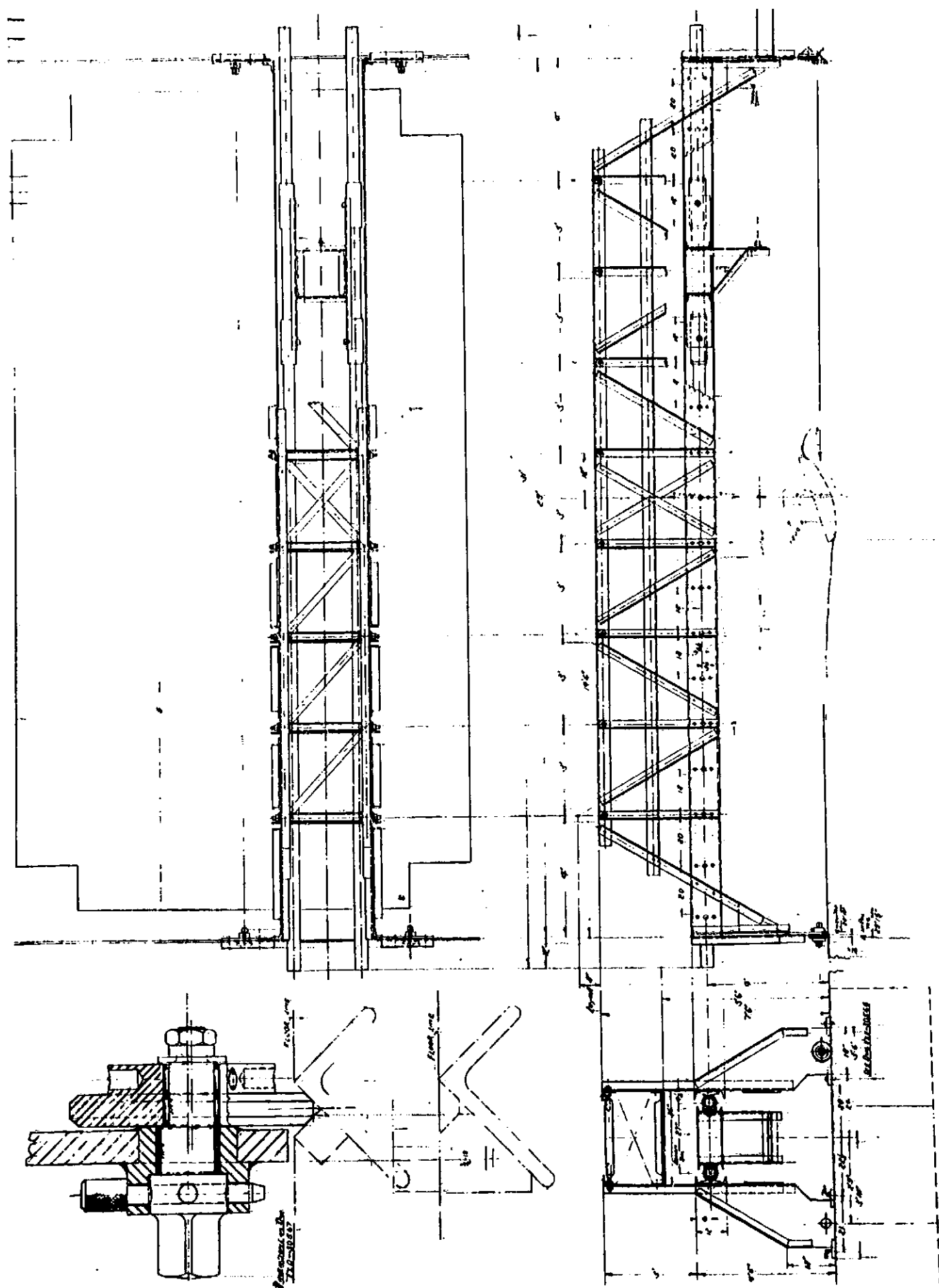
Figure D-6. Gantry Structure

The carriage is a rectangular five-foot long frame of welded 2-3/4- by 10-inch steel channels. Each corner is carried on a spring-loaded, elastomeric-isolated, tubular-bronze slide pivoted, for self-alignment, on a 1-1/2-inch diameter pin. The slides encircle a 300° arc of the guide rail circumference and incorporate appropriate lubricant grooves and wipers. (Refer to Figures D-7 and D-8.)

A rectangular 16- by 18-inch opening through the center of the carriage furnishes facilities for securing the upper end of the strut and allows space for instrumentation cables and air hoses. A substructure below the carriage provides a yoke for the power piston drawbar coupling and a secondary strut attachment.

The ends of the gantry bridge are supported on a pair of angle-reinforced seven-foot, eight-inch wide bipods fabricated from 1/2-inch structural plate. A normally retracted eight-inch diameter wheel is located near each corner. Each wheel is equipped with needle bearings and is mounted on an eccentric shaft. The shaft itself is mounted on needle bearings through a welded boss on the end plate.

During normal test operations, with the wheels retracted, the gantry structure is anchored to the test facility floor by bolts through plates welded adjacent to the wheels. Mobility of the structure can be achieved, when shifting test sites, by removing the hold-down bolts and rotating the shafts through 180°. The 1/8-inch eccentricity in the shafts brings the wheels in contact with a grooved track embedded in the test facility floor and elevates the assembly clear of floor contact. A 1-1/2-inch square driver on the end of the shaft is provided for wrenching rotation and a 5/8-inch diameter knurled pin, dropped into a set of indexing holes, serves as an anti-rotational lock.

Since a full-scale facility was not constructed as part of this program, no attempt has been made during the design study to finalize all those details normally common to actual equipment fabrication and installation.
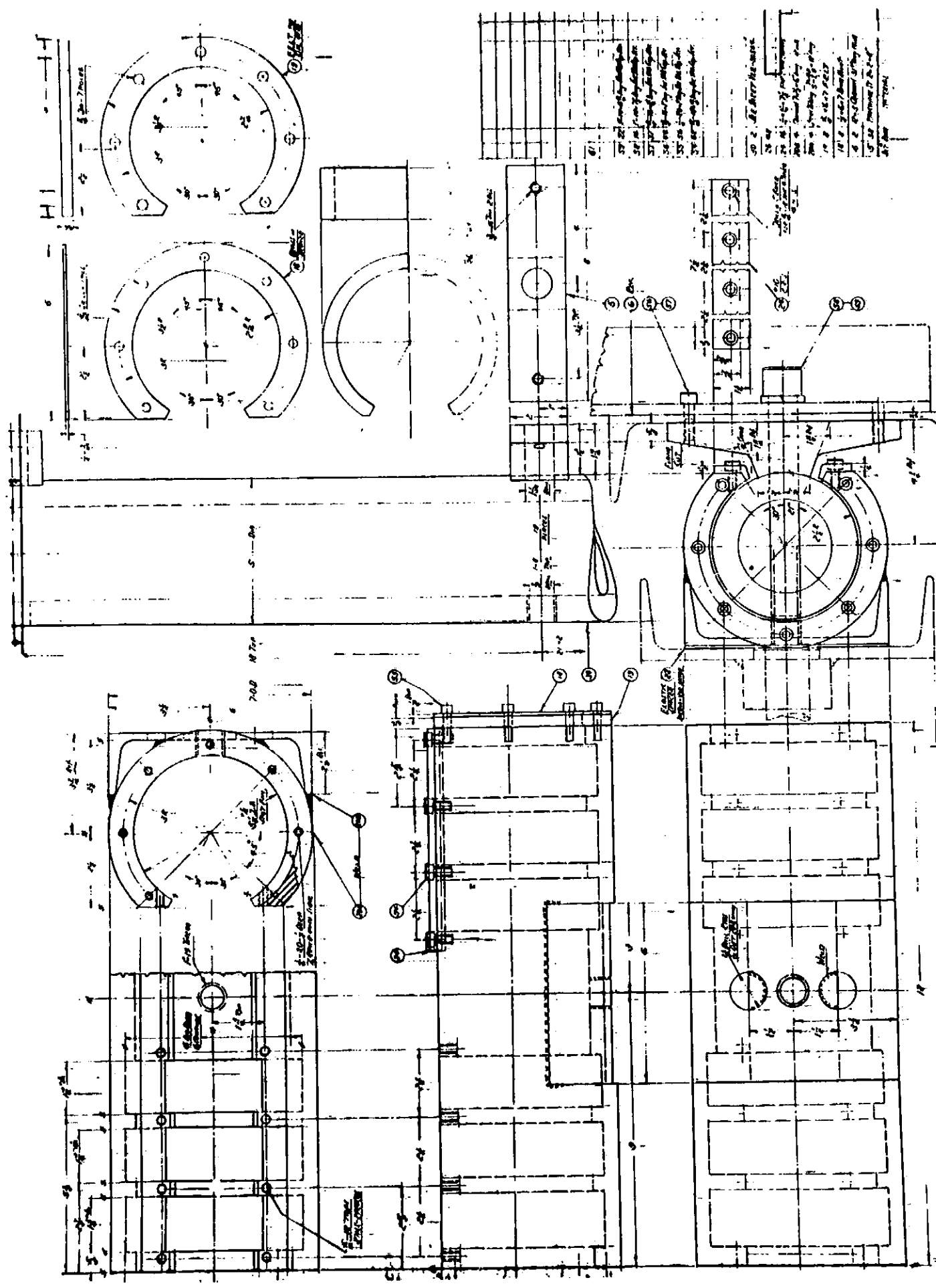
Figure D-7. Gantry Carriage Details
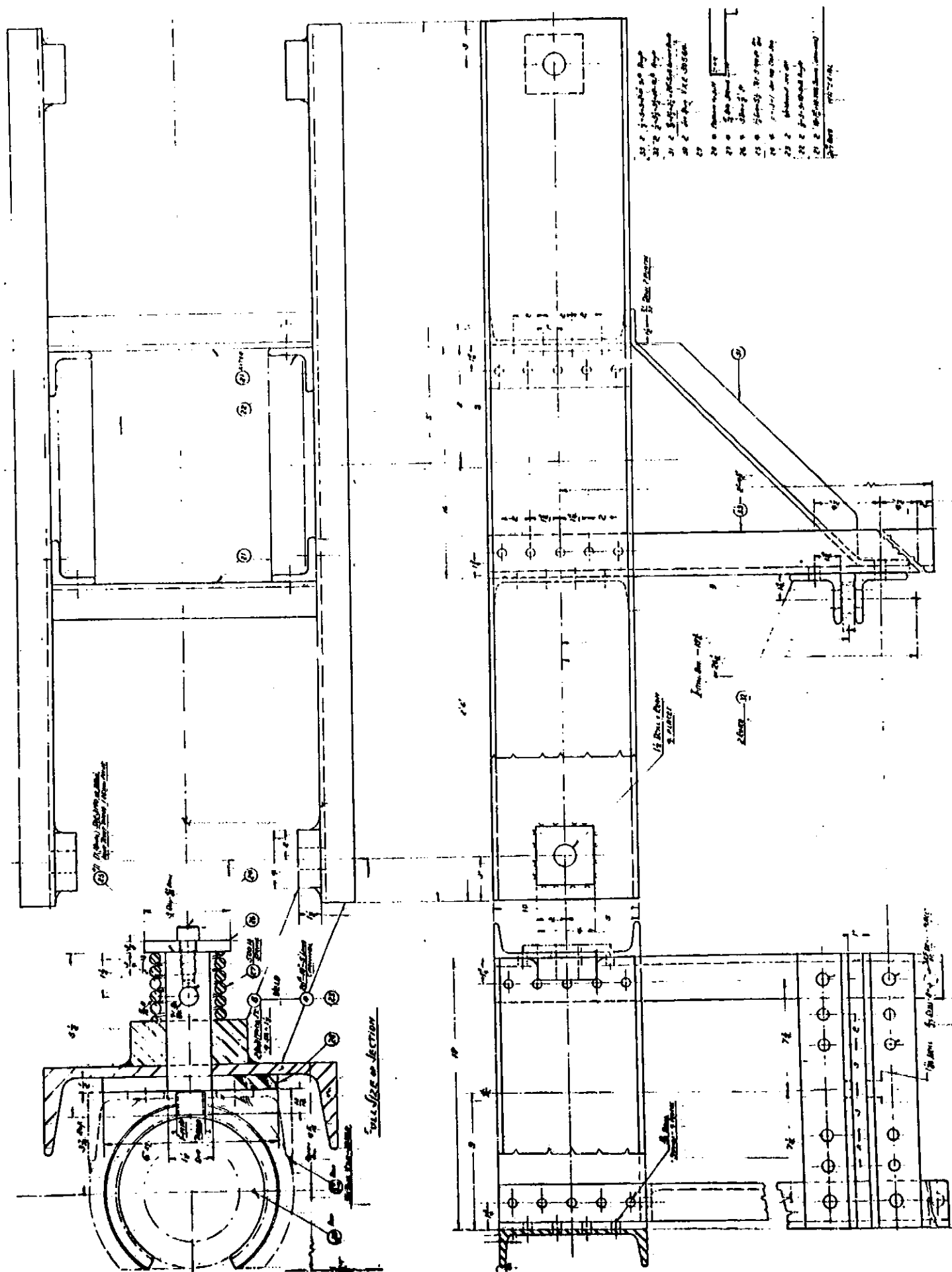
Figure D-8. Gantry Carriage

Those areas which would require further definition prior to fabrication include:

Actual requirements and locations for limit and/or safety switches mounted on the gantry and triggered by carriage/strut location.

Cable reels or cable traveller rings for instrument wiring leads.

Strut/carriage interface and brackets.

Strut/footpad retraction mechanism.

Flexible pneumatic connections from the gantry to the strut or carriage-mounted pressure tanks.

Provision for either electrical or lanyard "firing" of the strut/footpad release.

D.4   THE INSTRUMENTED STRUT AND FOOTPAD

Figure D-9 illustrates the full-scale instrumented strut and footpad assembly, suspended from the carriage. The fully-extended length of the assembly is about 88 inches.

The support strut is basically a pneumatically loaded piston mounted rigidly within the gantry carriage and terminates at the lower end with an instrumented load cell and clevis. A similar clevis on the upper surface of the footpad together with a pair of large diameter intersecting pins forming a cross, constitutes a rugged universal joint for the footpad attachment.

The strut components consist of a pair of telescoping tubular elements, the outer (about ten inches in diameter) serving as a support cylinder while the inner (about eight inches in diameter) acts as a piston. The cylinder is capped at the upper end and provides a tube/adapter fitting for air pressurization. The footpad loading schedule is established by the degree of cylinder pressurization during tests (refer to Figure D-10).
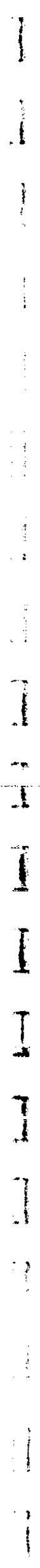
Figure D-9. Full-scale Strut and Footpad Assembly

Figure D-10. Instrumented Strut Details

Both the upper end of the piston and the gland end of the cylinder are fitted with leaded bronze bushing rings to minimize friction and wear when the piston is extended. An "O"-ring-backed Teflon seal within the cylinder gland prevents air leakage. The cylinder gland also incorporates a felt wiper to protect the seal from mineral debris during normal tests. Provision has been made so that drag tests may be run with the cylinder manually locked rather than pneumatically loaded. This may be accomplished by replacing the felt wiper ring with a set of four tapered sectors or collets which, when pulled snug with a box wrench, wedge between the tapered inner diameter of the cylinder gland ring and the outer diameter of the piston and prevent piston movement. The rings can be easily unlocked by backing off the clamping bolts and then tightening a set of extractor screws which withdraw the sectors from the taper of the gland ring. The piston can be locked at any height within its stroke range.

Total stroke of the strut has been optimized at 30 inches. This provides for a maximum footpad-soil penetration of 24 inches under either pneumatic loading (for constant load) or manually locked (for constant penetration) test conditions.

The piston and cylinder are linked by a pair of hinged torque arms which prevent relative rotation between the strut piston and the cylinder. This, coupled with the design of the footpad universal joint, prevents footpad yaw and assures instrumentation orientation. The torque arms limit the maximum piston extension and the common hinge joint provides a convenient location for mounting a rotary potentiometer to sense strut length or depth of footpad penetration.

A mechanism on the outer cylinder wall incorporates a toggle latch which locks the piston in the "cocked" position (refer to Figure D-11). With the trigger lever in the safety position, the latch cannot disengage to release or "fire" the strut. During drag tests, the trigger will be fired by a trailing lanyard after a specified distance of footpad-carriage-travel across the soil test pit. Firing is accomplished by raising the trigger lever, to disengage the positive lock, then, by further movement, to cam the latch over the toggle dead center. Once over dead center, the latch swings violently free and comes to rest on the inner surface of the lower torque arm.
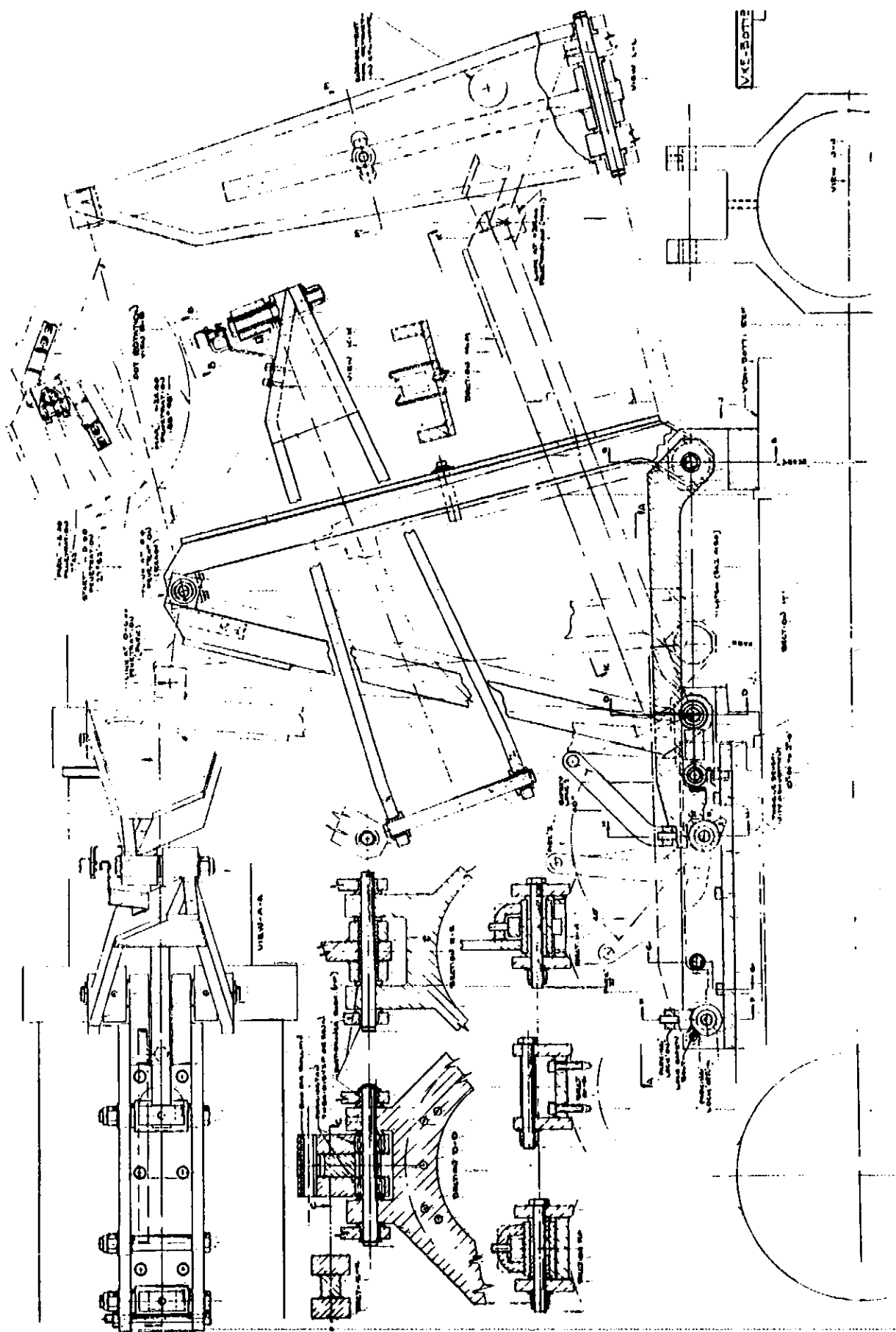
Figure D-11. Strut Torque Link and Release

A second location for the latch provides a "parking" position. In this state the footpad is raised six inches off the soil bed or partitions, and the latch is engaged over a solid, nontripping pin. A pivoted retaining ring drops over the latch end to prevent disengagement with the pin. Provision is made to lock the retainer with either a bolt or a padlock to prevent any but intentional release.

The footpad attachment clevis extends from a cylindrical sleeve that forms the inner element of the three-axis instrumented load cell. The load cell is designed to measure vertical loads and both drag and lateral horizontal loads acting on the footpad. Except for physical size of its components, the basic design of this unit and the load sensing principles used are identical to those developed for the subscale drag test equipment.

The footpad used for full-scale drag tests, shown in Figure D-12, is identical to the LM footpad in physical diameter, height, contour radii and inside periphery, but it differs radically in construction due to the rigorous and recurrent service schedule to which it must be subjected.

The footpad is an epoxy/glass fiber composite, generated over a disposable form, cured, and then machined to precise contour. This method of construction is simplified by simultaneously forming two identical footpads, as indicated in Figure D-12, and then separating them at the intersecting plane. The mounting clevis is actually embedded into the structure during fabrication. A spun-aluminum skin is bonded over the lower surface to provide frictional characteristics similar to those of the actual LM footpad.

The footpad mounting clevis attaches to the mating load cell clevis through a rotating cross-pin arrangement that forms a sturdy nonyawing universal joint. Mechanical stops are machined into the clevis and U-joint to restrict footpad pitch motion to ±25°, and footpad roll motion to ±17-1/2° to simulate the motion restraints of the actual LM footpad.*

___

*(The actual LM footpad is a freely rotating structure mounted on a ball joint and capable of 25° roll and pitch. Instrumentation and durability requirements for a test device dictated the nonyawing universal joint concept and reduced roll travel. An identical footpad has survived approximately 20 full-scale impact cycles without failure or measurable deterioration.)

D-26

Figure D-12. Simulated LM Footpad

Pitch and/or roll attitude of the footpad during test is measured by two rotary potentiometers located at 90° to each other on one end of each of the U-joint cross-pins. The cross-pins are aligned in the drag and lateral axis of the system such that each potentiometer measures footpad motion in only one plane.

During tests a heavy plastic-boot would protect the U-joint and all instrumentation components from abrasion and impingement of dust and soil particles. With the boot installed the lower end of the strut/footpad assembly simulates the shape and silhouette of the full-scale LM footpad/strut assembly.

D.5   OPERATION OF THE FULL SCALE DRAG TEST FACILITY

The purpose of this section is to describe the procedures necessary for proper and safe operation of the full-scale drag test equipment. Since test system operation and control is effected by the hydraulic power/control unit, this equipment is covered in detail with attention directed to both the preparation and activation phases of its operation. In addition, comments pertinent to the general setup and arrangement of the mechanical equipment are given. Although not procedures, these are noted as precautions or guides to help insure that test runs are both nonhazardous and productive of meaningful data.

The soil test bed and associated handling equipment does not fall within the scope of this section, however, its proper preparation and maintenance is essential to any useful test program. This includes the correct selection of soil material and use of proper bed preparation procedures followed by appropriate soil control tests. Soil material physical properties and, especially, health hazards must be known so that adequate safety measures for handling and dust control can be implemented.

The footpad should be checked for freedom of motion and U-joint lubrication, and for instrumentation read-out and calibration. Any loose soil from previous tests should be removed and the dust protector (plastic boot) inspected for tears and tightness. The strut should stroke smoothly and its inflation pressure be verified for footpad constant load test requirements. If the strut length is locked for constant penetration tests, the locking features should be checked for tightness and proper adjustment. The strut trip latch

D-28

should be examined for "cocked" readiness and the tripping lanyard set to provide the required drop-point. All instrumentation circuitry should be carefully checked and loose wiring cables secured to prevent damage.

The gantry bridge must be properly positioned over the soil bed, aligned with the hydraulic actuator, and securely anchored to its attachment points. The tubular rails must be wiped clean and lubricated immediately prior to each test run. Both the strut and drawbar attachments to the carriage and the drawbar to power piston coupling should be inspected. The footpad, strut, carriage, and gantry rails must be free of any loose tools or other objects that could become lethal missiles during the test run.

Prior to first-time usage of the hydraulic power/control unit there should be positive assurance that all components have been carefully and securely assembled; that the system has been thoroughly purged of all foreign materials, chips, grease, moisture, etc. and completely oil flushed; and that all gages, seals, controls, etc., have been tested and certified.

The hydraulic unit is powered by the stored energy of high pressure nitrogen introduced above and acting upon the surface of the oil in the pressure storage tank which, in turn, supplies the force to drive the actuator piston. A separate electrically-driven oil pump is used for oil transfer through the system. Shop air pressure and nitrogen pressure are employed for the operation of certain valves and regulators.

A specific test schedule is controlled by the metering orifice (located below the control valve assembly) and by the air pressure setting on the constant force pneumatic piston in the control valve assembly. The air pressure is regulated from the control panel immediately prior to test. However, the metering orifice can be installed or changed only when the system is unpressurized, since disassembly is required. Accordingly, this operation should be performed prior to filling, bleeding, and pressurizing the system.

The hydraulic power/control unit cannot be activated or "fired" unless the following safety precautions are satisfied. The limit switch or switches on the gantry carriage must be in closed position, a keylock switch at the control panel must be manually unlocked and activated, and the "firing" button must be manually tripped.

The following procedures cover the hydraulic system charging, filling, bleeding, pressurizing, activation, and shutdown operations (refer to schematic diagram Figure D-4).

D.5.1 Charging the System with Hydraulic Oil

Close all valves and regulators. Insure that all electrical circuits are "off" and that the keylock switch on the control panel is locked and the key removed.

Transfer approximately fifty (50) gallons of MIL-H-5606 hydraulic oil into the supply and discharge drum (1).

Open main valve (2), fill and drain valve (3), tank bleed valve (4) and isolation valve (5).

Open the control valve (6) by turning on the shop air pressure and adjusting the pressure regulator (7) to apply approximately five psi to the valve actuator.

Energize the hydraulic pump (8) and transfer approximately 45 gallons of oil (six cubic feet) into the pressure storage tank (9) and connecting lines. The oil volume transferred may be readily determined by observing a drop of 26-27 inches in the supply tank level. There will be a tendency for the power piston to creep toward the extended position if charging is initiated with the piston retracted.

Add an additional 20 gallons (3.7 cubic feet) of oil to the supply and discharge drum (1). This can be measured by a 12-13-inch level rise at the drum.

Shut off the hydraulic pump (8), close main valve (2) and shut off air pressure regulator (7) to relieve the control valve constant force piston and close the control valve (6).

D.5.2   Filling the Power Cylinder

Open the power cylinder low-pressure bleed valve (10) and high-pressure bleed valve (1).
Energize the solenoid valve (12) and adjust the nitrogen pressure regulator (13) to open
the programmed (Annin) valve (14). The valve position can be determined visually.

Start and run hydraulic pump (8). When oil is observed to discharge into the drum (1)
de-energize the solenoid to close the programmed valve (14).

Continue running the hydraulic pump until the piston travels to the fully extended position.
Shut off the pump and crack isolation valve (5) momentarily to relieve the pressure buildup
in the hydraulic accumulator (15).

Close all valves and shut down the nitrogen regulator (13).

D.5.3   *Bleeding the System

The entire system must be "bled" to remove all trapped air or gas (except in the pres-
sure storage tank (9) and the accumulator (15)) which would cause "softness" and erratic
operation.

Open the main valve (2), fill and drain valve (3), high-pressure bleed valve (11), isolation
valve (5) and low-pressure bleed valve (10).

Adjust air pressure regulator (7) to apply approximately five psi air pressure signal to
open the control valve (6).

Slowly open the tank pressurizing valve (20) until nitrogen pressure gage (16) indicates
approximately 50 psig applied to the surface of the oil in the pressure storage tank (9).
The flow of oil from the storage tank will flush any air trapped in the system into the
supply and discharge drum (1).

---

*Note: This operation should be performed prior to each test run until sufficient experi-
ence has been gained to warrant reducing its frequency.

D-31

As soon as the intermittent oil discharge into the drum becomes a steady flow, close the low-pressure bleed valve (10), and then all remaining valves and regulators.

D.5.4   Pressurization

Open the tank pressurization valve (20) to charge the system with 15 cubic feet of nitrogen at 2000 psi. Tank pressure is indicated on nitrogen pressure gage (16). Tank bleed valve (4) is provided to bleed down or completely release tank pressure when required. A separate normally closed solenoid valve (17) is mounted on top the pressure-storage tank to provide instant depressurization on demand.

Caution! Once the system is pressurized extreme care must be exercised, since the forces generated within the equipment and by the piston are very high.

D.5.5   The Drag Test "Run"

After the hydraulic system has been charged, the power piston positioned, and the system "bled" and pressurized, the hydraulic power/control unit is functionally ready for use.

At this time, final checks should be made to insure that all of the mechanical equipment and instrumentation is in order and ready for test. Immediately prior to test, any area safety regulations and warning devices would be activated.

The test run is accomplished as follows:

Open the main valve (2).

Adjust the air pressure regulator (7) to the setting required for the control valve constant force piston (6). The correct pressure setting is obtained from the system calibration sheets.

Check and record all valve positions and gage pressures as required and insure that electrical circuits are energized. Determine that all data recording devices are ready for activation.

D-32

Unlock the key-locked safety switch.

Activate data recording systems and immediately depress the "firing" button. The complete test run-from acceleration through deceleration is then controlled by the hydraulic system. After the carriage and footpad have decelerated to a full stop, relock the safety switch.

Retraction of the strut and footpad will probably not be performed before a thorough visual or photographic examination of the test bed has been made.

Release the strut loading pneumatic pressure, and raise the strut and footpad clear of the soil test bed and lock in the "parked" position. Uncouple the power-piston drawbar and return the carriage to its starting position on the gantry. This should be done manually to avoid the possibility of buckling the drawbar. To avoid interference with test bed renovation, the power cylinder should remain retracted.

D.5.6 System Depressurization

In the interest of safety, the equipment should not remain pressurized for extended periods when not scheduled for immediate re-use.

Open tank bleed valve (4) to permit the gradual escape of nitrogen until the nitrogen gage (16) drops to 200 psi. Close the bleed valve.

In an emergency the nitrogen pressure can be instantly "dumped" by firing the normally closed solenoid valve (17).

D.5.7 Draining the System

Normally, the hydraulic system would be drained only for major maintenance operations. Change of the orifice requires only that the main valve (2) and bleed valves (10) and (11) be closed in addition to activating the solenoid valve (12) to open the programmed (Annin) valve (14). The system must be "re-bled" after orifice change.

Complete drainage can be accomplished by opening the system bleed valve (19) and the fill and drain valve (3). The oil will discharge into the supply and discharge drum (1). The auxilliary discharge drum must be employed to receive the entire charge of oil. When the system is completely drained (i.e., no further oil flow into the discharge drum is observed), close the bleed valve and fill and drain valve.

- - - - - --- -

The preceding operational procedures are based on currently conceived hardware and would be subject to expansion and possible change to accommodate variations dictated by actual procurement items and unique facility installation. However, as given, they would form the basis for a detailed "Operational Guide" or "Manual" for the system as it is finally evolved.

D.6 LISTING OF DESIGN DRAWINGS

Listed below are the engineering design and/or manufacturing drawings of major components that were prepared during this design study. Some of these are reproduced in reduced size in appropriate sections of this Appendix. Although these drawings are not included as a direct attachment to this report, copies of each will be furnished to NASA-MSC in a separate package.

Item	Bendix Drawing	Applicable Figure	Drawing Size (in.)
Complete System			
Drag Test Facility, Perspective View	*VXE-30828	D-1	34 x 44
Drag Test Facility, 1/20-Scale Layout	*VXE-30826	D-2	34 x 44
Hydraulic Power Unit			
Schematic Diagram	*VXD-30827	D-4	22 x 34
Semischematic, Control Valve Assy.	*VXD-30830	D-5	22 x 34
Layout, Power/Control Assy.	VXR-30594-1		34 x 76
	VXR-30594-2		34 x 66
Control Valve	VXR-30588		34 x 132
Hydraulic Cylinder Adapter	VXD-30589		22 x 34
Orifice Plate, Control Valve	VXC-30590		17 x 22
Piston, Control Valve	VXC-30591		17 x 22
Sleeve, Control Valve	VXC-30592		17 x 22
Platform	VXR-30593		34 x 84

Item	Bendix Drawing	Applicable Figure	Drawing Size (In)
Gantry Structure			
Drag Test Equipment, List of Material	VXE-30564		34 x 44
Gantry Structure, Bridge	*VXE-30565	D-6	34 x 44
Gantry Detail, End Plates	VXE-30566		34 x 44
Lift Rolls	VXD-30567		22 x 34
Carriage Details and Bearings	*VXE-30568	D-7	34 x 44
Carriage Assembly	*VXE-30569	D-8	34 x 44
Strut and Footpad			
Strut, Instrumented	*VXE-30771	D-10	34 x 44
Torque Link and Release Mechanism	*VXE-30773	D-11	34 x 44
Installation, Strut	*VXC-30775	D-9	17 x 22
Footpad, Glass Fiber	*VXE-3064?	D-12	34 x 44
Clevis and Plug	VXD-30643		22 x 34

*Drawings reproduced in the text.

D.7   ANALYTICAL PREDICTIONS OF SYSTEM PERFORMANCE

Results of analytical studies that predict performance of the full-scale drag test facility are summarized in this section. The studies were conducted as part of the power/control unit design effort to investigate control system dynamics and to optimize the hardware design.

The analysis was carried as far as practical during the control system design phase and would necessarily continue through a development phase when experimental data from actual control system hardware was made available. However, the techniques used were based on previous experience with related types of systems, and the results shown here are believed to reflect the performance that can be expected from the full-scale system.

The theoretical results indicate that, except for one extreme situation, essentially full compliance with the specified performance requirements (see paragraph D.1) can be expected. The exception involves a worst-on-worst condition of carriage velocity (15 feet/second), maximum drag load (7000 pounds), and peak break-away load fluctuation

(+10 percent or +700 pounds), in which the carriage reaches a peak velocity of 0.139 foot/second greater than that obtained with no load fluctuation. However, under less stringent condition (i.e., slightly slower speed, or smaller constant load, or smaller load fluctuations), the specified maximum velocity deviation of ±0.1 foot/second is expected to be met.

Table D-1 presents the parametric design specifications for the hydraulic power/control system. The table lists nominal criteria (plus tolerances, in several cases) for 28 parameters which were determined to be most influential in their effects on overall system performance. These parameters were optimized to the values shown via earlier detailed studies.

Figure D-13 indicates the programmed (Annin) valve design requirements (item 27 of Table D-1) in terms of required flow performance as a function of time. From valve supplier specifications a size two-inch valve with 900 to 1500 pound ASA body rating appears to be adequate. Although opening and closing characteristics of this unit are not available, these would be experimentally determined and then optimized during the development phase. Figure D-13 indicates the acceptable range for opening and closing flow performance; the analysis assumed a linear opening and closing in 0.2 second (along the upper and lower bounds, respectively, of Figure D-13).

Figure D-14 illustrates the throttling orifice design requirements, all dimensions being nominal.

Figure D-15 presents control valve calibration data from which the metering orifice selection and constant - force pneumatic-piston air pressure setting is determined. The calibration predictions are based on nominal velocity and nominal load requirements (i.e., no tolerance included).

Figure D-16 indicates the expected steady-state performance variation with constant load using the calibration data from Figure D-15. The performance variations shown are over the entire range of specified loads, i.e., zero to 7000 pounds, and are considered 3σ variations.

D-36

TABLE D-1
PARAMETRIC DESIGN SPECIFICATIONS

Item No.	FORTRAN Nomenclature	Item Description	Design Requirement	Units
1	ACP	Cross-sectional area of control valve piston.	2.074	in²
2	ACR	Cross-sectional area of control valve piston rod.	0.02776	in²
3	ACVL	Orifice area equivalent of control valve piston leakage.	0.005±0.002	in²
4	ACYL	Cross-sectional area of main cylinder (corresponds to inside diameter).	19.635	in²
5	AFP	Cross-sectional area of main piston.	19.635	in²
6	AFR	Cross-sectional area of main piston rod.	4.909	in²
7	AMO	Cross-sectional area of metering orifice.	Four metering orifice sizes must be available and readily interchangeable between tests. The four orifice sizes are: 0.302 ± 0.010 0.453 ± 0.010 0.807 ± 0.010 1.210 ± 0.010	in²
8	APIPCL	Cross-sectional area of pipe housing control valve piston (corresponds to inside diameter).	2.0778	in²
9	APIPMO	Cross-sectional area of pipe housing metering orifice (corresponds to inside diameter).	12.4	in²

TABLE D-1
PARAMETRIC DESIGN SPECIFICATIONS (CONT.)

Item No.	FORTRAN Nomenclature	Item Description	Design Requirement	Units
10	APIPTO	Total cross-sectional area of inlet to all eight ports of the throttling orifice. Actually, the surface area of a cylindrically shaped mathematical surface surrounding that part of the throttling orifice exposed to the tank supply.	5.93	in^2
11	CCVL = CCCVL*CVCVL	Discharge coefficient for control valve piston leakage flow. This is the product of the coefficient of contraction (CCCVL) and the coefficient of velocity (CVCVL).	0.6	dimensionless
12	CMO = CCMO*CVMC	Discharge coefficient for metering orifice flow.	0.95	dimensionless
13	CTO = CCTO*CVTO	Discharge coefficient for throttling orifice flow.	0.6	dimensionless
14	FB	Constant force applied to control valve piston by regulated pneumatic pressure source.	$100 \leq FB \leq 480$ All forces must be available within the above range. A given force must be maintained within a tolerance of ±10 during each test.	lbs.
15	KFO*AFO	Ratio of the mass flow rate through the feedback orifice in lbs./sec. to the square root of the pressure drop across the feedback orifice, where the pressure drop is in psi, i.e.:	0.0645 This feedback orifice flow characteristic should be established and maintained as closely as possible. It should never fall below 0.053,	$\dfrac{in.lb^{1/2}}{sec.}$

Item No.	FORTRAN Nomenclature	Item Description	Design Requirement	Units
15 cont.		$KFO*AFO = \dfrac{QFO}{\sqrt{\Delta P_{FO}}}$	nor exceed 0.073. (A first estimate for the feedback orifice size is 0.022 in.^{2})	
16	PRES	Reservoir pressure.	0	psig
17	PTO	Initial tank pressure (at beginning of each test).	2000 ± 20	psig
18	SPECWT	Specific weight of oil.	0.031 (MIL-H-5606)	lbs./in^3
19	TABS	Absolute temperature of oil, air, and nitrogen.	529.6^{+30}_{-10} (This nominal corresponds to 70° F.)	degrees/Rankine
20	TCPMAX	Maximum travel limit of the control valve piston.	0.63 The zero-reference here is TCPMIN (see Item No. 21). The positive travel of the control valve piston must be mechanically limited at TCPMAX.	in
21	TCPMIN	Minimum travel limit of the control valve piston.	0 The negative travel of the control valve piston must be mechanically limited at TCPMIN. This zero-reference limit must be designed so that it corresponds exactly to the physical condition	in

TABLE D-1
PARAMETRIC DESIGN SPECIFICATIONS (CONT.)

Item No.	FORTRAN Nomenclature	Item Description	Design Requirement	Units
21 cont.			where the leading edges of the eight throttling orifice ports are directly aligned with the front edge of the tank outlet (i.e., ATO is theoretically zero).	
22	VLAIRO	Initial volume of air in accumulator (at beginning of each test).	14 at 2000 psig (This is equivalent to 198 at 0 psig.) The equivalent spring constant of the bladder must be very small over the expected operating range from 10 psig to 2000 psig.	in^3
23	VOLN20	Initial volume of nitrogen in tank.	25920 at 2000 psig (Corresponds to 20 cubic feet supply tank containing five cubic feet of oil, with the remaining volume occupied by nitrogen.)	in^3
24	WEIGHT	Combined weight of main piston, main piston rod, and entire carriage structure and instrumentation pulled during test.	1500	lbs.
25	WTCPCR	Combined weight of control valve piston, control valve piston rod, and all other parts whose motion is governed by differential pressure across control valve piston.	1	lbs.

TABLE D-1

PARAMETRIC DESIGN SPECIFICATIONS (CONC.)

Item No.	FORTRAN Nomenclature	Item Description	Design Requirement	Units
26	XCLOSE	Main (force) piston position at which programmed (Annin) valve must start closing down.	$18^{+0.5}_{-0.2}$	ft.
27	–	Programmed (Annin) valve.	See Figure D-13	–
28	–	Throttling orifice	See Figure D-14	–

Note: Tolerances are specified for those parameters which are considered most critical to overall system performance and stability and/or most likely to vary, with the exception of the three discharge coefficients (CCVL, CMO and CTO). These three discharge coefficients must be established in Phase II calibration tests and assessed as part of Phase II analysis effort. The other parameters which have no tolerance allocation in the above table must be established and maintained at the nominal specified value as nearly as possible.

Figure D-13. Programmed (Annin) Valve Performance Requirements

Notes:
1. $t_c\Delta$ = time when Annin valve is completely closed.
2. $QPV\Delta$ = mass flow rate through Annin valve, in. lb./sec.
3. $\Delta P\Delta$ = pressure drop across Annin valve, in psi.
4. Annin valve must be completely closed when time ≤ 0.
5. Annin valve must be completely closed when time ≥ t_c.
6. Indicated performance is required for 10 psi ≤ ΔP ≤ 2000 psi.

D-42

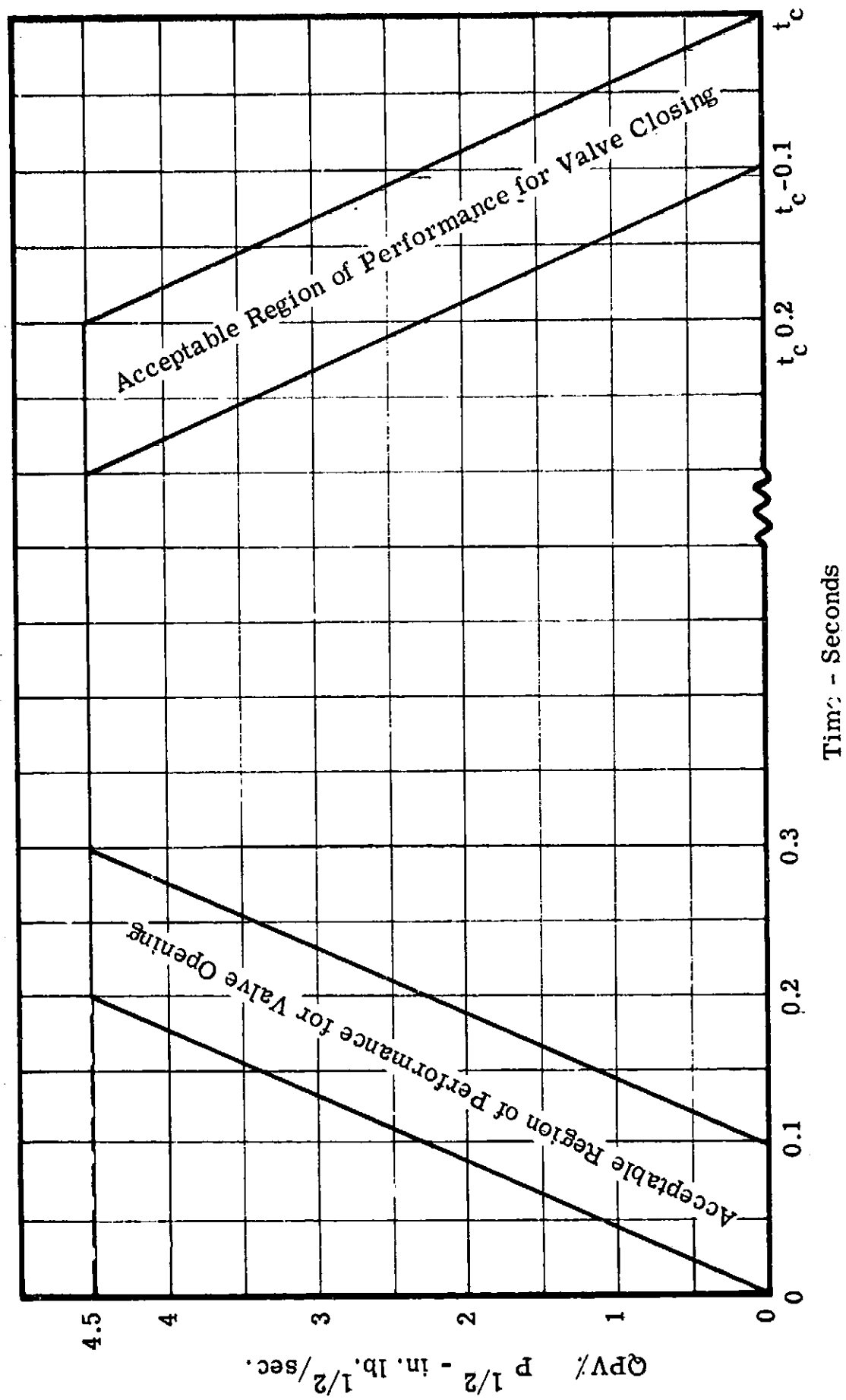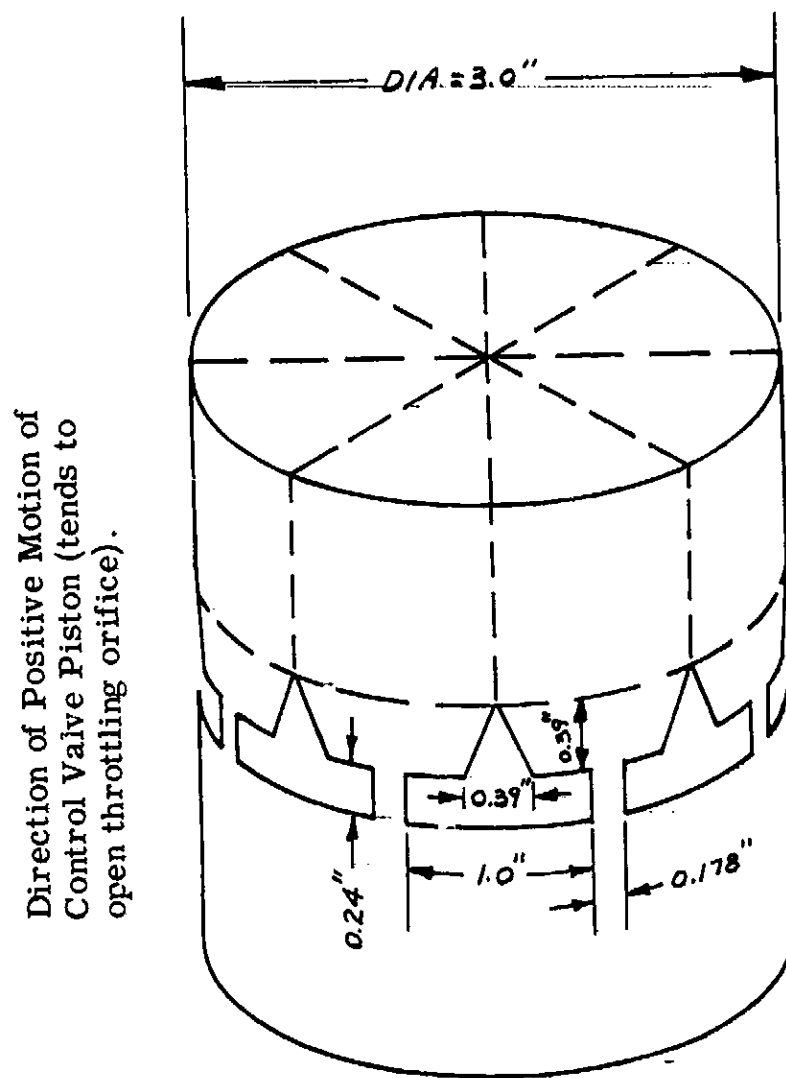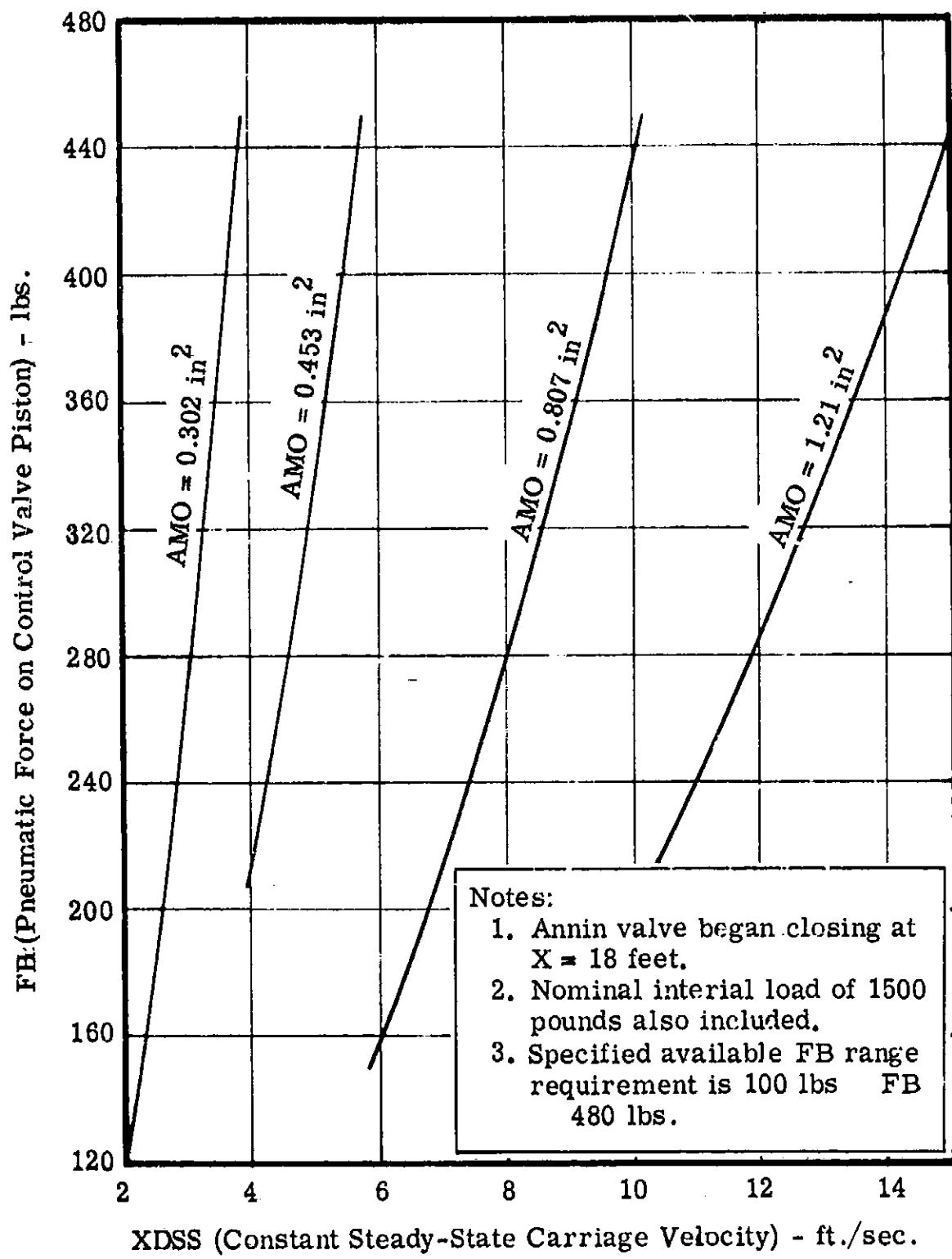Figure D-14. Throttling Orifice Design Requirements
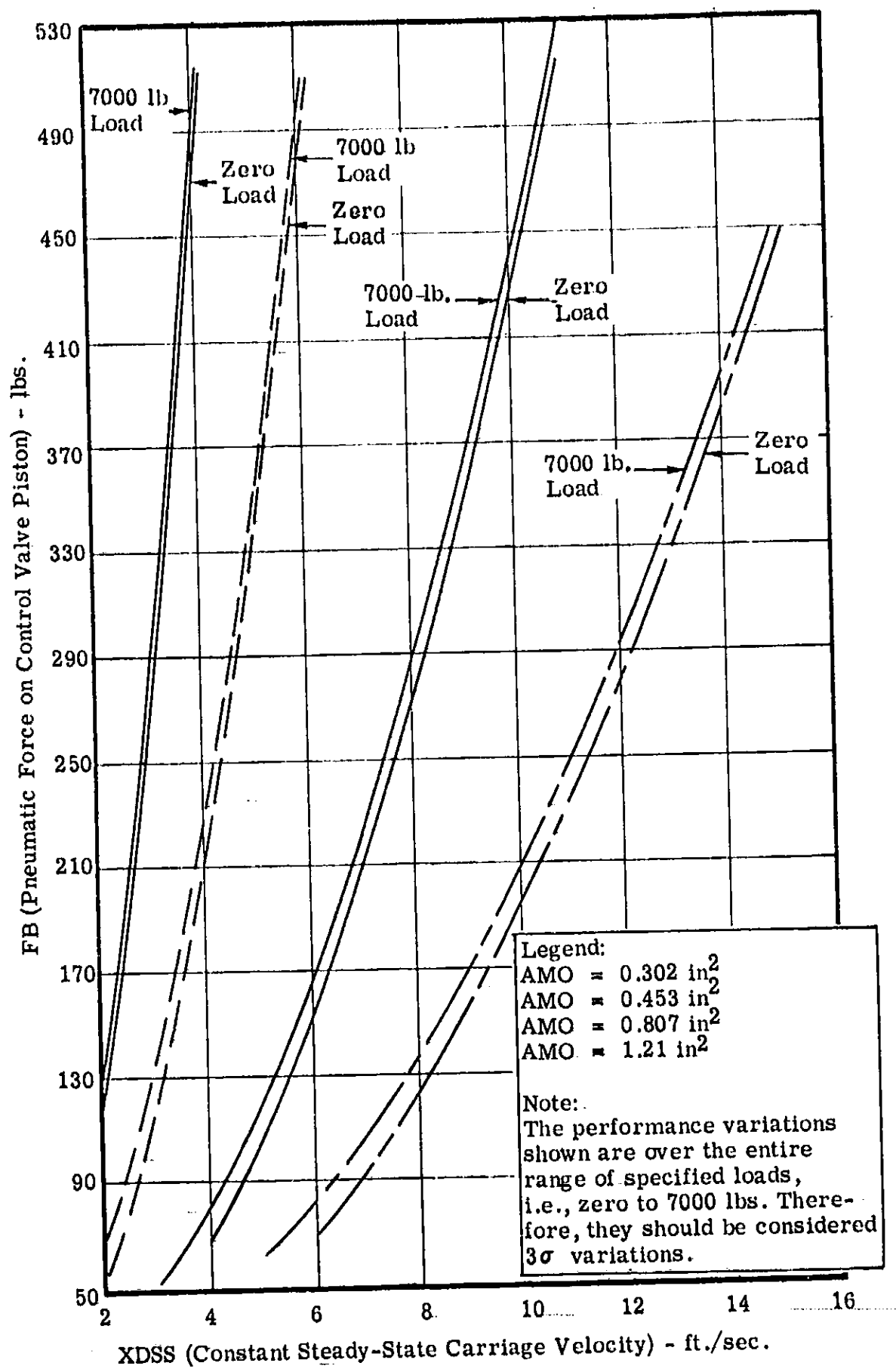
Figure D-15. System Calibration Prediction

Figure D-16. Expected Steady-State Performance Variation With Constant Load

The data presented in Table D-2 was obtained by cross referencing the curves presented in Figures D-15 and D-16. Note that the predicted 3σ variation in steady-state performance (i.e., the actual velocity obtained) with constant load is relatively small.

Figures D-17 and D-18 indicate the expected dynamic response of the nominal system under no load conditions, (i.e., with no soil impeding the motion of the footpad), although a nominal inertial load of 1500-pounds was assumed. All three phases of the test run (acceleration, constant velocity, deceleration) are shown, with Figure D-17 representing a 15-foot/second constant velocity run and Figure D-18 a two-foot/second run. In Figure D-18, the theoretical test run distance was shortened only to reduce computer time.

The next four figures show the predicted dynamic response of the system under conditions that simulate both low and high drag loads with break-away load fluctuations superimposed. The frequency of load fluctuation was assumed to be uniform, beginning just after steady-state velocity was reached and ending with initiation of the deceleration phase. The load pulse period and shape was arbitrarily established to effect fluctuating load buildup to full value as a first order time constant then drop sharply off as shown.

Figures D-19 and D-20 present expected system response at steady-state velocities of 15 and 2 feet/second, respectively, under a small (500 pound) load with +10 percent (or +50 pounds) break-away loads superimposed.

Figures D-21 and D-22 are similar predictions but under maximum load (7000 pound) conditions with the +10 percent (or +700 pound) load fluctuation superimposed.

Figure D-21 is the test condition noted earlier in which the maximum steady-state velocity variation of ±0.1 foot/second is exceeded. This variation is not felt to be of particular significance, since the analysis does indicate that drag system load variations can be effectively accommodated by the control valve.

TABLE D-2

PREDICTED 3σ VARIATION IN STEADY-STATE PERFORMANCE DUE TO SPECIFIED RANGE OF CONSTANT LOAD

XDSS Desired (ft./sec.)	AMO (in^2) from Figure D-15	FB (lbs) from Figure D-15	Prediction of XDSS Obtained (nom. ±3σ Tolerance) (Nominal predicted from Figure D-16. Tolerance due to total specified constant load range, i.e., 0 ≤ load ≤ 7000 lbs.)
2	0.302	125	2 ± 0.05 ft/sec
3	0.302	273	3 ± 0.05 ft/sec
4	0.453	219	4 ± 0.07 ft/sec
5	0.453	338	5 ± 0.05 ft/sec
6	0.807	160	6 ± 0.12 ft/sec
7	0.807	215	7 ± 0.11 ft/sec
8	0.807	279	8 ± 0.1 ft/sec
9	0.807	352	9 ± 0.09 ft/sec
10	0.807	433	10 ± 0.08 ft/sec
11	1.21	242	11 ± 0.17 ft/sec
12	1.21	286	12 ± 0.15 ft/sec
13	1.21	335	13 ± 0.14 ft/sec
14	1.21	388	14 ± 0.11 ft/sec
15	1.21	444	15 ± 0.1 ft/sec

Nomenclature: XDSS $\triangleq$ constant steady-state carriage velocity.

AMO $\triangleq$ metering orifice area.

FB $\triangleq$ pneumatic force on control valve piston
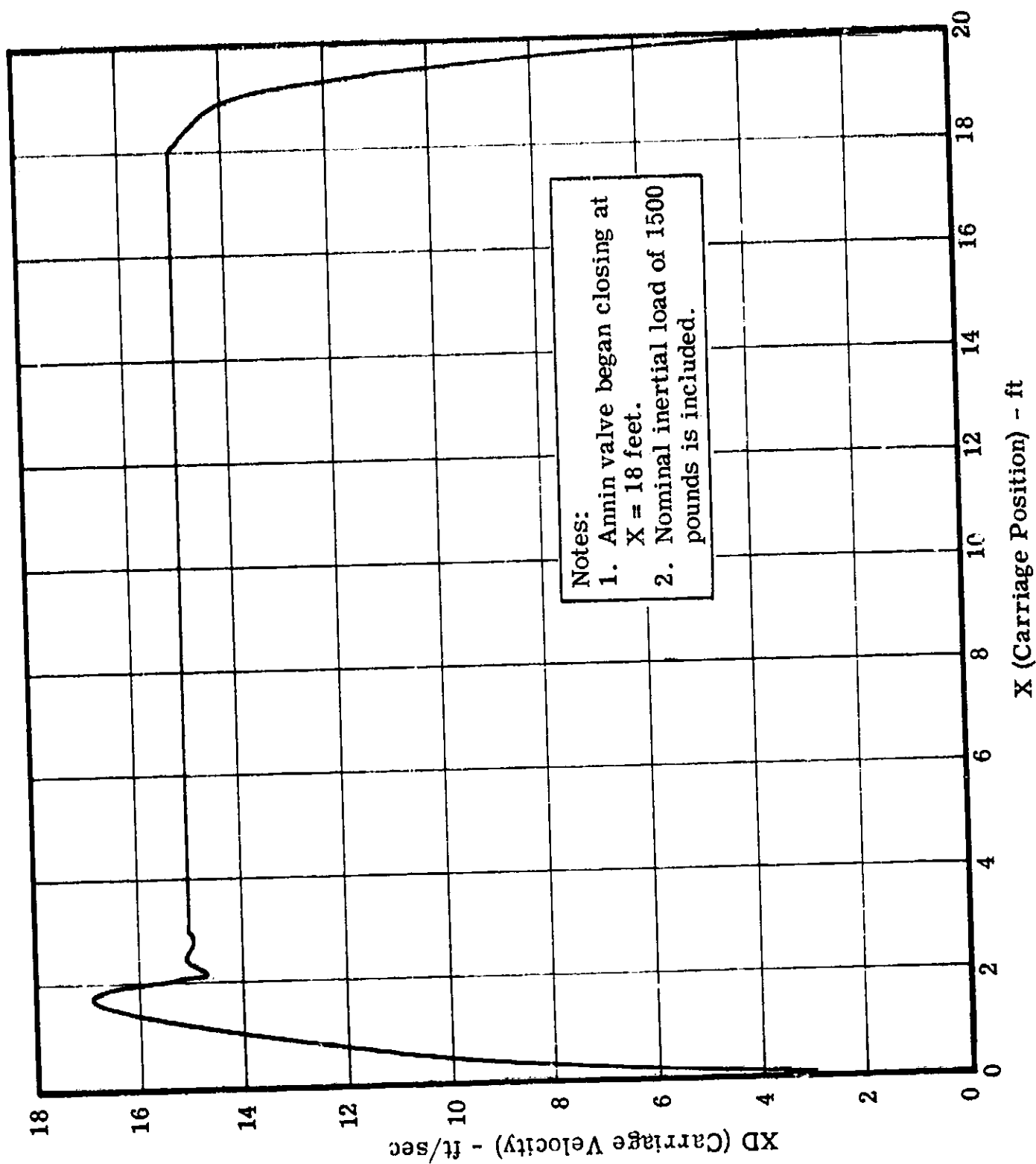
Figure D-17. Expected Dynamic Response of Nominal System Under No-Load (15 ft/sec Constant Velocity)

Notes:
1. Annin valve began closing at X = 18 feet.
2. Nominal inertial load of 1500 pounds is included.

X (Carriage Position) – ft

XD (Carriage Velocity) – ft/sec

Notes:
1. Annin valve began closing at X = 6 feet.
2. Nominal inertial load of 1500 pounds is included

XD (Carriage Velocity) – ft/sec

X (Carriage Position) – ft
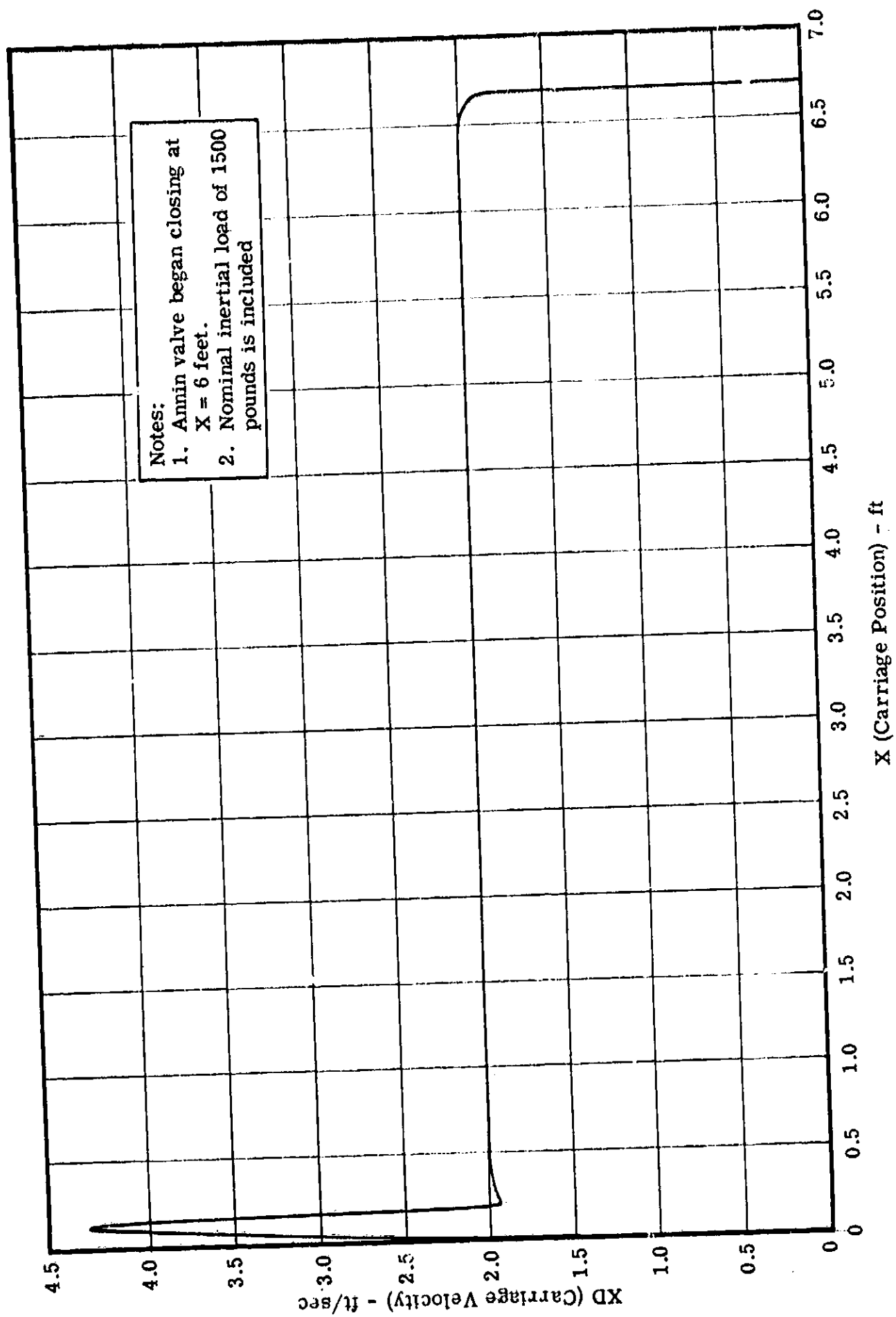
Figure D-18. Expected Dynamic Response of Nominal System Under No-Load (2 ft/sec Constant Velocity)

Figure D-19. Expected Dynamic Response of Nominal System Under +10 Percent Fluctuations of Small (500 Pound) Load (15 ft/sec Constant Velocity)

Notes:
1. Annin valve began closing at X = 18 feet.
2. Nominal inertial load of 1500 pounds also included.
3. Fluctuations in steady-state XD response not visible on this scale.

XD (Carriage Velocity) - ft/sec

X (Carriage Position) - ft

Load - Pounds

X (Carriage Position) - ft

Figure D-20. Expected Dynamic Response of Nominal System Under +10 Percent Fluctuations of Small (500 Pound) Load (2 ft/sec Constant Velocity)

Notes:
1. Annin valve began closing at X = 6 feet.
2. Nominal inertial load of 1500 pounds also included.
3. Fluctuations in steady-state XD response not visible on this scale.

XD (Carriage Velocity) - ft/sec

X (Carriage Position) - ft

Load - Pounds

X (Carriage Position) - ft

Notes:
1. Annin valve began closing at X = 18 feet.
2. Nominal inertial load of 1500 pounds also included.
3. Broken XD scale shows XD fluctuations during steady-state phase.

Figure D-21. Expected Dynamic Response of Nominal System Under +10 Percent Fluctuations of Maximum (7000 Pounds) Load (15 ft/sec Constant Velocity)

Notes:
1. Annin valve began closing at X = 6 feet.
2. Nominal inertial load of 1500 pounds also included.
3. Fluctuations in steady-state XD response not visible on this scale.

X (Carriage Position) - ft

XD (Carriage Velocity) - ft/sec
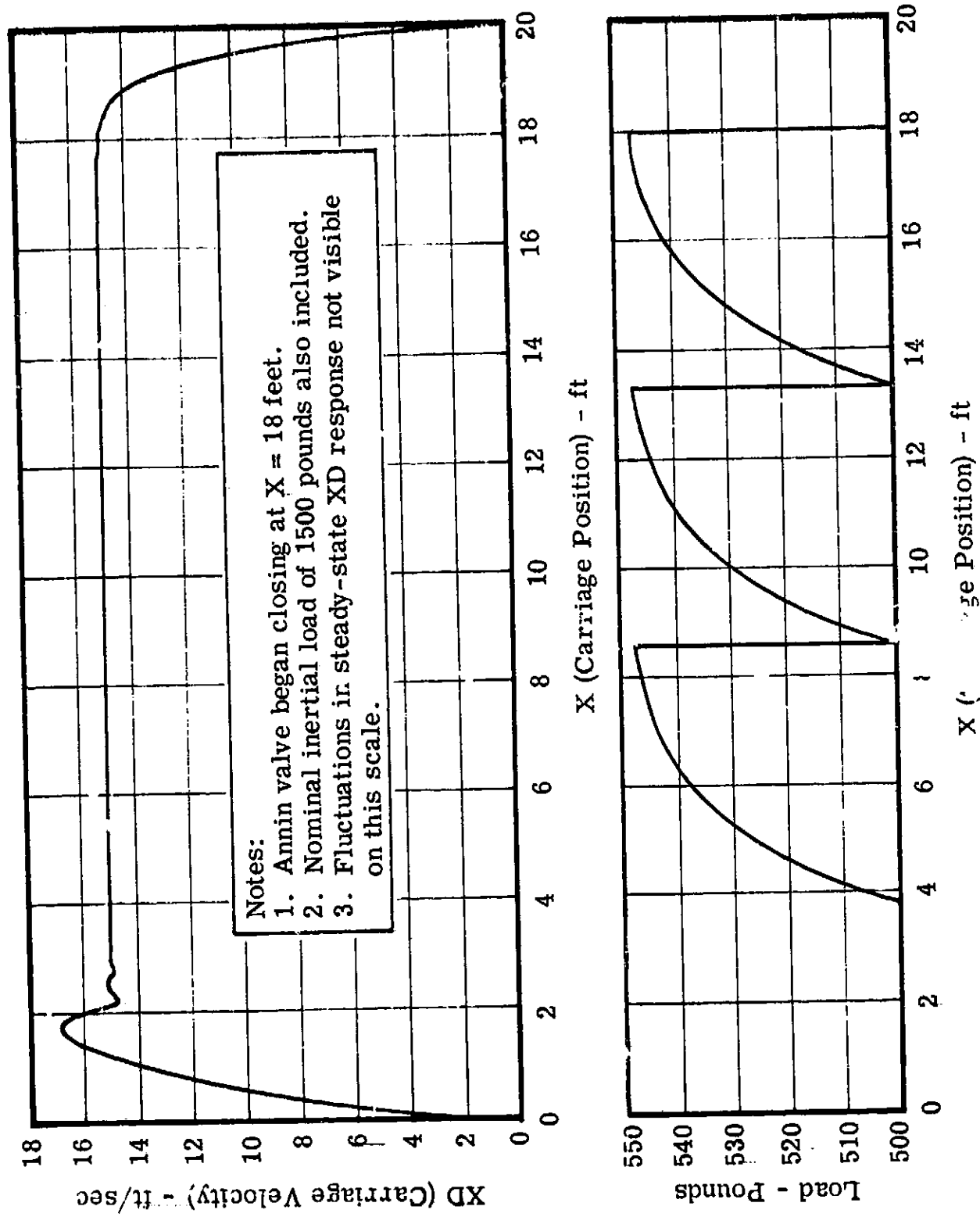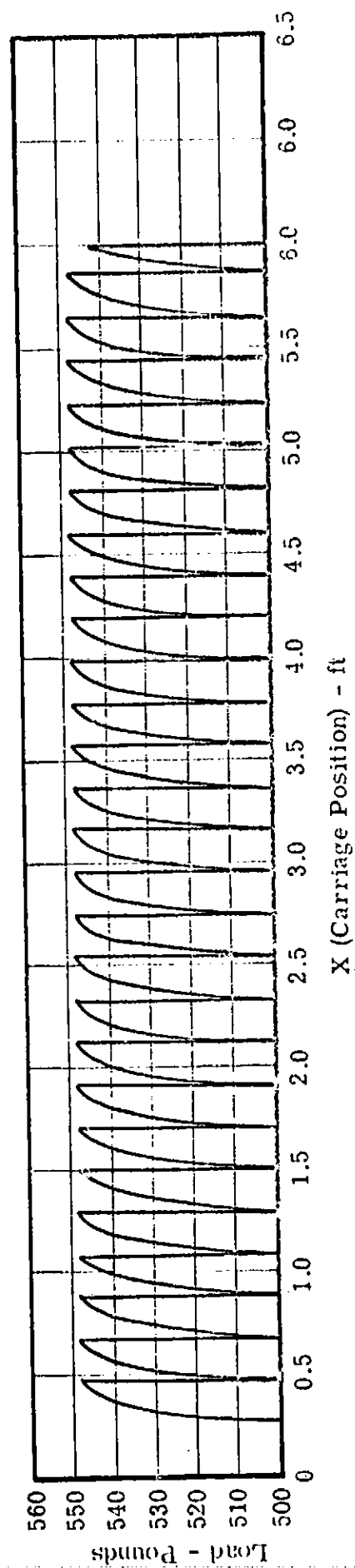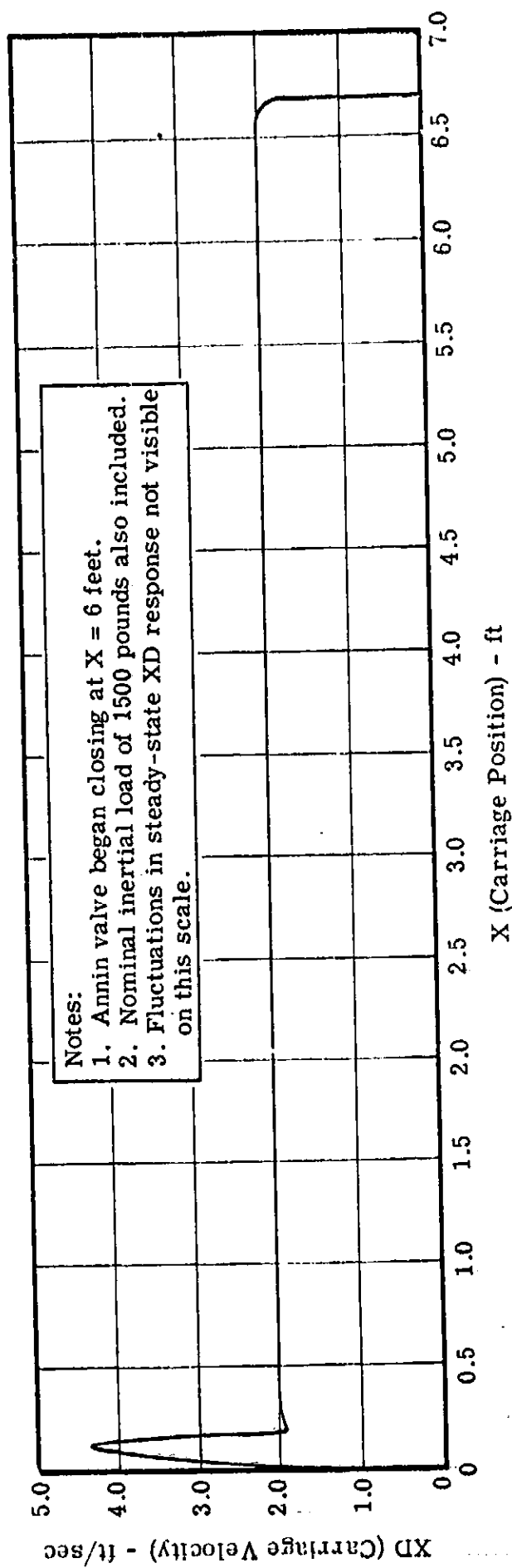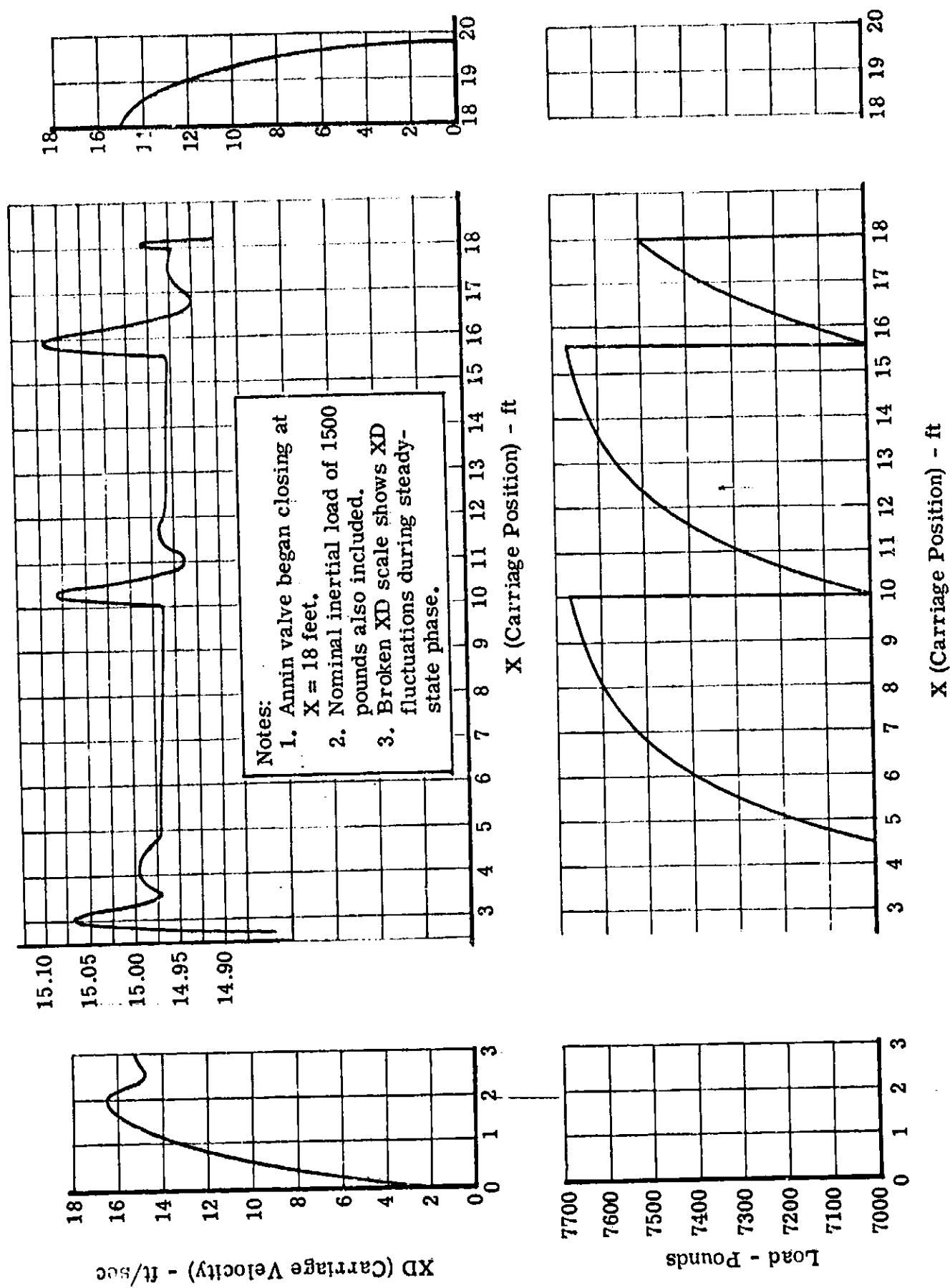
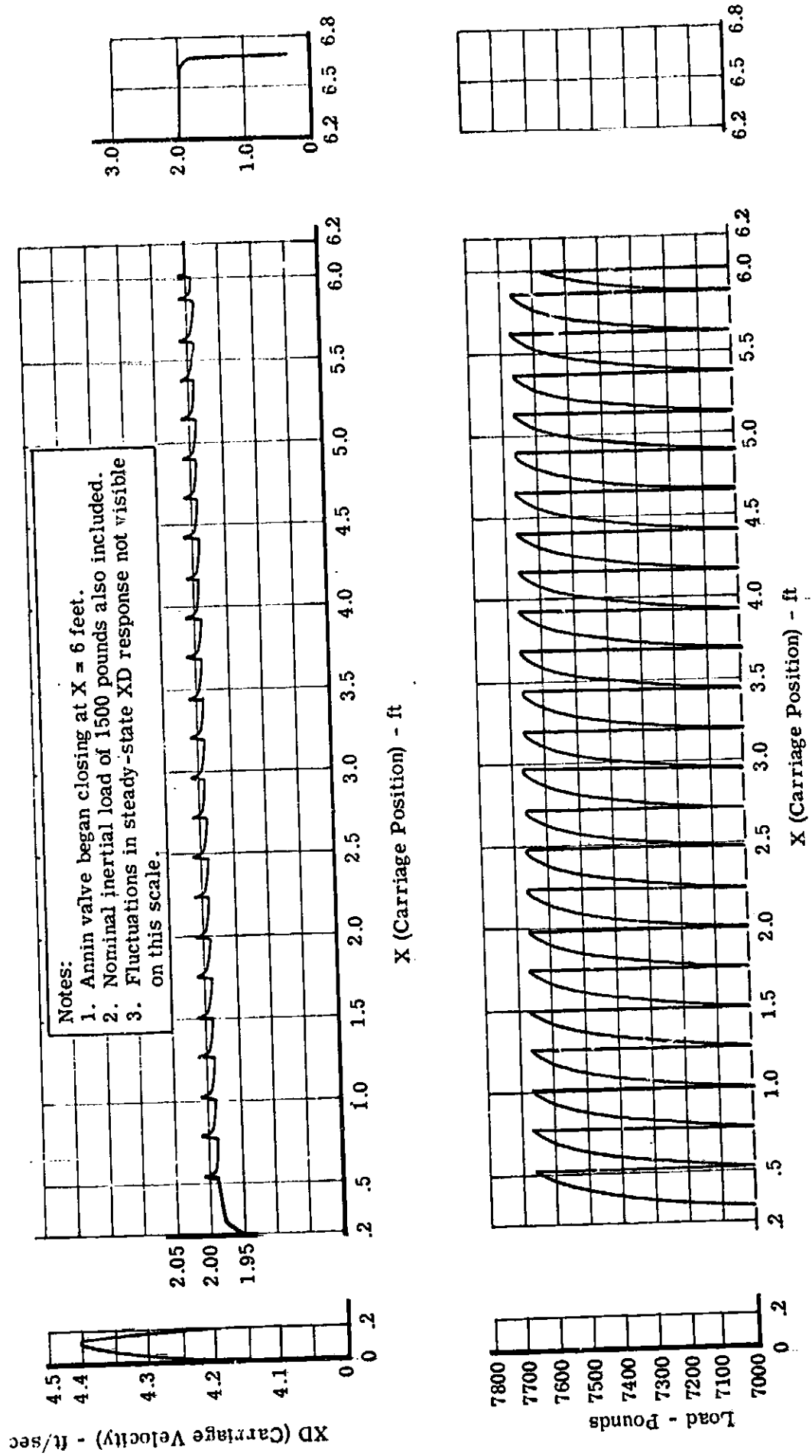Load - Pounds

X (Carriage Position) - ft

Figure D-22. Expected Dynamic Response of Nominal System Under +10 Percent Fluctuations of Maximum (7000 Pounds) Load (2 ft/sec Constant Velocity)

In the transition from acceleration to steady-state velocity, the "overshoot" evident on each of the test runs is a result of the assumed linear opening of the Annin valve in 0.2 second mentioned earlier. This can be accommodated during development by "tailoring" of the valve opening characteristics within the range indicated in Figure D-13. The range was established by considering various other linear valve opening characteristics that maintained system stability and accelerated the carriage within the first three feet of travel.

Table D-3 summarizes the highlights of Figures D-17 through D-22 in tabular form. The predicted nominal dynamic response characteristics listed bound the range of system response expected for the specified carriage velocity range of 2 to 15 feet/second, under loads ranging from zero to 7000 pounds, and with +10 percent break-away load fluctuations superimposed.

Table D-4 presents the predicted actual steady-state carriage velocity which should be obtained (nominal ± tolerance) as a function of the system and operating tolerances. These predictions are shown for all desired velocities between 2 and 15 feet/second at one-foot/second intervals. A breakdown of the predicted effects of individual tolerances is also shown. These were combined using the square root of the sum of the squares of the individual variations to obtain the overall expected variations due to all tolerances (columns 7 and 8).

Although many parameters were considered nominal in the analysis leading to Table D-4, the effects of tolerances on those parameters believed most critical to overall system performance and stability and/or most likely to vary, have been considered. Where no tolerances were assumed, either the parameter values shown are design criteria to be maintained (as near as possible) on the hardware, or - as in the case of flow discharge coefficients --the values would be determined experimentally and their effects reassessed during development phase analytical studies. In addition, for certain parameters, the assumed tolerances used here can be reduced in later studies when detail hardware sizes are known.

D-54

TABLE D-3

SUMMARY OF NOMINAL DYNAMIC RESPONSE CHARACTERISTICS

Reference Figure No.	XDSS (ft/sec)	Constant Load (Pounds)	Magnitude of Super-imposed Load Fluctuations (Lbs.)	Peak XD (ft/sec)	% Over-Shoot	X at Initiation of Steady-State XD (ft)	Max. Steady-State XD Flc. Due to Load Fluctuations (±ft/sec)	Carriage Travel While Stopping (ft)	Steady State Travel (ft)
D-17	15	0(wt = 1500 lb)	0	16.940	12.9	2.507	None	1.989	15.493
D-18	2	0(wt = 1500 lb)	0	4.379	119	0.177	None	0.694	17.923*
D-19	15	500	0 to +50	16.924	12.8	2.541	(+0.006 (-0.001)	1.979	15.459
D-20	2	500	0 to +50	4.360	118	0.176	(+0.001 (-0	0.694	17.824*
D-21	15	7000	0 to +700	16.482	9.9	2.778	(+0.139** (-0.028	1.825	15.222
D-22	2	7000	0 to +700	4.061	103.1	0.182	(+0.021 (-0	0.694	17.818*

*The corresponding figures actually show 12 feet less steady-state carriage travel than given in the table. That is only because these three computer runs were shortened.

**This is the only response characteristic in the whole table which does not satisfy the design objectives.

Notes:
1. X ≜ carriage position in feet.
2. XD ≜ carriage velocity in ft/sec.
3. XDSS ≜ steady-state carriage velocity in ft/sec, i.e., excluding effects of load fluctuations.

D-55

TABLE D-4
SUMMARY OF OPERATING ACCURACY PREDICTIONS

1 XDSS Desired (ft/sec)	2 XDSS Variation Due to ±3σ Tolerance in Control Valve Piston Leakage Area, ACVL (ft/sec)	3 XDSS Variation Due to ±3σ Tolerance in Pneumatic Force, PB (ft/sec)	4 XDSS Variation Due to ±3σ Tolerance in Absolute Oil Temperature, TABS (ft/sec)	5 XDSS Variation Due to ±3σ Tolerance in Metering Orifice Area, AMO (ft/sec)	6 ±3σ Variation in XDSS Due to Unpredictability of Constant Load (ft/sec)	7 Prediction of XDSS Obtained (Nom.+3σ Tol.) (ft/sec)	8 Prediction of XDSS Obtained (Nom.+1σ Tol.) (ft/sec)
2	+.09 / -.06	+.06 / -.03	+.01 / -0	+.07 / -.07	+.05 / -.05	2 +.15 / -.13	2 +.05 / -.04
3	+.14 / -.09	+.05 / -.06	+.01 / 0	+.10 / -.10	+.05 / -.05	3 +.19 / -.16	3 +.06 / -.05
4	+.19 / -.13	+.09 / -.05	+.02 / -.01	+.09 / -.09	+.07 / -.07	4 +.24 / -.20	4 +.08 / -.07
5	+.24 / -.16	+.06 / -.07	+.02 / -.01	+.11 / -.11	+.05 / -.05	5 +.25 / -.21	5 +.09 / -.07
6	+.28 / -.15	+.19 / -.10	+.03 / -.01	+.07 / -.07	+.12 / -.12	6 +.31 / -.30	6 +.11 / -.10
7	+.35 / -.22	+.16 / -.16	+.05 / -.01	+.08 / -.08	+.11 / -.11	7 +.35 / -.30	7 +.14 / -.10
8	+.36 / -.25	+.14 / -.14	+.04 / -.01	+.10 / -.10	+.10 / -.10	8 +.42 / -.32	8 +.14 / -.12
9	+.45 / -.28	+.13 / -.13	+.04 / -.01	+.11 / -.11	+.09 / -.09	9 +.47 / -.34	9 +.15 / -.11
10	+.45 / -.32	+.12 / -.12	+.05 / -.02	+.12 / -.12	+.08 / -.08	10 +.37 / -.37	10 +.17 / -.12
11	+.52 / -.35	+.23 / -.23	+.05 / -.02	+.09 / -.09	+.17 / -.17	11 +.60 / -.46	11 +.20 / -.15
12	+.57 / -.38	+.20 / -.22	+.08 / -.02	+.10 / -.10	+.15 / -.15	12 +.53 / -.48	12 +.21 / -.16
13	+.61 / -.41	+.20 / -.15	+.06 / -.02	+.10 / -.10	+.14 / -.14	13 +.67 / -.45	13 +.22 / -.16
14	+.66 / -.44	+.15 / -.16	+.07 / -.02	+.11 / -.11	+.11 / -.11	14 +.71 / -.50	14 +.24 / -.17
15	+.71 / -.47	+.17 / -.16	+.07 / -.02	+.12 / -.12	+.10 / -.10	15 +.75 / -.52	15 +.25 / -.17

Nomenclature: XDSS ≜ Steady-State Carriage Velocity in ft/sec.

Notes:
1. Column 2 due to only ±3σ ACVL tolerance (i.e., +.002 in²)
2. Column 3 due to only ±3σ PB tolerance (i.e., +10 lbs / -10 lbs)
3. Column 4 due to only ±3σ TABS tolerance (i.e., +300°F / -100°F)
4. Column 5 due to only ±3σ AMO tolerance (i.e., -.01 in²)
5. Column 6 due to only specified range of constant load (i.e., zero → 7000 lbs)
6. Column 7 tolerances are RSS of columns 2 through 6
7. Column 8 tolerances are "expected", ±1σ, tolerances in XDSS
8. The following approximate relationships were used (considered good approximations):
   a. $XDSS \propto 0.586/{\pm}1215\,(ACVL)^2$
   b. $XDSS \propto [PB]^{1/2}$
   c. $XDSS \propto [\text{specific wt. of oil}]^{1/2} = f(TABS)$
   d. $XDSS \propto AMO$

D-56

APPENDIX E

VACUUM/ATMOSPHERIC IMPACT TESTER AND SUBGRAVITY SIMULATOR

This Appendix describes the subscale impact tester and subgravity simulator experimental apparatus and the associated instrumentation systems used for the atmospheric and vacuum footpad impact tests and the reduced gravity impact tests. These experiments were conducted by the IIT Research Institute at Chicago, Illinois during the period from November 1966 to May 1967. The test equipment was designed and constructed by IITRI to meet technical requirements established by Bendix.

The following pages are reproduced from appropriate portions of IITRI Final Report No. M6173, submitted to Bendix at the conclusions of the study.

III. EXPERIMENTAL APPARATUS

The apparatus used in the experiments in atmosphere is shown in Figure 1 and consisted basically of an impact drive mechanism to accelerate the footpad prior to impact, a soil container 24 in. in diameter and 20 in. deep, and the associated instrumentation. For the experiments in vacuum the impact drive mechanism was mounted on a similar frame in the vacuum system as shown in Figure 2.

A. IMPACT DRIVE MECHANISM

The impact drive mechanism, illustrated in Figure 3, represented the most significant item with respect to program performance. The purpose of the impact drive mechanism was to provide controlled motion and controlled orientation for the scale model footpad up to and during soil impact and penetration. The mechanism consisted of a shaft riding in two bronze bushings contained within a rigid frame. Attached to the end of this shaft was a universal adjustment mechanism on which a scale model of the LM footpad was mounted. A load cell was inserted between the pad and the shaft. These four items, weighing approximately 32 pounds constituted the moving elements of the drive mechanism.

The energy required to drive the impacting assembly was provided by the elastic strain energy stored in a helical compression drive spring. The spring acted upon the upper end of the shaft, and reacted against an extension to the frame. The spring and shaft were held in their cocked position by a sear, fitting into a latching groove in the shaft, and were released by solenoid action. The axial forces on the sear were balanced by means of a small balancing spring and an adjustment screw. The amount of energy stored in the spring could be varied by means of the preload adjustment screw on the upper end of the shaft.
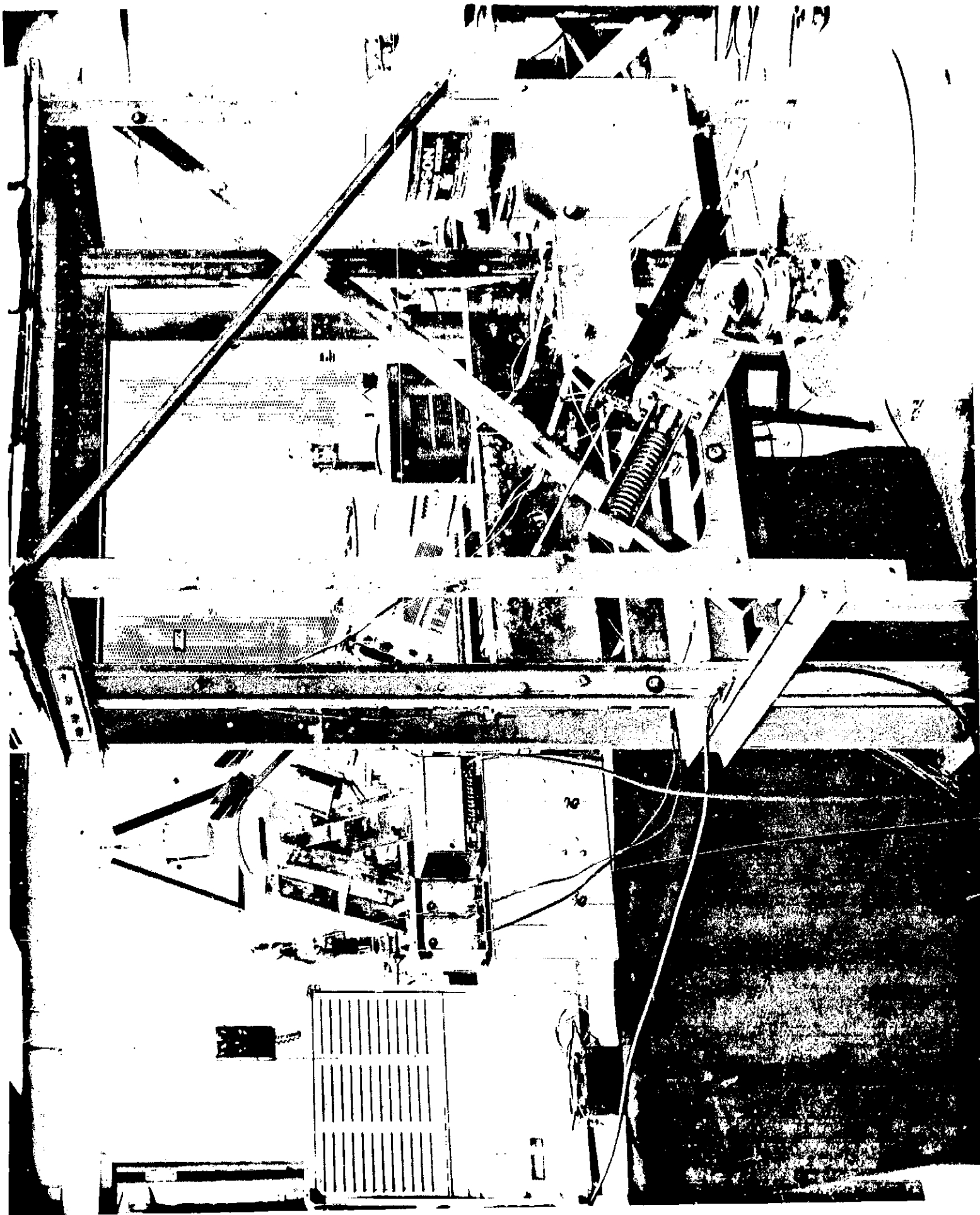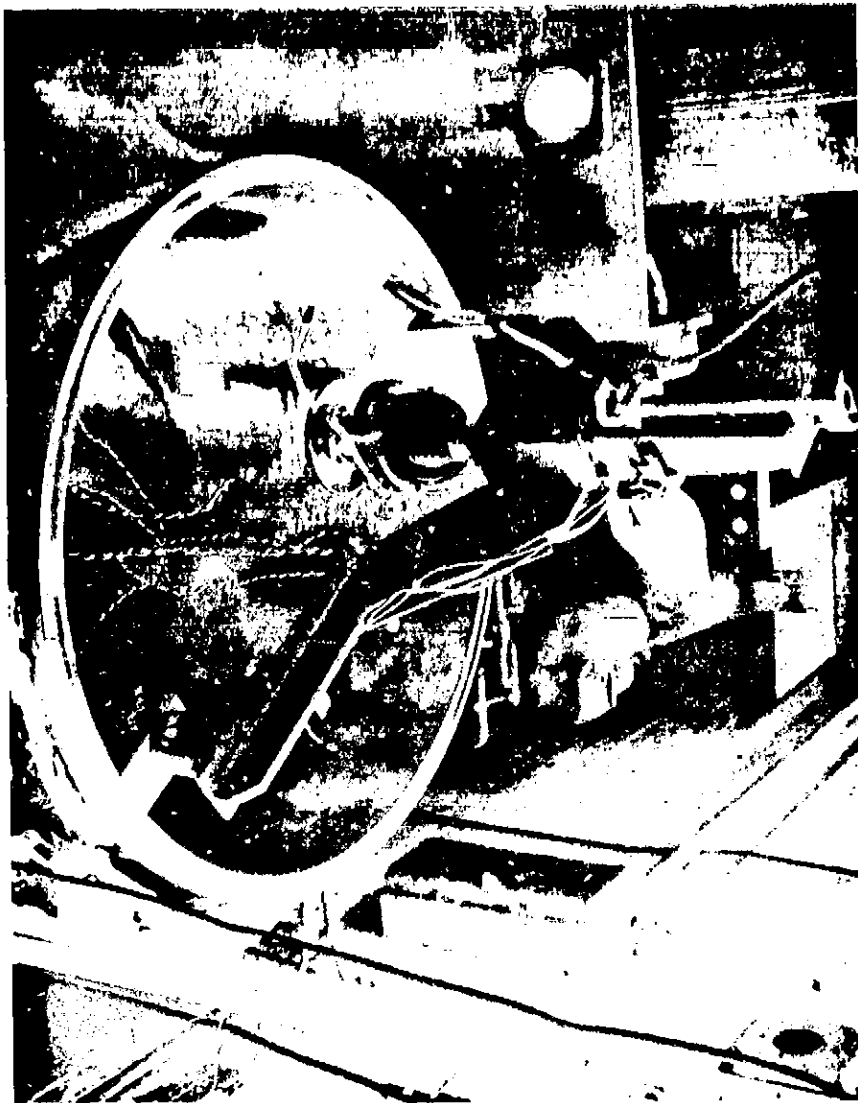
Fig. 1 IMPACT DRIVE MECHANISM IN ATMOSPHERE

Fig. 2   IMPACT DRIVE MECHANISM IN VACUUM CHAMBER

Strain Gauges

Load Cell

Solenoid

Balancing Spring

Sear

Adjustment Screw

Latch Groov

Drive Spring

Anti-Rotation Bearing

Frame

Main Bearings

Shaft

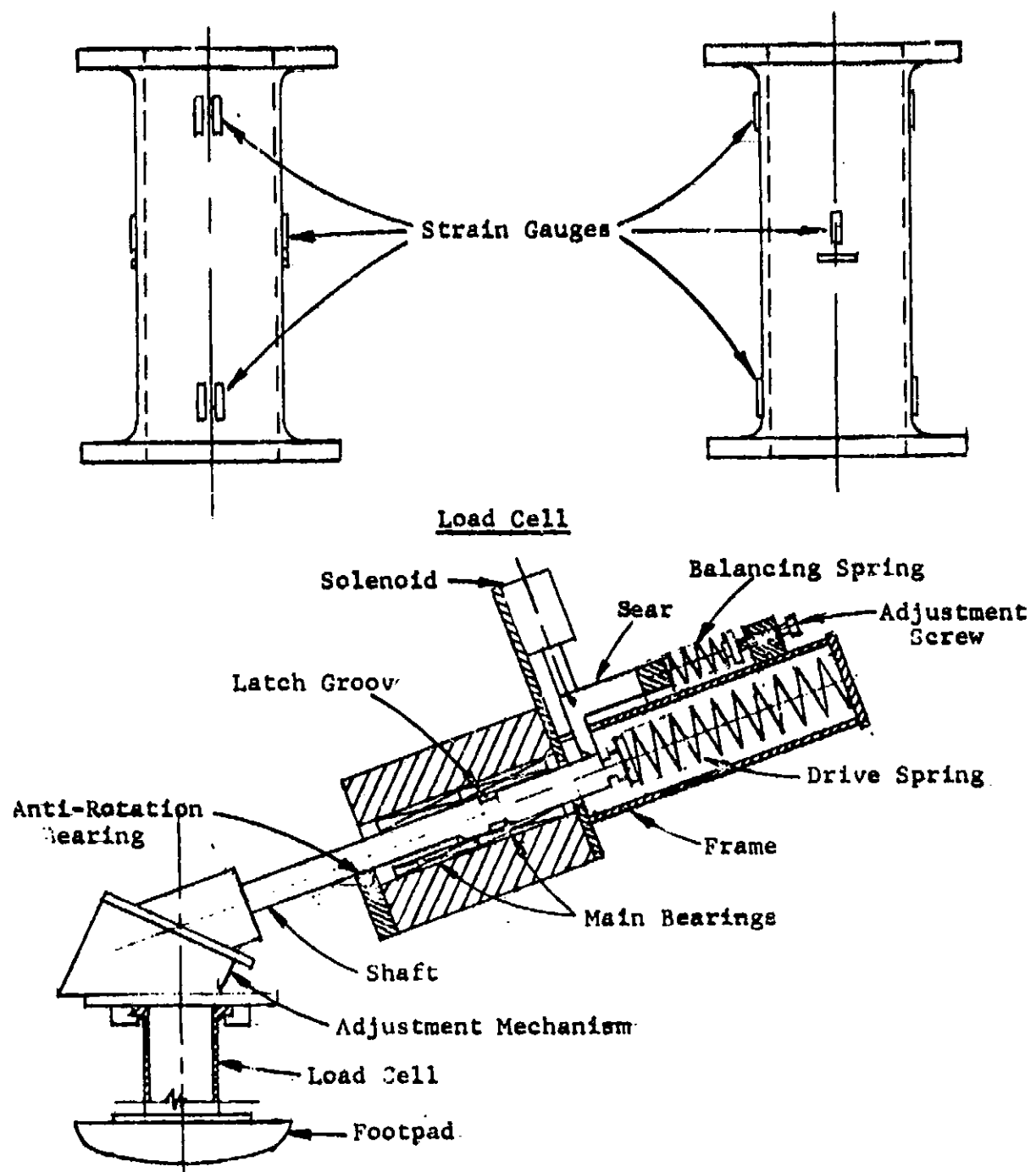Adjustment Mechanism

Load Cell

Footpad

Fig. 3   IMPACT DRIVE MECHANISM

Upon release of the sear, the spring drove the shaft and its attachments downward for the major portion of its travel. Near the end of its stroke and before impact, the shaft separated from the spring and experienced "free" travel.

The experiments in vacuum required the adaptation of the impact drive mechanism and its mounting bracket to existing vacuum facilities. The limited space available within the vacuum chamber necessitated the design of a mounting bracket which could be easily removed permitting the placement and removal of the soil container. This bracket consisted of a stiffened aluminum plate, mounted on a pivot, and constrained by a bolted lock (Figure 2). Additional stiffness, in the form of guy wires, was provided, primarily for the oblique angle impact tests.

B. SUBGRAVITY SIMULATOR

For the experiments in a reduced gravitational field a subgravity simulator was designed, and is shown in Figure 4. It consisted of a drop tower approximately 20 feet high, containing a drop platform, a counter weight system, a hoisting and release system, and a means for decelerating and stopping the drop platform.

The drop platform itself was a stiffneed plate structure on which a vertical frame was mounted. The soil specimen rested on the plate and the vertical frame supported the impact drive mechanism and its mounting bracket. In addition, this frame provided an attachment point for the hoisting cable and guide rollers. The guide rollers were rubber tired casters providing a stable constraint, in a horizontal plane, for the platform during its descent. The rollers rode upon the web and flanges of the supporting columns in a two point support configuration (across the plate diagonal).

The drop platform rode within four vertical wide flange beams, arranged in a rectangular configuration, constrained at the top and the bottom and braced diagonally along
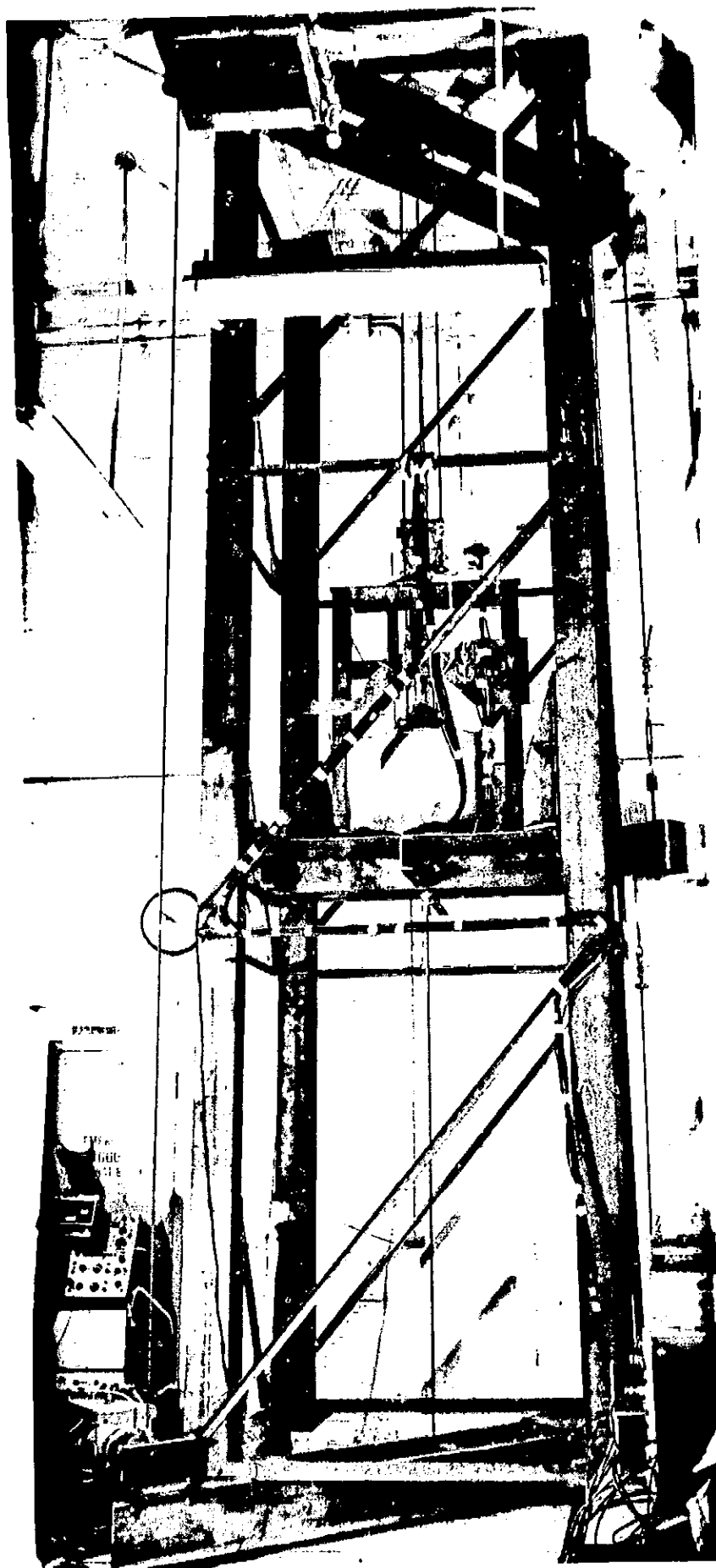
E-6

Fig. 4 SUBGRAVITY SIMULATOR

their length. Across the top of this structure was a yoke arrangement, carrying the upper pulleys necessary for the hoisting and counterbalance cables. The lower pulleys for these systems were contained within the base structure. The support structure, also, had attached to it, the reaction members for the friction deceleration device.

The hoisting system consisted of a winch, cable, solenoid actuated release mechanism, and associated pulleys. The release mechanism consisted of a solenoid actuated toggle linkage attached to the locking hooks (Figure 5). The counter-balance system, permitting the simulation of reduced gravity, consisted of a double cable, counter-weights, and associated pulleys. The double cable was attached to the drop platform at both the top and the bottom, permitting the use of a single deceleration device to control both the drop platform and the counter weights.

The counter weight assembly was composed of a number of steel slabs, permitting variation of the retarding force. This, in turn, permitted the simulation of any gravity field from earth normal (no drop) to almost "zero g" (free fall).

The friction decelerator (Figure 5 and 6) consisted of spring loaded friction pads and associated reaction members The friction pads were attached to the stiffened plate structure of the drop platform by load springs to provide an essentially constant normal force between the friction pad and the reaction member during the deceleration phase. The pad was arranged so that any desired material may be used as the friction element. The friction element used for these experiments was a commercially available brake lining material.

The reaction members were attached to the main supporting structure through a parallel bar linkage arrangement. This linkage permitted the reaction member to rotate away from the friction pad when the direction of travel of the drop platform
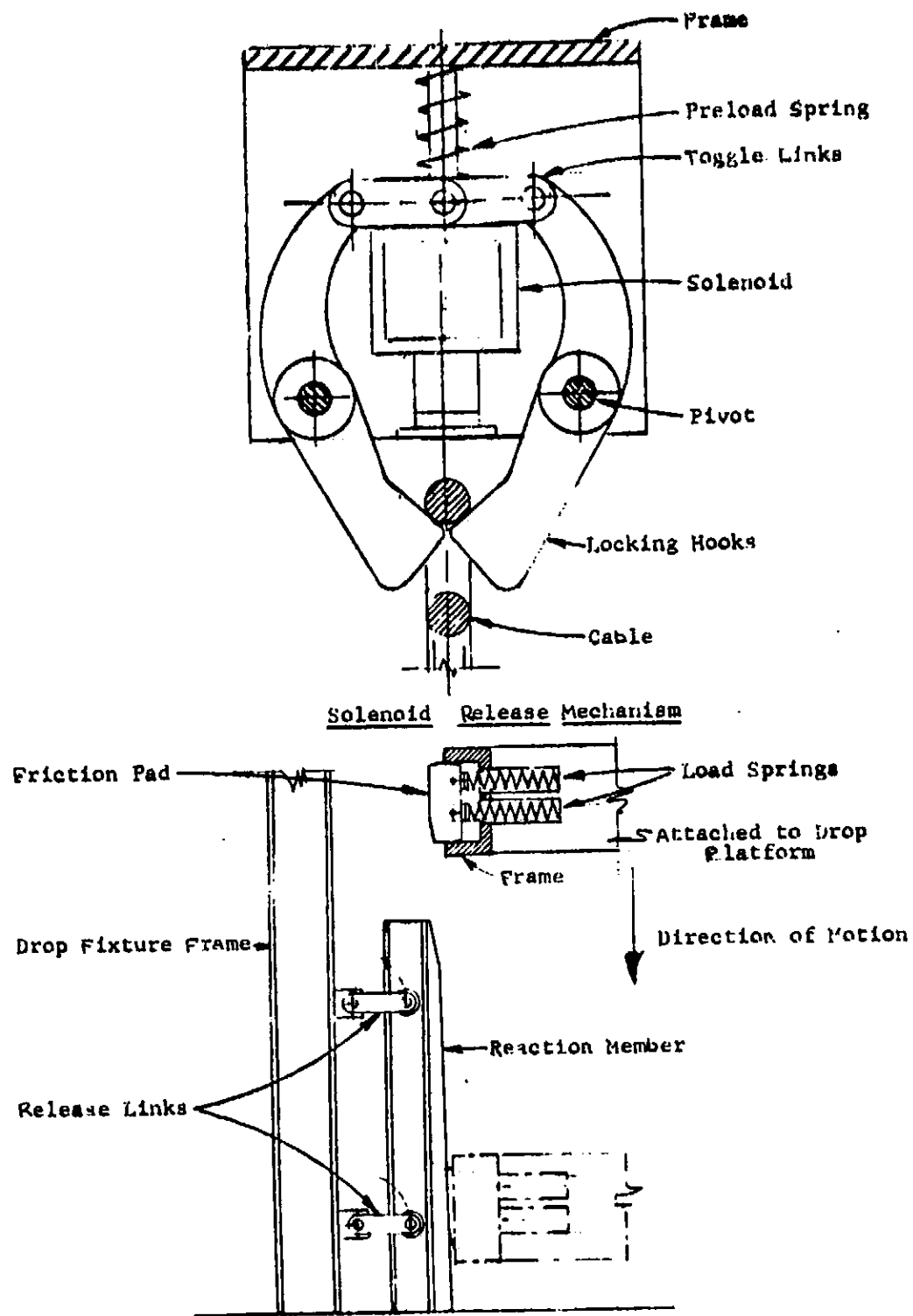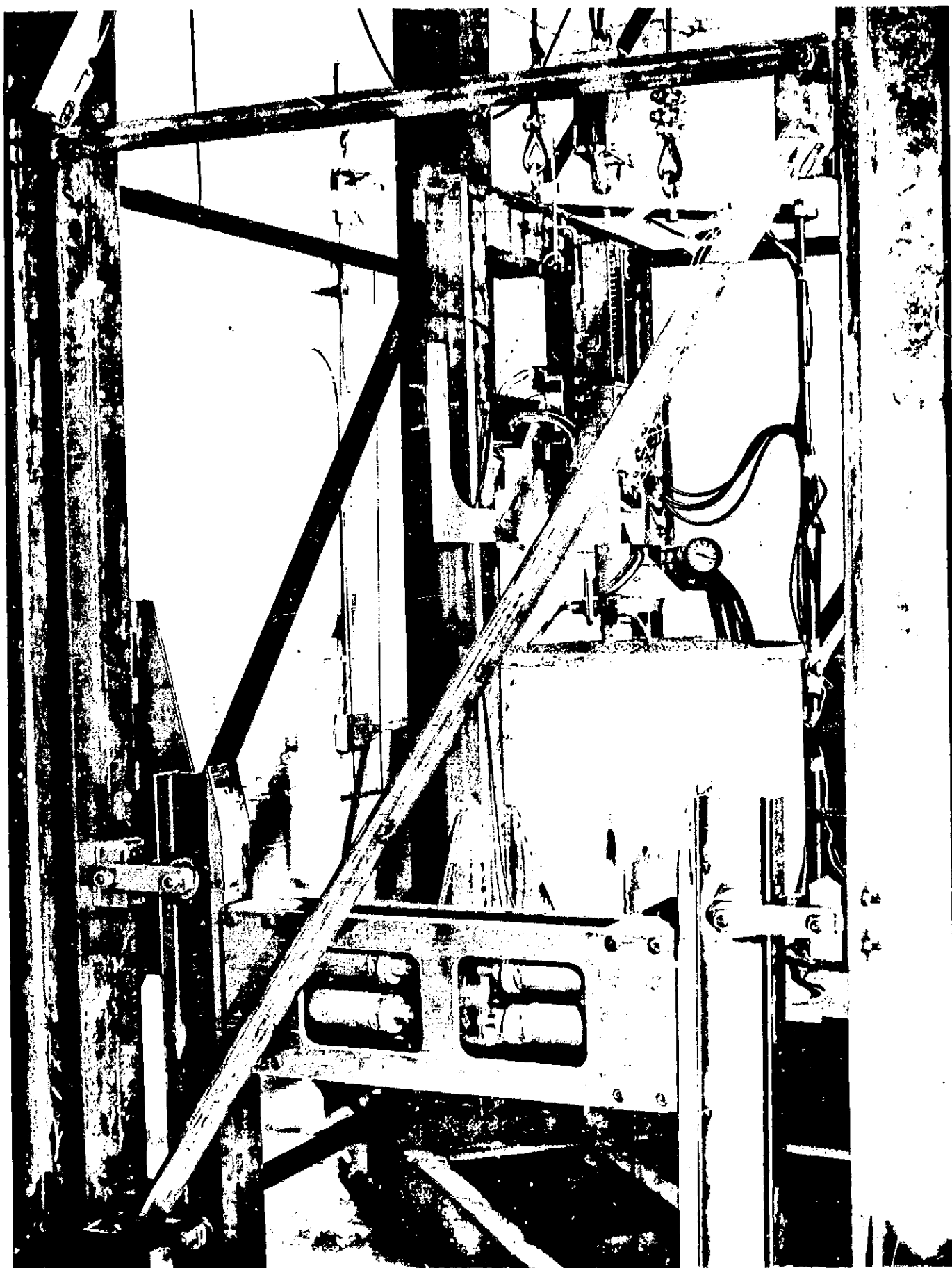
E-8

Fig. 5   FRICTION DECELERATOR

Fig. 6 FRICTION DECELERATOR

was reversed and, thus provided an automatic unlocking feature. The members themselves were made from a structural steel shape and were faced with a steel plate for the friction surface. A total travel of four feet was allowed for deceleration.

The required drop height depended upon the time necessary to conduct the impact experiment while the platform was falling. The distance required for deceleration depended upon the drop height; but the friction deceleration was designed for free fall of the loaded drop platform from a height of 16 feet. In the experiments a total drop height of approximately 4 feet was used and provided a total time for testing of approximately 550 msec at a gravity field of 1/6g. The total drop height of 16 feet would provide a time of approximately 1.0 sec under free fall.

IV. INSTRUMENTATION

The instrumentation system consisted of eight record/reproduce channels. Six channels were used to record analog data signals and two were used to record time information (one channel for a time base channel and the second for "time of event" data).

Figures 7 and 8 are block diagrams of the recording instrumentation and the reproduce equipment. Data signals recorded on magnetic tape, were reproduced as oscillogram traces.

The signal output of each measuring system was terminated into a patchbay located in a monitoring unit which contained the circuitry to perform the electrical calibration. It also contained visual monitors and test equipment that was used to assure that the measuring systems were in proper operating condition prior to conducting the test.

A. TRANSDUCERS

Bending and axial loads were measured by electrical strain gages mounted on the load cell as shown in Figure 3. The strain gages were metal film gages and were connected in a four active element Wheatstone-bridge configuration. The strain gages were placed so as to provide maximum data signals for the parameter being measured and, at the same time, be non responsive to other effects. The cross sensitivity of the different elements were observed to be less than 5 percent and were taken into account in the reduction of the data.

The load cell contained two piezoelectric accelerometers, mounted in an orthogonal array to monitor the horizontal and vertical component of the acceleration. A Kistler 802 unit was used to measure the vertical acceleration and a Kistler 808A was used in the horizontal position. Both units had an electrical frequency response from near DC to 8,000 Hz. The transverse sensitivity was less than five percent of the normally applied load.
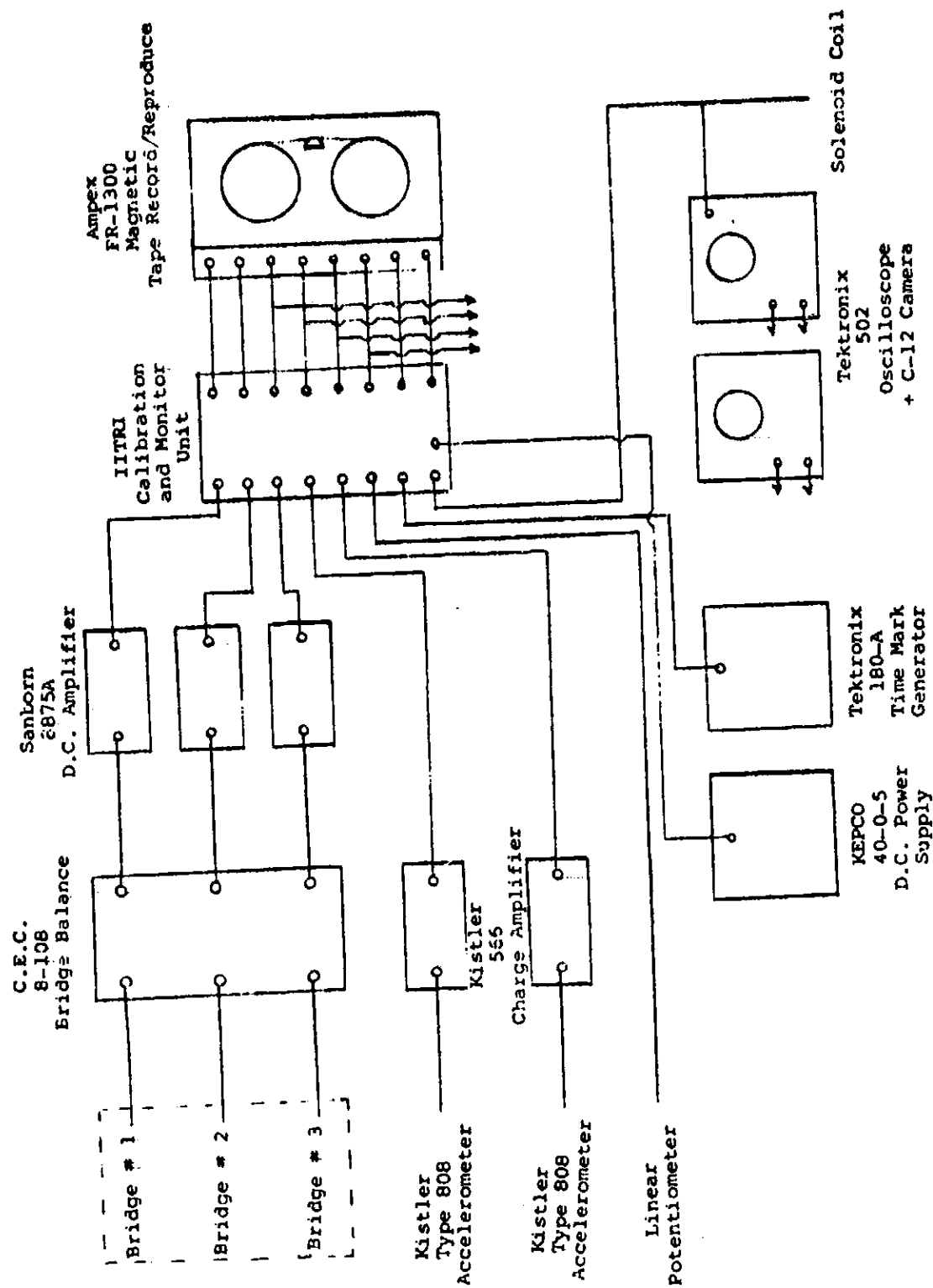
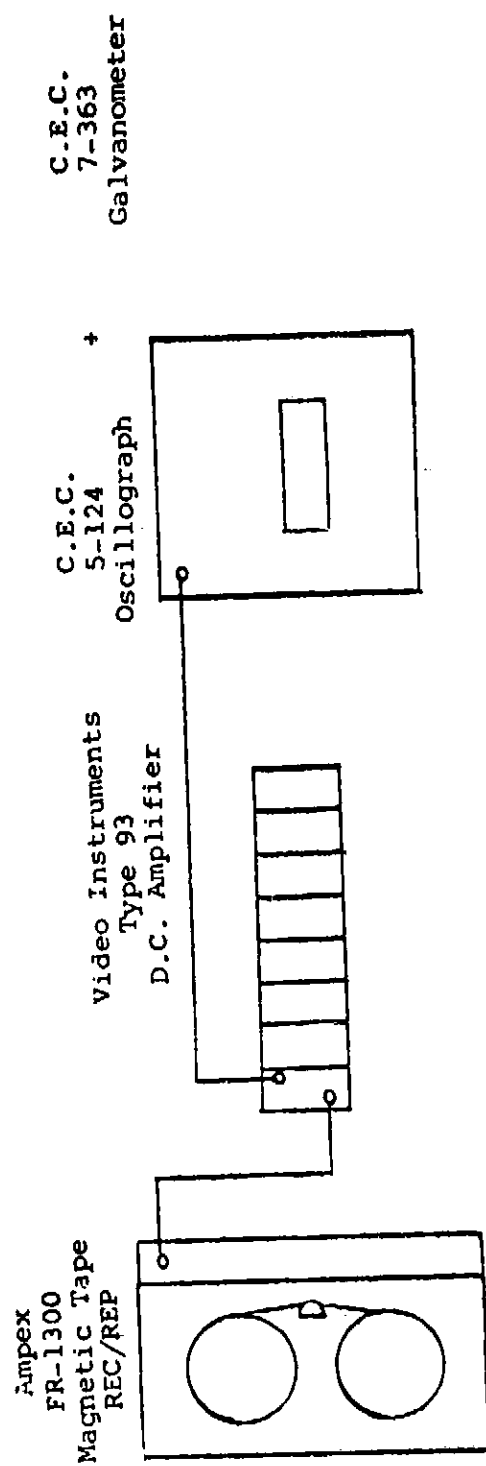Fig. 7 BLOCK DIAGRAM OF RECORDING INSTRUMENTATION

E-13

Fig. 8 BLOCK DIAGRAM OF REPRODUCE EQUIPMENT

A variable potentiometer was used to provide time-displacement data of the footpad.

B. RECORDING EQUIPMENT

The recording equipment used on the test program were analog magnetic tape recorders. The initial tests were run at a recording speed of 60 ips and reproduced at a speed of 1-7/8 ips. These conditions produced oscillogram recordings with an effective band pass of DC to 20,000 Hz. A cursory review of the oscillogram recordings indicated that there was no pertinent data in the frequency range about 3,000 Hz. In view of this, the remaining tests were run at a recording speed of 15 ips, providing an effective band pass of DC to 5,000 Hz. Oscillograms were used to produce traces of the data recorded on magnetic tape.

C. CALIBRATION

The transducers were initially calibrated over the anticipated range of application by applying the load stimulus to the transducer and then recording the output signal voltage. The signal voltages were then converted to units characteristic of the sensing element (i.e., ΔR per pounds for the load cell, pcb per g for the accelerometer and ΔR per inch for the linear potentiometer).

Electrical calibration was conducted prior to each experiment to verify the integrity of the signal conditioning equipment and recording system. The electrical calibration signal was recorded on each data channel immediately preceding the recording of the data signal from the test run.

The electrical strain bridge circuits were electrically calibrated by shunting one element of the bridge R_g with an accurately known resistor R_s causing an unbalance, ΔR, in the bridge circuit. This, in turn, caused a voltage rise, ΔE, proportional to ΔR, at the output of the bridge circuit. The calibration signal ΔE was equivalent to $\Delta R/K$ units of force.

(K being the sensitivity factor, ΔR/pound, determined in the pre-test calibration.)

The accelerometer channels were electrically calibrated by injecting a known calibration voltage signal E_c, at the output of the charge amplifier. The acceleration equivalent, A_c, of the calibration voltage could be determined by the relationship:

$$A_c = \frac{E_c}{SK}$$

where S is the range setting of the charge amplifier (mv/pcb) and K is the sensitivity factor of the accelerometer (pcb/g).

The linear potentiometer channel was electrically calibrated by recording, in turn, the voltages at the two ends and at the center of the resistance elements. This method produced a calibration signal that represented 0 percent, 50 percent, and 100 percent of full potentiometer travel.

D. DATA REDUCTION

The data was reduced by manually digitizing the oscillogram records and key punching this data for reduction on the IBM 7094 computer.

The horizontal force on the load cell was determined by noting that the difference between bending moments at the two extreme strain gage bridges on the load cell was due to the horizontal force. Thus, the difference between bending moments divided by the spacing between the bridges yielded the horizontal force. The axial force on the load cell was simply a linear function of the output voltage of the middle strain gage bridge.

The forces acting on the footpad were determined by adding the mass of the footpad times the appropriate component of acceleration (which was measured) to the force on the load cell. The cross sensitivity of the various elements in the load cell were also taken into account in the computer program.

E-16

REFERENCES

1. Black, R. J., et al, "Final Report - Lunar Landing Dynamics Specific Systems Engineering Studies," Bendix Report No. MM-65-4. Energy Controls Division, The Bendix Corporation, South Bend, Indiana. June 1965.

2. Black, R. J., et al, "Development of a Mathematical Analysis for Predicting the Dynamic Behavior of the Apollo Command Module during Earth Landing," Bendix Report No. MM-66-15. Energy Controls Division, The Bendix Corporation, South Bend, Indiana. May 1966.

3. Meyerhof, G. G., "The Bearing Capacity of Foundations under Eccentric and Inclined Loads," Session 4/24, Proceedings of the 3rd International Conference of Soil Mechanics, pp. 439-445, Switzerland 1953.

4. Mizuno, T., "On the Bearing Power of Soil under Uniformly Distributed Circular Load," Session 4/25 Proceedings of the 3rd International Conference of Soil Mechanics, pp. 446-449, Switzerland 1953.

5. Shipley, E. N., "Surveyor and LM Penetration into a Model Lunar Soil," Bellcomm Technical Memorandum 67-1014-1, February 23, 1967.

6. Biarez, Jean, "Contribution of l'etude des proprietes mecaniques des sols et des materiaux pulverulents" (Doctor Thesis) - University of Grenoble, Grenoble, France.

7. Terzaghi, K. and Peck, R. B., "Soil Mechanics in Engineering Practice," John Wiley and Sons, Inc. 1948.

8. Surveyor Scientific Evaluation and Analysis Team, "Surveyor I - A Preliminary Report," NASA SP-126, June 1966.

9. Surveyor Investigator Teams, Scientific Evaluation Advisory Team, and Working Groups, "Surveyor III Mission Report - Part II Scientific Results," JPL Technical Report 32-1177, June 1967.

10. Barkan, D. D., Dynamics of Bases and Foundations, McGraw-Hill Book Co., 1962, 11. 14.

11. Harr, M. E., Foundations of Theoretical Soil Mechanics, McGraw-Hill Book Co., 1966, pp. 3-49.

12. Leonards, G. A., (editor), Foundation Engineering, McGraw-Hill Book Co., 1962, pp. 74-76.

13. Means, R. E. and Parcher, J. V., Physical Properties of Soils, Charles E. Merrill Books, Inc., 1963, pp. 323-331.

14. Schimming, B. B., Haas, H. J., and Saxe, H. C., Study of Dynamic and Static Failure Envelopes, Journal of the Soil Mechanics and Foundations Division, American Society of Civil Engineers, March 1966.

15. Scott, R. F., Principles of Soil Mechanics, Addison-Wesley Publishing Co., Inc., 1963, pp. 304-310.

16. Taylor, D. W., Fundamentals of Soil Mechanics, John Wiley and Sons, Inc., 1948, pp. 210-211.

17. Jaffe, L. D., et al, "Surveyor I Mission Report - Part II. Scientific Data and Results," JPL Technical Report No. 32-1023, Pasadena, California, September 10, 1966.

18. Jaffe, L. D., et al, "Surveyor I - A Preliminary Report," National Aeronautics and Space Administration, Report No. SP-126, Washington D. C., June 1966.

19. Gault, D. E., Quaide, W. L., Oberbeck, V. R., Moore, H. J., "Luna 9 Photographs: Evidence for a Fragmental Surface Layer" Science Vol. 153, No. 3739, pp. 985-988, August 26, 1966.

20. Mitchell, J. K., "Current Lunar Soil Research," Journal of the Soil Mechanics and Foundation Division (ASCE), pp. 53-83, May 1964.

21. Green, Jack, "The Moon's Surface," International Science and Technology, pp. 59-67, September 1966.

22. Halajian, "Gravity Effects on Soil Behavior," Lunar Surface Materials Conference, Boston, Massachusetts, May 21-23, 1963.

23. Vey, E. and Nelson, J. D., "Studies of Lunar Soil Mechanics," Final Report Contract No. NASR-65(02) IITRI Report No. M272 (Phase II), National Aeronautics and Space Administration, Washington, D.C., February 1965.

24. Johnson, L. D. and Black, R. J., "Analysis of Size - Frequency Distribution Function for Soil Grains on the Lunar Surface," Bendix Report No. MM-66-24, South Bend, Indiana, August 1, 1966 (Unpublished).

25. Fielder, G., Structure of the Moon's Surface, Pergamon Press, London, 1961.

26. UPI and AP press releases and photographs covering Luna 12, October 22, 1966, (Landed in Sea of Rains) and Luna 13, December 24, 1966. (Landed in Ocean of Storms and Activated Penetrometer.)

27. Rausch, H., "Russian Moon Lander Yields Data on Lunar Soil Firmness, Density," Aviation Week, January 16, 1967.

28. Dobar, W. I., Tiffany, O. L., Gnaedinger, J. P., "Simulated Extrusive Magma Solidification in Vacuum," Icarus, Volume 3, No. 4, Academic Press, November 1964.

29. Mackrill, F. P., Black, R. J., and Schmidt, R. E., "Progress Report No. 7-LM Soil Mechanics Study," Bendix Report No. MM-67-1, South Bend, Indiana, January 1967 (Unpublished - an estimated grain size distribution curve for the lunar soil is given and discussed in this report).

30. Lambe, T. W., Soil Testing for Engineers, John Wiley and Sons, Inc., 1951.

31. American Society for Testing and Materials, Procedures for Testing Soils, ASTM, Philadelphia 3, Pennsylvania, 4th Edition, 1964.

32. ——— New Products Catalog 65-1, Soiltest, Inc., 2205 Lee Street, Evanston, Illinois 60202, 1965.

33. Soiltest, Inc., Engineering Testing Equipment, Catalog Edition III, Soiltest, Inc., 2205 Lee Street, Evanston, Illinois 60202, 1964.

34. Testlab Corporation, Engineering Testing Approaches, General Catalog No. 2, Testlab Corporation, 216 N. Clinton Street, Chicago, Illinois 60606, 1965.

35. Burmister, D. M., Soil Mechanics, Vol I, Columbia University, New York, New York, 1948.

36. Teng, W. C., Foundation Design, Prentice-Hall, Inc., 1962.

37. Wu, T. H., Soil Mechanics, Allyn and Bacon, Inc., Boston, 1966.

38. Terzaghi, K., Theoretical Soil Mechanics, John Wiley and Sons, Inc., 1943.

39. U. S. Bureau of Yards and Docks, "Design Manual - Soil Mechanics, Foundations and Earth Structures," Navdocks DM-7, Dept. of the Navy, Bureau of Yards and Docks, Washington 25, D. C., November 1, 1961.

40. Miller, I. and Freund, J. E., Probability and Statistics for Engineers, Prentice-Hall, Inc., 1965.

41. Graybill, F. A., An Introduction to Linear Statistical Models, Volume I, McGraw-Hill, 1961.

42. Hildebrand, Introduction to Numerical Analysis, McGraw-Hill, 1956.

43. Draper, N. and Smith, H., Applied Regression Analysis, John Wiley and Sons, Inc., 1967.

44. Timoshenko and Goodier, Theory of Elasticity, McGraw-Hill, New York, 1951.

45. Clarke, F. W., The Data of Geochemistry, Bulletin 770, 5th Ed., U. S., Geol. Surv., Government Printing Office, Washington, D. C., 1924.

46. Tyrrell, G. W., The Principles of Petrology, Methuen and Co., Ltd., London, E. P. Dutton and Co., Inc., New York, 1926.

47. Black, R. J., et al, "Interim Report of Lunar Landing Dynamics Specific Systems Engineering Studies," Bendix Report No. MM-65-2, an extension to Bellcomm Subcontract No. 10002 prepared by Bendix Products Aerospace Division (Dept. 870), South Bend, Indiana, February 17, 1965.

ADDITIONAL BIBLIOGRAPHY

48. American Geological Institute, Glossary of Geology and Related Sciences, NAS-NRC Publication 501, Published by American Geological Institute operating under the National Academy of Sciences - National Research Council, Washington, D. C., 1957.

49. Barkan, D. D., Dynamics of Bases and Foundations, McGraw-Hill Book Co., Inc., 1962.

50. Bishop, A. W. and Henkel, D. J., The Measurement of Soil Properties in the Tri-axial Test, Edward Arnold (Publishers), Ltd., London, 2nd Edition, 1962.

51. Dobor, W. I., Tiffany, O. L., and Gnaedinger, J. P., "Simulated Extrusive Magma Solidification in Vacuum," Icarus, Vol. 3, No. 4, Academic Press, November 1964.

52. Brnevich, V. P., Hall, J. R., Jr., and Richart, F. E., Jr., "Transient Loading Tests on a Rigid Circular Footing," Contract Report No. 3-146, prepared by Department of Civil Engineering, U iversity of Michigan for U. S. Army Engineer Waterways Experiment Station under contract No. DA-22-079-eng-340, NWER Subtask 13.009, February 1966.

53. Gault, D. E., Quaide, W. L., Oberbeck, V. R., and Moore, H. J., "Luna 9 Photographs: Evidence for a Fragmental Surface Layer," Science, Vol. 153, No. 3739, August 26, 1966, pp. 985-988.

54. Guttman, I. and Willes, S. S., Introductory Engineering Statistics, John Wiley and Sons, Inc., 1965.

55. Hampton, D. and Wetzel, R. A., "Stress Wave Propagation in Confined Soils," Technical Report No. AFWL-TR-66-56 prepared for Air Force Weapons Command by IIT Research Institute, October 1966.

56. Huang, W. T., _Petrology_, McGraw-Hill Book Co., 1962.

57. Jaffe, L. D., et al, "Surveyor I – A Preliminary Report," Report No. SP-126, Washington, D. C., June 1966.

58. Jumikis, A. R., _Soil Mechanics_, D. Van Nostrand Co., Inc., Princeton, New Jersey, 1962.

59. Krynine, D. P. and Judd, W. R., _Principles of Engineering Geology and Geotechnics_, McGraw-Hill Book Co., Inc., 1957.

60. Mitchell, J. K., "Current Lunar Soil Research," _Proceedings_, ASCE, Vol. 90, No. SM3, May 1964, pp. 53-83.

61. Nelson, J. D., "Environmental Effects on Engineering Properties of Simulated Lunar Soils," PhD Thesis Submitted to Illinois Institute of Technology, January 1967.

62. Poplin, J. K., "Dynamic Bearing Capacity of Soils; Report 2 - Dynamically Loaded Small - Scale Footing Tests on Dry, Dense Sand," Technical Report No. 3-599, U. S. Army Engineer Waterways Experiment Station, CE, Vicksburg, Mississippi, September 1965.

63. Richmond, S. B., _Statistical Analysis_, The Ronald Press Company, 2nd Edition, 1964.

64. Schimming, B. B., Haas, H. J., and Saxe, H. C., "Study of Dynamic and Static Failure Envelopes," _Proceedings_, ASCE, Vol. 92, No. SM2, March 1966, pp. 105-124.

65. Scott, R. F., _Principles of Soil Mechanics_, Addison - Wesley Publishing Co., Inc., 1963.

66. Selig, E. T. and Vey, E., "Shock Induced Stress Wave Propagation in Sand," _Proceedings_, ASCE, Vol. 91, No. SM3, May 1965, pp. 19-49.

67. Taylor, D. W., _Fundamentals of Soil Mechanics_, John Wiley and Sons, Inc., 1948.

68. Tschebotarioff, G. P., _Soil Mechanics, Foundations, and Earth Structures_, McGraw-Hill Book Co., Inc. 1951.

69. U. S. Bureau of Reclamation, _Earth Manual_, U. S. Government Printing Office, Washington 25, D. C., 1st Edition, 1960.

70. Vey, E., Nelson, J. D., "Engineering Properties of Simulated Lunar Soils," _Proceedings_, ASCE, Vol, 91, No. SM1, January 1965, pp. 25-52.

71. Wahlstrom, E. E., _Petrographic Mineralogy_, John Wiley and Sons, Inc., 1955.

72. Whitman, R. V. and Healy, K. A., "Shear Strength of Sands During Rapid Loadings," _Proceedings_, ASCE, Vol. 88, No. SM2, April 1962, pp. 99-132.